Observations and modelling of super-luminous supernovae

A thesis submitted for the degree of
Doctor of Philosophy

by

Matthew Nicholl, M.Phys.
(Oxford University 2012)

Faculty of Engineering and Physical Sciences

School of Mathematics and Physics
Department of Physics and Astronomy
Queen's University Belfast
Belfast, Co. Antrim, Northern Ireland

September 2015

For Ashley

Acknowledgements

I would like to start by thanking my supervisor, Professor Stephen Smartt. I can't imagine a better supervisor than Stephen, who gave me space to pursue ideas, but was always available (despite his *many* other commitments!) to discuss progress and push me in the right direction. It was a real privilege to be able to draw on a wealth of knowledge and academic nous from such a respected researcher. So thank you, Stephen; I don't think I could have achieved half as much without your help and encouragement. And of course thank you for all the travel money and opportunities to further my career.

I have received invaluable assistance from the supernova group here. I'd especially like to thank Drs. Cosimo Inserra, Anders Jerkstrand, Stuart Sim, Morgan Fraser, and my second supervisor, Rubina Kotak, who between them have taught me most of what I know about astronomy. Thanks to Janet (now Dr. Chen) for being a great person to work alongside on SLSNe, and for all the Taiwanese treats! To all the other members of the SN group and ARC, thank you for making Queen's such a stimulating – and most importantly, fun – place to work. In particular, I'd like to thank my fellow PhD students. The burritos, curries and nerf wars were an essential part of my Queen's experience!

One of the great things about coming back to Northern Ireland for these three years has been the chance to spend more time with my amazing family. Thank you, Mum and Dad, for making home such a thoroughly enjoyable place to spend a weekend – and not just because of the free food! Your encouragement during my PhD studies is just the tip of the iceberg when I think of the love and help and support that you've always shown me. And it would be remiss of me not to mention that Mum bravely proofread this entire thesis! I have also found myself in the lucky position to have a brother, James, who I count among my best friends. I'm proud of you and can't wait to see you fulfil your own ambitions, be it in music, software, or something totally unexpected!

To all of the friends I have made in Belfast, Derry and Oxford: thank you for all of the fun times over the years. You've helped me to remain a rounded person whenever science has threatened to take over! I know we'll continue to stay in touch, and hopefully have many more reunion weekends. Special thanks to James and Susie Dickey for being the best possible housemates, and to Ryan Nicholl (no relation) for first introducing me to Stephen Smartt and the QUB physics department back in 2011.

Finally, I want to thank Marisa. I met you at the halfway point in my PhD, and I don't think it's a coincidence that I've enjoyed the second half so much more than the first (not that it was bad before!). Thank you for the love and adventures, and for being as interested in my studies as I am in yours. To the rest of the McVey family: I cannot thank each of you enough for the warmth and hospitality you've shown me; it's been like having a second family here in Belfast.

M.N.
July 2015, Belfast

Abstract

In the last decade, supernova science has undergone a revolution. Technological advances have made it possible to search for transients over the whole sky with no inherent galaxy bias. This strategy has revealed a population of extremely bright explosions – in otherwise anonymous galaxies – that are now known as super-luminous supernovae (SLSNe). While this discovery has increased our knowledge of the diverse ways in which massive stars end their lives, it is still unclear what conditions lead to a SLSN (though low metallicity seems to be required). Even more fundamentally, we do not know the power source underlying their luminosity. The nature of these explosions is one of the biggest outstanding questions in stellar astrophysics. If we wish to build a complete picture of massive-star evolution, it is essential to understand the properties of SLSNe. Moreover, their intrinsic brightness and blue colours will offer a new window into the high-redshift Universe with next-generation instrumentation.

In this thesis, we present the results of extensive ground-based monitoring campaigns for a number of hydrogen-poor (Type Ic) SLSNe at relatively low-redshift ($0.1 < z < 0.35$), making these some of the best-observed examples of this class in the literature. We use photometric and spectroscopic data, primarily in the optical but also in the UV and NIR, to constrain their luminosities, velocities and temperatures. We measure the characteristic diffusion time for all objects in the literature with reasonable light curve coverage and use this to infer ejected masses, showing that masses are typically larger than in normal-luminosity hydrogen-poor supernovae (including GRB supernovae). High ionisation may also be a factor in broadening the light curves of SLSNe Ic. However, we show that even for the slowest-evolving objects, the light curve rise time and inferred ejecta mass are well below the predictions for hypothetical pair-instability supernovae (PISNe). This is true even for slowly fading SLSNe identical to the well-studied SN 2007bi, an object caught during the decline phase and that was thought to be a strong candidate for a PISN. We therefore argue that no SLSNe observed so far are PISNe. For one SLSN Ic caught soon after explosion, a double-peaked light curve seems to indicate a surprisingly extended progenitor, which may be an important new clue.

These properties are modelled using a semi-analytic code that we have adapted and helped to develop as part of this work. Three possible power sources are investigated:

radioactive ^{56}Ni; a central engine such as magnetar spin-down; and interaction with a massive circumstellar medium. We find that the latter two can reproduce the light curves of all objects reasonably well, but that ^{56}Ni-powering requires unrealistic model parameters, even for slowly fading objects. The observed spectra of SLSNe Ic may be able to break the degeneracy between central engine and interaction models. The lack of narrow emission or absorption lines, the presence of broad lines well before light curve maximum, high velocities with little sign of deceleration, the overall similarity to SNe Ic, and agreement with literature models for magnetar-energised ejecta all suggest that a millisecond magnetar (or possibly black hole accretion) engine is the most probable power source in SLSNe Ic.

Contents

List of Tables

List of Figures

Publications

Publications resulting from the work presented in this thesis

1. **Nicholl, M.**, Smartt, S. J, Jerkstrand, A., et al.
   Slowly fading super-luminous supernovae that are not pair-instability explosions
   2013, Nature, 502, 346

2. Benetti, S., **Nicholl, M.**, Capellaro, E., et al.
   The supernova CSS121015:004244+132827: a clue for understanding superluminous supernovae
   2014, Monthly Notices of the Royal Astronomical Society, 441, 289

3. **Nicholl, M.**, Smartt, S. J, Jerkstrand, A., et al.
   Super-luminous supernovae from PESSTO
   2014, Monthly Notices of the Royal Astronomical Society, 444, 2096

4. **Nicholl, M.**, Smartt, S. J, Jerkstrand, A., et al.
   LSQ14bdq: a Type Ic super-luminous supernova with a double-peaked light curve
   2015, The Astrophysical Journal Letters, 807, L18

5. **Nicholl, M.**, Smartt, S. J, Jerkstrand, A., et al.
   On the diversity of super-luminous supernovae: ejected mass as the dominant factor
   2015, Monthly Notices of the Royal Astronomical Society, 452, 3869

Other publications co-authored during this period

1. Inserra, C., Smartt, S. J., Jerkstrand, A., et al.
   Super-luminous Type Ic Supernovae: Catching a Magnetar by the Tail
   2013, The Astrophysical Journal, 770, 128

2. McCrum, M., Smartt, S. J., Kotak, R., et al.
   The superluminous supernova PS1-11ap: bridging the gap between low and high redshift
   2014, Monthly Notices of the Royal Astronomical Society, 437, 656

3. Inserra, C., Sim, S. A., Wyrzykowski, L., et al.
   OGLE-2013-SN-079: a lonely supernova consistent with a helium shell detonation
   2015, The Astrophysical Journal Letters, 799, L2

4. Smartt, S. J., Valenti, S., Fraser, M., et al.
   PESSTO : survey description and products from the first data release of the Public ESO Spectroscopic Survey of Transient Objects
   2015, Astronomy & Astrophysics, 579, A40

5. Elias-Roas, N., Pastorello, A., **Nicholl, M.**, et al.
   Explosion of a massive, He-rich star at z=0.16
   2015, Monthly Notices of the Royal Astronomical Society, 451, 3151

6. Chen, T.-W., Smartt, S. J., Jerkstrand, A., **Nicholl, M.**, et al.
   The extreme emission line host galaxy and late time light curve of the superluminous supernova PTF12dam
   2015, Monthly Notices of the Royal Astronomical Society, 452, 1567

Chapter 1

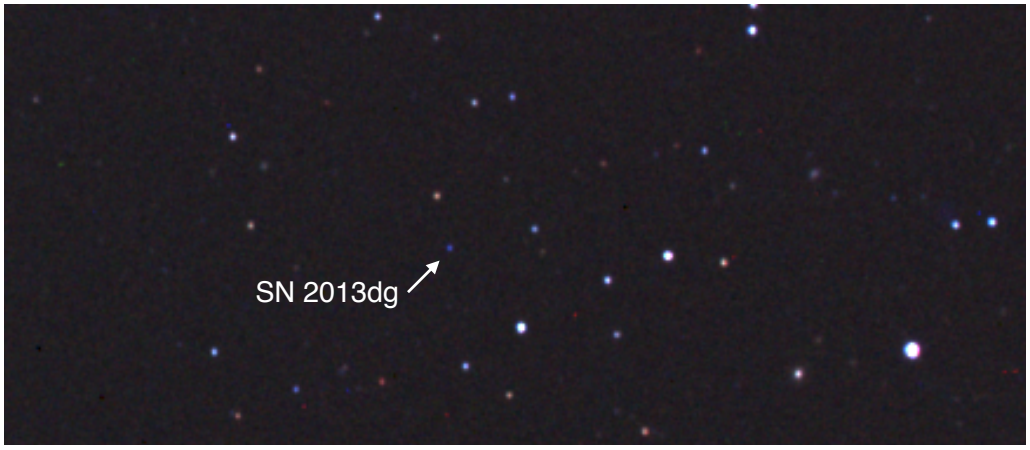

Introduction

"Tiger got to hunt, bird got to fly
Man got to sit and wonder 'why, why, why?'
Tiger got to sleep, bird got to land
Man got to tell himself he understand."
- Kurt Vonnegut ('Cat's Cradle')

1.1 Novae and Supernovae

The term ‘nova’, meaning ‘new’, describes astronomical point sources that appear suddenly, and then fade back into obscurity. In reality, these sources are not new. They are existing binary systems that brighten rapidly as gas is accreted onto a white dwarf from its companion and burns explosively (e.g. Bode & Evans 1985).

The word ‘supernova’ was first coined by Baade & Zwicky (1934), who noticed that not only did some observed novae originate at ‘nebular distances’ (i.e. in other galaxies), but a number of these outshone their parent galaxies. The required radiative output, $\sim 10^{48}$ erg over a period of weeks to months, is many orders of magnitude greater than in classical novae, proving that these objects formed an entirely separate class of astrophysical transients. These luminous events are in fact the final, destructive stage in the lives of stars, wherein much or all of the stellar material is explosively ejected, enriching its galactic environment with nucleosynthetic products.

Because of their brightness, supernovae (SNe) have in fact been observed since antiquity. ‘Guest stars’, now known to be SNe, were recorded by astronomers as far back as AD 185, with further examples in AD 386, 393, 1006, 1054, 1181, 1572 (Tycho’s SN) and 1604 (Kepler’s SN). All of these historical SNe occurred in our own Galaxy (see Stephenson & Green 2002, for details). The estimated rate of events in the Milky Way is approximately 1 or 2 per century.

1.2 Observational properties of supernovae

Spectroscopic observations of SNe show them to be a diverse family (for a review, see Filippenko 1997). Objects are divided into an array of subtypes, based primarily on the dominant atomic lines in their spectra, beginning with the most abundant element in the Universe: hydrogen. Figure 1.1 outlines the classification scheme. The most basic observational classes are Type I SNe, which are hydrogen-poor (and originate from compact stars), and hydrogen-rich Type II SNe, for which the progenitors have been shown to be red and blue supergiants (Smartt 2009). These types can be further subdivided: SNe IIb show hydrogen only in the first days after the explosion; SNe Ib show no hydrogen; SNe Ic show neither hydrogen nor helium. The physical interpretation here is an increasing degree of envelope-loss prior to explosion, either through binary interaction or in a Wolf-Rayet wind. In some cases, the temporal evolution in brightness (the light curve) can also play a role: SNe IIP exhibit a luminosity ‘plateau’, compared to ‘linear’-declining SNe IIL, (though note that this distinction is contentious; see e.g. Patat et al. 1994; Anderson et al. 2014; Faran et al. 2014; Gall et al. 2015). Another group, SNe IIn, show spectra dominated by narrow Balmer emission lines (Schlegel

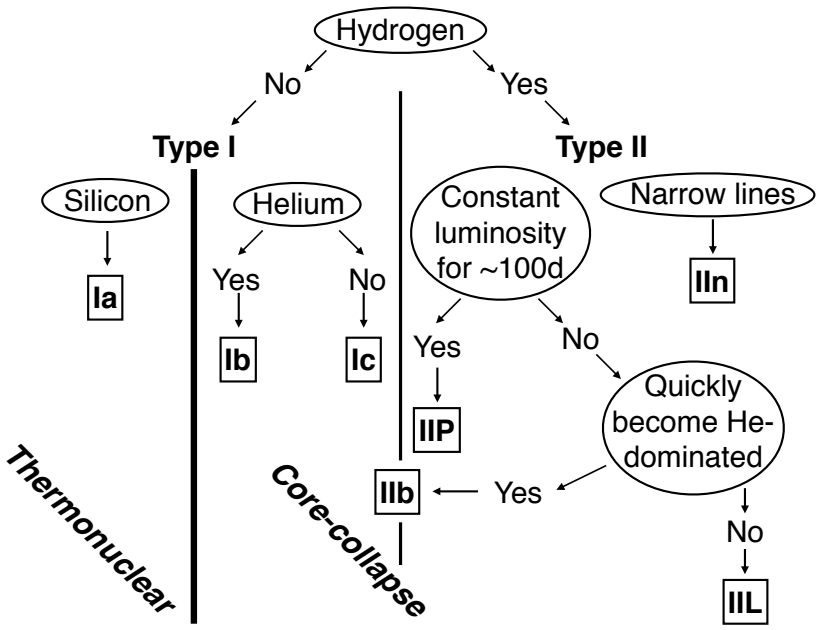

Figure 1.1: The observational classification scheme used to type normal SNe. Note that Type Ibc SNe may also exhibit silicon (specifically, the Si II λ 6355 line), but only weakly compared to SNe Ia (see Figure 1.2).

1990). Type Ia SNe, which show spectra dominated by silicon and iron-group elements, are fundamentally different from the other classes, as will be explained in Section 1.3.1.

Example spectra for the major SN types are given in Figure 1.2. The figure also demonstrates a few properties that are common between the subtypes. The spectral energy distribution (SED) typically peaks in the optical when the SN is at its brightest, which is convenient for ground-based study. The inferred effective and colour temperatures are $\sim 10^4$ K. However, the spectrum deviates significantly from that of a black-body, as the continuum is altered by very broad (thousands of kilometres per second) absorption and emission lines, often exhibiting P Cygni profiles (Figure 1.3). While the ionic species responsible for these transitions vary between the SN subtypes, the observed line profiles indicate that the material comprising the SN is in all cases rapidly expanding.

1.3 Energy generation in supernovae

While there are a broad range of observational subtypes of SNe, the explosion itself is generally triggered by one of only two mechanisms: thermonuclear runaway, and iron core-collapse.

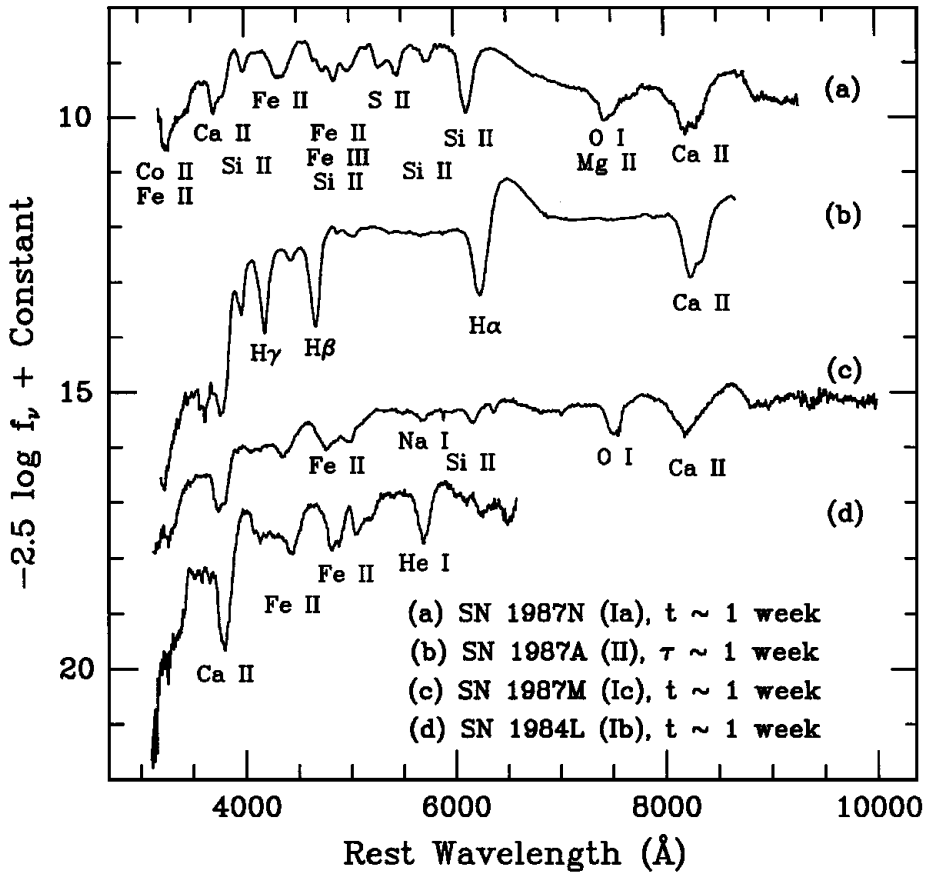

Figure 1.2: Spectra, taken around the epoch of maximum luminosity, of the main subtypes of SNe. *Credit*: Filippenko (1997).

1.3.1 Thermonuclear supernovae

Type Ia SNe are the thermonuclear detonations of carbon-oxygen white dwarfs. These are the remnants of stars with zero-age main sequence mass $M_{\rm ZAMS} < 8\,{\rm M}_\odot$, where $\rm M_\odot$ is the mass of our Sun. Following core hydrogen- and then helium-burning, such stars do not achieve the core temperature necessary to begin carbon fusion. They lose their outer layers during a planetary nebula phase, while the core remains supported by electron degeneracy pressure.

However, there is a maximum mass that this can support: the Chandrasekhar mass, $M_{\rm Ch} \approx 1.4\,{\rm M}_\odot$. If the white dwarf subsequently increases in mass above this limit, contraction leads to carbon ignition under degenerate conditions (i.e. with no increase in pressure to regulate temperature), hence runaway fusion occurs. It is not yet known where the additional mass comes from - it may be transferred from a non-degenerate companion star ('single-degenerate model'), or result from the merging of two white dwarfs ('double-degenerate model'). Both channels may contribute to the observed SN Ia population. In either case, most of the white dwarf is burned rapidly to silicon and iron peak elements. This releases sufficient energy to explode the star with $\sim 10^{51}$ erg

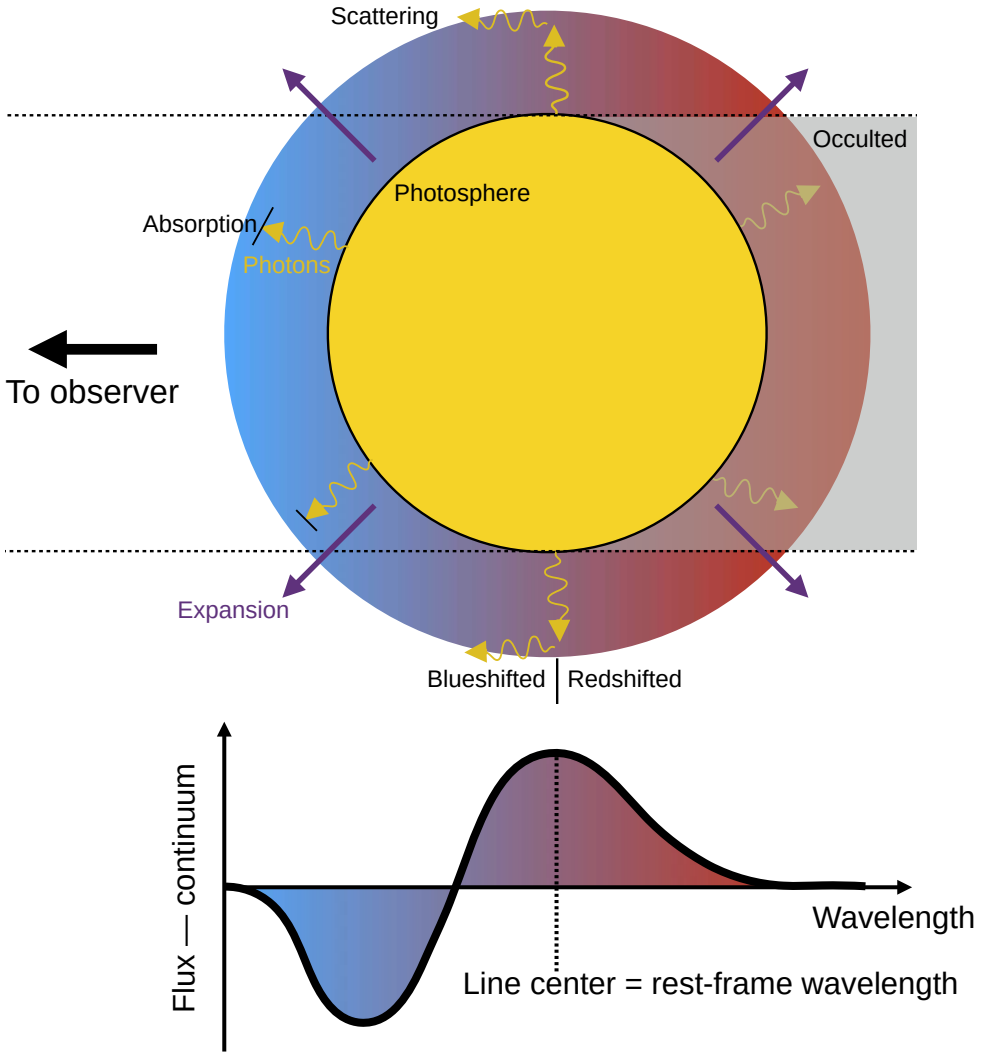

Figure 1.3: Schematic of P Cygni line formation in SNe. The continuum emission is formed at the opaque photosphere, where the opacity is high due to electron scattering in highly ionised material. Above this, photons are absorbed and scattered by atomic lines in an expanding atmosphere. This expansion leads to blueshifted absorption, and a scattering peak around the rest-frame wavelength of the transition. We do not see redshifted absorption, as the material moving away from the observer is hidden from view by the photosphere.

of kinetic energy. Although adiabatic expansion of the ejecta causes rapid cooling, a bright SN is powered by radioactive decays. The explosion synthesises $\gtrsim 0.5\,M_\odot$ of radioactive nickel $\left(^{56}\mathrm{Ni}\right)$, which decays to ^{56}Co with a half-life of 6 days. The ^{56}Co then decays to ^{56}Fe, with a half life of 77 days; this is the main power source at later times.

SNe Ia have attracted much interest in recent decades because their peak luminosities can be standardised using the subsequent decline rate (Phillips 1993). Thus the distance modulus can be inferred from the light curve. They are also bright enough to observe at cosmological distances. The combination of these properties allowed two teams, the High-Z Supernova Search Team (Riess et al. 1998) and the Supernova Cos-

mology Project (Perlmutter et al. 1999), to show that the expansion of the Universe is accelerating. This revolutionary result has since been confirmed by independent measurements.

1.3.2 Core-collapse supernovae

More massive stars, with $M_{\rm ZAMS} > 8\,{\rm M}_{\odot}$, do burn carbon stably in their cores, and go on to ignite neon, then oxygen, then silicon. While the initial phase of core hydrogen-burning typically lasts for several million years, the final silicon-burning stage lasts only for about a day. The silicon burning ash is primarily iron. Because iron nuclei have the highest binding energy per nucleon, no further energy generation can take place from nuclear fusion in the core. The iron core is supported by electron degeneracy pressure, while around it lighter nuclei burn in shells of successively lower temperature, leading to a layered 'onion-skin' structure.

The innermost shell, where silicon fusion takes place, feeds the iron core until its mass reaches $M_{\rm Ch}$. As in thermonuclear SNe, this is the point at which electron degeneracy pressure can no longer support the star. The collapse is catastrophic. The high density leads to spontaneous electron-capture reactions, $p + e^- \rightarrow n + \nu_e$, reducing the pressure and allowing the collapse to proceed essentially on a free-fall timescale, while the iron nuclei undergo photodisintegration, undoing millions of years of nuclear fusion in about a second. The gravitational potential energy of the pre-collapse core, $\sim 10^{53}\,{\rm erg}$, provides a huge energy reservoir, most of which is released in the form of neutrinos. Detection of neutrinos from the nearby SN 1987A confirmed the basic picture of core-collapse, originally proposed by Zwicky (1939).

At sufficiently high density ($\sim 10^{15}\,{\rm g\,cm^{-3}}$), neutron degeneracy pressure halts the collapse of the inner core, at a radius of a few tens of kilometres. Infalling material from the outer core then encounters this solid ball of nuclear matter, and its kinetic energy is converted to heat, increasing the pressure and driving a shock outwards – this is the 'bounce' phase of core-collapse. However, this shock loses most of its energy to photodisintegration reactions in the outer core, causing it to stall. The exact mechanism by which the shock is revived, in order to eject the stellar envelope with the observed kinetic energy of $\sim 10^{51}\,{\rm erg}$, is an important and longstanding problem. The general consensus is that a few percent of the neutrino energy is tapped through weak interactions. It is hoped that as numerical simulations become more advanced, the details of this picture will be confirmed (e.g. Janka & Müller 1996; Janka et al. 2007; Buras et al. 2003; Nordhaus et al. 2010; Ott et al. 2013).

The light curves of Type I core-collapse SNe (Types Ib and Ic) are powered by the

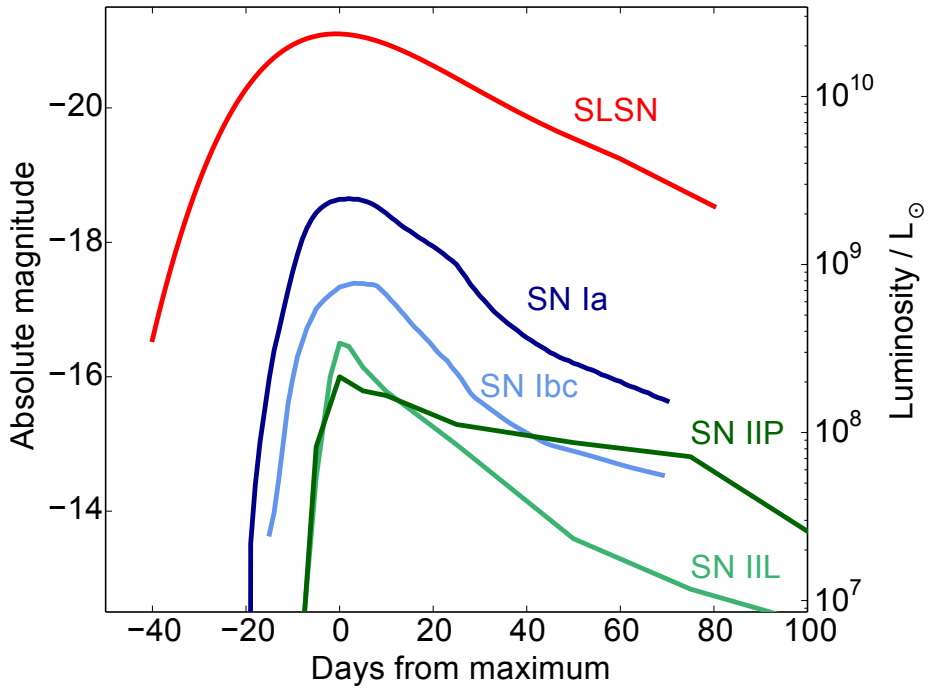

Figure 1.4: Template light curves of SN subtypes. Despite very different explosion mechanisms, the light curves of Type Ia and Type Ib/Ic SNe are similar, as both are powered by the decay of ^{56}Ni. Type II SNe are often divided into IIP and IIL based on the light curve decline rate after maximum. Super-luminous SNe are brighter than the other SNe by a factor of 10-100, and evolve slowly.

decay of ^{56}Ni (typically a few tenths of a solar mass). Type II SNe tend to synthesise less than 0.1 $M_\odot$ of ^{56}Ni; their light curves are instead powered by recombination and radiative cooling of the extended hydrogen envelope, which suffers much less from adiabatic losses than do the ejecta from compact, stripped-envelope stars. Type IIn SNe may have their luminosity boosted by further shock heating in circumstellar material (the shocked, low-velocity CSM is also responsible for the narrow emission lines). Typical light curves for the various SN types are shown in Figure 1.4.

1.4 Supernovae and gamma-ray bursts

Some Type Ic SNe are associated with another group of luminous transients: long-duration gamma-ray bursts (GRBs). Long GRBs are the only explosions in the modern Universe to rival SNe in terms of their energetics (see Woosley & Bloom 2006, for a review). Despite lasting only a few seconds, the apparent energy released in γ-rays (assuming isotropy) can reach $\sim 10^{53}$ erg. However, this emission is now known to be beamed, and the true integrated output is more like $\sim 10^{51}$ erg, similar to the kinetic energy in SNe. The tantalising connection of long GRBs with SNe was confirmed when

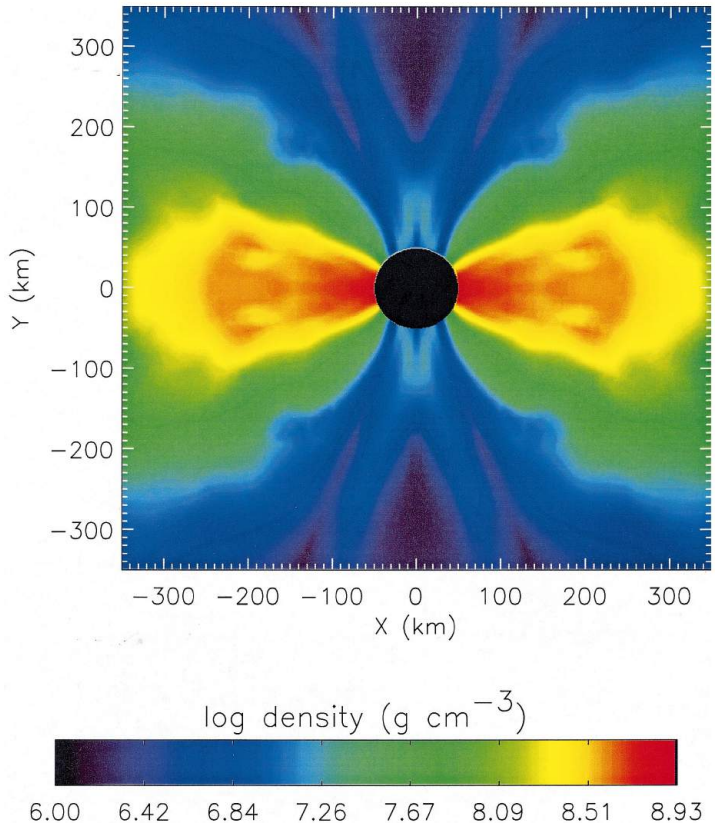

Figure 1.5: The collapsar model of GRBs: The density structure in the central region of a rapidly-rotating 14 $M_\odot$ helium star, 7.6 s after core-collapse. Conservation of angular momentum supports a torus around the equator, while low-density regions form at the poles due to efficient accretion onto the black hole. This structure supports the formation of bipolar jets. The accretion power acts as an engine to drive the explosion. A similar model may be applicable to SLSNe (Dexter & Kasen 2013). *Credit*: MacFadyen & Woosley (1999).

Galama et al. (1998) discovered SN 1998bw at the location of GRB 980425, in the nearby galaxy ESO184-G82. This turned out to be one of the brightest core-collapse SNe known at the time, and also exhibited an unprecedented spectrum. While technically a SN Ic, the spectral lines were extraordinarily broad, with an inferred expansion velocity of $\sim 30000\,\mathrm{km\,s^{-1}}$ (Patat et al. 2001).

With the discovery of further GRB-associated, over-energetic SNe Ic, such as SN 2003dh (Stanek et al. 2003; Hjorth et al. 2003; Matheson et al. 2003) and SN 2006aj (Campana et al. 2006; Mazzali et al. 2006a; Modjaz et al. 2006; Sollerman et al. 2006), a consistent picture emerged. These explosions result from the core-collapse explosions of massive stars that have lost their hydrogen and helium envelopes; however, only a few percent of SNe Ic are hyper-energetic, and less than 1 percent produce long GRBs (Podsiadlowski et al. 2004; Guetta & Della Valle 2007). The collimated γ-ray emission requires relativistic jets of material breaking out of the stellar envelope, suggesting a

bipolar explosion. The total kinetic energy of the SN ejecta is $\sim 10^{52}$ erg, which is too high to be explained by the neutrino mechanism favoured for normal core-collapse SNe.

The preferred model to explain these properties is the 'collapsar' model of Woosley (1993). In this model, the inner core of the star collapses to a black hole (implying a massive progenitor, expected to end its life as a hydrogen-free Wolf-Rayet star). If the core has sufficient angular momentum, the outer material cannot collapse directly, and instead forms an accretion disk (Figure 1.5). Accretion power is then assumed to provide the energy to drive the outflow, which is collimated by the geometrically thick disk. The necessary combination of large mass and rapid core rotation explains why these events are rare compared to the normal SN population. A competing model, in which the engine powering the explosion is a strongly magnetised neutron star (e.g. Thompson et al. 2004, also see Section 1.6.1 below), is subject to similar constraints on the progenitor. GRB-associated SNe tend to exhibit broad and bright light curves, indicating high ejecta mass and ^{56}Ni mass. The origin of this ^{56}Ni is still uncertain, with some models suggesting it is synthesised in the accretion disk (Nagataki et al. 2006). Analysis of their host galaxies suggests that GRB-SNe favour low-metallicity environments (Modjaz et al. 2008).

1.5 Super-luminous supernovae

1.5.1 Discovery

At the turn of the century, virtually all known SNe could be incorporated into the observational and theoretical framework outlined in Sections 1.2-1.4. However in the last decade, transient astronomy has been revolutionised by the proliferation of expansive, untargetted sky surveys, such as the Palomar Transient Factory (PTF; Rau et al. 2009), Pan-STARRS1 (PS1; Kaiser et al. 2010), the La Silla QUEST survey (LSQ; Baltay et al. 2013) and the Catalina Real-Time Transient Survey (CRTS; Drake et al. 2009), and spectroscopic follow-up resources such as the Public ESO Spectroscopic Survey of Transient Objects (PESSTO; Smartt et al. 2015). Thousands of SNe are now being discovered each year, revealing unexpected new types of explosions with some puzzling properties.

Perhaps the most surprising of these are the "super-luminous" supernovae (SLSNe; Gal-Yam 2012), so called because of peak luminosities that are 2-5 magnitudes – or a factor 10-100 – brighter than the bulk of the SN population, as shown in Figure 1.4. Previous SN searches missed the SLSNe for two reasons: firstly, because they are exceptionally rare events, making up only ~0.01% of SNe (Quimby et al. 2013;

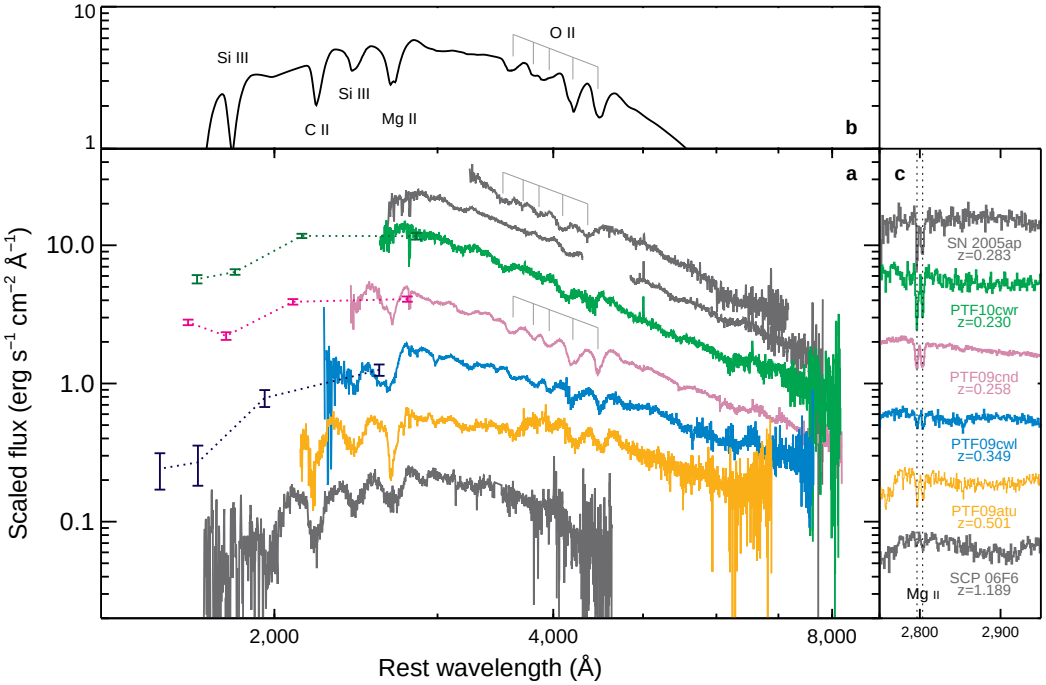

Figure 1.6: Early spectra of SLSNe Ic, obtained prior to maximum light. The strongest features in the optical have been attributed to O II. *Credit*: Quimby et al. (2011)

McCrum et al. 2015); secondly, they tend to occur in faint galaxies, which were ignored by targeted surveys. Because of their high luminosities, spectroscopically-confirmed SLSNe have been found by PS1 at redshifts out to $z \sim$ 1-1.5 (Chomiuk et al. 2011; Berger et al. 2012), and candidates have even been detected photometrically at $z \sim$ 2-4 in stacked SNLS data (Cooke et al. 2012).

1.5.2 Hydrogen-poor SLSNe

Extensive studies of SLSNe in the last few years illustrate a diversity in their spectroscopic and photometric properties. Many display no signs of hydrogen (i.e., are SLSNe of Type I, by analogy with normal-luminosity SNe). The earliest examples of such objects are SN 2005ap (Quimby et al. 2007), the brightest SN then known, and SCP06F6 (Barbary et al. 2009) a mysterious transient at an unknown redshift. For a number of years, these SNe were unexplained outliers, but this situation changed when Quimby et al. (2011) showed that they matched a sample of four objects discovered by PTF, and demonstrated that together these formed a new class of SNe. Common features of the class include spectra with very blue continua, peaking in the near-ultraviolet, and broad absorption features attributed to O II (Figure 1.8). Secure redshift measurements, determined from interstellar Mg II narrow absorption lines, showed that these

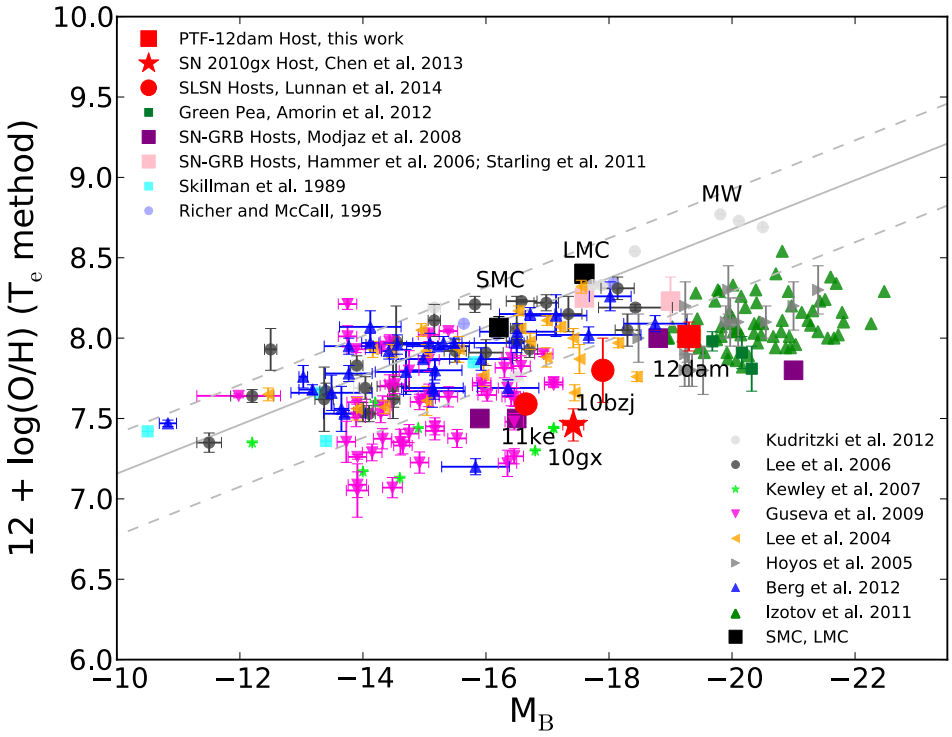

Figure 1.7: The distribution of oxygen abundance versus *B*-band luminosity for a combined literature sample of dwarf galaxies. The SLSN Ic hosts (red) lie at the metal-poor edge. *Credit*: Chen et al. (2015)

objects exhibited absolute photometric magnitudes brighter than −21. The authors also showed that the light curves of these objects cannot be explained using only the standard paradigms of SN shock-heating and the decay of synthesised ^{56}Ni.

For one of these new objects, SN 2010gx, spectra obtained by Pastorello et al. (2010) several weeks after light curve maximum showed a surprising transformation to resemble normal SNe Ic. This evolution has since been shown to be ubiquitous (Inserra et al. 2013), and objects in this class are now usually referred to as SLSNe Ic. Inserra & Smartt (2014) found that SLSN Ic peak magnitudes may be standardisable in a similar fashion to those of SNe Ia. If this is the case, these objects would be perfectly suited to cosmological studies of the very distant Universe, due to their extreme luminosities and blue colours.

The environments where SLSNe Ic have been found may offer a clue to their nature. They seem to occur only in low-metallicity dwarf galaxies (Neill et al. 2011; Chen et al. 2013) as shown in Figure 1.7; metallicity has therefore been proposed as the key requirement to form SLSNe (Chen et al. 2015). These host galaxies have been shown to be similar to those of long GRBs (Lunnan et al. 2014), and often show signs of extreme star-formation (Leloudas et al. 2015), which may indicate high-mass progenitors.

1.5.3 Hydrogen-rich SLSNe

Another group, SLSNe II, do have hydrogen in their spectra. This is sometimes in the form of strong, multi-component emission lines, almost certainly indicating interaction with a circumstellar medium (CSM). The prototypical example here is SN 2006gy (Ofek et al. 2007; Smith et al. 2007). Quite a few such objects are now known – e.g. SNe 2006tf (Smith et al. 2008), 2008fz (Drake et al. 2010), 2008am (Chatzopoulos et al. 2011) and 2003ma (Rest et al. 2011) – and these are quite correctly dubbed 'SLSNe IIn', by analogy with the fainter SNe IIn, which are hydrogen-rich SNe showing narrow spectral lines from shocked CSM. The physical mechanism thought to power their luminosity is essentially the same as for normal SNe IIn: reprocessing of the kinetic energy of the ejecta when it collides with the CSM (see Section 1.6.3).

However, a few SLSNe have much weaker hydrogen lines visible, which are not obviously multi-component and do not unambiguously point to interaction being the dominant power source for the radiated energy. The earliest example of this class is SN 2008es (Gezari et al. 2009; Miller et al. 2009). Although they are classed as SLSNe II, they resemble SLSNe Ic with H lines superimposed. Their overall light curve and other spectral properties may be closer to SLSNe Ic than to the SLSNe IIn. One object in particular, CSS121015, prompted Benetti et al. (2014) to propose that the two spectroscopic classes of SLSNe may in fact come from the same underlying physical process, with their observational properties modified by the hydrogen mass in the ejecta and/or CSM. The authors favoured the interaction scenario, due to the presence of time-variability in the narrow Balmer emission lines, indicating slow-moving material close to the SN. While SLSNe II have been found in faint galaxies similar to the hosts of SLSNe Ic, SLSNe IIn have also been found in massive, metal-rich hosts (Leloudas et al. 2015).

1.6 Proposed models for SLSNe

Three main models have been proposed to account for the enormous energy radiated by SLSNe. These are outlined below.

1.6.1 Central engine

The first model is a core-collapse SN that is boosted in energy by a central engine. The earliest suggested example of such an engine was a highly magnetised neutron star ($B \sim 10^{14}$ G), spinning with a period of order milliseconds (often referred to as the magnetar model; Kasen & Bildsten 2010; Woosley 2010). Magnetars (albeit with longer spin periods) have been observed in our Galaxy, and are thought to originate

from stars with main-sequence masses $M_{\rm ZAMS}$ = 30-40 $\rm M_\odot$ (Gaensler et al. 2005; but see also Davies et al. 2009). It has been suggested that rapid rotation of the stellar core at collapse can support a dynamo mechanism in the proto-neutron star, which generates the enormous B-field (Duncan & Thompson 1992). The rotation of the magnetar gives a large energy reservoir (2×10^{52} erg for a maximally spinning pulsar: $P_{\rm spin}$ = 1 ms), and as it spins down, this reservoir is tapped via the magnetic field to heat the ejected SN gas (though it is an open question as to exactly how this energy can thermalise in the ejecta; Metzger et al. 2014). Inserra et al. (2013) showed that this model gives good fits to the light curves of SLSNe Ic. Up to $\sim$ 10% of core-collapses may form magnetars (Kasen & Bildsten 2010); however, the initial-spin distribution is not known.

For very massive stars ($M_{\rm ZAMS} > 20\,\rm M_\odot$), many core-collapse events are thought to produce black holes rather than neutron stars. In this case, another central engine is possible. Material that remains bound to the compact remnant after the explosion may turn around and fall back on a timescale of days (Dexter & Kasen 2013). This can form an accretion disk, and the energy liberated in accretion can then significantly affect the energy and observed properties of the SN. This model has been suggested as a potential explanation not only for super-luminous SNe, but for a variety of transients with unusual light curves.

1.6.2 Pair instability

Some hydrogen-poor SLSNe, such as SN 2007bi, have light curve gradients after peak magnitude that are consistent with the radioactive decay of ^{56}Co. These have been proposed (Gal-Yam et al. 2009; Gal-Yam 2012) to be the observational counterparts of the long-predicted pair-instability supernovae (PISNe; Barkat et al. 1967; Rakavy & Shaviv 1967). In these models, photons in the carbon-oxygen cores of 130-250 $\rm M_\odot$ stars are sufficiently energetic to decay into electron-positron pairs. This conversion of pressure-supporting radiation to rest mass triggers contraction, leading to thermonuclear run-away as the temperature rises. The resultant explosion is predicted to synthesise several solar masses of ^{56}Ni, which could power a bright light curve.

This physical scenario may be responsible for at most a small fraction of the SLSN population, since the slowly fading types appear to be rare compared to faster objects (which are not ^{56}Co-powered). McCrum et al. (2015) estimate the slowly fading SLSNe to make up around 10% of the total SLSN population. However, the physical reality of pair-instability explosions is not firmly established, and theory predicts that sufficiently massive stellar cores should form only at very low metallicity (e.g. Heger & Woosley 2002, but see also Yusof et al. 2013). Other models have been proposed to account for SN 2007bi, such as the core-collapse of a very massive star (Young et al. 2010;

Moriya et al. 2010), and some authors have argued that the observables of SN 2007bi were not fully consistent with PISN models. Dessart et al. (2012b) pointed out that SN 2007bi was much bluer than PISN models, which are very red due to line blanketing from the large mass of synthesised intermediate-mass and iron-group elements (Kasen et al. 2011; Dessart et al. 2013).

1.6.3 Circumstellar interaction

Another model, already mentioned briefly, is a collision with (or shock breakout from) a highly opaque CSM, releasing shock energy at a large radius (Ofek et al. 2010; Chevalier & Irwin 2011; Ginzburg & Balberg 2012). For the peak luminosities and temperatures (1-2 $\times 10^4$ K) observed in SLSNe, the required blackbody radius is $\sim 10^{15}$ cm ($\sim 10^5$ $R_\odot$). The mass of the CSM must be comparable to the ejected mass from the SN, in order to efficiently thermalise the ejecta kinetic energy.

This is the favoured model to explain SLSNe IIn (which clearly show signs of low-velocity material external to the SN), but it may also be applicable to SLSNe Ic. In this case, the interaction may require collisions between hydrogen-free SN ejecta and CSM, unless some other effect can obscure the presence of hydrogen. One model which can produce hydrogen-free shells is a 'pulsational' pair-instability SN (Woosley et al. 2007), in stars with $M_{\rm ZAMS}$ in the range 95-130 $M_\odot$. In this case, the core encounters the pair-instability described in Section 1.6.2, but the energy released by the explosive carbon/oxygen burning is less than the binding energy of the star. Many solar masses of material may be ejected before the star contracts again and resumes stable burning, and the instability may be encountered several times before the star ends its life in a normal iron core-collapse SN. No definitive objects of this type have been identified, but Ben-Ami et al. (2014) have presented SN 2010mb, an energetic SN Ic (though not technically super-luminous) with an extremely extended light curve and narrow oxygen emission lines, and their analysis gave strong evidence for a SN interacting with hydrogen-free circumstellar material, matching predictions of pulsational-PISN models.

Comparisons with data have shown that magnetar engines and circumstellar interaction can both reproduce the range of shapes of SLSN light curves, and distinguishing between them has been problematic (e.g. Chatzopoulos et al. 2013). However, it remains to be seen whether interaction models can produce the spectra of SLSNe Ic, which do not display narrow lines.

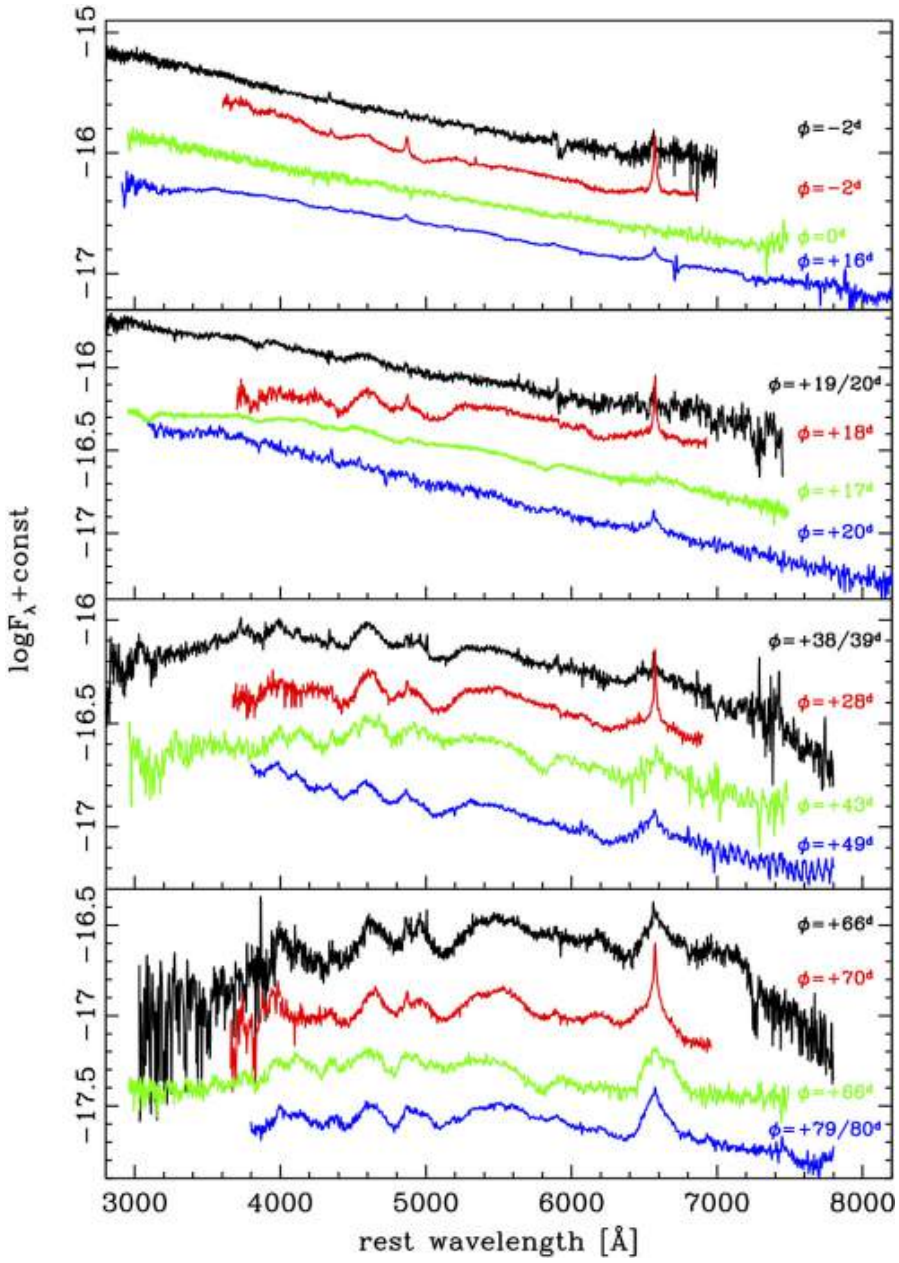

Figure 1.8: Spectral evolution of Type II SLSNe, CSS121015 (black; Benetti et al. 2014) and SN 2008es (green; Gezari et al. 2009; Miller et al. 2009), and the more typical SLSN IIn, SN 2008fz (blue; Drake et al. 2010). Particularly at early times, SN 2008fz shows narrow hydrogen lines, as are seen in other interacting SNe such as SN 2005gj (red), thought to be a SN Ia interacting with CSM (Aldering et al. 2006; Prieto et al. 2007). The narrow lines are weak in the other SLSNe II, which show broad hydrogen and metal lines. *Credit*: Benetti et al. (2014)

1.7 Thesis structure

As SLSNe are extremely rare events, and were largely unknown a decade ago, the number of well-studied events is small. This situation is now beginning to change, as transient surveys are becoming better at picking out these objects and dedicating resources to follow them up. This thesis focusses on detailed study of a number of SLSNe discovered by modern surveys. In particular, the various theoretical power sources are put to the test through the application of semi-analytic models to fit the observed light curves. The primary sky surveys used to collect the data are outlined in Chapter 2, along with some essential data reduction techniques. Chapter 2 also describes the development of the light curve models.

In Chapter 3, a sample of SLSNe from PESSTO is presented and analysed in the context of the competing theories. Chapter 4 looks at an unusual SLSN Ic from PS1, with a slowly declining light curve reminiscent of the pair-instability candidate, SN 2007bi; in contrast to that event, these SLSNe were caught and followed photometrically and spectroscopically from well before maximum light. This is followed in Chapter 5 by another slowly evolving SLSN Ic discovered by LSQ, which is detected within a day of explosion and exhibits an early peak prior to the main light curve rise, placing new constraints on the explosion mechanism. In Chapter 6, a larger sample of SLSNe from PESSTO and the literature is compiled, and studied to characterise the diversity in their physical parameters. This thesis is concluded in Chapter 7, with discussion of the main results and questions for further research.

Chapter 2

Methods

"Ah, there's nothing more exciting than science.
You get all the fun of sitting still,
being quiet, writing down numbers,
and paying attention... Yep, science has it all."
- Principal Seymour Skinner (The Simpsons, 'Bart's Comet')

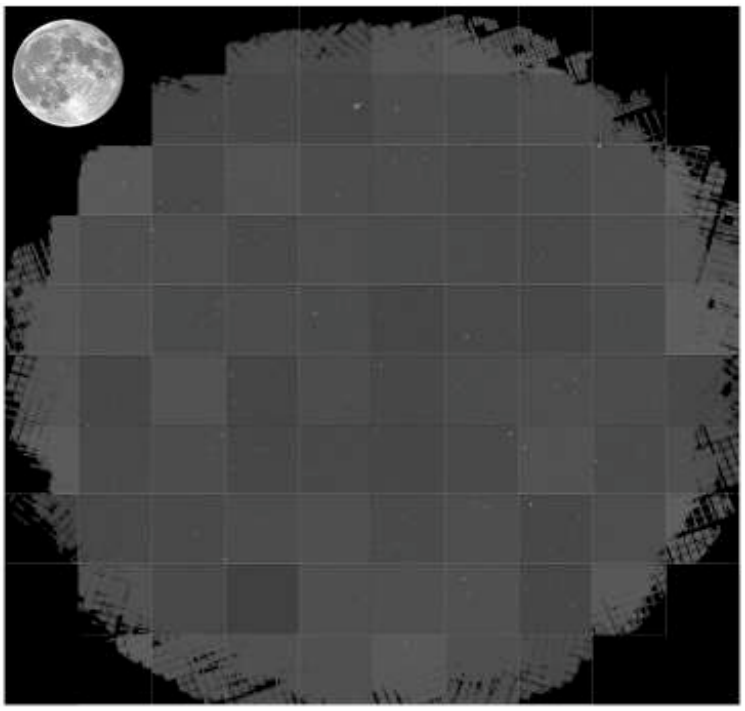

Figure 2.1: The field of view of the Pan-STARRS1 Gigapixel camera. In a single exposure, the 7 deg^2 field of view covers an area on the sky 40 times the size of the full moon.

2.1 Sky surveys

Virtually all SLSNe, in this thesis and the literature, have been discovered by untargetted, large-volume surveys, combined with spectroscopic follow-up. The surveys most relevant to the work undertaken here are outlined below.

2.1.1 Pan-STARRS1

PS1 is a high-etendue wide-field imaging system designed for dedicated survey observations, on a 1.8 meter telescope on Haleakala, Hawaii, with a 1.4 Gigapixel camera and a 7 deg^2 field of view. Observations are obtained through a set of five broadband filters, which are $g_{\rm P1}$ ($\lambda_{\rm eff}$ = 483 nm), $r_{\rm P1}$ ($\lambda_{\rm eff}$ = 619 nm), $i_{\rm P1}$ ($\lambda_{\rm eff}$ = 752 nm), $z_{\rm P1}$ ($\lambda_{\rm eff}$ = 866 nm), and $y_{\rm P1}$ ($\lambda_{\rm eff}$ = 971 nm). Tonry et al. (2012b) give a full description of the bandpasses, which are shown in Figure 2.2.

The PS1 Science Consortium ran a series of science surveys between 2010-2014. We make use of two such surveys for transient detection: the Medium Deep Field survey (MDS) and the wide 3π Survey. The goal of the 3π Survey is to observe the entire sky North of -30° declination. Every position on the sky within the survey area is observed four times in each of the five filters during a 12 month period, although

this can be interrupted by weather. The 4 epochs in a calendar year are typically split into two pairs called Transient Time Interval (TTI) pairs, which are single observations separated by 20-30 minutes to allow for the discovery of moving objects. The exposure times at each epoch (i.e. in each of the TTI exposures) are 43s, 40s, 45s, 30s and 30s in $g_{\rm P1}$, $r_{\rm P1}$, $i_{\rm P1}$, $z_{\rm P1}$, and $y_{\rm P1}$, leading to 5σ depths of roughly 22.0, 21.6, 21.7, 21.4, and 19.3 magnitudes (Inserra et al. 2013) in the PS1 AB system described by Tonry et al. 2012b. The PS1 images are processed by the Pan-STARRS1 Image Processing Pipeline (IPP), on a computer cluster hosted in the Maui High Performance Computer Center. This performs automatic bias subtraction, flat fielding, a flux-conserving warping to a sky-based image plane, masking and artifact removal, object detection, photometry and astrometry (Magnier et al. 2006, 2008). The TTI pairs are not stacked together, but kept as individual frames. Full stacking of all data across the sky over the 3.5 years of the survey is now underway, but for the purposes of transient searches the individual exposures are kept separate.

The PS1 MDS obtains deep multi-epoch images of 10 fields in the $g_{\rm P1}$, $r_{\rm P1}$, $i_{\rm P1}$, $z_{\rm P1}$, and $y_{\rm P1}$ bands, with a typical cycle of observations being $g_{\rm P1}$ and $r_{\rm P1}$ on one night, followed by $i_{\rm P1}$ and $z_{\rm P1}$ bands on the subsequent nights. In some cases this cycle is broken to optimise for sky brightness. Observations in the $y_{\rm P1}$ band are taken close to the full moon. The MDS images are also processed through the IPP, and are stacked to give a single nightly image containing eight exposures in a dithered sequence. The observing season for each field is 6 months per year.

In both surveys, transient detection is achieved by difference imaging with respect to deep reference images, and PSF-fitting photometry is carried out on the subtracted frames (see Section 2.3.2 for a description of this technique). Transient candidates are vetted as real/bogus by a machine learning algorithm (Wright et al. 2015), before 'eyeballing' by humans confirms the promising candidates. This process is carried out through the Transient Science Server (TSS) at Queen's University Belfast. Various aspects of the PS1 system and its application to transients have been described in detail by Inserra et al. (2013); Tonry et al. (2012a); Berger et al. (2012); Young et al. (2010); Gezari et al. (2012); Tonry et al. (2012b).

PS1 Science Consortium survey operations officially ended in mid-2014. Since then, the PS1 system has been used primarily for the Pan-STARRS NEO Science Consortium survey. Observations are taken in the $w_{\rm P1}$-band (a broad throughput filter, effectively a *gri* composite; Tonry et al. 2012b) during dark time, and in a combination of $i_{\rm P1}$, $z_{\rm P1}$, and $y_{\rm P1}$ filters during bright time. The cadence is optimised for finding moving objects, taking four 30-45 s exposures separated by 10-20 mins. In parallel with this

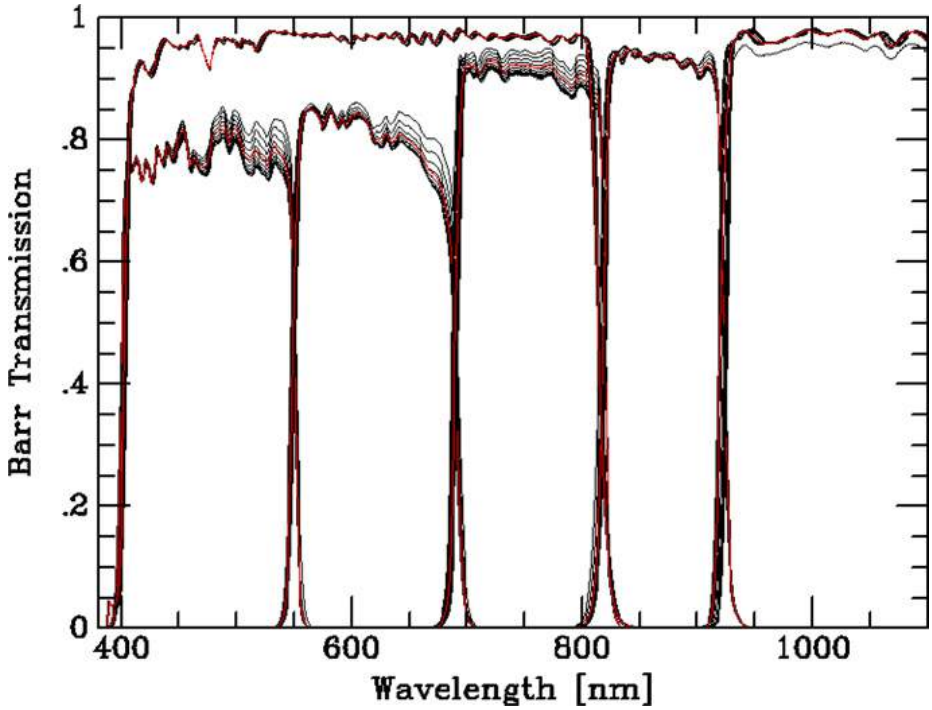

Figure 2.2: The PS1 filter set is based on the *griz* filters (left to right) used by SDSS, plus the $y_{\rm P1}$ (NIR; rightmost) and $w_{\rm P1}$ (wide *gri*) bands. *Credit*: Tonry et al. (2012b)

survey, Pan-STARRS continues to find stationary transients in the data using the IPP and TSS. The Pan-STARRS Survey for Transients (PSST) is effectively a continuation of the 3π transient survey, with the major difference being that discoveries are now made publicly available[1] (Smartt et al. 2014; Huber et al. 2015).

2.1.2 PESSTO

Photometric surveys, like PS1, have become very efficient at detecting supernova candidates. However, once a transient is discovered, spectroscopic follow-up is essential in order to determine the SN type and redshift (and hence the distance modulus). Transient surveys are currently limited by the amount of spectroscopic follow-up available, as spectroscopy of faint targets requires long exposure times, and often 4-8 m class telescopes. The burden of classification can be eased by dedicated spectroscopic follow-up surveys.

The Public ESO Spectroscopic Survey of Transient Objects (PESSTO; Smartt et al. 2015) uses the European Southern Observatory (ESO) 3.58m New Technology Telescope (NTT) in La Silla, Chile, for classification and follow-up of transients. PESSTO runs for 9 months of the year, with a break from May-July when the Galactic centre is over La Silla. In each month during the observing season, 10 nights of observations are

[1] http://star.pst.qub.ac.uk/ps1threepi/psdb/

divided into 3 runs, which are scheduled to avoid the full moon. Optical observations are carried out using the EFOSC2 spectrograph (Buzzoni et al. 1984), with a choice of grisms. Gr#13 (3650-9250 Å), used for classification, has a resolution of 18 Å, while follow-up can be done using a combination of Gr#11 (blue; 3345-7470 Å) and Gr#16 (red; 6000-9995 Å), which have resolutions $\sim$ 13 Å. Near-infrared (NIR) data are obtained with the SOFI instrument (Moorwood et al. 1998). PESSTO began operations in 2012.

Targets are provided to PESSTO by a variety of imaging surveys, including LSQ (Baltay et al. 2013), CRTS (Drake et al. 2009), SkyMapper (Keller et al. 2007), OGLE-IV (Wyrzykowski et al. 2014), the All-Sky Automated Search for SNe (ASAS-SN[2]) and PS1, as well as amateur discoveries. Photometric data from these surveys are ingested into a web-based aggregator known as the PESSTO Marshall, which also pulls information from The Astronomers Telegram[3] and the IAU Central Bureau for Electronic Telegrams[4] (for example, reports of previous classifications). The Marshall forms the backbone of the PESSTO workflow, displaying up-to-date light curves of all classification targets, and allowing PESSTO members interested in a particular object to provide comments and request data from the observing team at the NTT.

Data obtained by PESSTO is reduced using the custom PESSTO pipeline (developed in PYTHON by S. Valenti; see Smartt et al. 2015 for details), which calls standard IRAF (Image Reduction and Analysis Facility) tasks through PYRAF, to de-bias and flat-field the 2D frames. For imaging observations, the pipeline applies an astrometric solution using VIZQUERY (Ochsenbein 1994), while spectroscopic data are wavelength- and flux-calibrated using arc lamps and spectrophotometric standard stars, respectively. The data are cleaned of cosmic-ray contamination using LACOSMIC (Van Dokkum 2001) before the 1D spectrum is extracted. The pipeline also uses a model to subtract telluric features. The pipeline offers 'fast' and 'final' modes for reducing spectra. In fast mode, used simply to classify transients, data are reduced using archival sensitivity curves and wavelength solutions. In final mode, for producing publication-quality data, master biases and flats are created from calibration frames obtained close in time to the science exposure, sensitivity curves are derived from spectroscopic standard stars obtained on the same night as the data, and the dispersion is found using standard lamps, again taken on the same night as the transient.

As PESSTO is a public survey, all raw data are immediately available to the community in the ESO archive[5]. In addition, reduced classification spectra are made available

[2]http://www.astronomy.ohio-state.edu/ assassin/index.shtml
[3]http://www.astronomerstelegram.org
[4]http://www.cbat.eps.harvard.edu/cbet/RecentCBETs.html
[5]

via WISeREP[6] (Weizmann Interactive Supernova data REPository; Yaron & Gal-Yam 2012) and the result of the classification is released in an ATel within one day of observing. Final reductions of all data, at the end of each PESSTO year, are released through ESO[7].

The primary goal of PESSTO is to find young and/or unusual SNe, as these objects give the greatest science return on the time invested. To this end, targets are prioritised for classification and follow-up according to the following criteria, listed by Smartt et al. (2015):

- Nearby SNe, for possible progenitor studies
- **Extremely bright** or extremely faint SNe
- Fast-declining (steeper than $1\,\mathrm{mag}\,(5\,\mathrm{d})^{-1}$) or **slowly rising (rise-time $\gtrsim 30\,\mathrm{d}$) light curves**
- History of variability (e.g. pre-discovery outbursts)
- SNe associated with GRB and X-ray flash alerts (none yet detected)
- Peculiar environments - e.g. **SNe with low-luminosity or undetected host galaxies**, large offsets from host, intensely star-forming regions.

Criteria in bold are used to select SLSNe. Clearly, these SNe are unusual in a number of ways, and form an important part of PESSTO's survey strategy. Objects satisfying any of these criteria are promoted, using the Marshall, as high-priority classification targets for PESSTO observers. As a general rule-of-thumb, a transient coincident with a very faint host from the Sloan Digital Sky Survey (SDSS) with photometric redshift $\gtrsim 0.1$, with a light curve rising by $\sim 0.1\,\mathrm{mag\,d^{-1}}$ for a few weeks, and peaking at an apparent magnitude $m \sim 17-19$, is a good candidate for a SLSN.

2.1.3 La Silla QUEST

One of the most important feeder surveys for PESSTO is La Silla QUEST (Baltay et al. 2012; Rabinowitz et al. 2012). LSQ uses the $10\,\mathrm{deg}^2$, 160 megapixel QUEST camera, installed on the ESO 1.0-m Schmidt telescope at La Silla Observatory. The LSQ low-redshift supernova survey (Baltay et al. 2013) commenced in late 2011.

[6] http://www.weizmann.ac.il/astrophysics/wiserep/
[7] For details on how to get the PESSTO Phase 3 data, see www.pessto.org

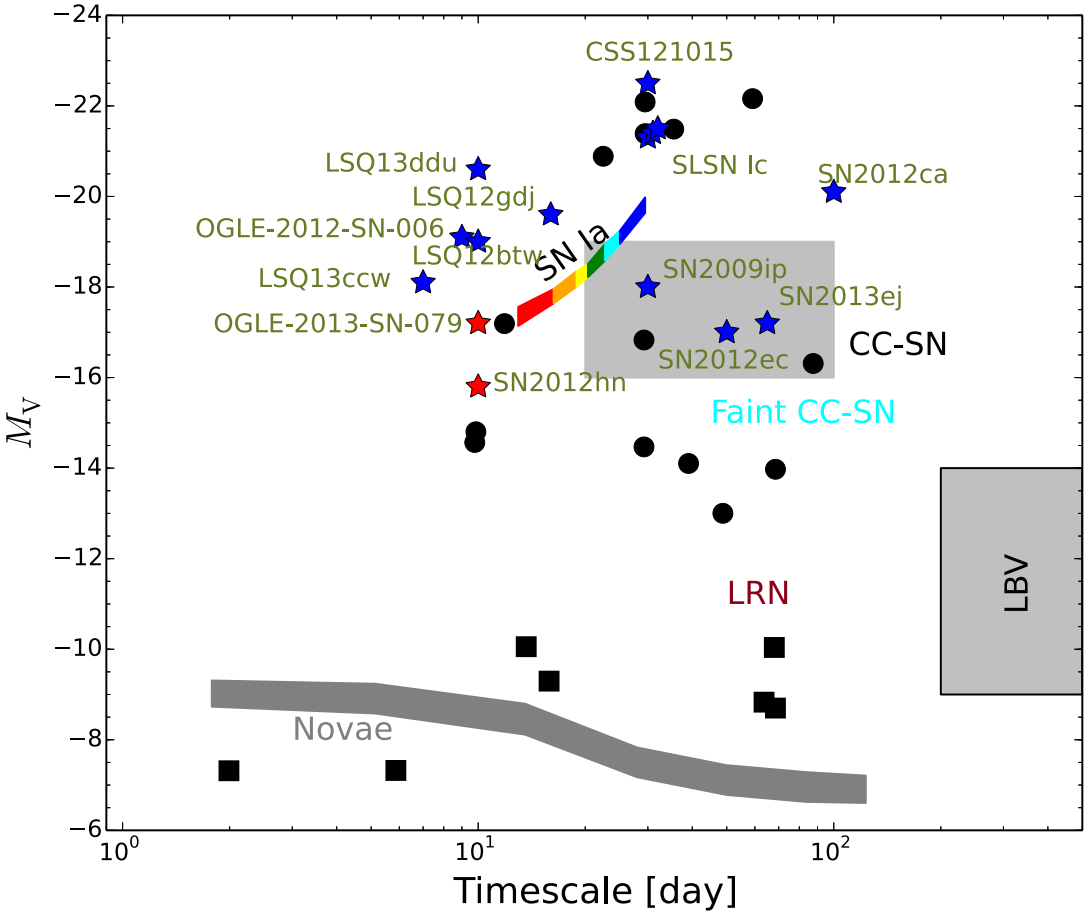

Figure 2.3: The phase space of cosmic explosions (Kulkarni & Kasliwal 2009), showing the locations of the various subtypes of supernovae and fainter novae. The super-luminous supernovae are characterised by peak luminosities of $M_V \sim -22$ and timescales of a few weeks. Filled stars show follow-up targets from the first year of PESSTO. Many of these targets are in unusual regions of parameter space (e.g. fast-evolving or super-luminous). *Credit*: Smartt et al. (2015)

There are several reasons why LSQ has had such a productive partnership with PESSTO. The fact that the NTT and ESO Schmidt are located at the same observatory means that any transient seen by LSQ is at a position on the sky that is also observable by PESSTO. The limiting magnitude for LSQ images is $R \simeq 21$ (Baltay et al. 2013), which is also the limiting magnitude for spectroscopy with EFOSC2. Thus, all LSQ objects can, in principle, be classified by PESSTO (although old, faint targets are unlikely to pass the selection criteria in Section 2.1.2). The biggest advantage of LSQ is the cadence. The SN search typically covers 1300 deg^2 twice per night. Each pointing is revisited every 1-2 nights (weather permitting) over a window of several months. Therefore the light curves of transients are densely sampled. This is particularly useful, for example, in picking out slowly-rising SNe that could be super-luminous. Well-sampled early light curves are also very important for SLSN science, as these place

strong constraints on the various models; this will become a theme throughout this thesis.

2.2 Other large programs and data pipelines

2.2.1 VLT and X-Shooter

For targets with apparent magnitudes $m \gtrsim 21$, a larger diameter telescope is needed for spectroscopy. In this case, our main resource has been the X-Shooter spectrograph (Vernet et al. 2011), which is mounted on one of the four 8.0-m Unit Telescopes comprising the ESO Very Large Telescope (VLT), located at Cerro Paranal observatory in Chile. The X-Shooter program for SLSNe in PESSTO is also used to look for interstellar absorption lines in the spectrum, in order to determine precise redshifts of faint host galaxies, where the usual nebular emission lines may be absent. This is possible because of the superior resolution of X-Shooter, which is ~ 1 Å in the optical.

X-Shooter is an echelle spectrograph, and has three individual arms for different wavelength ranges: near-ultraviolet (UV) and blue; optical; and NIR. We reduce the data using the interactive X-Shooter pipeline within ESO's REFLEX environment. As well as applying standard procedures (de-bias, flat-field), a geometric solution is obtained for the various diffraction orders, which are mapped onto a single trace. The resulting 2D frames are flux and wavelength calibrated using standard stars and lamps, respectively. Finally, the pipeline allows us to extract the 1D spectrum. X-Shooter routinely observes telluric standard stars for all targets, and we used these to remove telluric features from our spectra within IRAF.

2.2.2 Las Cumbres Observatory Global Telescope Network

Much of the photometry for bright PESSTO targets is provided by the Las Cumbres Observatory Global Telescope Network (LCOGT; Brown et al. 2013). The network consists of nine 1.0-m telescopes in Chile, Australia, South Africa and Texas, and 2.0-m telescopes in Hawaii and Australia (The Faulkes Telescope North and South). The telescopes operate robotically, carrying out observations scheduled at LCOGT headquarters in California. Users can request data through a web-based interface called the Supernova Exchange, similar to the PESSTO Marshall. Data are reduced by a dedicated pipeline, including de-biasing, flat-fielding, dark correction, bad-pixel masking, astrometric solution, and source extraction and aperture photometry using SExtractor.

2.2.3 The Liverpool Telescope

The Liverpool Telescope (LT; Steele et al. 2004) is a robotic 2.0-m telescope located at Roque de los Muchachos observatory on La Palma, in the Canary Islands, built and maintained by Liverpool John Moores University. The LT is perfectly suited to transient follow-up at a variety of cadences, due to its fully autonomous scheduling of observations. Imaging is currently obtained with the IO:O camera (replacing RATCam in early 2014). The LT pipeline automatically outputs reduced 2D frames, corrected for bias level and flat-fielding, with a basic astrometric solution applied.

2.3 Manual data reduction

2.3.1 Reducing data with IRAF

For some of the telescopes used in this work, data were reduced manually using the suite of routines offered by IRAF[8]. This includes: the 4.2-m William Herschel Telescope (WHT), using ISIS for spectroscopy and ACAM for imaging; the 3.58-m Telescopio Nazionale Galileo (TNG) with NICS, a NIR instrument; and the 2.5-m Nordic Optical Telescope (NOT), with ALFOSC for optical data and NOTcam for NIR. All are situated in La Palma.

IRAF is an interactive environment with a library of packages designed to handle astronomical data. The main packages used to reduce data here are CCDRED, TWODSPEC and ONEDSPEC. The basic workflow is to first de-trend the 2D exposures using master bias and flat-fields, and trim the frame, using the task CCDPROC. The images are cleaned of cosmic rays using LACOSMIC (Van Dokkum 2001). Multiple exposures can be combined with IMALIGN and IMCOMBINE. In the case of imaging data, photometry can now be performed on sources in the frame (Section 2.3.2).

For spectroscopic data, the 1D spectrum is extracted by following the 2D trace using APALL. Extracting the spectrum from a standard arc lamp observation, obtained with the same instrumental configuration, the dispersion solution can be found with the task IDENTIFY. All of the above steps are also applied to a standard star spectrum, obtained on the same night as the science exposure. Comparing the standard with archival data, we construct a sensitivity curve (using SENSFUNC) to flux-calibrate our science data (using CALIBRATE), remembering to correct for the difference in airmass between the telescope pointings for the target and for the standard star.

[8]Image Reduction and Analysis Facility (IRAF) is distributed by the National Optical Astronomy Observatory, which is operated by the Association of Universities for Research in Astronomy, Inc., under cooperative agreement with the National Science Foundation.

2.3.2 Photometry with SNOoPY

Most of the photometry in the following chapters was done using the SuperNOva PhotometrY (SNOoPY) package[9]. This is a user-friendly wrapper for the IRAF task, DAOPHOT. While stars and distant SNe are theoretically point sources, atmospheric turbulence and diffraction in the optical system conspire to blur the imaged star to a finite size, called the point-spread function (PSF), shown in Figure 2.4. Thus, although aperture photometry (counting all the flux in a fixed region and subtracting the average background counts) is the simplest way to measure brightness, it may result in flux lost to the wings of the PSF.

A better method is PSF-fitting photometry, as implemented in SNOoPY. The image is displayed in SAOIMAGE DS9, and a model PSF is constructed from user-selected stars in the image. The model is checked by subtracting off the PSF stars and checking the residuals; stars which leave large residuals are rejected. This model is then scaled to fit the target, giving a measure of the total flux contained within the PSF. A polynomial fit to the sky close to the target is used to remove the background contribution to the counts. This method also has the advantage of disentangling light from nearby sources, as each can be fit with separate PSFs. Errors are calculated in SNOOPY using an artificial star experiment. The fitted supernova PSF is placed at different locations on the image, and the magnitude is computed each time. The standard deviation of these measurements gives the error in fitting the background.

The instrumental magnitude is defined by

$$m_{\text{inst}} = -2.5 \log_{10}\left(\int \lambda F_\lambda(\lambda) T(\lambda) d\lambda \right), \tag{2.1}$$

where $F_\lambda(\lambda)$ is the apparent flux per unit wavelength of the source and $T(\lambda)$ is the transmission through the instrument, including a bandpass filter. Both are functions of wavelength. To convert this to a useful magnitude in a standard photometric system (AB or Vega magnitudes), we must find the zero-point of the image. This is done in one of two ways. If the observation took place in photometric conditions, with clear skies and good seeing, an additional image of a standard field can be used to find the zero-point for that night. Alternatively, if stars in the same field-of-view as the target have well-calibrated magnitudes (which may have been derived by using the standard field method on other nights), these stars can be used. In both cases, instrumental magnitudes of stars are compared to their known magnitudes in the appropriate standard system, with the difference giving the zero-point. If the standard stars were observed

[9] http://sngroup.oapd.inaf.it/snoopy.html

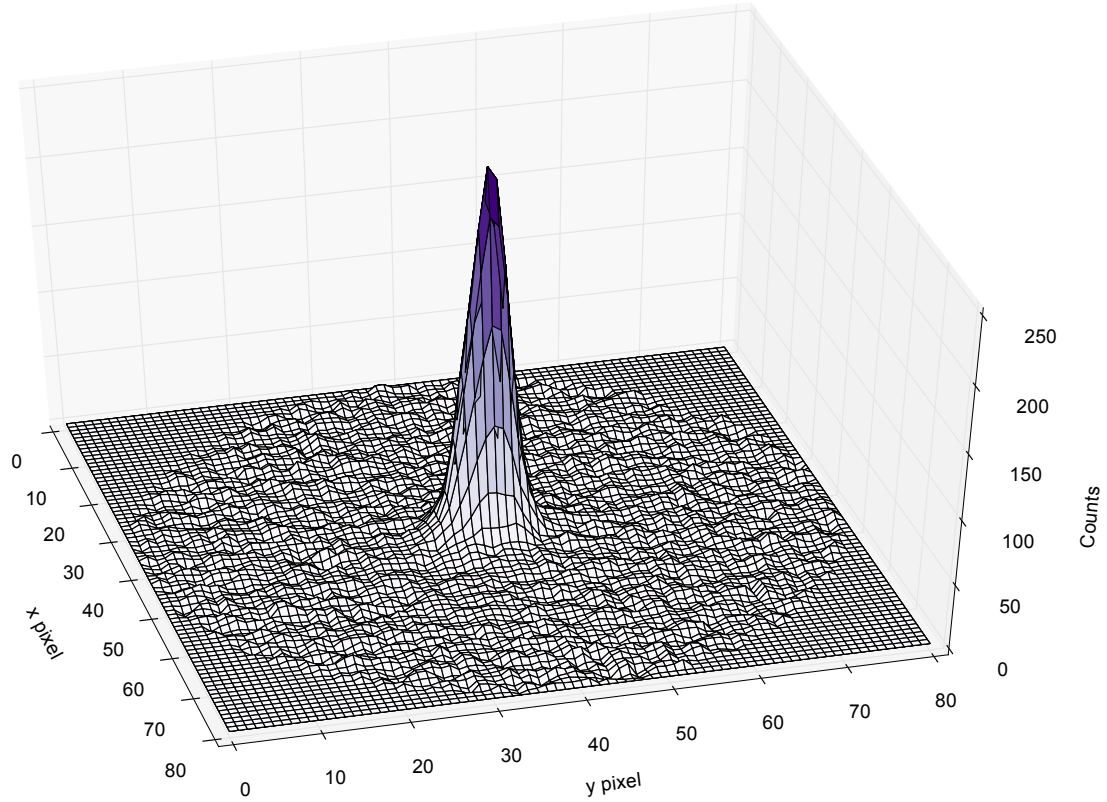

Figure 2.4: A typical example of the point-spread function in astronomy. This PSF model was constructed from stars in an *r*-band image taken on 2013 June 13 with an LCOGT 1.0-m telescope.

at a different airmass from the target, differential atmospheric extinction must also be taken into account.

The sensitivity of the camera is not uniform in wavelength, and no two sets of colour filters are exactly the same. For this reason, a colour-based correction is also usually applied to convert the measured magnitude into a standard filter system (for example, the PS1 system shown in Figure 2.2). To first order, this is simply a colour (e.g. $g-r$) multiplied by a coefficient. As with the zero-point, this coefficient is determined by comparing the instrumental magnitudes of standard stars with their known values in the desired system.

The final, calibrated apparent magnitude of the source in an arbitrary filter, j, is given by:

$$m_j \;=\; m_{j,\mathrm{inst}} + Z + C\left(m_i - m_j\right) - X\sec\theta \;=\; -2.5\log_{10}\left(\frac{F_j}{F_{j,\mathrm{ref}}}\right), \tag{2.2}$$

where Z is the zero-point, C is the colour coefficient, X is the site extinction and θ is the angle of observation from the zenith. After correcting for zero-point and extinction in the filters i and j, the colour term and final magnitude are found iteratively. The right-

hand side of equation 2.2 gives the physical definition of apparent magnitude, where F_j is the flux in filter j and $F_{j,\mathrm{ref}}$ is the flux of a zero-magnitude reference source defined for filter j. This reference source is the star Vega in the Vega magnitude system, or a synthetic source with a uniform flux density of 3631 Jy at all frequencies in the AB magnitude system.

2.3.3 Absolute magnitudes and K-corrections

The absolute magnitude in the rest-frame of an extragalactic source is defined as

$$M_j = m_i - \mu - K_{i\to j} - A_{i,\mathrm{MW}} - A_{j,\mathrm{host}}, \tag{2.3}$$

where $\mu = -2.5\log_{10}(d_\mathrm{L}/(10\mathrm{pc}))$ is the distance modulus and d_L is the luminosity distance to the source, $A_{i,\mathrm{MW}}$ is the Milky Way foreground extinction in the direction of the source in filter i, $A_{j,\mathrm{host}}$ is the internal extinction in the host galaxy in filter j, and $K_{i\to j}$ is the K-correction from observed filter i to rest-frame filter j. The K term is needed to correct for the redshifting of light due to cosmological expansion, as this changes the part of the SED probed by the observer, compared to what would be probed in the rest-frame of the source (see Oke & Sandage 1968; Hogg et al. 2002, for full descriptions).

Throughout this work, K-corrections are calculated using the method of synthetic photometry on spectra. Using the IRAF task CALCPHOT, the PYTHON package PYSYNPHOT[10], or a custom K-correction code, SNAKE (SuperNova Algorithm for K-correction Evaluation; Inserra in prep.), the principle is always the same. The observer-frame SN spectrum is convolved with the transmission function of a chosen filter (i), giving the apparent magnitude we would expect to observe in that band. The spectrum is then corrected for cosmological expansion, i.e. Doppler shift: the wavelength is divided by $(1+z)$, where z is the redshift of the SN, and flux per unit wavelength is multiplied by the same factor (see Figure 2.5). Synthetic photometry is carried out on the rest-frame spectrum, choosing a filter (j) with $\lambda_{\mathrm{eff},j} \approx \lambda_{\mathrm{eff},i}/(1+z)$. The K-correction is then simply $K_{i\to j} = m_{j,\mathrm{rest}} - m_{i,\mathrm{obs}}$.

The Milky Way extinction in equation 2.3 can be found by consulting the Galactic dust maps of Schlafly & Finkbeiner (2011). The host galaxy extinction can be calculated by comparing the Balmer decrement (the ratio of flux in Hα to Hβ) for the nebular emission lines; however in most SLSNe the host galaxy is too faint to detect strong emission lines, so this is not always possible. However, as most show no sign of interstellar absorption in Na I D, thought to correlate strongly with extinction (Poznan-

[10] http://stsdas.stsci.edu/pysynphot/

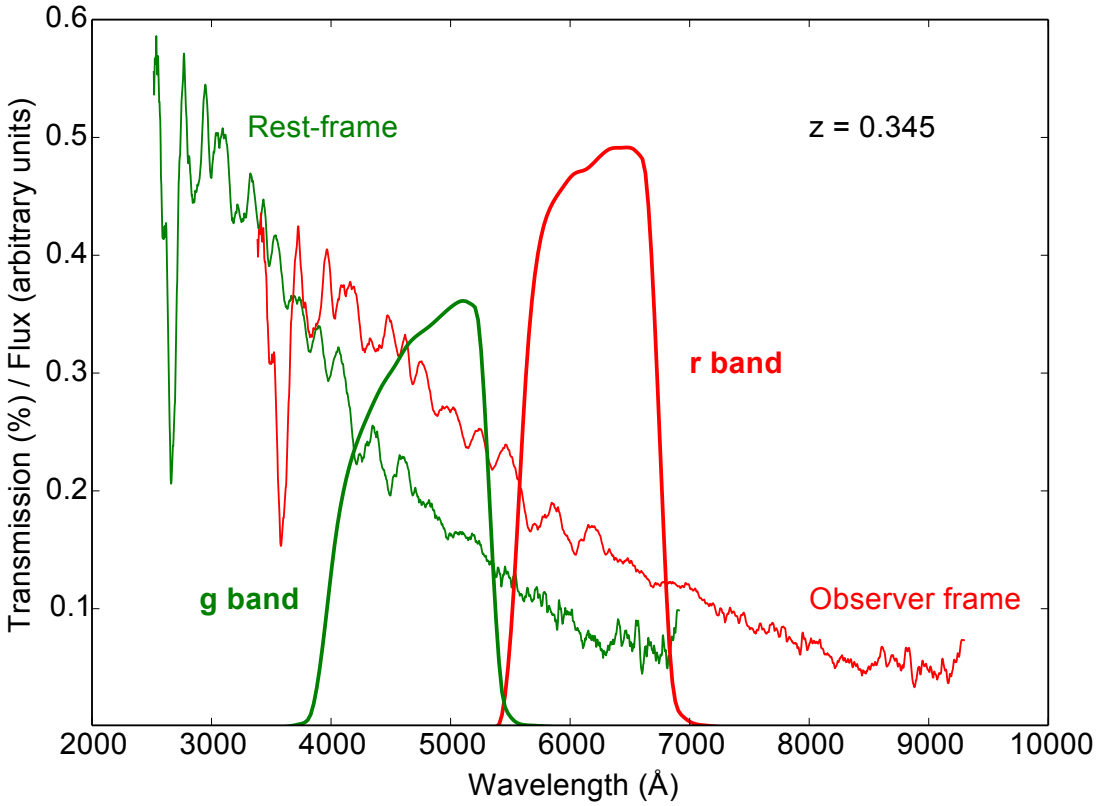

Figure 2.5: An example of the K-correction for a SLSN at $z = 0.345$. At this redshift, images taken in the r-band probe a wavelength range corresponding roughly to the g-band in the rest-frame of the SN. The correction $K_{r\to g}$ is the difference between the rest-frame g magnitude and the observed r magnitude.

ski et al. 2012), host extinction is usually assumed to be negligible.

SLSNe have been found only at $z > 0.1$, so they are well within the Hubble Flow, and the distance modulus is therefore straightforward to determine. The redshift is found using host galaxy emission or absorption features whenever possible. If no such lines are seen, cross-correlating the spectrum with those of other SLSNe at known redshifts gives a good estimate. The distance to the SN is then calculated using standard cosmological models, as implemented by Wright (2006). Throughout this work, we adopt a flat ΛCDM cosmology, with $H_0 = 72\,\mathrm{km\,s^{-1}Mpc^{-1}}$, $\Omega_\Lambda = 0.73$ and $\Omega_M = 0.27$.

2.3.4 Bolometric light curves

Obtaining photometry in different filters provides essential information on the slope of the SED and its evolution in time. However, we are often interested in knowing the total power radiated by an object, in particular when we wish to fit simple models to constrain the energy source. The integrated luminosity across all filters gives the *bolometric* luminosity, $L(t) = \int F_\lambda(t)\,d\lambda$. The precise method for obtaining a bolometric

light curve varies, but the main pre-requisite is photometry with good time sampling in as many bands as possible.

The simplest method is to construct an approximate SED by converting magnitudes at each epoch into fluxes at the effective wavelengths of the available filters, by inverting equation 2.2 (RHS). If photometry covers the UV to the NIR, this can be trivially integrated over wavelength to give the bolometric light curve. However if, for example, only optical photometry is available, integrating the SED will give the total luminosity in the optical window, but will neglect UV and NIR contributions. In this case we have a *pseudobolometric* light curve. Depending on the data available, corrections can be made to estimate the full bolometric light curve even if observations at some wavelengths are sparse or absent. These will be discussed for individual SNe in the course of the thesis.

2.4 Models

Interpreting astronomical data relies heavily on the construction of models, and the agreement (or lack thereof) between models and data. Models range from simple predictions of an expanding, cooling blackbody (Howell et al. 2013) to state-of-the-art 3D simulations of core-collapse (Couch & Ott 2015). In this study, we use semi-analytic diffusion models to reproduce the light curves of SNe. The pioneering work in this area was carried out by Arnett (1980, 1982). His models for the light curves of Type I supernovae were built on a few basic assumptions:

- The SN ejecta are in homologous expansion, i.e. $v(r) = (r/R)\,v(R)$, where $v(r)$ is the velocity of the ejecta at a radius $r(t)$ at time t, and $R(t)$ is the outer radius of the ejecta. This is a natural consequence of a spherical shock.
- The gas is radiation-dominated (an excellent approximation at such high energy).
- The heating source (^{56}Ni in the original formulation) is located centrally.
- The opacity of the ejecta is uniform and constant in time.
- The radius of the progenitor is small compared to R.

With these assumptions, and removing the restriction of a ^{56}Ni power source, an analytic equation for the light curve can be derived from the First Law of thermodynamics. The energy budget is controlled by time-dependent energy injection, $L_{\rm in}(t)$,

from a generalised central power source, diffusion of radiation out of the SN, and cooling due to adiabatic expansion. The final expression for the bolometric luminosity is

$$L(t) = e^{-(t/\tau_m)^2} \int_0^t 2\, L_{\rm in}(t') \frac{t'}{\tau_m} e^{(t'/\tau_m)^2} \frac{dt'}{\tau_m}, \tag{2.4}$$

and the characteristic *diffusion timescale* of the SN (formally, the geometric mean of the expansion timescale and the diffusion time) is given by

$$\tau_m = \left(\frac{2\kappa M_{\rm ej}}{\beta c v}\right)^{1/2} = \frac{1.05}{(\beta c)^{1/2}} \kappa^{1/2} M_{\rm ej}^{3/4} E_{\rm k}^{-1/4}, \tag{2.5}$$

where κ is the opacity in $\mathrm{cm^2\,g^{-1}}$, $M_{\rm ej}$ is the ejected mass in grams, and v is a scaling velocity for the homologous expansion, in $\mathrm{cm\,s^{-1}}$ (Arnett 1980, 1982). The speed of light is $c = 3 \times 10^{10}\,\mathrm{cm\,s^{-1}}$, while $\beta \approx 13.8$ (for a wide range of plausible density profiles) is an integration constant. With this choice of units, τ_m is given in seconds. The alternative formulation on the right of equation 2.5 comes from substituting $v = \sqrt{10E_{\rm k}/(3M_{\rm ej})}$, where $E_{\rm k}$ is the kinetic energy of the explosion in erg.

Equations 2.4 and 2.5 form the basis of semi-analytic light curve modelling, as the power source term can be varied and the equations solved numerically to produce a range of light curves. Moreover, the simplicity of this formulation allows estimates of physical parameters to be made by fitting computationally-inexpensive models directly to data. This technique was used by Inserra et al. (2013) and Chatzopoulos et al. (2012) to examine possible power sources in SLSNe. The following sections describe our implementation of these models, which will be used throughout this thesis.

2.4.1 Nickel-powered models

The original model developed by Arnett (1982) used the radioactive decay chain, $^{56}\mathrm{Ni} \rightarrow {}^{56}\mathrm{Co} \rightarrow {}^{56}\mathrm{Fe}$, which is the power source in normal Type I SNe. In this case, the form of the energy input is given by

$$L_{\rm in,Ni}(t) = M_{\rm Ni}\left(\epsilon_{\rm Ni} e^{-t/\tau_{\rm Ni}} + \epsilon_{\rm Co} \frac{e^{-t/\tau_{\rm Co}} - e^{-t/\tau_{\rm Ni}}}{1 - \tau_{\rm Ni}/\tau_{\rm Co}} D_{\rm Co}(t)\right), \tag{2.6}$$

where $M_{\rm Ni}$ is the mass of ^{56}Ni present in the ejecta, $\epsilon_{\rm X}$ is the energy generation rate per unit mass released by the decay of nucleus X, $\tau_{\rm X}$ is the lifetime of nucleus X, and $D_{\rm Co}(t)$ is the fraction of the energy released by ^{56}Co decay (in the form of γ-rays and positrons) that is thermalised in the ejecta (the ^{56}Ni decays at early times, when the ejecta can fully trap the emitted energy). Different trapping functions are used for the ^{56}Co decay energy (e.g. Wang et al. 2015); we follow Arnett (1982) in using that of

Colgate et al. (1980).

Apart from a recoding in PYTHON, the implementation of the model is the same as that used by Inserra et al. (2013), who also describe in detail how the photospheric velocity and temperature are calculated, assuming a dense core surrounded by a low-mass envelope with a steep density gradient. We fit the output luminosity of the model to bolometric light curve data using the χ^2 minimisation routine SCIPY.OPTIMIZE.FMIN, after a coarse grid scan through parameter space has initialised the variables with sensible values. The free parameters in the model are $M_{\rm Ni}$, τ_m, and the explosion epoch, $t_{\rm shift}$ (i.e. we can arbitrarily shift the whole light curve model along the time axis to match the data, without loss of generality). τ_m is a function of $M_{\rm ej}$, κ, and $E_{\rm k}$ (equation 2.5). Fixing κ and $E_{\rm k}$ thus allows an estimate of the ejected mass. For hydrogen-poor material, and an opacity dominated by electron scattering, we have $\kappa = 0.1\text{-}0.2\,{\rm cm^2\,g^{-1}}$ for half- and fully-ionised material, respectively. The canonical explosion energy in SNe is $E_{\rm k} = 10^{51}$ erg, though this may be higher in SLSNe. In practice, we find that it is difficult to fit SLSN light curves with ^{56}Ni-powered models in which $E_{\rm k} = 10^{51}$ erg. In this case we also try kinetic energies – in units of 10^{51}erg – of 1, 3, 10 and 30 (if still no satisfactory fit is obtained, we also try 100; see Section 2.4.4).

Inserra et al. (2013) found that ^{56}Ni-powered models gave mostly poor fits to a sample of SLSNe Ic, and required the ejecta to be mainly ^{56}Ni, by mass. This model was therefore disfavoured by the authors.

2.4.2 Magnetar-powered models

In one of the most popular models, discussed in Section 1.6.1, SLSNe are powered by a central engine that re-shocks the ejecta after it has expanded to a large radius, thus overcoming adiabatic losses. The most widely studied theory in this class is the magnetar spin-down model, in which the energy source is the rotational energy of a millisecond pulsar, tapped via a strong magnetic field. It is generally assumed to radiate with the functional form of a magnetic dipole (Kasen & Bildsten 2010; Ostriker & Gunn 1971):

$$L_{\rm in,mag}(t) = \frac{E_p}{\tau_p}\frac{1}{\left(1+t/\tau_p\right)^2}\ {\rm erg\ s^{-1}}. \tag{2.7}$$

The energy input timescale for magnetar spin-down is given by $\tau_p = 4.75 B_{14}^{-2} P_{\rm ms}^2$ days, where B_{14} is the magnetic field in units of 10^{14} Gauss and $P_{\rm ms}$ is the initial spin period in milliseconds. For a neutron star with a radius of 10 km, the rotational energy is $E_p = 2\times10^{52} P_{\rm ms}^{-2}$ erg. In this case there are four free parameters for the diffusion model: B, P, τ_m, and $t_{\rm shift}$. We fit the model to data with the same χ^2 minimisation

routine used for the ^{56}Ni models. Again wishing to estimate $M_{\rm ej}$ from τ_m, we apply constraints to $E_{\rm k}$ and κ.

The presence of the magnetar affects not only the luminosity of the SN, but also its dynamics. Kasen & Bildsten (2010) showed that the central over-pressure tends to accelerate the ejecta and sweep it up into a dense shell at constant velocity. We approximate this effect crudely, as follows. After fitting the light curve and determining B, P, τ_m, and $t_{\rm shift}$, the total energy injected by the magnetar, $E_{\rm mag}$ (which approaches E_p for sufficiently long t), is calculated by integrating equation 2.7. The total radiated energy, $E_{\rm rad}$, is found by integrating the model light curve. The kinetic energy is then set to $E_{\rm k} = 10^{51} + \frac{1}{2}\left(E_{\rm mag} - E_{\rm rad}\right)$ erg, where the second term is the time-averaged energy injected by the magnetar and not lost by radiation. Inserra et al. (2013) showed that this treatment of $E_{\rm k}$ gives light curves in excellent agreement with the hydrodynamical models of Kasen & Bildsten (2010), for the same $M_{\rm ej}$ and κ.

A fiducial value of $\kappa = 0.2\,{\rm cm^2\,g^{-1}}$ is assumed for the opacity , as the magnetar ejecta is likely ionised by a hard radiation field (Kotera et al. 2013; Metzger et al. 2014). The effect of using $\kappa = 0.1\,{\rm cm^2\,g^{-1}}$, as is generally assumed for normal-luminosity SNe Ic, is also investigated. The first study with this model, by Inserra et al. (2013), assumed the latter value for the opacity. From equation 2.5, for fixed $E_{\rm k}$ we have $M_{\rm ej} \propto \kappa^{-2/3}$. Therefore, varying the opacity by a factor of 2 changes the extracted mass estimate by a factor ~ 1.6. The importance of this factor will be discussed in Chapter 6.

In contrast to the ^{56}Ni models, the magnetar model could reproduce the light curves of the SLSNe Ic modelled by Inserra et al. (2013).

2.4.3 Interaction-powered models

The final power source proposed for SLSNe is an interaction between the ejecta and CSM. Mass loss is a ubiquitous part of stellar evolution, especially in massive stars, and it is proposed that this can build up a dense shell of gas around the star, which the SN ejecta then collide with. In contrast to the radioactive and magnetar models, Inserra et al. (2013) did not fit their SLSN light curves with an interaction model. Developing a synthetic light curve tool based on ejecta-CSM interaction is therefore an important step in discriminating between the three main models of SLSNe.

Our simple CSM model is based on the formulae detailed in Chatzopoulos et al. (2012). Their derivation assumes that the CSM is stationary – this is justified by the slow expansion velocity of the CSM relative to typical velocities in SNe. Energy is input efficiently by self-similar forward and reverse shocks (i.e. all of the kinetic energy of the shocks converts to radiation) generated at the ejecta-CSM interface (Chevalier 1982;

Chevalier & Fransson 1994), as well as by radioactive decay of ^{56}Ni and ^{56}Co deep in the ejecta (using equation 2.6). In this approximation, the time-dependence of the energy input from the shocks depends only on the density profiles of the interacting media (the ejecta and the CSM). The shock luminosity is input at the ejecta-CSM interface at all times in this model (to make the problem analytically tractable), but two important timescales are found: heat input by the forward shock is terminated abruptly when the shock breaks out of the CSM, and the reverse shock stops depositing heat when it has swept up all of the ejecta, leading to some discontinuity in the gradient of the light curve at these two epochs. The analytic expressions for $L_{\rm in,CSM}$ and the shock breakout times can be found in equations 14, 15 and 16 from Chatzopoulos et al. (2012).

While the treatment of the shocks is based on that of Chevalier (1982) and Chevalier & Fransson (1994), those works dealt with an optically thin stellar wind, where we normally see X-ray emission from the shock fronts, and strong narrow lines from pre-shock gas excited by these energetic photons. This is not the case for an optically thick CSM, which is necessary to explain the SLSNe (Chevalier & Irwin 2011; Ginzburg & Balberg 2012). In this regime, the energy diffuses out of the shell, as in the Arnett (1982) models discussed previously, but in the special case of zero expansion velocity. Dessart et al. (2015) present detailed radiation-hydrodynamical models in which the photosphere, inside the CSM, stays at a constant radius for tens of days. In this case, Chatzopoulos et al. (2012) show that equation 2.4 simplifies to

$$L(t) = \frac{1}{t_0} e^{-t/\tau_0} \int_0^t L_{\rm in}(t') e^{t'/\tau_0} dt', \tag{2.8}$$

where the diffusion time for a fixed photosphere at radius $R_{\rm ph}$ is

$$\tau_0 = \frac{\kappa M}{\beta c R_{\rm ph}}. \tag{2.9}$$

Shock-deposited energy diffuses out of the region where the CSM is optically thick ($M = M_{\rm CSM,\tau>2/3}$), whereas energy from radioactive decays must first diffuse out of the ejecta ($M = M_{\rm ej} + M_{\rm CSM,\tau>2/3}$). Thus two different diffusion times are calculated. After shock heating ends, the solution for the light curve is governed simply by radiative diffusion from the opaque shell, unless there is significant heating from radioactivity.

Taking all of this into account, the output luminosity is a function of ejected mass ($M_{\rm ej}$), CSM mass ($M_{\rm CSM}$), nickel mass ($M_{\rm Ni}$), explosion time ($t_{\rm shift}$), ejecta kinetic energy ($E_{\rm k}$), interaction radius (R_0), CSM density ($\rho_{\rm CSM}$, as well as density scaling index, s), density scaling exponents for the SN core and envelope (δ and n, respectively), and the opacity (κ). We fit the model to bolometric light curve data using the same method of χ^2 minimisation.

To reduce the number of free parameters in our fits, we fix several variables at typical values. The most uncertain is perhaps the opacity. As discussed previously, for hydrogen-free material κ is generally taken to be 0.1-0.2 $\mathrm{cm^2\,g^{-1}}$. For hydrogen-rich material, $\kappa = 0.33\,\mathrm{cm^2\,g^{-1}}$ may be more appropriate (Chatzopoulos et al. 2012). Since we do not know the composition of the CSM (but expect it to be H-poor, from the spectra we observe), we take an intermediate value, $\kappa = 0.2\,\mathrm{cm^2\,g^{-1}}$. This has the added advantage of consistency with the magnetar and radioactive models. We fix $n = 10$ and $\delta = 0$ (Chatzopoulos et al. 2012; Chevalier & Fransson 1994). We also set $s = 0$, corresponding to a uniform density shell produced by a massive outburst of the progenitor, as previous interaction-powered models of SLSNe have required very massive CSM, such that the mass-loss rates would have to be extraordinarily high if this material were lost in a steady wind (e.g. see the discussion in Benetti et al. 2014).

Chatzopoulos et al. (2013) were not surprised to find a large degeneracy between some of the parameters in the model, with M_{ej} and R_0 being particularly weakly constrained. We also find that the models are largely insensitive to R_0; it affects the light curve only insofar as it alters the radius of the photosphere (R_{ph}). We initially allowed R_0 to vary from 10^{12}-10^{15} cm, but because the CSM shells required to fit SLSN light curves are $\sim 10^{15}$ cm thick, with the photosphere located close to the outer edge (as expected, since these shells are highly optically thick), the 'best-fit' R_0 is typically much smaller than R_{ph}, and can in fact be changed by factors of 10 or more with little to no effect on the other parameters of the light curve. We therefore fix R_0 at 10^{13} cm ($\sim$150 $\mathrm{R_\odot}$) for simplicity. This leaves M_{ej}, M_{CSM}, E_{k}, ρ_{CSM}, t_{shift}, and (optionally) M_{Ni} as parameters to fit. We have 1-2 more free parameters in this model, compared to the magnetar model, so we expect that it will be easier to fit a wider range of light curve shapes.

The peak luminosity is most sensitive to E_{k} and M_{ej}, with a larger ratio of $E_{\mathrm{k}}/M_{\mathrm{ej}}$ giving a brighter peak. The light curve timescales depend on ρ_{CSM}, M_{ej} and M_{CSM}. Denser CSM results in a faster rise but slower decline, whereas more massive CSM tends to broaden the whole light curve, by increasing the diffusion time from the shell. More massive ejecta result in a slower rise, and can broaden the peak as it weakly increases the termination time for the forward shock while greatly increasing that for the reverse shock, but it has little effect on the final decline rate in the model, as the shock energy is input at the base of the CSM shell (however, M_{ej} does affect the diffusion time for the radioactive decay energy). In most cases, the forward shock luminosity is greater than that of the reverse shock, so the discontinuity at reverse shock termination is only visible in the light curve if this occurs after forward shock termination.

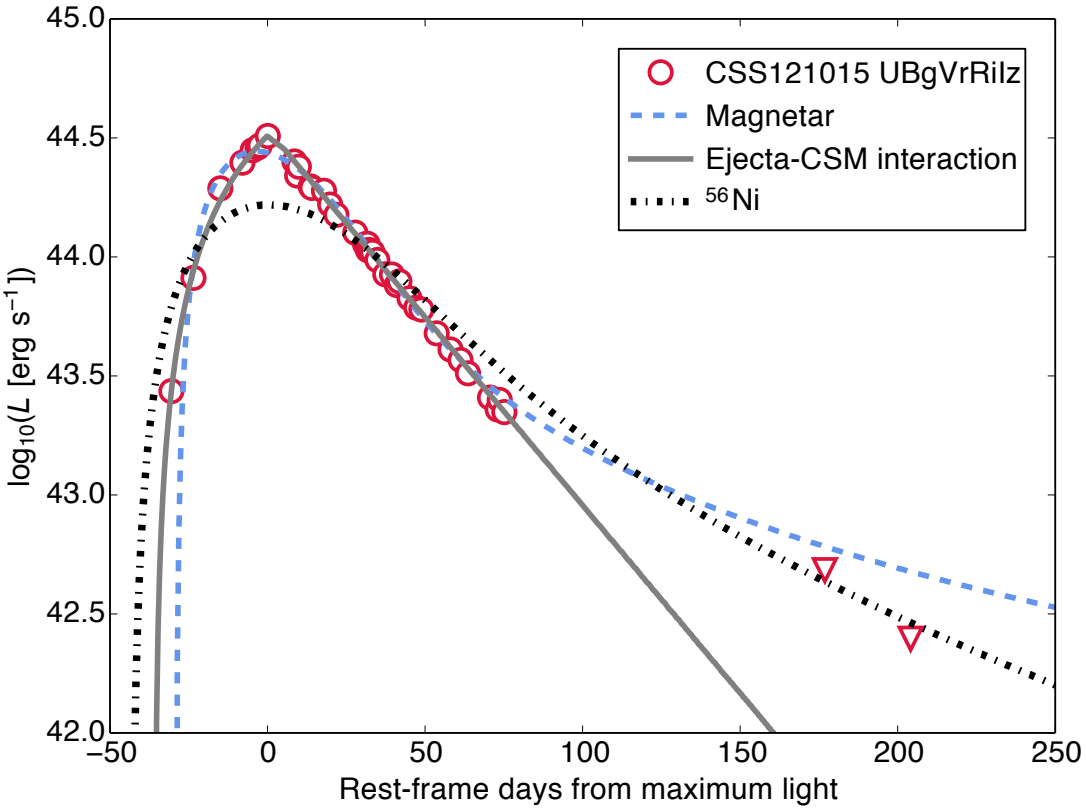

Figure 2.6: Light curve fits to CSS121015 (all fit parameters are listed in Table 2.1). The ^{56}Ni model is a poor fit, but the magnetar and interaction models both give good matches to the light curve from −30 to +80 days around maximum light. The models behave very differently at late times; photometry at these epochs should provide an important constraint on the power source.

Of course, there are limitations to this analytical framework, many of which were pointed out by Chatzopoulos et al. (2012). The assumption of 100% efficiency in converting kinetic energy to radiation is unrealistic for models with $M_{\rm CSM} \ll M_{\rm ej}$, and in this case we would also expect the photosphere to expand quickly, since the modest swept-up mass is insufficient to slow it down, in contrast to the fixed photosphere we use in the model. In our fits, we typically find $M_{\rm CSM} \gtrsim M_{\rm ej}/2$, so these approximations are appropriate for our purposes. In general, the hydrodynamics of this model are quite complex. However, comparisons by Chatzopoulos et al. (2012) between the analytic models and more realistic hydrodynamical simulations indicate that these simplified models are, at the very least, a useful guide to the regions of parameter space that are relevant to SLSNe.

Table 2.1: Light curve fit parameters for CSS121015 in Figure 2.6

Magnetar					
$M_{ej}/M_\odot$	$B/10^{14}$G	P/ms	χ^2/d.o.f.		
5.5	2.1	2.0	10.39		
^{56}Ni decay					
$M_{ej}/M_\odot$	$M_{Ni}/M_\odot$	$E_k/10^{51}$erg	χ^2/d.o.f.		
20.3	20.2	100	329.14		
CSM interaction					
$M_{ej}/M_\odot$	$M_{CSM}/M_\odot$	$E_k/10^{51}$erg	$\log(\rho_{CSM}/g\,cm^{-3})$	χ^2/d.o.f.	$R_{ph}/10^{15}$cm (not fit)
6.7	4.9	2.3	−12.54	4.12	2.0

2.4.4 Exploring the models

To demonstrate some of the concepts described in this section more clearly, we now test these models using the light curve of a SLSN. CSS121015 is a SLSN II that showed spectral and light curve properties similar to SLSNe Ic (i.e. it showed signs of hydrogen but was not a typical SLSN IIn). A detailed analysis by Benetti et al. (2014) concluded that the spectral evolution, in particular narrow emission lines which faded over time, pointed towards an interaction model with several solar masses of CSM.

Fits to the light curve, integrated from the U- to z-band, are shown in Figure 2.6, with fit parameters given in Table 2.1. Our CSM interaction model provides an excellent match, with a best-fit $M_{CSM} \sim 5\,M_\odot$– similar to the $\sim 8\,M_\odot$ estimated by Benetti et al. (2014). Despite being one of the brightest SLSNe to date, the kinetic energy in the model is not particularly high ($E_k = 2\times10^{51}$ erg). The peak is bright because the ejected mass is similar to the CSM mass, so that kinetic energy is thermalised efficiently. No ^{56}Ni is needed to fit the light curve. In the table we also show that $R_{ph} \sim 10^{15}$ cm – although this is not one of the parameters that we fit in the model, we see that the derived value is typical of estimates for SLSNe (e.g. Quimby et al. 2011).

The magnetar model also gives a very good fit over the observed lifetime of the SN, for parameters well within the expected range of $P \sim$ a few ms and $B \sim$ a few times 10^{14} G. However, the upper limits obtained $\sim$ 200 days after maximum light prove to be useful discriminants. The t^{-2} magnetar tail over-predicts the flux at late epochs, whereas in the interaction model, shock heating terminates a few days after maximum, and the light curve is subsequently controlled only by radiative diffusion; the SN therefore lacks a power input to drive a bright tail-phase (though small ^{56}Ni mass cannot be excluded, as a radioactive tail similar to normal core-collapse SNe would not

have been detected at this distance). Of course, there is also the possibility that the ejecta no longer traps all of the high-energy magnetar input at late epochs (e.g. Kotera et al. 2013), causing the optical emission to drop below the prediction of our fully-trapped model. ^{56}Ni cannot be the dominant power source, as our fit is poor even for very optimistic parameters: ejecta composed almost entirely of ^{56}Ni, with an explosion energy of 10^{53}erg.

This illustrates the utility of our simple models, and lends support to the arguments presented by Benetti et al. (2014). In the following chapters we will apply these models in a similar manner to a number of SLSNe.

Chapter 3

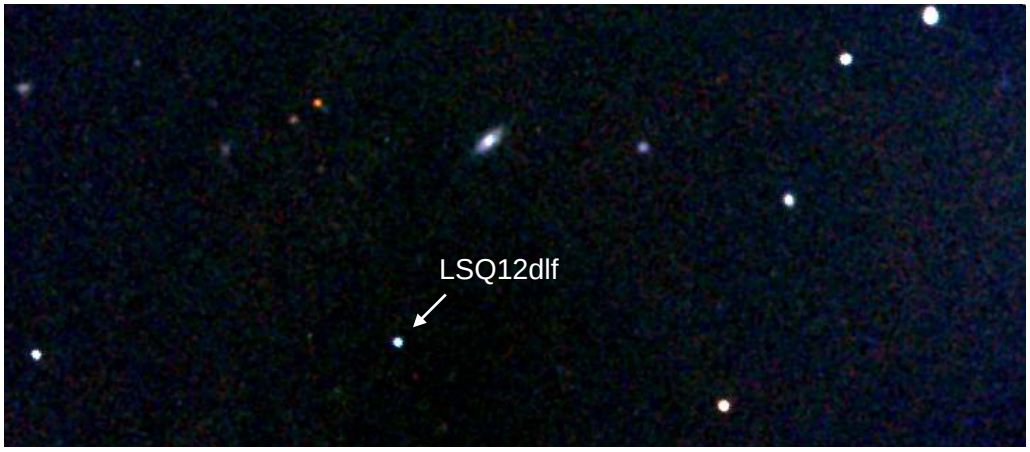

Three SLSNe Ic from PESSTO year one

"This is a very complicated case, Maude.
A lot of ins, a lot of outs,
a lot of 'what-have-yous'..."
- Jeffrey 'The Dude' Lebowski ('The Big Lebowski')

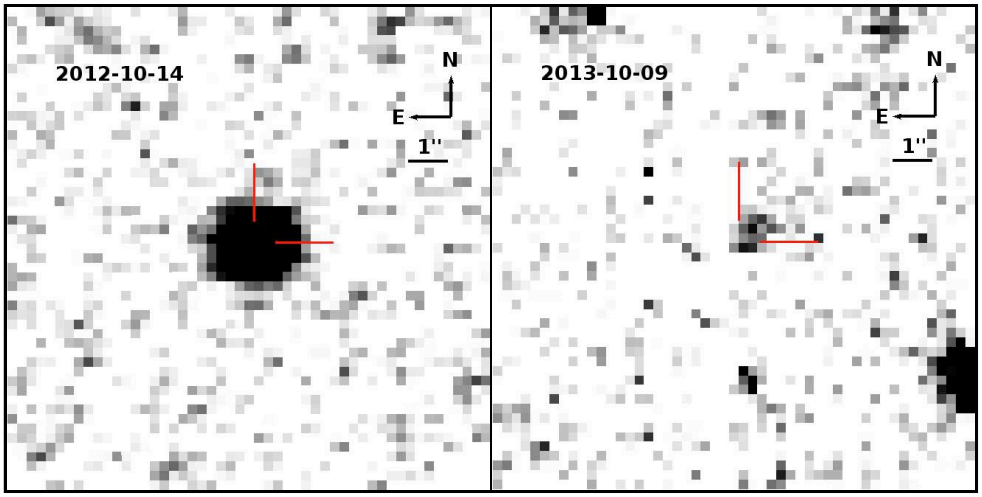

Figure 3.1: NTT+EFOSC2 *V*-band images of LSQ12dlf (200 s; *left*) and a faint, extended source at the SN location, likely to be the host galaxy (18×200 s; *right*).

3.1 Introduction

In this Chapter, we present and analyse the first three SLSNe Ic to be classified and followed by PESSTO. These are relatively low-redshift events, with $z \simeq 0.12$-0.26. We have collected time-series spectroscopy, beginning close to maximum light and continuing for ∼100 days. This is complemented by multicolour photometry spanning 100-200 days in the rest-frames of the objects, enabling us to disentangle host galaxy light from fading SN flux and making these some of the best-observed SLSNe in the literature. The data are used to constrain the various model power sources (radioactive decay, magnetar/central engine heating, circumstellar interaction) detailed in Chapters 1 and 2.

The layout of this chapter is as follows. In section 3.2, we describe the discovery and classification of each SN. Section 3.3 discusses and compares their spectral evolution, while section 3.4 does the same for the multi-band and bolometric light curves. Models for the luminosity (detailed in section 2.4) are applied in section 3.5. We summarize our findings in section 3.6.

3.2 Discovery and classification

3.2.1 LSQ12dlf

LSQ12dlf was identified as a hostless transient by La Silla QUEST (Baltay et al. 2013) on 2012 July 10.4 UT, at RA = 01:50:29.8, Dec = −21:48:45.4 (all coordinates are given

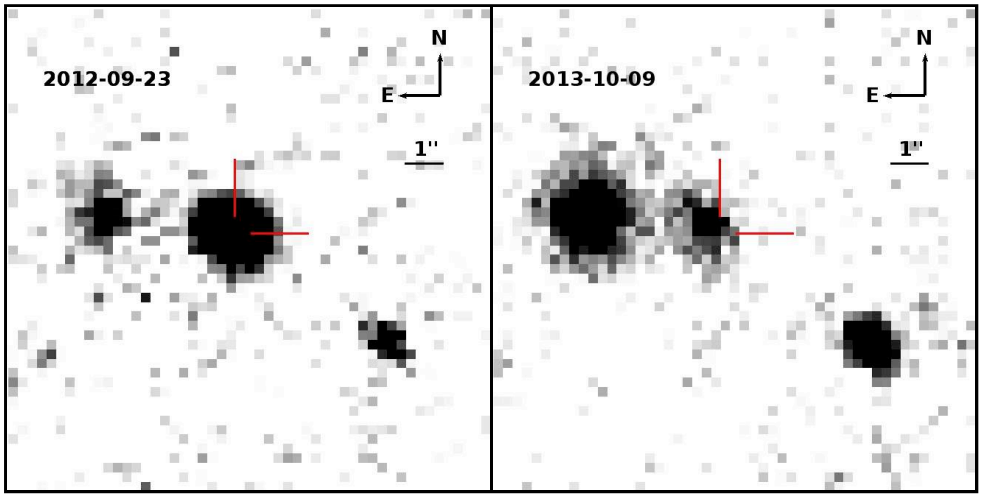

Figure 3.2: NTT+EFOSC2 *R*-band images of SSS120810 (60 s; *left*) and its host galaxy (18×200 s; *right*). The SN is offset ~ 0.″5 from the centre of the host.

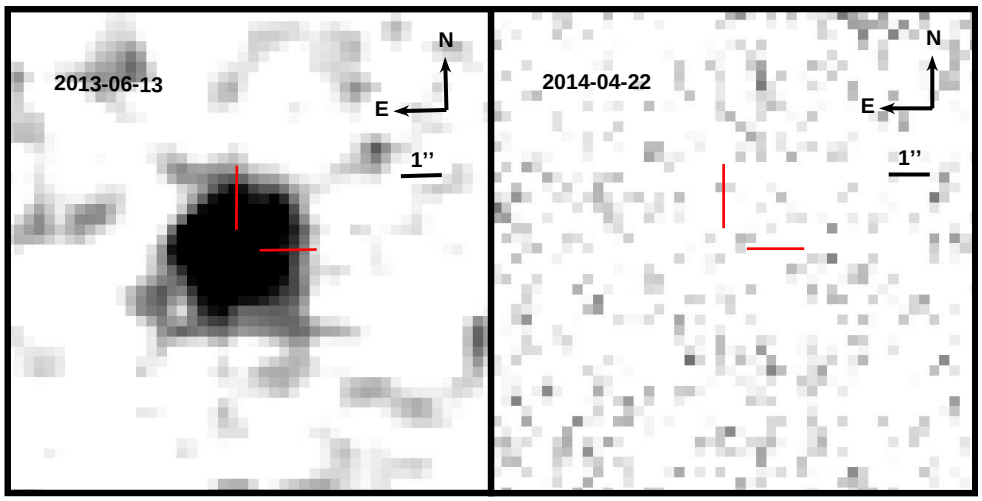

Figure 3.3: LCOGT 1.0-m *r*-band image of SN 2013dg (120 s; *left*). Also shown is an NTT+EFOSC2 *r*-band image (18×200 s; *right*), taken after the SN had faded. No host is detected to a limiting magnitude $r > 25.6$.

in J2000.0). A spectrum obtained by PESSTO on 2012 Aug 08.3 UT, showed it to be a SLSN Ic about 10 days after peak luminosity. Comparison with SN 2010gx, and the other members of this PESSTO SLSN sample, indicated a redshift $z \approx 0.25$ (Inserra et al. 2012). No host galaxy emission or absorption lines are visible, even in a higher-resolution follow-up spectrum obtained with X-Shooter on the VLT. To determine the redshift, we cross-correlated the X-shooter spectrum (which we found was at an epoch of +36 d after maximum light, see Section 3.3.2) with a spectrum of SN 2010gx at +29 d (Pastorello et al. 2010). We found a minimum relative shift in the cross-correlation function for a redshift of $z = 0.255 \pm 0.005$. Deep EFOSC2 imaging on 2013 Oct 10.3 UT, ~300 days after peak in the SN rest frame, and further follow-up in Jan-Feb 2014, showed a very faint host galaxy, with a magnitude $V \approx 25$ (Figure 3.1).

Table 3.1: Spectroscopic observations of LSQ12dlf

Date	MJD	Phase*	Instrument	Range (Å)	Resolution (Å)
2012-08-07	56147.3	+7	NTT+EFOSC2	3700-9200	18
2012-08-09	56149.3	+9	NTT+EFOSC2	3400-10000	13
2012-08-18	56158.3	+16	NTT+EFOSC2	3700-9200	18
2012-08-24	56164.3	+21	NTT+EFOSC2	3700-9200	18
2012-09-09	56180.3	+34	NTT+EFOSC2	3700-9200	18
2012-09-12	56182.5	+36	VLT+Xshooter	3100-24000	1
2012-09-22	56193.3	+44	NTT+EFOSC2	3700-9200	18
2012-12-09	56270.5	+106	Gemini S.+GMOS	4660-8900	2

* Phase in rest-frame days from maximum light.

3.2.2 SSS120810

SSS120810:231802-560926 (hereafter: SSS120810) was discovered by the Siding Spring Survey (SSS), a division of the Catalina Real-Time Transient Survey (Drake et al. 2009) with the 0.5-m Uppsala Schmidt Telescope, on 2012 Aug 11.2. No host was present in SSS reference images at the location of the SN (RA = 23:18:01.8, Dec = −56:09:25.6). PESSTO classified it on 2012 Aug 17-18 as a SLSN Ic, again roughly 10 days after maximum light (Inserra et al. 2012). The redshift was initially estimated as $z \approx 0.14$-0.16, from comparisons with other SLSNe Ic. A spectrum taken at +44 d after peak with X-shooter (see Section 3.3.2), showed a distinct, narrow emission line at 7587.5 Å, with a full-width-half-maximum of FWHM = 9.4 Å. The line is resolved and is almost certainly Hα at $z = 0.156$. Unfortunately, this is right in the telluric A band, which compromises a definitive measurement of the flux and width. Assuming this redshift, the X-Shooter spectrum also shows weak and narrow lines at wavelengths corresponding to two other common host galaxy emission lines: [O II] λ3727 and [O III] λ5007. This gives confidence that the strongest narrow emission line is indeed Hα at $z = 0.156$, and this is the redshift we adopt. Deep *BVRI* imaging with EFOSC2 on 2012 Oct 10.1 and 25.0, ~380 rest-frame days after peak, revealed a clear host galaxy, which is likely the source of the narrow emission lines. The SN is offset from the centre of this galaxy by $0.''51 \pm 0.04$ (Figure 3.3).

3.2.3 SN 2013dg

SN 2013dg was detected by the Mount Lemmon Survey (MLS) and Catalina Sky Survey (CSS), both of which are part of CRTS (Drake et al. 2009). MLS initially discovered the transient, MLS130517:131841-070443, on 2013 May 17.7 UT

Table 3.2: Spectroscopic observations of SSS120810

Date	MJD	Phase*	Instrument	Range (Å)	Resolution (Å)
2012-08-17	56158.3	+10	NTT+EFOSC2	3700-9200	18
2012-08-18	56158.3	+11	NTT+EFOSC2	3700-9200	18
2012-08-24	56164.3	+16	NTT+EFOSC2	3700-9200	18
2012-09-15	56186.2	+35	NTT+EFOSC2	3700-9200	18
2012-09-23	56194.2	+42	NTT+EFOSC2	3700-9200	18
2012-09-26	56196.5	+44	VLT+Xshooter	3100-24000	1
2012-10-14	56215.3	+60	NTT+EFOSC2	3700-9200	18

* Phase in rest-frame days from maximum light.

Table 3.3: Spectroscopic observations of SN 2013dg

Date	MJD	Phase*	Instrument	Range (Å)	Resolution (Å)
2013-06-10	56454.0	+4	WHT+ISIS	3260-10000	4.1-7.7
2013-06-13	56457.0	+6	Gemini S.+GMOS	4660-8900	2
2013-06-25	56469.0	+16	VLT+Xshooter	3100-24000	1
2013-07-03	56477.0	+22	Gemini S.+GMOS	4660-8900	2
2013-07-20	56493.0	+35	VLT+Xshooter	3100-24000	1
2012-08-03	56508.0	+47	Gemini S.+GMOS	4660-8900	2

* Phase in rest-frame days from maximum light.

with the 1.5-m Mt. Lemmon Telescope, while CSS independently found it with the 0.68-m CSS Schmidt Telescope on May 30.7 UT, giving the alternative designation CSS130530:131841-070443. The exact coordinates are RA = 13:18:41.38 and Dec = −07:04:43.1. PESSTO identified MLS130517 as an interesting target, but could not take an EFOSC2 spectrum at this time, as the survey takes a break from May-July when the Galactic centre is over La Silla. We instead classified this object using the William Herschel Telescope and ISIS spectrograph on 2013 Jun 11.0. The spectrum was dominated by a blue continuum, and resembled SLSNe Ic a few days after maximum light (Smartt et al. 2013). The WHT spectrum has two features that were identified as possible Mg II absorption, from either the host galaxy of SN 2013dg or intervening material, at a redshift of $z = 0.192$ (Smartt et al. 2013). These are not visible in the X-shooter spectrum, but the signal-to-noise of the data at 3300 Å precludes a useful quantitative check. The features are at the correct separation if they were the Mg II $\lambda\lambda$ 2795.5, 2802.7 doublet, but the data are noisy, as the lines are close to the edge of the CCD, and cannot be confirmed as real. Nevertheless, this redshift is ruled out by the broad SN features in the spectrum. We cross-correlated the X-shooter spectrum (which we found was at an epoch of +16 d after maximum, see Section 3.3.2) with a spectrum of SN2010gx at +11 d (Pastorello et al. 2010). We found a minimum relative shift in the cross-correlation function when we set $z = 0.265 \pm 0.005$. Hence we suspect the possible absorption is either not real or is foreground and we adopt a redshift of

$z = 0.265 \pm 0.005$ for the SN. No host galaxy emission lines are visible in any of our spectra and the host is not detected in deep imaging taken 250 days after peak (in April 2014) down to $r > 25.6$.

3.3 Spectroscopy

3.3.1 Data aquisition and reduction

The majority of our spectroscopy was carried out within PESSTO, using the NTT and EFOSC2. The data were reduced using the PESSTO pipeline (Smartt et al. 2015), described in Section 2.1.2. Each of our SLSNe were also observed with X-Shooter. SN 2013dg was classified with WHT at the beginning of the PESSTO off-season, and additional spectra were obtained with GMOS on the Gemini South telescope (Hook et al. 2004). These were processed using standard IRAF tasks in CCDPROC and ONEDSPEC; GMOS spectra were extracted using the GEMINI package, while the WHT spectrum was extracted with APALL. More details of the reduction procedures can be found in Sections 2.2.1 and 2.3.1. All spectra are listed in Tables 3.1, 3.2 and 3.3.

All spectra have been corrected for redshift and Milky Way extinction, according to the recalibration of the infrared galactic dust maps by Schlafly & Finkbeiner (2011); we use $E(B-V) = 0.013, 0.019, 0.047$, for LSQ12dlf, SSS120810 and SN 2013dg, respectively. We assume negligible internal extinction, since narrow Na I D absorption features are always very weak or absent. All phases are given in days, in the SN rest-frame, from the date of maximum luminosity.

3.3.2 Spectral evolution

The observed spectral evolution of our objects is shown in Figure 3.4. Between ~ 10-60 days after peak, we have excellent time-series coverage of all three, which we compare to one of the best-observed SLSNe Ic, SN 2010gx (Pastorello et al. 2010). Our earliest spectrum is the WHT classification spectrum of SN 2013dg, obtained at 4 days after maximum light. At this phase, the spectra are dominated by a blue continuum with a blackbody temperature $T \sim 13000$ K, with a few weak absorption features between 4000-5000 Å. These may be attributable to O II, which tends to dominate this region of SLSN Ic spectra before and around peak, as can be seen in SN 2010gx. However, these lines seem to be at slightly redder wavelengths in SN 2013dg. It is possible that we have observed SN 2013dg during the transition from the O II-dominated early spectrum to the nearly-featureless spectrum (with broad, shallow iron lines) seen just after peak in SN 2010gx. This interpretation is supported by our GMOS spectrum, 2 days later, which closely resembles the first post-maximum spectrum of SN 2010gx. It should be

noted, however, that radiative transfer models by Howell et al. (2013) instead favoured C II/III and Fe III as the dominant species in the early (around maximum light) spectra of some SLSNe.

The spectral evolution over days 10-60 is remarkably consistent across these four SNe. The epochs with X-Shooter spectra are highlighted in Figure 3.5. In Figure 3.6, we focus on the spectrum of LSQ12dlf at 36 days after light curve maximum, showing the spectroscopic similarity at this epoch to a normal-luminosity SN Ic at peak (SN 1994I; Richmond et al. 1996). A synthetic spectrum generated using SYN++ is used for line identification (Thomas et al. 2011). The spectrum is dominated by singly-ionised metals. The strongest lines in the optical are Ca II H&K, Mg II λ 4481 (blended with Fe II), a broad Fe II feature between $\sim$ 4900-5500 Å, and the Si II λ 6350 doublet feature. Beyond a phase of $\sim$ 50 days, the peak of the feature around $\sim$ 4500 Å appears to move to slightly redder wavelength, suggesting Mg I] λ 4571 emission is dominant. These are the same features identified by Inserra et al. (2013) in a sample of SLSNe Ic at similar redshifts.

The Fe II lines in the spectrum of LSQ12dlf are stronger and develop earlier than in the other objects of the sample, and are already quite pronounced less than 10 days after peak light. This is very similar to the behaviour of PTF11rks, in the Inserra et al. (2013) sample. That object also transitioned to resemble a normal SN Ic by this epoch, compared to the 20-30 days required in most SLSNe Ic. The authors suggested that this faster evolution could be related to its lower luminosity, relative to the other members of their sample. However, LSQ12dlf peaks at an absolute AB magnitude of $r \sim -21.4$, which is quite typical for SLSNe Ic, and in line with the rest of our sample, and in fact declines more slowly in luminosity than the other PESSTO objects (see Section 3.4).

The final spectrum of LSQ12dlf, 106 days after maximum light, was taken with GMOS. By this time, the SN has cooled to only a few thousand kelvin. The spectrum at this epoch seems to be dominated by a fairly red continuum (i.e. it has still not reached the nebular phase), as well as the same broad lines of singly-ionized metals that have remained present throughout the observed lifetime of the SN. This latest spectrum may also show a weak Na I D absorption; however, given the low signal-to-noise, such an identification is not firm. The colour evolution towards the red is also present in our K-corrected photometry, which suggests $B - V \approx 0.04$ at 44 days after peak, and $B - V \approx 0.58$ at $\sim$ 100 days (the epochs of our last two spectra).

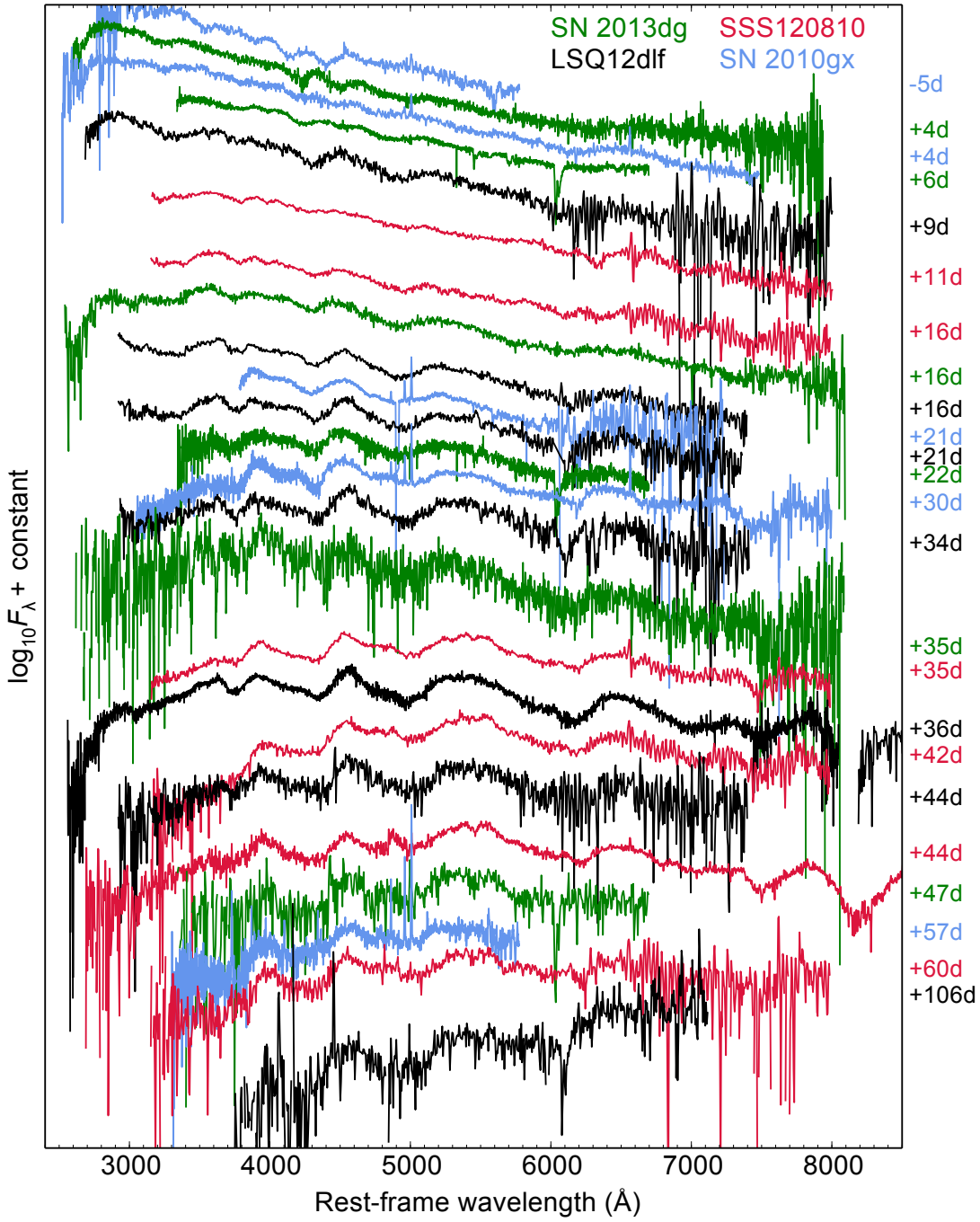

Figure 3.4: The spectral evolution of the PESSTO SLSNe, compared to SN 2010gx, a well-observed SLSN Ic. The four SNe show virtually identical evolution, dominated initially by blue continua, and then by broad lines of Ca II, Mg II, Fe II and Si II (see Figure 3.5). Phases (RHS) are given in rest-frame days from maximum light.

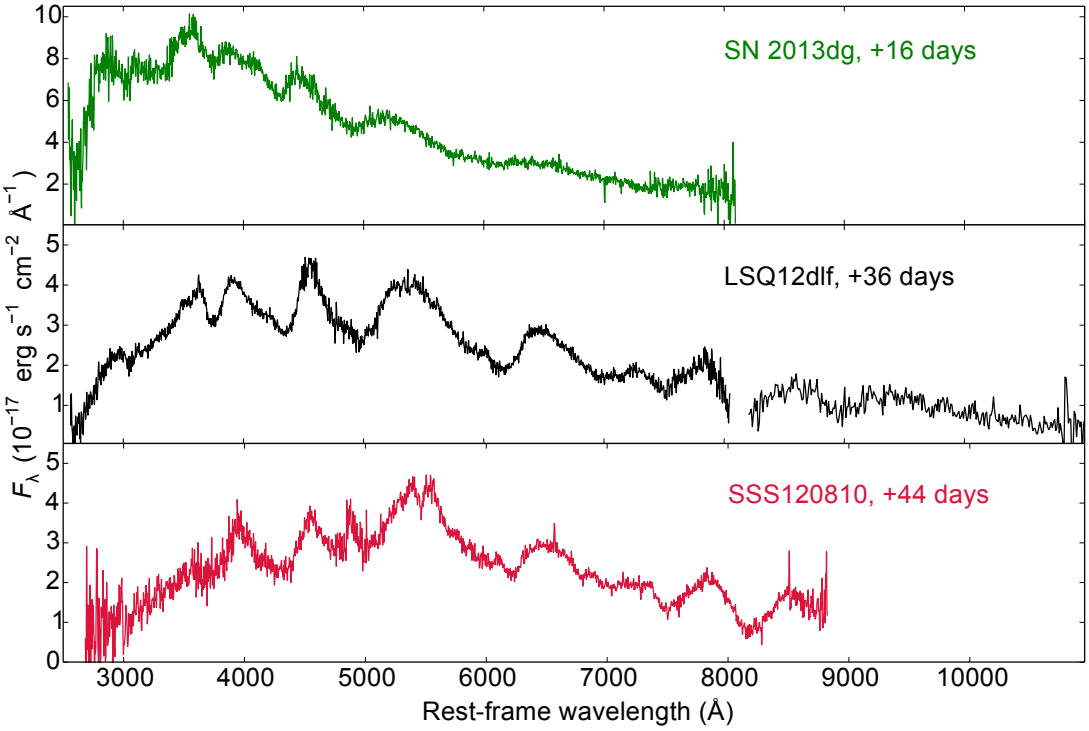

Figure 3.5: X-shooter spectra of our 3 SLSNe, at 2-6 weeks after maximum light (rest-frame). The data have been binned by 10 pixels to improve the signal-to-noise.

In the last spectrum of SSS120810, at 60 days, we do detect a weak Na I D line. The spectra of SSS120810 beyond 35 days all show some structure in the iron blends between $\sim$ 4500-5500 Å, matching that in SN 2011kf (Inserra et al. 2013). X-Shooter spectra of SSS120810 and LSQ12dlf extend the wavelength range into the near-infrared. We can see strong Mg II absorptions at around 7500 and 9000 Å, the former of which is probably blended with O I λ 7774, and a clear Ca II NIR triplet. Overall, the spectral evolution of our objects seems to be much in line with the general picture of SLSNe Ic that has been emerging over the last few years.

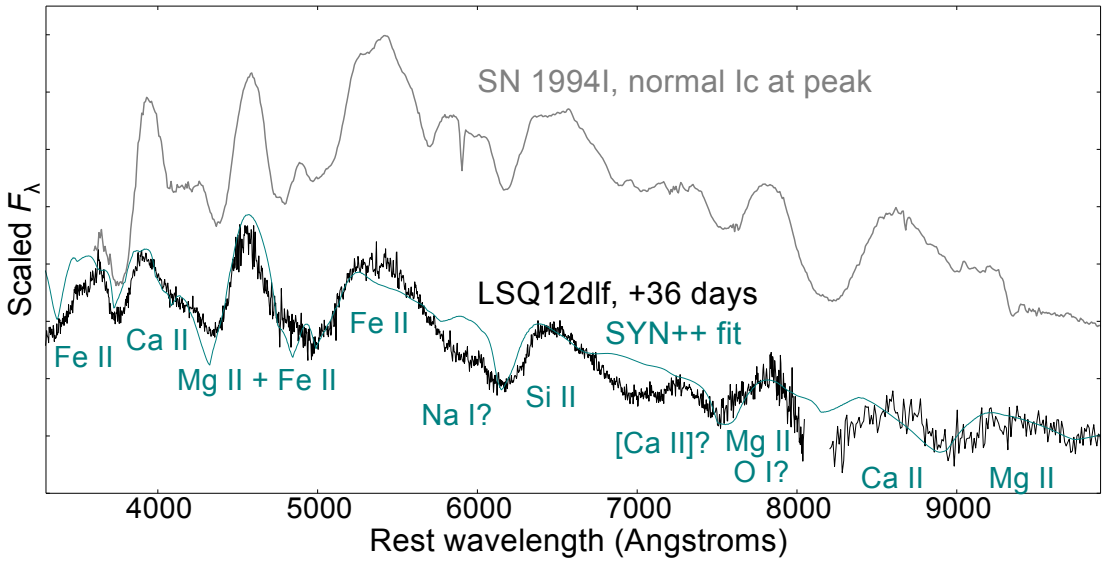

Figure 3.6: LSQ12dlf at around one month after maximum light, compared to the normal Type Ic SN 1994I at maximum. The dominant lines in the two spectra are identical. LSQ12dlf shows stronger continuum emission in the blue, despite being older. Also shown is a synthetic spectrum, generated using SYN++ (Thomas et al. 2011), used to identify the main line-forming ions. The best-fitting model spectrum has a photospheric velocity of 11000 km s^{-1}, and temperature of 7000 K. We see that the spectra are dominated by singly-ionised intermediate-mass metals and iron.

Table 3.4: Observed photometry of SSS120810

Date	MJD	Phase*	U	B	V	R	I	Inst.**
2012-08-10	56149.7	3.2				17.76 (0.11)		SSS
2012-08-18	56158.3	10.6	17.38 (0.03)	18.16 (0.03)	18.09 (0.02)	17.97 (0.02)	17.82 (0.03)	NTT
2012-08-24	56164.3	15.8	17.68 (0.01)	18.42 (0.01)	18.23 (0.02)	18.11 (0.02)	17.90 (0.03)	NTT
2012-08-26	56166.4	17.6	17.80 (0.01)	18.44 (0.02)	18.22 (0.02)	18.12 (0.02)	17.93 (0.02)	NTT
2012-09-08	56179.6	29.1				18.57 (0.09)		SSS
2012-09-15	56186.3	34.9	19.92 (0.03)	19.99 (0.01)	19.21 (0.02)	18.80 (0.02)	18.42 (0.02)	NTT
2012-09-23	56194.3	41.8	20.63 (0.12)	20.56 (0.03)	19.62 (0.02)	19.14 (0.03)	18.70 (0.04)	NTT
2012-10-09	56210.3	55.6		21.26 (0.14)	20.27 (0.06)	19.69 (0.06)	19.14 (0.17)	NTT
2012-10-23	56223.5	67.0			20.78 (0.30)	20.12 (0.30)	19.58 (0.30)	FTS
2012-11-02	56233.4	75.6				20.85 (0.24)		FTS
2012-11-22†	56254.2	93.6		24.62 (0.50)	23.16 (0.13)	21.57 (0.07)	20.88 (0.07)	NTT
2012-12-06†	56268.2	105.7		24.20 (0.38)	22.33 (0.08)	21.30 (0.07)	20.72 (0.10)	NTT
2013-01-02†	56295.2	129.0		> 25.39	> 25.06	23.19 (0.18)		NTT
Host								
2013-10-09	56575.1	371.2				21.89 (0.07)	21.14 (0.07)	NTT
2013-10-24	56590.0	384.1		22.91 (0.06)	22.27 (0.04)			NTT

* Phase in rest-frame days from estimated epoch of maximum light

** SSS = Siding Springs Survey (CRTS); NTT = ESO NTT + EFOSC2 (PESSTO); FTS = Faulkes Telescope South + Faulkes Spectral 01

† Magnitudes measured after subtracting host images from Oct 2013

Table 3.5: Observed photometry of LSQ12dlf

Date	MJD	Phase*	U	B	V	R	I	Inst.**
2012-06-18	56097.41	−32.7			>22.32			LSQ
2012-06-18	56097.44	−32.6			>21.93			LSQ
2012-06-22	56101.36	−29.5			>22.08			LSQ
2012-06-22	56101.41	−29.5			>22.17			LSQ
2012-07-09	56118.35	−15.9			19.33 (0.03)			LSQ
2012-07-09	56118.41	−15.9			19.25 (0.02)			LSQ
2012-07-15	56124.41	−11.1			19.07 (0.02)			LSQ
2012-07-15	56124.43	−11.1			19.02 (0.02)			LSQ
2012-07-17	56126.41	−9.5			19.04 (0.03)			LSQ
2012-07-17	56126.43	−9.5			19.06 (0.03)			LSQ
2012-07-21	56130.31	−6.4			18.89 (0.03)			LSQ
2012-07-21	56130.38	−6.3			18.92 (0.03)			LSQ
2012-07-23	56132.41	−4.7			18.92 (0.02)			LSQ
2012-07-23	56132.42	−4.7			18.91 (0.02)			LSQ
2012-07-27	56136.24	−1.6			18.87 (0.04)			LSQ
2012-07-27	56136.32	−1.5			18.90 (0.02)			LSQ
2012-07-29	56138.25	0.0			18.78 (0.04)			LSQ
2012-07-29	56138.34	0.1			18.80 (0.03)			LSQ
2012-08-09	56149.40	8.9	18.46 (0.09)	19.43 (0.04)	19.15 (0.04)	19.01 (0.09)	18.82 (0.10)	NTT
2012-08-12	56152.10	11.1		19.45 (0.23)	19.22 (0.14)	19.09 (0.15)	18.93 (0.12)	LT
2012-08-18	56158.10	15.9		19.71 (0.13)	19.22 (0.10)	18.96 (0.06)	18.91 (0.05)	LT
2012-08-18	56158.30	16.0	18.91 (0.09)	19.63 (0.06)	19.26 (0.07)	19.04 (0.05)	18.83 (0.17)	NTT
2012-08-18	56158.40	16.1			19.29 (0.02)			LSQ
2012-08-18	56158.41	16.1			19.39 (0.03)			LSQ
2012-08-20	56160.31	17.6			19.39 (0.08)			LSQ
2012-08-20	56160.39	17.7			19.44 (0.03)			LSQ
2012-08-24	56164.30	20.8	19.34 (0.07)	19.90 (0.04)	19.42 (0.03)	19.20 (0.04)	18.88 (0.05)	NTT
2012-08-24	56164.35	20.9			19.49 (0.03)			LSQ
2012-08-24	56164.38	20.9			19.60 (0.04)			LSQ
2012-08-26	56166.21	22.4			19.53 (0.04)			LSQ
2012-08-26	56166.29	22.4			19.45 (0.03)			LSQ
2012-08-26	56166.40	22.5	19.48 (0.03)	19.99 (0.03)	19.59 (0.04)	19.27 (0.04)	19.00 (0.04)	NTT
2012-09-09	56180.40	33.7	20.31 (0.34)	20.69 (0.08)	20.07 (0.06)	19.59 (0.06)	19.13 (0.09)	NTT
2012-09-12	56183.10	35.9		20.86 (0.15)	20.00 (0.05)	19.50 (0.07)	19.43 (0.10)	LT
2012-09-15	56186.30	38.4		21.05 (0.03)	20.24 (0.02)	19.79 (0.03)	19.45 (0.04)	NTT
2012-09-19	56190.10	41.5		21.28 (0.18)	20.30 (0.09)	19.82 (0.06)	19.57 (0.13)	LT
2012-09-22	56193.40	44.1		21.62 (0.07)	20.46 (0.07)	19.92 (0.06)	19.56 (0.05)	NTT
2012-09-24	56195.00	45.4			20.49 (0.31)	19.98 (0.16)	19.64 (0.16)	LT
2012-10-04	56205.10	53.5			20.66 (0.30)	20.12 (0.10)	20.01 (0.13)	LT
2012-10-06	56207.40	55.3			20.79 (0.11)	20.11 (0.15)	19.63 (0.24)	NTT
2012-10-12	56213.00	59.8			21.20 (0.20)	20.44 (0.20)	20.01 (0.18)	LT
2012-10-20	56221.00	66.2		22.64 (0.31)	21.16 (0.19)	20.76 (0.18)	20.45 (0.14)	LT
2012-11-06	56238.20	80.0		23.32 (0.07)	21.92 (0.06)	21.18 (0.05)	20.59 (0.04)	NTT
2012-12-05	56267.20	103.2		24.43 (0.33)	22.82 (0.09)	22.17 (0.08)	21.72 (0.51)	NTT
2012-01-04	56297.00	127.2				22.71 (0.30)		NTT
2012-01-11	56304.10	132.7			24.00 (0.14)			NTT
Host								
2013-10-09	56575.3	354.8			25.02 (0.15)	> 23.98	> 22.65	NTT
2014 stack†					24.81 (0.34)			NTT

* Phase in rest-frame days from epoch of maximum light

** LSQ = La Silla QUEST survey; NTT = ESO NTT + EFOSC2 (PESSTO); LT = Liverpool Telescope + RATCam

† Sum of images obtained on 4 nights in Jan and Feb 2014

Table 3.6: Observed photometry of SN 2013dg

Date	MJD	Phase*	g	r	i	z	Instrument**
2013-05-13	56425.2	−19.0		20.27 (0.54)			CSS
2013-05-17	56429.2	−15.9		19.72 (0.17)			MLS
2013-05-30	56442.2	−5.6		19.16 (0.23)			CSS
2013-06-06	56449.2	0.0		19.11 (0.17)			CSS
2013-06-12	56456.0	5.4	19.26 (0.03)	19.31 (0.06)	19.50 (0.07)	19.60 (0.07)	LT
2013-06-13	56456.9	6.1	19.36 (0.03)	19.31 (0.06)	19.56 (0.10)		LCO
2013-06-14	56457.9	6.9	19.26 (0.07)	19.36 (0.04)	19.39 (0.08)	19.40 (0.17)	LT
2013-06-15	56459.1	7.9	19.41 (0.03)	19.36 (0.07)			LCO
2013-06-15	56459.3	8.0			19.47 (0.08)	19.44 (0.22)	FTN
2013-06-16	56459.9	8.5	19.42 (0.10)	19.39 (0.05)	19.56 (0.10)	19.69 (0.15)	LT
2013-06-16	56460.1	8.7	19.48 (0.06)	19.34 (0.05)			LCO
2013-06-19	56463.4	11.3		19.52 (0.17)			FTN
2013-06-20	56464.1	11.8	19.57 (0.05)	19.55 (0.05)	19.68 (0.12)		LCO
2013-06-22	56465.9	13.3	19.68 (0.10)	19.52 (0.09)	19.71 (0.13)	19.62 (0.20)	LT
2013-06-25	56468.0	14.9	19.81 (0.05)	19.54 (0.05)	19.61 (0.05)		LCO
2013-06-29	56473.0	18.9	20.03 (0.03)	19.74 (0.03)	20.04 (0.22)	19.74 (0.19)	LT
2013-07-01	56475.0	20.5	20.20 (0.03)	19.81 (0.04)	19.93 (0.06)		LCO
2013-07-01	56475.3	20.7	20.25 (0.17)	19.80 (0.14)	19.84 (0.08)	19.92 (0.18)	FTN
2013-07-02	56476.0	21.3	20.26 (0.04)	19.87 (0.04)	20.02 (0.08)		LCO
2013-07-10	56483.8	27.5	20.71 (0.08)	20.23 (0.08)	20.27 (0.11)		LCO
2013-07-13	56487.0	30.0	20.95 (0.07)	20.23 (0.06)	20.24 (0.11)		FTN
2013-07-29	56502.0	41.9	21.48 (0.23)	20.82 (0.39)	20.88 (0.22)	20.52 (0.30)	NTT
2013-08-03	56508.0	46.7	22.23 (0.05)	21.21 (0.04)	20.95 (0.06)	20.79 (0.10)	NTT
2013-08-14	56519.0	55.4		21.88 (0.07)			NTT
2013-08-15	56520.0	56.2			21.62 (0.16)		NTT
2013-08-16	56520.5	56.6				20.91 (0.30)	NTT
2014-01-30†	56688.3	189.8		25.21 (0.41)	24.68 (0.28)		NTT
2014-02-07†	56696.3	196.1		25.48 (0.36)	25.21 (0.36)		NTT
2014-04-22	56770.0	254.6		> 25.63	> 25.06		NTT

* Phase in rest-frame days from epoch of maximum light

** CSS = Catalina Sky Survey Survey (CRTS); MLS = Mt. Lemmon Survey (CRTS)
LT = Liverpool Telescope + RATCam; LCO = Las Cumbres Observatory Global Telesope 1m Network; FTN = Faulkes Telescope North + Faulkes Spectral 02; NTT = ESO NTT + EFOSC2 (PESSTO)

† May include significant host contribution

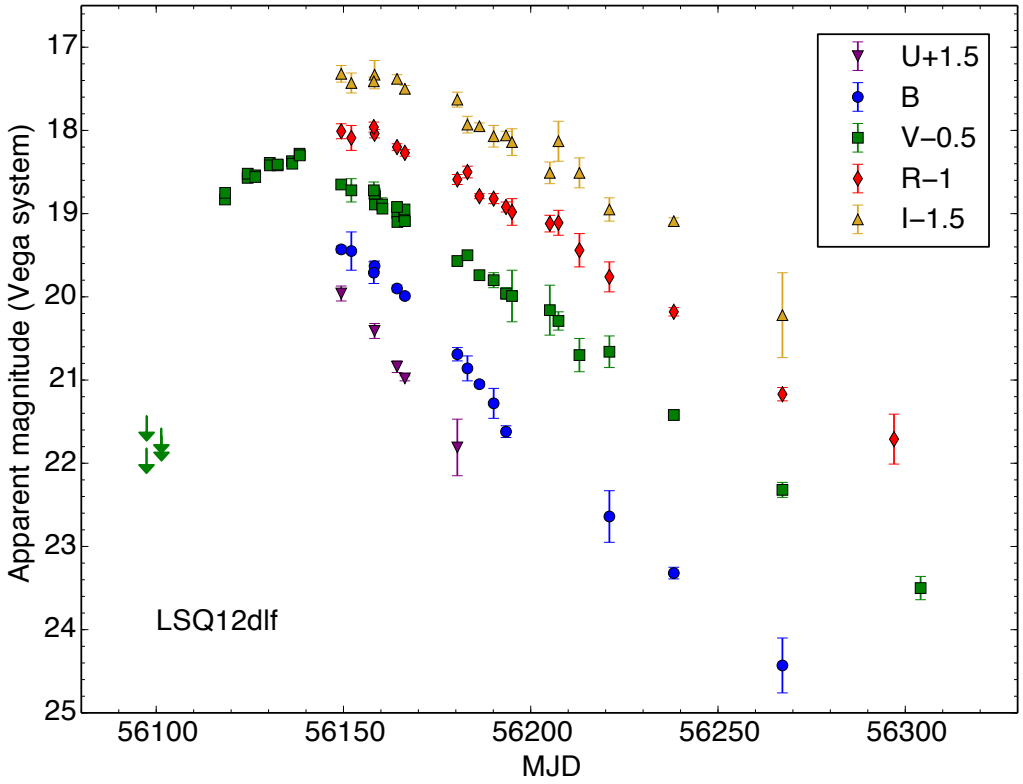

Figure 3.7: Multi-colour light curve of LSQ12dlf, in the observer frame.

3.4 Photometry

3.4.1 Data aquisition and reduction

Imaging of our SLSNe came from a variety of sources. In addition to EFOSC2, we collected data with the Liverpool Telescope, the LCOGT 1.0-m network, and the 2.0-m Faulkes Telescopes (operated by LCOGT). These data were automatically de-trended by their instrument-specific pipelines. SN magnitudes were measured by PSF-fitting photometry in SNOoPY (Section 2.3.2), while zero-points were calculated using a local sequence of nearby stars (themselves calibrated to standard fields over several photometric nights).

The EFOSC2 *i* filter is closer to SDSS than to Johnson-Cousins; however for LSQ12dlf and SSS120810, we calibrate to Johnson-Cousins *I* (Vega system) in keeping with the *UBVR* photometry. For SN 2013dg, we used the SDSS-like *griz* filters on EFOSC2, and calibrated to the AB magnitude system, in order to stay consistent with the Liverpool Telescope and LCOGT data obtained during the PESSTO off-season. The magnitudes we measured for the three SNe are reported in Tables 3.4, 3.5 and 3.6, where the final column in each table lists the data source.

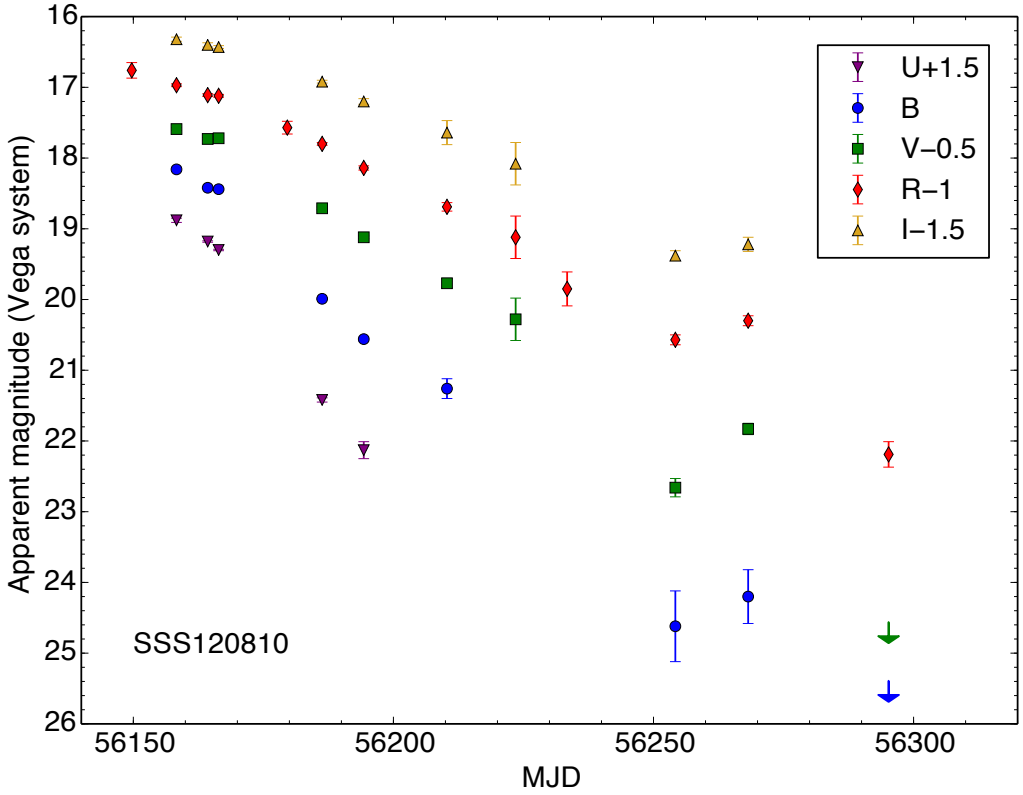

Figure 3.8: Multi-colour light curve of SSS120810, in the observer frame.

Our light curves were supplemented with early data provided by LSQ, and public data from CRTS, which allowed a determination of the rise times for two of our SNe. Synthetic photometry on our spectra showed that magnitudes calculated from LSQ images are almost identical to those in the V band, apart from a shift of -0.02 magnitudes to convert from LSQ AB mags to the more standard Vega system. For the public CRTS data, which are in the R-band, we averaged the (typically four) measured magnitudes from each night. In the case of SN 2013dg, we used the measured colour at peak, $r - R \approx 0.2$, to convert to SDSS r, matching the LT and LCOGT photometry.

3.4.2 Light curves

Figures 3.7-3.9 show the multi-colour photometric evolution of our three objects. The earliest observations from LSQ and CRTS captured the rising phases of LSQ12dlf and SN 2013dg, respectively, while unfortunately the rise of SSS120810 was missed. Judging from the similarity in the spectrum of SSS120810 taken on 2012 Aug 24 with that of SN 2013dg from 2013 Jun 26, we estimate that SSS120810 peaked around MJD 56146 (2012 Aug 7), so the earliest detection is likely just after maximum. All three objects exhibit a more rapid post-peak decline in the bluer bands, which is typical for

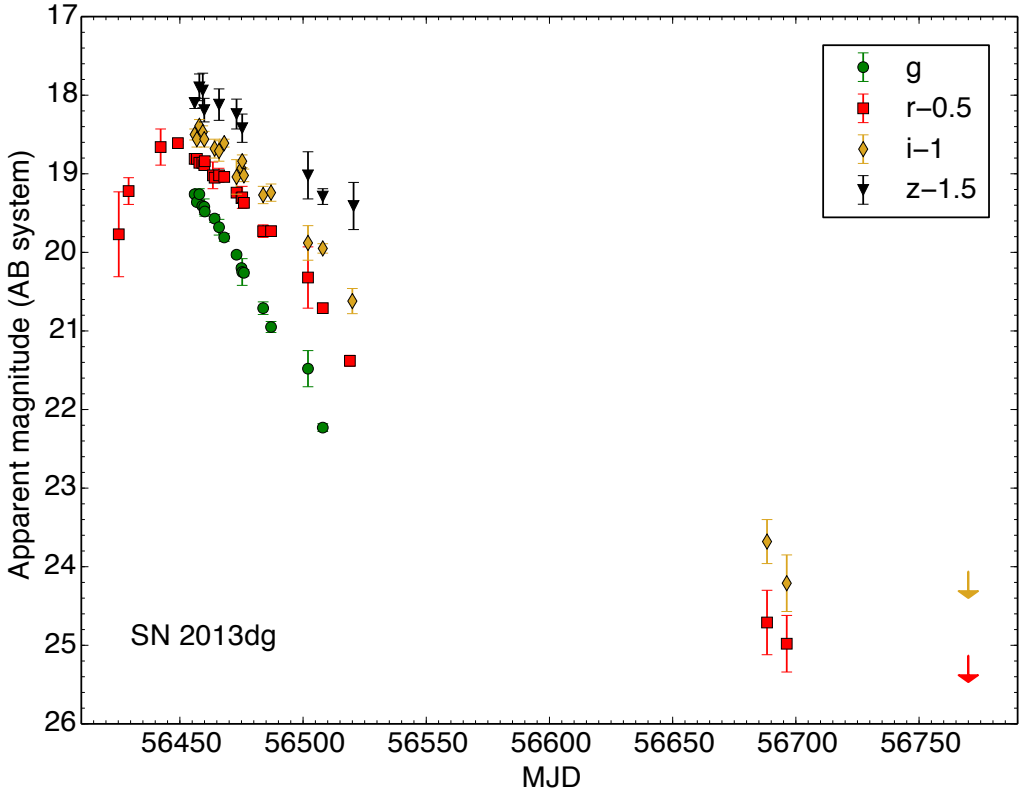

Figure 3.9: Multi-colour light curve of SN 2013dg, in the observer frame.

SNe of this kind, and should be expected as they expand and cool.

The light curve of SSS120810 shows some unusual behaviour at $\gtrsim$100 days after peak: a rebrightening, which is more pronounced in the blue. Such a feature has not been witnessed in any previous SLSN. The host galaxy of SSS120810 contributes significantly to the observed brightness at the critical late epochs (beyond $\sim$ 70 d after peak), so we have subtracted deep EFOSC2 images of the host, obtained in the second PESSTO season, after the SN had faded. Subtractions were carried out using the code HOTPANTS[1] (based on algorithms developed by Alard & Lupton 1998), which matches the seeing in the two images by computing a convolution kernel from the PSFs of point sources. The rebrightening remains significant even after template subtraction, and the measured zero points and sequence star magnitudes are consistent within <0.1 magnitudes between these nights; we therefore conclude that this is real.

The host galaxy of LSQ12dlf, by contrast, is barely detected in our late imaging, so image subtraction need not be applied. SN 2013dg was in solar conjunction during Sept 2013 to Jan 2014. When it reappeared, we detected a faint source in Jan and Feb 2014 (+190 d and +196 d after peak in rest-frame), which disappeared by April (+254 d) in similarly deep imaging. Hence it is likely that the source at $\sim$ 200 days is SN 2013dg,

[1] http://www.astro.washington.edu/users/becker/v2.0/hotpants.html

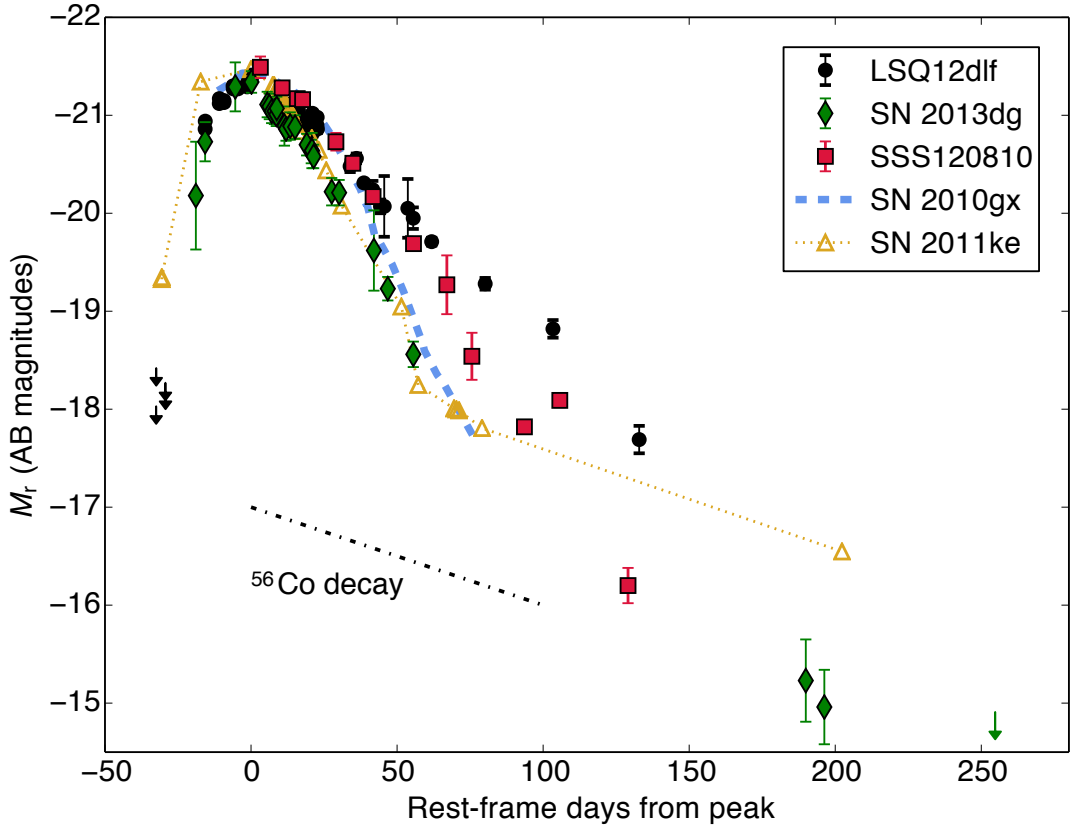

Figure 3.10: Absolute *r*-band light curves. These have been corrected for time dilation and galactic extinction. *K*-corrections, based on our spectra, have been applied to convert the effective filter to rest-frame *r*. The rising phases of LSQ12dlf and SN 2013dg are similar, and last approximately 25-35 days. However, our three objects show quite different declines after maximum light, though all fade more rapidly than fully-trapped ^{56}Co decay. Also shown for comparison are SNe 2010gx and 2011ke (typical SLSNe Ic, Inserra et al. 2013).

which has faded by 250 days, leaving no detection of the host galaxy. This means that image subtraction is not needed for any of the data points for SN 2013dg. The two late detections also suggest that there is a tail phase for SN 2013dg, as observed for several SLSNe Ic in the Inserra et al. (2013) sample.

It is instructive to directly compare the absolute light curves of our sample. The absolute *r*-band light curves are shown in Figure 3.10, along with two other SLSNe Ic (2010gx and 2011ke, Pastorello et al. 2010; Inserra et al. 2013). Time-dilation, galactic extinction corrections and *K*-corrections have all been applied. SN 2013dg is most similar to the archetypal SLSNe Ic, including a likely flattening to a tail phase, albeit steeper than that seen in SN 2011ke at 50 days. LSQ12dlf shows a similar rise to SN 2013dg, though possibly slightly longer – the two SNe taking somewhere between 25-35 days to reach peak – and declines significantly more slowly. Moreover, LSQ12dlf shows no sign of a break in the light curve slope even out to 130 days after maximum.

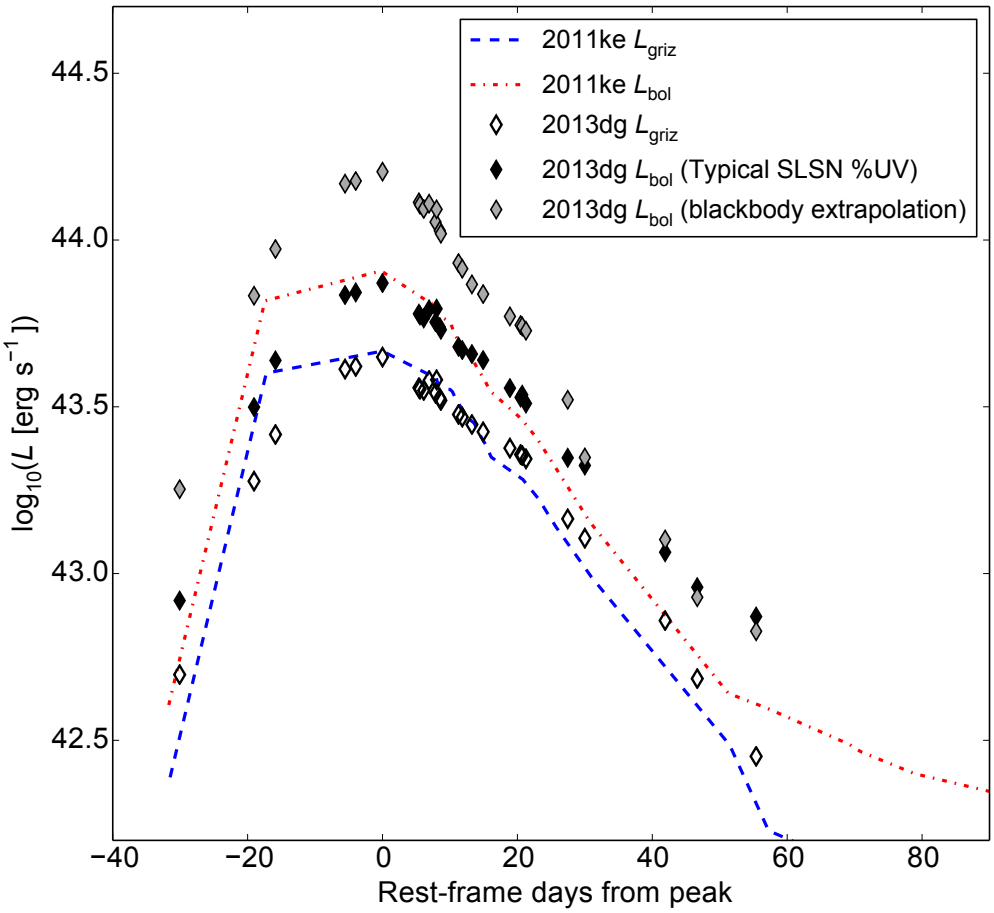

Figure 3.11: The UV+NIR correction to the *griz* pseudo-bolometric light curve of SN 2013dg, compared to the bolometric and *griz* light curves of SN 2011ke (from Inserra et al. 2013). We add the percentage UV flux, as a function of time, for a typical SLSN Ic (Inserra et al. 2013), to SN 2013dg, preserving the similarity in peak luminosity between these two SNe. We model the NIR flux by fitting a blackbody to the optical data. If we do the same for the UV flux, we overestimate the flux contribution from wavelengths shorter than rest-frame *g*-/*B*-band, as shown.

SSS120810 declines with a slope intermediate between LSQ12dlf and SN 2013dg. No clear radioactive or magnetar tail is seen; instead we see the rebrightening, which peaks at $\sim$ 100 days after maximum light. The light curve evolution of the three objects is therefore surprisingly diverse, given their spectroscopic similarity.

3.4.3 Bolometric light curves

In order to analyse our data using physical models, we constructed a bolometric light curve for each of our SNe. First we de-reddened and *K*-corrected our photometry. We then integrated the corrected flux in these optical bands, and applied appropriate corrections for the missing ultra-violet and near-infrared data as follows: Initially, we tried applying corrections based on fitting a blackbody to the optical photometry, and

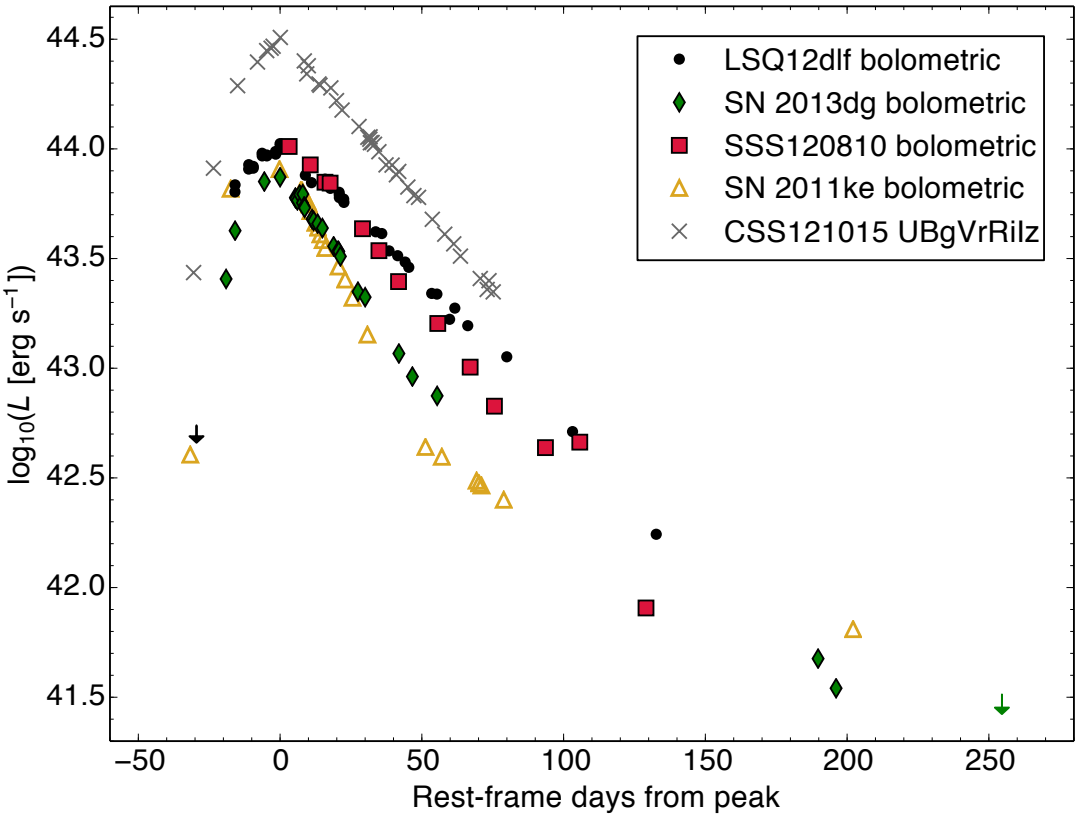

Figure 3.12: Bolometric light curves of LSQ12dlf, SSS120810, SN 2013dg and SN 2011ke (from Inserra et al. 2013), as well as CSS121015 (a SLSN from PESSTO with spectral similarities to both SLSNe Ic and SLSNe II; Benetti et al. 2014).

integrating the flux between 1700 Å (approximately the blue edge of the Swift UVOT filters) and 25000 Å. We compared the luminosity in the UV, optical and NIR regimes to the SLSNe studied by Inserra et al. (2013), and found that we were likely significantly over-estimating the UV contribution, as is often the case with blackbody fits. In a real SN, UV absorption lines cause the flux to fall well below that of a blackbody at the optical colour temperature (Chomiuk et al. 2011; Lucy 1987). We therefore chose not to use the simple blackbody fit in the UV, and instead applied a typical percentage UV correction for SLSNe Ic, using Figure 7 of Inserra et al. (2013). That work included both blackbody fits and real UV data, so should be slightly more reliable. The effect of this correction, and a comparison with SN 2011ke, is shown in our Figure 3.11. We did continue to use a blackbody estimate for the NIR contribution.

Our bolometric light curves are shown in Figure 3.12, along with SN 2011ke. Peak luminosities are in the range $0.7\text{-}1 \times 10^{44}\,\mathrm{erg\,s^{-1}}$. As we saw in our single-filter comparison, the SNe have different declines from maximum. Of our three objects, only SN 2013dg shows evidence of a flattening in the decline rate, though not to the extent seen in SN 2011ke. The bolometric light curve of LSQ12dlf has a similar shape to that of

Table 3.7: Light curve fit parameters

Magnetar	M_{ej}[a]	B[b]	P[c]	χ^2/d.o.f.
LSQ12dlf	10.0	3.7	1.9	5.61
SSS120810	12.5	3.9	1.2	10.63
SN 2013dg	5.4	7.1	2.5	1.01

^{56}Ni decay	M_{ej}[a]	M_{Ni}[a]	E_k[d]	χ^2/d.o.f.
LSQ12dlf	10.1	8.1	30	3.46
SSS120810	7.2	6.6	30	10.45
SN 2013dg	6.6	5.5	30	0.37

CSM interaction	M_{ej}[a]	M_{CSM}[a]	M_{Ni}[a]	E_k[d]	ρ_{CSM}[e]	χ^2/d.o.f.	R_{ph}[f,*]
LSQ12dlf	7.6	3.4	–	1.1	−11.95	0.80	1.1
SSS120810	15.8	2.3	–	0.84	−11.74	12.78	2.1
SN 2013dg (peak)	4.6	2.4	–	1.2	−12.22	0.38	0.6
SN 2013dg (full)	8.0	0.9	0.1	1.1	−11.34	0.47	0.45

[a] $M_\odot$; [b] 10^{14}G; [c] ms; [d] 10^{51} erg; [e] $\log_{10}(\rho_{CSM}/\mathrm{g\,cm^{-3}})$; [f] 10^{15} cm
* Determined by other fit parameters

another PESSTO SLSN, CSS121015 (Benetti et al. 2014), though it is significantly less luminous. CSS121015 showed evidence of circumstellar interaction, and the data were consistent with such a shocked-shell scenario, but it also exhibited similarities with SLSNe Ic, and its light curve was satisfactorily reproduced by our magnetar models (Figure 2.6). These two SLSNe show similar rise times and linear declines from peak magnitude. SSS120810 declines more rapidly than LSQ12dlf from a similar peak luminosity, though its linear decline is broken by the rebrightening at 100d. No published SLSN matches this behaviour. Possible mechanisms are proposed in section 3.5.2.

3.5 Modelling

In this section we fit the data using our three simple light curve models. We consider ^{56}Ni- and magnetar-powered light curves, where the magnetar functions as a representative central engine, using the method and analytical treatment discussed in Sections 2.4.1 and 2.4.2. We also investigate fits with the simple ejecta-CSM interaction model presented in Section 2.4.3. In practice, we find that no ^{56}Ni is required for the interaction-powered fits around peak luminosity, but we will include ^{56}Ni in fitting the light curve tail of SN 2013dg.

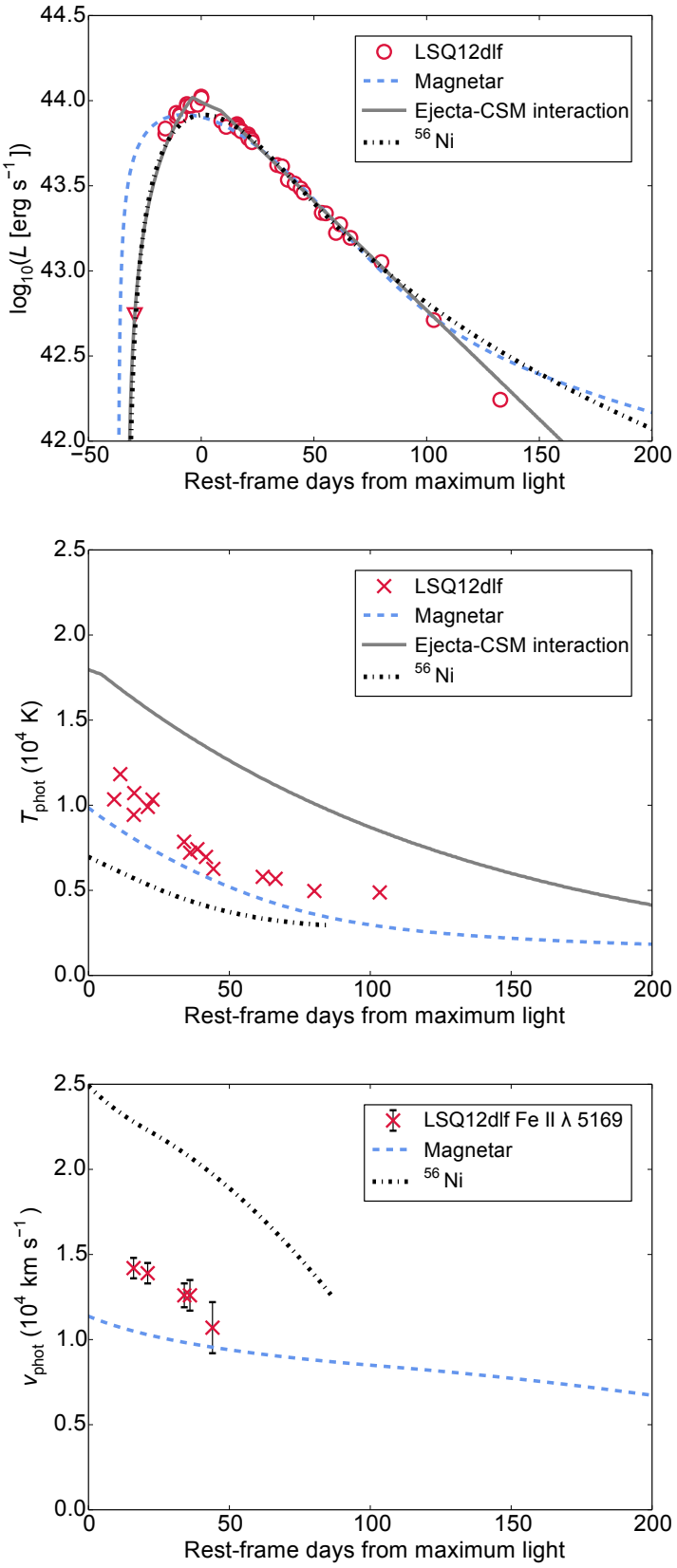

Figure 3.13: Magnetar-, interaction- and ^{56}Ni-powered models of LSQ12dlf. Parameters are listed in Table 3.7. Temperatures were estimated by fitting blackbody curves to multi-colour photometry; velocities were measured from absorption minima.

The best fitting light curve models for each SN are shown in Figures 3.13-3.15, and the parameters of all fits are listed in Table 3.7. Errors are approximately the same size as the circles; triangles represent upper limits. We measure velocities by fitting Gaussian profiles to the absorption component of the P Cygni lines (see Figure 1.3). The error in velocity is estimated from the scatter in multiple fits. Temperatures are estimated from blackbody fits to our photometry, as in section 3.4.3. The magnetar and ^{56}Ni-diffusion models give us photospheric velocities and temperatures for comparison, as described in Inserra et al. (2013); these curves end when the SN no longer has a well-defined photosphere (i.e. its atmosphere has become optically thin). The temperature is estimated in our interaction model simply by assuming that the output luminosity is blackbody emission from the photosphere, and therefore using $L = 4\pi R_{\rm phot}^2 \sigma T^4$. As the location of the photosphere, $R_{\rm ph}$, is fixed in this model, we simply have $T \propto L^{1/4}$.

3.5.1 LSQ12dlf

In contrast to the SLSNe studied by Inserra et al. (2013), LSQ12dlf (Figure 3.13) is difficult to fit with a magnetar model. It has a noticeably broader light curve than the other low-z SLSNe Ic. The decline in magnitude is linear for $\sim$ 130 days, showing no sign of a t^{-2} tail, as predicted by the magnetar model (or indeed a ^{56}Co tail). Although the magnetar model fits the majority of the light curve well, the fit is poor at late times, where it over-predicts the flux, and early times, as fitting the slow decline results in a broader peak and an earlier explosion date than our limit at -30 days suggests. The peak is not so problematic, since these luminosities are estimated from single-filter LSQ photometry, and are therefore subject to significant uncertainty. The discrepancy between the magnetar model and the data at 130 days could be explained by γ-ray leakage. Most of the magnetar power is expected to be released in the form of X-rays/γ-rays and/or high-energy particle pairs. If the ejecta become optically thin to this radiation as they expand, the reprocessed optical luminosity may drop below the predictions of our fully-trapped model. Therefore we cannot exclude the magnetar based on the late data point. The magnetar model best matches the temperature evolution, though all three models get the approximate shape correct. The ^{56}Ni-powered model greatly over-predicts the SN velocity, because of the large explosion energy (30×10^{51}erg) needed to fit the light curve timescales. This is also true for the ^{56}Ni-powered fits to our other SLSNe.

The interaction and radioactive models give a better fit to the early part of the light curve, though we exclude the latter because of the requirement for 80% ^{56}Ni ejecta (Table 3.7). The interaction model is for $\sim 8\,{\rm M}_\odot$ of ejecta and $\sim 3\,{\rm M}_\odot$ of CSM. This gives a satisfactory fit to the whole light curve, without invoking large $E_{\rm k}$.

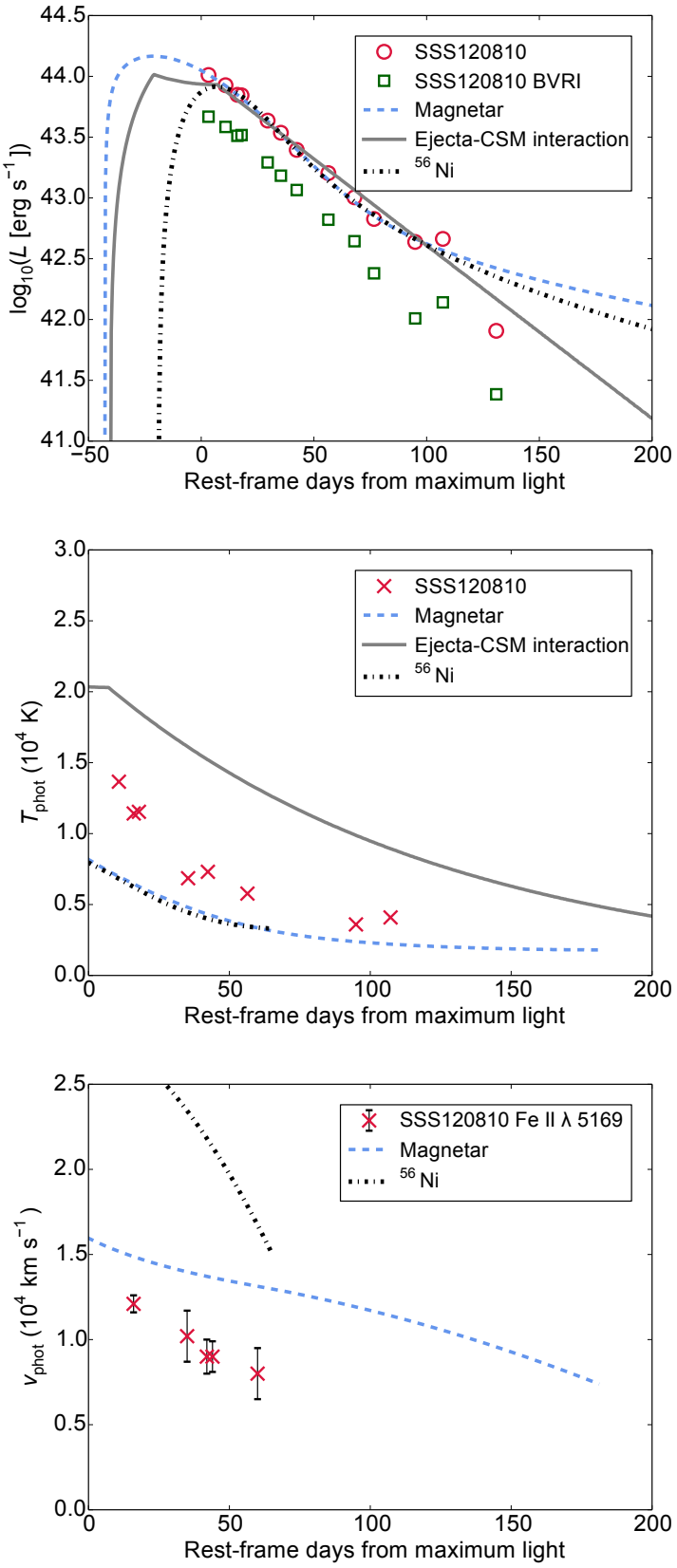

Figure 3.14: Magnetar-, interaction- and ^{56}Ni-powered models of SSS120810. Parameters are listed in Table 3.7. Temperatures were estimated by fitting blackbody curves to multi-colour photometry; velocities were measured from absorption minima.

3.5.2 SSS120810

This SN is the most difficult to fit, despite the lack of photometry before maximum brightness, because none of our simple light curve models naturally accommodate a late rebrightening as observed in the SSS120810 data. In Figure 3.14, we show both the bolometric and *BVRI* pseudobolometric light curve, to illustrate the uncertainty in the relative height of this feature. Regardless, the final point on the light curve falls well below the tails of our magnetar and radioactive fits. The ejected mass in our interaction fit is quite different from the other SLSNe, with $M_{\rm ej} \sim 16\,{\rm M}_{\odot}$, whereas the other fits have $M_{\rm ej} \sim$ 4-8 $\rm M_{\odot}$. The CSM mass, $M_{\rm CSM} \sim 2\,{\rm M}_{\odot}$, is more typical. However, the parameters for SSS120810 are by far the least well-constrained, due to the lack of early data. The magnetar model gives a good fit to the velocity, while the temperature is intermediate between the magnetar and interaction models. We again reject the radioactive model, because of the inferred 90% ^{56}Ni ejecta.

One possible explanation for the bump at 100 days could be circumstellar interaction with multiple shells of material. The peak emitted luminosity of a shocked shell should approximately obey the relation $L \sim \frac{1}{2} M_{\rm CSM} v_{\rm phot}^2 / t_{\rm rise}$, where $v_{\rm phot}$ is the photospheric velocity and $t_{\rm rise}$, the rise time, is a typical light curve timescale (Quimby et al. 2007; Smith & McCray 2007). Let us assume that the main light curve peak ($L \sim 10^{44}\,{\rm erg\,s^{-1}}$) is powered by an ejecta-CSM interaction as described by our best-fit model in Figure 3.14 ($M_{\rm ej} \sim 16\,{\rm M}_{\odot}$; $M_{\rm CSM} \sim 2\,{\rm M}_{\odot}$; $t_{\rm rise} \sim 30\,{\rm d}$). Although our code utilises a simplifying stationary photoshere, in reality the shocked shell is expanding, as momentum must be conserved. If it then encounters further material, another shock, and consequently a rebrightening, may occur, with a luminosity also roughly given by the above expression.

In our case, this anomaly appears to be much faster than the main light curve timescale: the final point on our light curve is consistent with the original decline, suggesting the rebrightening lasts $\lesssim 30\,{\rm d}$. This in turn suggests a much lower CSM mass compared to the first shell (as $M_{\rm CSM}$ is the dominant factor in setting the light curve width). In this scenario, we might expect the outer shell to be swept up by the inner shell/ejecta without causing the expanding material to decelerate significantly. Since the shell velocity is then similar before and after the second collision, we may write $(M_2/M_1) \sim (L_2/L_1)(t_2/t_1)$. Fitting a straight line to our bolometric light curve, we find that the bump is $\sim 2.4 \times 10^{42}\,{\rm erg\,s^{-1}}$ brighter than the predicted luminosity at this phase, and the rise time is $\gtrsim 10\,{\rm d}$. This gives an estimated mass of $\gtrsim 0.01\,{\rm M}_{\odot}$ for the outer CSM. This could be associated with a normal stellar wind, prior to ejection of the dense shell. There are related alternatives to this picture, for example a single CSM shell, but with clumpy structure in the outer layer. If the forward shock encounters

such a clump, the change in density may cause a rebrightening. Another possibility is a change in the density gradient towards the outside of the shell. However, it should be noted that in our fit the forward shock breaks out of the shell around peak, long before the rebrightening.

Another intriguing possibility is that we have the first optical observation of magnetar wind breakout in a SLSN. Metzger et al. (2014) predict that, under certain conditions, the ionisation front of the pulsar wind nebula could break out of the ejecta a few months after the optical light curve peak. Levan et al. (2013) observed X-ray emission from SCP06F6, one of the first known SLSNe Ic, at just such a phase, but no other SLSNe have been detected in X-rays (limits have been measured by Ofek et al. 2013). Metzger et al. (2014) found that the ionisation front is more likely to break out (and to break out earlier) for more energetic magnetars, and in fact our fit to SSS120810 suggests a spin period of 1.2 ms – close to the maximum allowed rotation rate for neutron stars. Those authors also point out that X-ray breakout may result in an abrupt change in the optical properties of the SN, such as the effective temperature. Our observations indicate that the rebrightening is more pronounced at bluer wavelengths, and our estimates of the blackbody colour temperature shown in Figure 3.14 seem to support the idea that the rebrightening is associated with a reheating of the ejecta.

3.5.3 SN 2013dg

As shown in section 3.4, the light curve of SN 2013dg is the most similar to typical low-redshift SLSNe Ic (Inserra et al. 2013). However, the possible host contamination to our late points, at ~200 d after maximum, is quite uncertain: the upper limit at 250 d is not much fainter than the last observed SN flux, thus the constraint on the host is weak. We will assume that the late points are dominated by SN light when fitting the models, though we also fit the interaction model to the peak only. The peak-only fit does not require significant ^{56}Ni in the ejecta, but ^{56}Ni is needed to produce a shallower decline at late times. Our fit suggests $M_{\rm Ni} \approx 0.1\,{\rm M}_{\odot}$, which is perfectly feasible for a core-collapse SN. Adding this moderate amount of ^{56}Ni has a significant effect on the derived ejecta and CSM masses in the model, increasing $M_{\rm ej}$ by about a factor of 2, and decreasing $M_{\rm CSM}$ by about the same factor. In this case the peak luminosity is powered by a combination of interaction and ^{56}Ni-decay energy. The pure ^{56}Ni and magnetar models can naturally explain the late-time decline as being either due to ^{56}Co decay or the power-law energy injection from the magnetar engine.

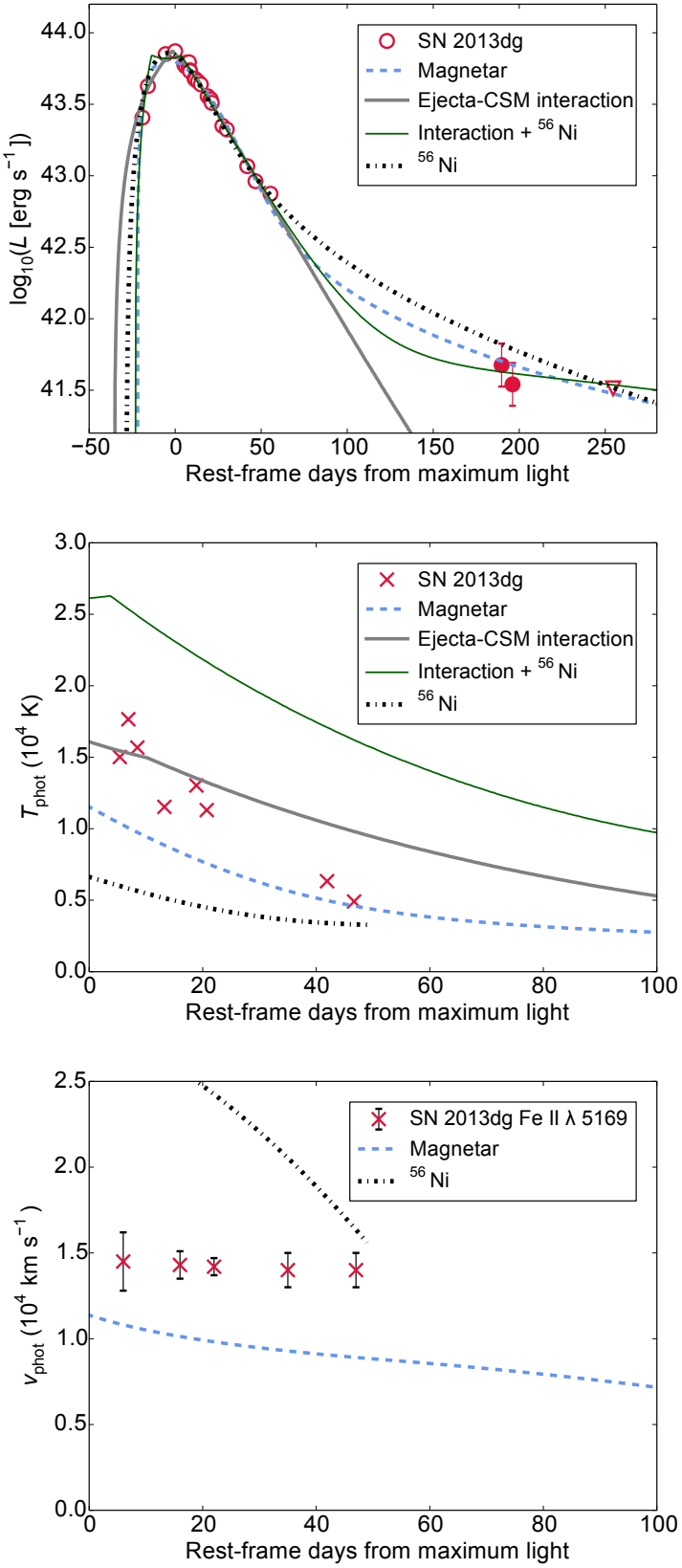

Figure 3.15: Magnetar-, interaction- and ^{56}Ni-powered models of SN 2013dg. Parameters are listed in Table 3.7. Temperatures were estimated by fitting blackbody curves to multi-colour photometry; velocities were measured from absorption minima.

The interaction model (without ^{56}Ni) best matches the high early temperatures seen in SN 2013dg, though the SN cools quite quickly, and by 40 days is closer to the magnetar model. Although the model with CSM and ^{56}Ni does a good job fitting the light curve, the temperature is too high by almost a factor of 2, whereas the pure ^{56}Ni model is rather cool compared to our observations. The flat velocity curve measured from the Fe II λ 5169 line matches the prediction of magnetar models.

3.5.4 CSM configuration

The interaction-powered fits require dense CSM extending to a radius $\sim 10^{15}$cm. To put this in context, we compare the model for LSQ12dlf to the densest known winds from Wolf-Rayet stars. These have mass-loss rates $\dot{M} \lesssim 10^{-4}\,\mathrm{M_\odot\,yr^{-1}}$, and terminal velocities $v_\infty \sim 1000\,\mathrm{km\,s^{-1}}$ (Crowther 2007; Gräfener & Hamann 2008; Hillier & Miller 1999). This is shown in Figure 3.16. To find the density profiles generated by these winds, we use the following parameterisation:

$$\dot{M} = 4\pi r^2 \rho(r) v(r), \tag{3.1}$$

from the equation of continuity, and

$$v(r) = v_\infty (1 - R_*/r)^\beta \tag{3.2}$$

(see Crowther 2007, and references therein), where R_* is the stellar radius. We take $R_* = 20\,\mathrm{R_\odot}$ and $\beta = 1$ as fiducial values. Values of β between 1-5 are typical, and the inferred density profiles are largely insensitive to these choices.

The Wolf-Rayet wind falls orders of magnitude short of the densities in our model fit. To get close to the required density, we need rapid mass loss ($\gtrsim 10^{-2}\,\mathrm{M_\odot\,yr^{-1}}$) at fairly low velocity ($v_\infty \lesssim 500\,\mathrm{km\,s^{-1}}$), which probably necessitates a massive outburst shortly before the explosion. As pointed out by Ginzburg & Balberg (2012), the extreme mass-loss needed may help to explain why SLSNe are so rare. Dwarkadas (2007) has simulated how SN evolution occurs in circumstellar environments shaped by Wolf-Rayet stars using mass-loss rates and wind velocities typical of such stars observed in the Local Group. He finds that the optical and X-ray light curves can be significantly affected, but the mass-loss regime explored ($\dot{M} \sim$ few $\times 10^{-5}\,\mathrm{M_\odot\,yr^{-1}}$and $v_\infty \sim$ 2000-3000 $\mathrm{km\,s^{-1}}$) is much lower than we require for the dense shell scenario.

Chatzopoulos & Wheeler (2012b) found that rapidly-rotating pulsational pair-instability SNe resulted in H-free, O-rich shells of about the right mass, with velocities $\sim$ 2000-4000 $\mathrm{km\,s^{-1}}$. This is a promising model to generate the required conditions,

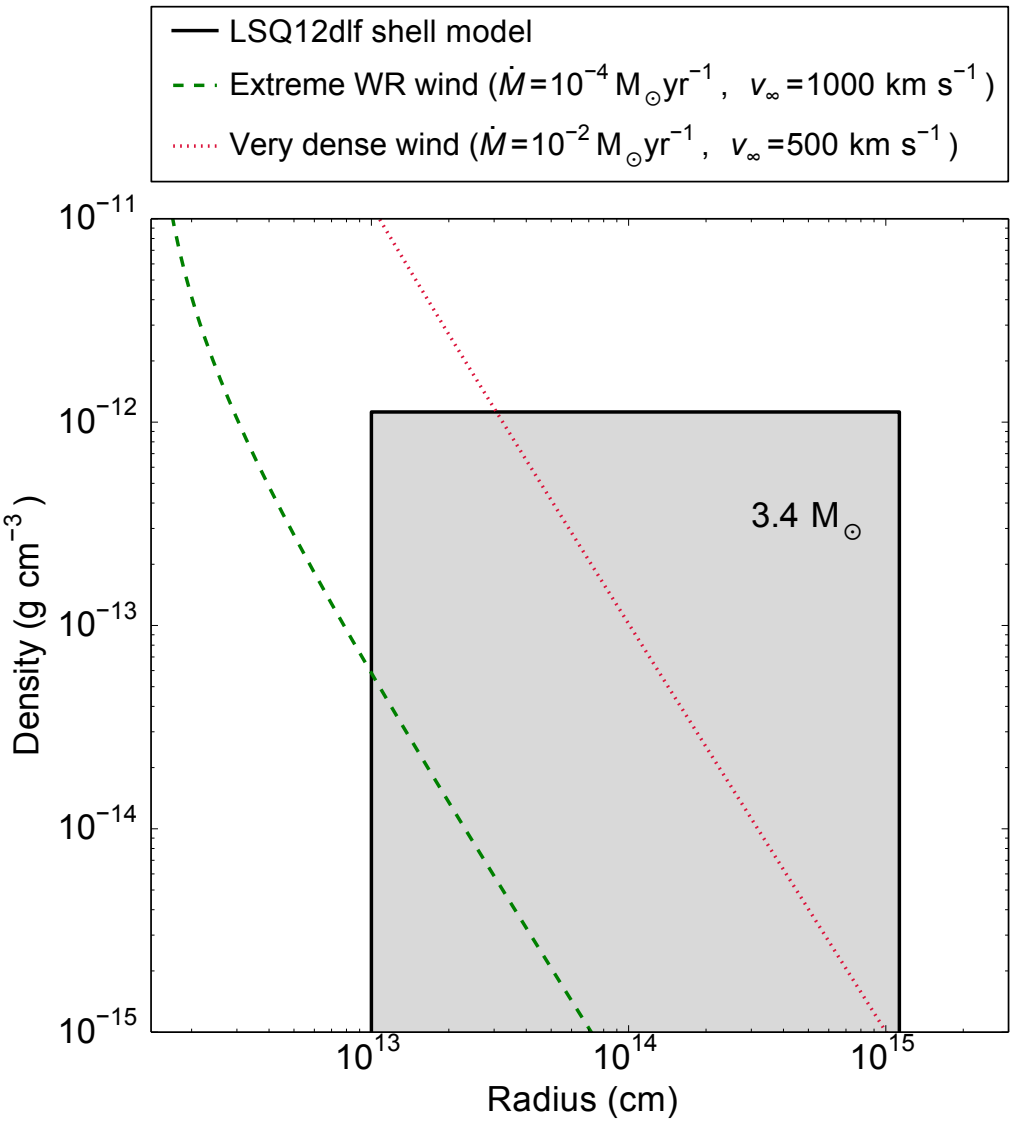

Figure 3.16: The circumstellar density profile used to fit the light curve of LSQ12dlf with our interaction model. Also shown for comparison are a somewhat extreme Wolf-Rayet wind (green dashed line) and a hypothetical dense, slow wind representing enhanced mass-loss shortly before explosion (red dotted line). This demonstrates the difficulty of achieving very high densities at large radii from the progenitor.

however their specific models assumed a progenitor metallicity $Z = 10^{-3}\,Z_\odot$, whereas the lowest observed metallicity in a SLSN host is $Z = 0.06\,Z_\odot$ (Chen et al. 2013), hence further exploration of the pulsational PISN parameter space is required.

3.6 Conclusions

We have presented light curves and spectra for the three SLSNe Ic classified in the first year of PESSTO. The spectra appear quite homogeneous, and very much in line with

other SLSNe Ic, such as SN 2010gx. Little evolution is seen over the post-maximum photospheric phase, during which time the spectra are dominated by broad lines of singly-ionised metals. Despite this similarity, we see a surprising degree of variety in their light curves, with very different decline rates after maximum and, in the case of SSS120810, evidence of a late re-brightening. SN 2013dg shows a possible break in the decline rate at ~ 50 d, as previously witnessed in SN 2011ke and others. Such a decline break is not seen in SSS120810 or LSQ12dlf. With these very different declines from maximum, we might expect to see these SNe becoming nebular at different relative phases, so coordinating late-time follow-up will be an important step in understanding the nature of these events.

The light curves were analysed using simple diffusion models with radioactivity, magnetar spin-down and ejecta-CSM interaction as power sources. We find that none of our light curves can be fit with plausible ^{56}Ni-powered models, but both magnetar and interaction models provide satisfactory fits. For several objects, the late-time evolution appears to be faint compared to magnetar model predictions. However, our models assume full energy trapping at all epochs, whereas in reality this may be a time-dependent process. Our magnetar tails are thus upper-limits to the late-time luminosities of magnetar-powered SNe.

Inserra et al. (2013) and Nicholl et al. (2013) proposed that magnetar-powered models could explain all of the SLSNe Ic then known, whereas other authors, such as Chatzopoulos et al. (2013) and Benetti et al. (2014), favour circumstellar interaction. Our fits here reinforce the validity of both of these interpretations, without particularly favouring either. More detailed hydrodynamical light curve modelling and synthetic spectra could help to disentangle the signatures of these two possible power sources. On the observational side, probing the physics of SLSNe will require spectra at very late times to examine the ejecta composition, and more data in the high-energy regime to look for signatures of magnetar wind breakout.

Chapter 4

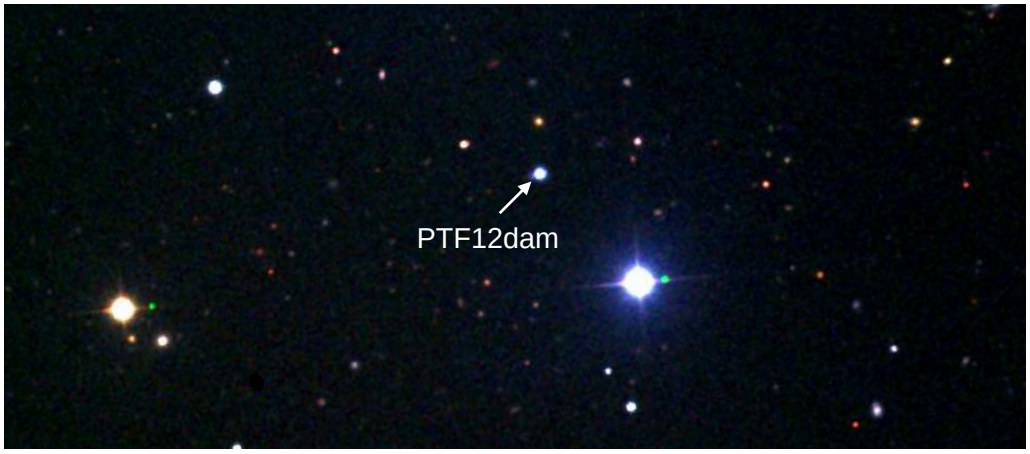

Slowly-fading SLSNe that are not pair-instability explosions

"Reach for the stars
so if you fall,
you land on a cloud"
- Kanye West ('Homecoming')

4.1 Introduction

Some SLSNe Ic evolve much more slowly than the objects presented in Chapter 3. It has been suggested that these objects form a separate class, termed 'Type R' SLSNe on the assumption that the radioactive decay chain ^{56}Ni→^{56}Co→^{56}Fe powers their slowly fading light curves (see Gal-Yam 2012). As mentioned in Section 1.6.2, these can resemble models of theorized 'pair-instability supernovae' (Barkat et al. 1967; Rakavy & Shaviv 1967). In such models, of 65-130 $M_\odot$ carbon-oxygen cores (from stars with initial masses of 140-260 $M_\odot$), the photons are converted to electron-positron pairs, causing a catastrophic loss of pressure in the core. This leads to rapid contraction and thermonuclear explosions that can synthesise many solar masses of ^{56}Ni.

Only one example of a possible PISN has been published to date. SN 2007bi (Gal-Yam et al. 2009; Young et al. 2010) occurred in a galaxy at redshift 0.127 ($\sim$ 12 billion years after the Big Bang) with metallicity $Z = Z_\odot/3$. However, the very massive progenitors of PISNe had been expected to form (and to avoid losing most of their mass in line-driven winds) only from extremely metal-poor gas in the early Universe (Heger & Woosley 2002). Thus, the finding that SN 2007bi resembled a fading PISN may be in some tension with stellar evolution theory (but see Yusof et al. 2013). Unfortunately, SN 2007bi was only discovered well after maximum light, and although a few light curve points were recovered around peak, the rise was missed and no spectra were obtained earlier than 50 days after maximum.

Here we report observations of a slow-to-fade SLSN, PTF12dam, similar to SN 2007bi but with early photometric detections from PS1 to constrain the rising light curve. Together with another similar Pan-STARRS object, PS1-11ap (McCrum et al. 2014), this allows for detailed comparison with PISN models in a previously unexplored regime. We discuss the implications for low-redshift PISNe in the context of this new data.

In Section 4.2, we describe the discovery of PTF12dam. The reduction and analysis of photometric data is detailed in Section 4.3, and the same is done for spectroscopy in Section 4.4. The bolometric light curve is compared with models in Section 4.5. We discuss implications for the PISN rate in Section 4.6, before concluding in Section 4.7.

4.2 Discovery

The discovery of a luminous transient, PTF12dam, was first reported by Quimby et al. (2012) on behalf of the Palomar Transient Factory, on 2012 May 23. We recovered the transient in PS1 3π survey data, between 2012 April 13-29, at RA = 14:24:46.21 and

Dec = +46:13:48.66. The object was given the internal designation PS1-12arh by the PS1 Transient Science Server. We triggered spectroscopic follow-up, beginning with Gran Telescopio Canarias and the William Herschel Telescope between 23-25 May 2012. No traces of hydrogen or helium were visible, leading to a type Ic classification, while strong host galaxy lines provided a redshift measurement z = 0.107. A similar transient, PS1-11ap, was discovered in the PS1 Medium Deep Survey on 2011 Jan 2 (RA = 10:48:27.72 , Dec = +57:09:09.2). The full dataset for PS1-11ap has been presented and analysed by McCrum et al. (2014), who showed it to be a slowly-declining SLSN, similar to PTF12dam and SN 2007bi, at $z = 0.523$.

4.3 Photometry

4.3.1 Data reduction

Optical imaging in SDSS-like *griz* filters was obtained with RATCam on the 2.0-m Liverpool Telescope, and FS02 on the 2.0-m Faulkes Telescope North. The data were automatically reduced by respective facility pipelines to produce de-trended images. Optical images obtained using ACAM on the 4.2-m William Herschel Telescope (WHT), OSIRIS on the 10.4-m Gran Telescopio Canarias (GTC), LRS on the 3.58-m Telescopio Nazionale Galileo (TNG), and ALFOSC on the 2.56-m Nordic Optical Telescope (NOT) were reduced using standard tasks in IRAF (Section 2.3.1).

Near infrared imaging was taken from three sources: NOTCam on the NOT, NICS on the TNG, and WFCAM on the UK infrared telescope (UKIRT). NOT and UKIRT data were reduced by facility pipelines, while we reduced TNG data using standard IRAF packages. Images were flat-field corrected and sky-subtracted. For each dithering position in the mosaic comprising the image, the necessary sky frame was created by median-combining exposures from all the other positions in the pattern (thus getting rid of stars and leaving only sky). The sky-subtracted individual dithers were aligned and combined to produce the final images.

UV observations were obtained with UVOT on board the *Swift* satellite. The frames were reduced using tools within HEASOFT. UVOT data were obtained in UVW2, UVM2, UVW1 and *u* filters, with spatial resolution of about 2" (full width at half maximum). Eight epochs, spread over a period of 50 days, are available. Individual images for each epoch were first co-added, before aperture magnitudes were measured following the prescription of Poole et al. (2008).

Optical and NIR magnitudes were measured with SNOoPY (Section 2.3.2). The zero point for each observation was calibrated by comparing multiple point sources in

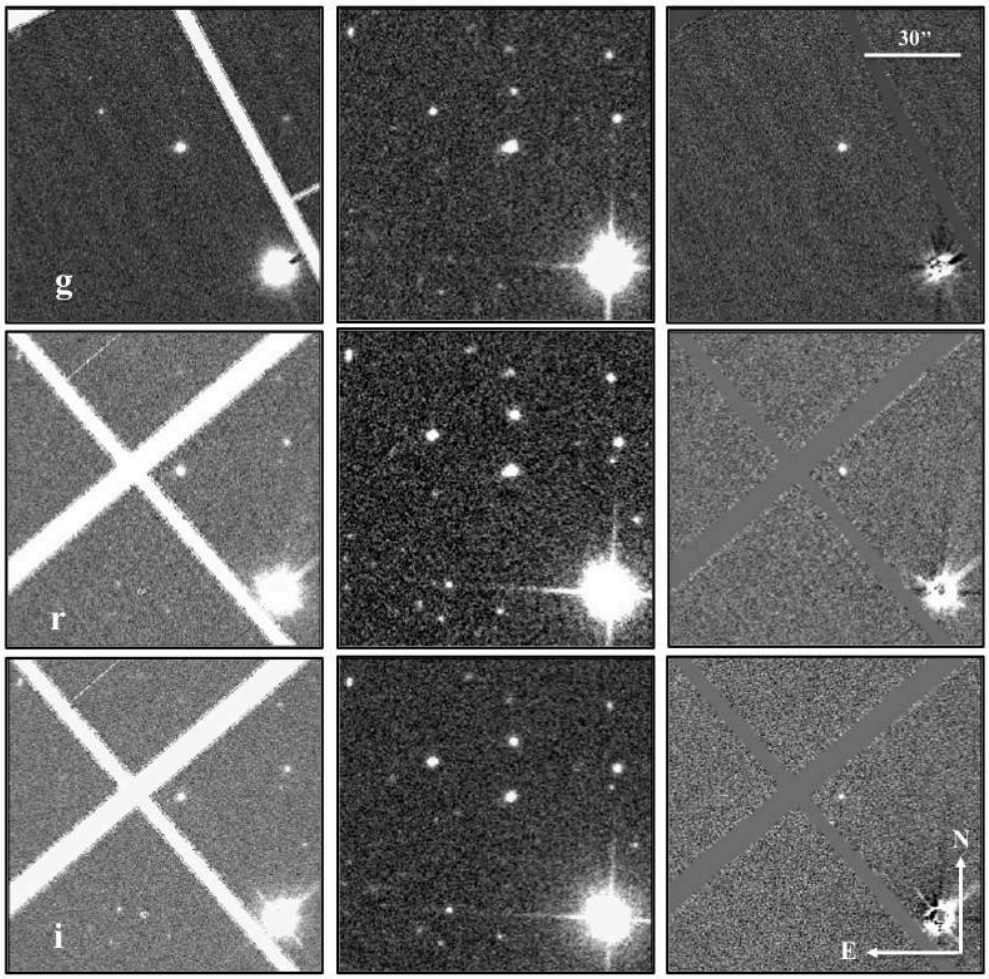

Figure 4.1: Image subtraction for the three earliest Pan-STARRS1 epochs of PTF12dam in g_{P1}, r_{P1} and i_{P1}, using SDSS frames as reference images (taken on 2003-02-11). These illustrate the reliable image subtraction, resulting in clear detections of PTF12dam at early phases. The images on the left are the PS1 detections, those in the centre are the SDSS templates, and on the right are the differences between the two. The bright star in the lower right was saturated and hence does not subtract cleanly. At each PS1 epoch there are two images, taken as TTI pairs. Photometry was carried out and determined in the SDSS photometric system to match the bulk of the follow-up *griz* imaging. The white areas are gaps between the 590×598 pixel cells in the PS1 chip arrays.

the field with SDSS (Ahn et al. 2012) and 2MASS (Skrutskie et al. 2006) photometry, respectively. Colour corrections and extinction for each site were then used to refine the measured magnitudes.

The host galaxy of PTF12dam is bright (from SDSS, $g = 19.30$, or $M_g = -19$) compared to most SLSN hosts (e.g. Neill et al. 2011; Chen et al. 2013; Lunnan et al. 2014; Leloudas et al. 2015) and we correct for galaxy flux as follows. For observations in *griz* where the combined light from PTF12dam and its host is more than a magnitude brighter than the host alone, we subtract the contribution from the host flux in a given

Table 4.1: Ground-based optical photometry of PTF12dam

Date	MJD	Phase*	*g*	*r*	*i*	*z*	Instrument**
2012-04-13	56030.5	−51.9		19.65 (0.17)	20.28 (0.21)		PS1
2012-04-14	56031.5	−51.0	19.73 (0.15)				PS1
2012-04-25	56042.5	−41.1	18.76 (0.14)				PS1
2012-04-28	56045.5	−38.4			18.91 (0.21)		PS1
2012-04-29	56046.5	−37.5		18.5 (0.17)			PS1
2012-05-23	56071.1	−15.2	17.197 (0.01)	17.515 (0.01)	17.771 (0.01)		GTC
2012-05-25	56072.9	−13.6	17.244 (0.01)	17.444 (0.01)	17.827 (0.01)	17.80 (0.01)	WHT
2012-05-29	56076.9	−10.0	16.991 (0.01)	17.268 (0.01)	17.606 (0.01)	17.65 (0.04)	LT
2012-06-02	56080.9	−6.4	16.956 (0.01)	17.187 (0.01)	17.555 (0.02)		LT
2012-06-03	56081.9	−5.5	16.959 (0.01)	17.154 (0.01)	17.548 (0.01)	17.55 (0.03)	LT
2012-06-20	56098.0	9.1	16.820 (0.01)	17.161 (0.01)	17.435 (0.01)	17.34 (0.01)	TNG
2012-06-25	56104.0	14.5	17.030 (0.01)	17.255 (0.01)	17.465 (0.01)	17.35 (0.01)	WHT
2012-07-07	56116.0	25.3	17.021 (0.01)	17.347 (0.01)	17.547 (0.01)	17.44 (0.01)	NOT
2012-07-17	56128.0	36.2		17.420 (0.05)			GTC
2012-08-09	56148.9	55.0	17.659 (0.01)	17.724 (0.01)	17.812 (0.01)	17.63 (0.04)	NOT
2012-08-21	56160.9	65.9	17.924 (0.01)	17.825 (0.01)	18.019 (0.01)	17.65 (0.01)	WHT
2012-09-04	56174.8	78.5	18.184 (0.01)	17.957 (0.01)	18.155 (0.01)	17.85 (0.02)	NOT
2012-09-21	56191.9	93.8	18.590 (0.01)	18.238 (0.01)	18.387 (0.01)	17.99 (0.01)	WHT
2012-12-23	56285.2	178.1	20.083 (0.06)	19.298 (0.02)	19.522 (0.10)	19.02 (0.20)	LT
2012-12-25	56287.6	180.3		19.332 (0.09)	19.534 (0.10)	19.18 (0.16)	FT
2013-01-19	56312.1	202.5	20.378 (0.05)	19.763 (0.04)	20.144 (0.20)	19.22 (0.24)	LT
2013-01-27	56320.2	209.8	20.690 (0.10)	19.836 (0.05)	19.783 (0.14)	19.33 (0.12)	LT
2013-02-10	56334.2	222.4		20.006 (0.04)			LT

* Phase in rest-frame days from epoch of maximum light
** PS1 = Pan-STARRS1
GTC = Gran Telescopio Canarias
WHT = William Herschel Telescope + ACAM
LT = Liverpool Telescope + RATCam
TNG = Telescopio Nazionale Galileo + LRS
NOT = Nordic Optical Telescope + ALFOSC
FTN = Faulkes Telescope North + Faulkes Spectral 02

band simply using the magnitudes (specifically, 'modelMags') from SDSS DR9 (Ahn et al. 2012). The host is a compact source, such that essentially all of the flux falls within the SN PSF. When the brightness of the supernova and galaxy are comparable, we subtract an SDSS template image from our target image using HOTPANTS (Alard & Lupton 1998). Examples of image subtraction for the crucial early PS1 observations are shown in Figure 4.1 The observed light curve of PTF12dam, from UV to NIR and spanning −50 to 250 rest-frame days, is shown in Figure 4.2. Magnitudes in optical, UV and NIR are listed in Tables 4.1, 4.2 and 4.3, respectively.

K-corrections (not shown in Figure 4.2) were computed from spectra and applied to the *gri* magnitudes. The *z* band lies at the red edge of the optical spectra, and hence was not covered by both the observed and rest-frame (Doppler corrected) spectra simultaneously. For these magnitudes, colour-based *K*-corrections were used instead

Table 4.2: *Swift* UV photometry of PTF12dam

Date	MJD	Phase*	UVW2	UVM2	UVW1	u
2012-05-22	56070.4	−15.9	18.83 (0.08)	18.29 (0.07)	17.81 (0.07)	16.86 (0.06)
2012-05-30	56077.8	−9.2	18.85 (0.07)	18.24 (0.06)	17.75 (0.07)	16.71 (0.06)
2012-06-07	56085.7	−2.1	18.87 (0.08)	18.36 (0.08)	17.87 (0.08)	16.62 (0.07)
2012-06-13	56091.7	3.3	18.99 (0.08)	18.46 (0.08)	18.01 (0.08)	16.58 (0.06)
2012-06-20	56098.5	9.5	19.27 (0.08)	18.76 (0.08)	18.19 (0.08)	16.80 (0.06)
2012-06-27	56106.1	16.3	19.50 (0.10)	18.93 (0.10)	18.47 (0.10)	16.99 (0.08)
2012-06-28	56107.4	17.6	19.48 (0.10)	18.90 (0.10)	18.46 (0.10)	17.00 (0.09)
2012-07-04	56112.7	22.3	20.16 (0.09)	19.38 (0.09)	18.78 (0.09)	17.32 (0.08)

* Phase in rest-frame days from epoch of maximum light

Table 4.3: Ground-based NIR photometry of PTF12dam

Date	MJD	Phase*	J	H	K	Instrument**
2012-05-26	56074.9	−11.8	16.82 (0.05)	16.58 (0.07)	16.28 (0.08)	TNG
2012-06-03	56082.1	−5.4	16.74 (0.05)	16.39 (0.07)	16.21 (0.07)	TNG
2012-06-10	56089.0	0.9	16.62 (0.05)	16.35 (0.07)	16.12 (0.07)	NOT
2012-07-04	56113.1	22.6	16.47 (0.05)	16.34 (0.07)	16.11 (0.07)	NOT
2012-07-09	56118.0	27.1	16.54 (0.05)			TNG
2012-08-01	56141.3	48.1	16.68 (0.10)			UKIRT
2012-08-05	56145.0	51.5		16.44 (0.07)	16.08 (0.06)	NOT
2012-09-07	56177.0	80.4	16.73 (0.05)	16.48 (0.06)	16.16 (0.06)	NOT
2013-02-20	56343.0	230.4	18.05 (0.05)	17.61 (0.07)	16.97 (0.06)	NOT
2013-03-22	56374.0	258.4	18.20 (0.05)	17.72 (0.07)	17.13 (0.06)	NOT
2013-04-25	56407.0	288.2	18.22 (0.07)	17.94 (0.08)	17.25 (0.07)	NOT

* Phase in rest-frame days from epoch of maximum light
** TNG = Telescopio Nazionale Galileo + NICS
NOT = Nordic Optical Telescope + NOTCam
UKIRT = UK Infrared Telescope + WFCAM

(Chilingarian et al. 2010; Chilingarian & Zolotukhin 2012). No K-corrections have been applied to the UV or NIR data.

In the case of SN 2007bi, the published photometry has until now been in the Johnson-Cousins $UBVRI$ system (on the Vega magnitude scale). For ease of comparison, we converted the existing R-band data to SDSS r AB magnitudes. For the multicolour photometry of SN 2007bi from Young et al. (2010), we applied colour transformations in $V-R$ between the SDSS and Johnson-Cousins filter systems, from Jordi et al. (2006). However, most photometric data for SN 2007bi is in R only (Gal-Yam et al. 2009). For the multicolour data, we found that the conversion factor varied negligibly with time, and so we were able to apply a constant shift of +0.15 magnitudes to all R-band data to convert it to r-band.

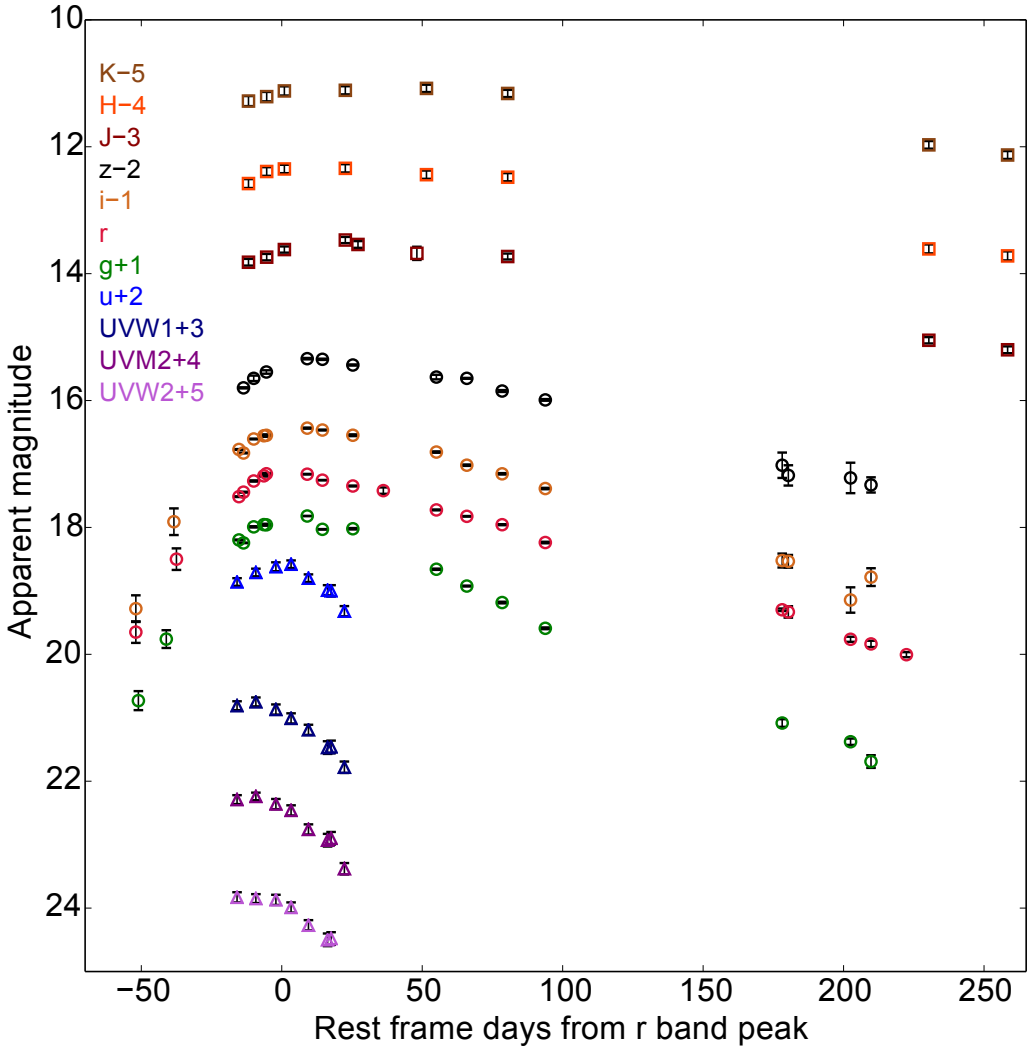

Figure 4.2: Observed multi band photometry of PTF12dam, from the *Swift* UV bands to the NIR.

4.3.2 Light curves

The light curves in *r*-band are shown in Figure 4.3. The high luminosities and slow declines of PTF12dam and PS1-11ap are very similar to the previously unique SN 2007bi, which is also plotted in the figure. The slow light curve decline from maximum matches the rate expected from ^{56}Co decay with close-to-full γ-ray trapping (although similar declines can be generated for ~ 100 d after peak from magnetar spin-down; Inserra et al. 2013). Powering these high luminosities radioactively requires at least 3-7 $M_\odot$ of ^{56}Ni (Gal-Yam et al. 2009; Young et al. 2010; Umeda & Nomoto 2008; Moriya et al. 2010), suggesting an extremely massive progenitor and possible pair-instability explosion (Gal-Yam et al. 2009). In the figure, we also plot published models from Kasen et al. (2011) and Dessart et al. (2013), of PISNe arising from the helium cores of very massive stars that have lost their hydrogen envelopes. These fit the decline phase well.

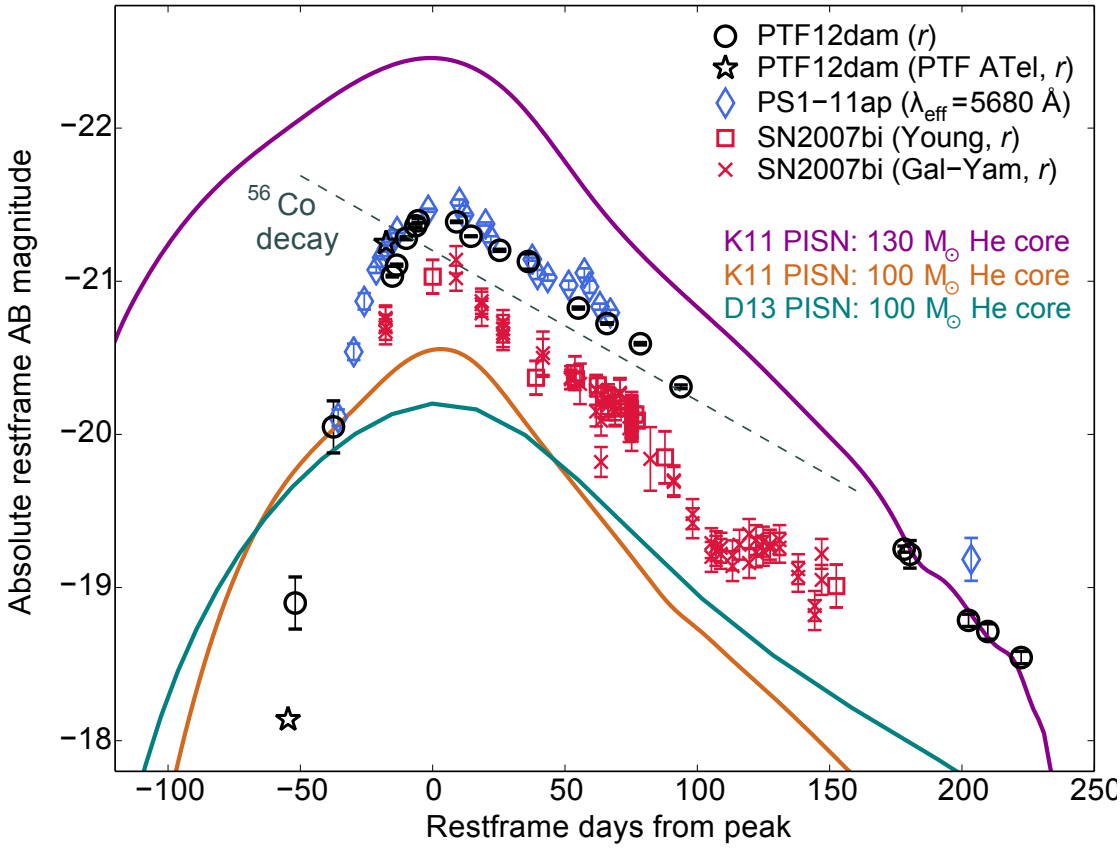

Figure 4.3: Optical light curves of PTF12dam and SN 2007bi in rest-frame r-band ($\lambda_{\rm eff}$ = 6230 Å). For PS1-11ap, at $z = 0.523$, the PS1 $z_{\rm P1}$ filter corresponds to a rest-frame filter of $\lambda_{\rm eff}$ = 5680 Å, similar to r. Synthetic r-band light curves were generated from published 1D models of PISNe from stripped progenitor cores by Kasen et al. (2011); Dessart et al. (2013). Despite a good match to the decline phase of SN 2007bi and the PISN models, PTF12dam and PS1-11ap rise to maximum light a factor of ~ 2 faster than these models.

The rise time of a PISN is necessarily long ($\sim$ 100 d), because heating from ^{56}Ni/^{56}Co decay occurs in the inner regions, and the resultant radiation must then diffuse through the outer ejecta, which typically has mass $M_{\rm ej} > 80\,{\rm M}_{\odot}$ (Kasen et al. 2011). The time to reach maximum light is therefore a crucial observational test. Our Pan-STARRS1 images reveal multiple early detections of PTF12dam and PS1-11ap in $g_{\rm P1}$, $r_{\rm P1}$ and $i_{\rm P1}$ at around 50 and 35 rest-frame days before peak brightness, respectively (some of these are shown Figure 4.1). PTF12dam is not detected in $z_{\rm P1}$ images on 2012 January 1, 132 d (rest-frame) before peak. The early light curves show only a moderately slow rise over 50-60 d. This is physically inconsistent with the PISN models, which rise 2.5 magnitudes to peak in 95-130 d. The rise time for SN 2007bi was estimated at 77 d (Gal-Yam et al. 2009), but this was based on a parabolic fit to the sparse data around peak, and so was not well constrained.

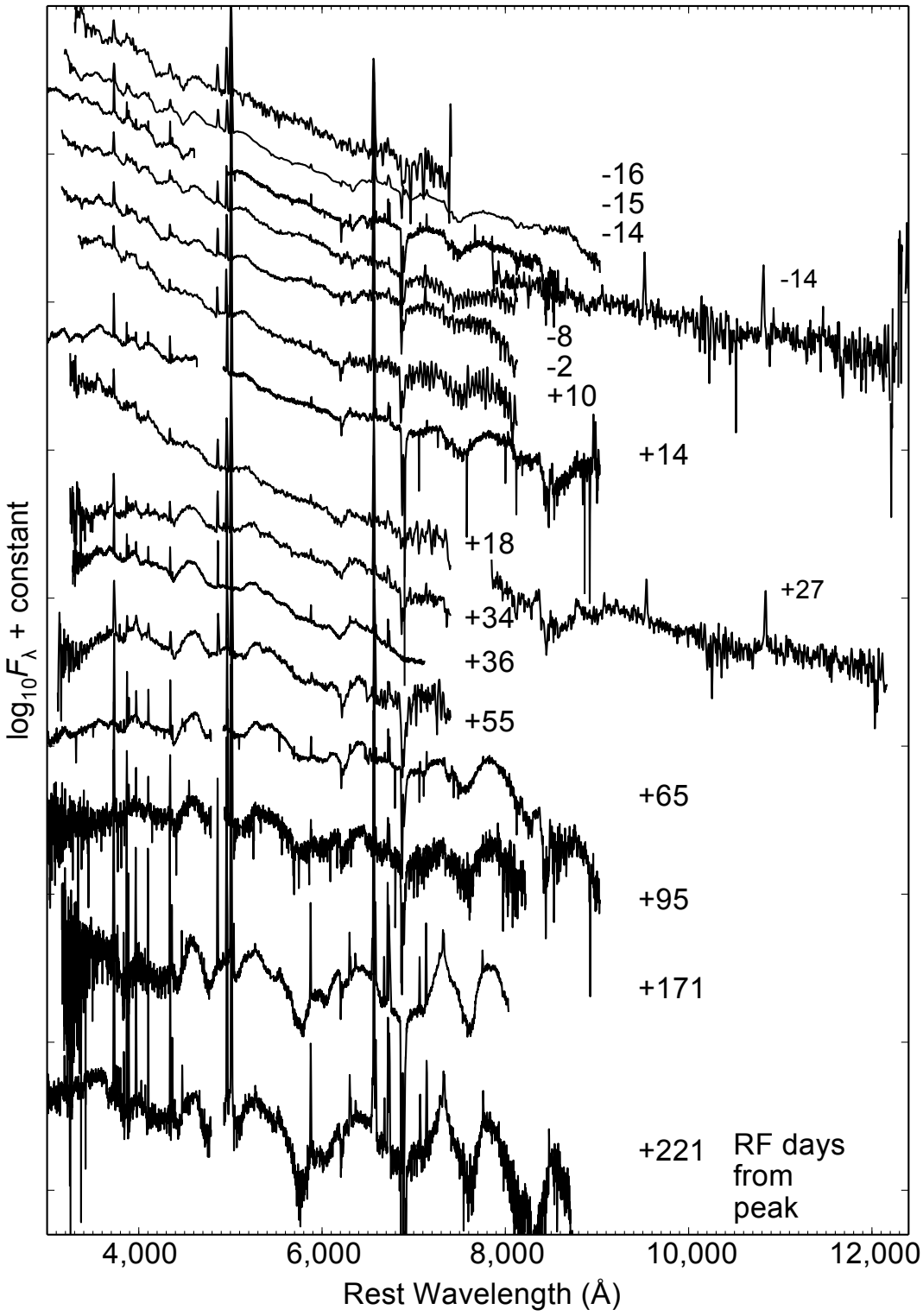

Figure 4.4: Full time-series optical and NIR spectroscopy of PTF12dam, from two weeks before maximum light to an extended pseudo-nebular phase at $\gtrsim$ 100-200 days afterwards. A Starburst99 model continuum SED for the host galaxy has been calibrated against SDSS and GALEX photometry and subtracted from the last three spectra.

Table 4.4: Spectroscopic observations of PTF12dam

Date	MJD	Phase*	Instrument	Range (Å)	Resolution (Å)
2012-05-23	56070.99	−16	Asiago+AFOSC	3400-8200	25
2012-05-24	56071.12	−15	GTC+OSIRIS	3500-10000	30
2012-05-25	56072.91	−14	WHT+ISIS	3250-9500	3-5
2012-05-26	56073.95	−13	TNG+NICS	8700-14500	35
2012-06-01	56079.96	−8	NOT+ALFOSC	3500-9000	15
2012-06-08	56086.95	−2	NOT+ALFOSC	3500-9000	15
2012-06-21	56100.04	+10	NOT+ALFOSC	3700-9000	15
2012-06-25	56103.99	+14	WHT+ISIS	3200-10000	6-11
2012-06-29	56107.97	+18	Asiago+AFOSC	3600-10000	15
2012-07-09	56117.99	+27	TNG+NICS	8700-13500	35
2012-07-17	56125.95	+34	Asiago+AFOSC	3900-8140	13
2012-07-19	56128.03	+36	GTC+OSIRIS	3600-7900	7
2012-08-09	56148.95	+55	NOT+ALFOSC	3500-8200	20
2012-08-20	56159.92	+65	WHT+ISIS	3200-10000	4-7
2012-09-22	56192.86	+95	WHT+ISIS	3200-10000	6-11
2012-12-16	56277.50	+171	GN+GMOS	3500-8900	3-4
2013-02-10	56334.17	+221	WHT+ISIS	3200-10000	5-10

* Phase in rest-frame days relative to epoch of maximum light.

4.4 Spectroscopy

4.4.1 Data reduction

Optical spectra of PTF12dam were taken with a variety of instruments. The details of the wavelength coverage and resolution are listed in Table 4.4. Standard procedures within IRAF were used to detrend the CCD data, as described in Section 2.3.1.

Prominent host galaxy lines in the observed spectrum (in particular Hα, Hβ, and the [O III] $\lambda\lambda$ 4959,5007 doublet) gave a redshift $z = 0.107$. We used a Milky Way extinction in the direction of PTF12dam of $A_{V,\mathrm{MW}} = 0.037$ mag, from the infrared dust maps of Schlafly & Finkbeiner (2011). In contrast to most SLSNe, the strong nebular lines allow an estimate of the extinction in the host galaxy. We measured the flux ratio of Hα/Hβ = 2.99 in the NOT spectrum from 2012 August 9. This compares to an expected intrinsic line ratio of Hα/Hβ = 2.86 for case B recombination (Osterbrock 1989). We assumed that R_V for this host galaxy is similar to that observed in the LMC ($R_V = 3.16$; Pei 1992), and hence we estimated a host galaxy extinction in the V-band of $A_{V,\mathrm{host}} = 0.1$ mag from the Balmer decrement. Within the uncertainties, we find similar results if we were to apply $R_V = 2.93$, which has been proposed for an SMC-like environment (Pei 1992). For PS1-11ap and SN 2007bi, host reddening was assumed to be negligible, and only a galactic extinction correction was applied.

Near infrared spectra were obtained using NICS on the TNG on 2012 May 26 and 2012 July 9. As for the optical, the spectra were calibrated in wavelength through spectra of comparison lamps acquired with the same configuration as for the PTF12dam observations. First-order flux calibrations were obtained using A0 standard stars taken on the same night with the same set-up used for PTF12dam. Solar analogues at a similar airmass were observed either before or after PTF12dam, to facilitate the removal of the strong telluric absorptions between 1 and 2 μm. The spectra show no broad hydrogen or helium (consistent with the optical spectra). The early (-13 d) spectrum is nearly featureless with two narrow host galaxy lines from [S III] (9500 Å) and He I (10580 Å), while the later one, at 27 days after peak, shows broad absorption due to the Ca II NIR triplet, which is also seen in the optical spectra with the reddest wavelength coverage.

The two latest optical spectra of PTF12dam, at 171 d and 221 d after peak, have significant contamination from the host galaxy in the continuum, as judged from the pre-discovery SDSS flux of the host and our photometric measurements. The host is not resolved from the SN hence no host subtraction is possible in the 2D spectroscopic reductions. As we do not currently have a spectrum of the host, we constructed a galaxy template to subtract. We used STARBURST99 (Leitherer et al. 1999) to calculate a series of model galaxy spectra for both continuous star-formation and an initial burst, settling on a 30 Myr-old stellar population with a continuous star-formation history (at a metallicity of $Z = 0.05\,Z_{\odot}$, and a Salpeter initial mass function). This does not include nebular emission lines, hence we added narrow emission lines with fluxes as measured from the spectrum of PTF12dam at 221 d (after continuum subtraction) to provide a galaxy template with continuum and lines. We scaled and reddened the template until synthetic photometry (with the IRAF task SYNPHOT) through SDSS *ugriz* and GALEX FUV and NUV filters matched pre-discovery measurements (Ahn et al. 2012). Thus we have a model galaxy spectrum that reproduces the observed flux. The continuum from this model spectrum was then subtracted from the PTF12dam spectra and NUV photometry in Figures 4.4, 4.5 and 4.6. A similar fit was made for the host of PS1-11ap, and subtracted accordingly.

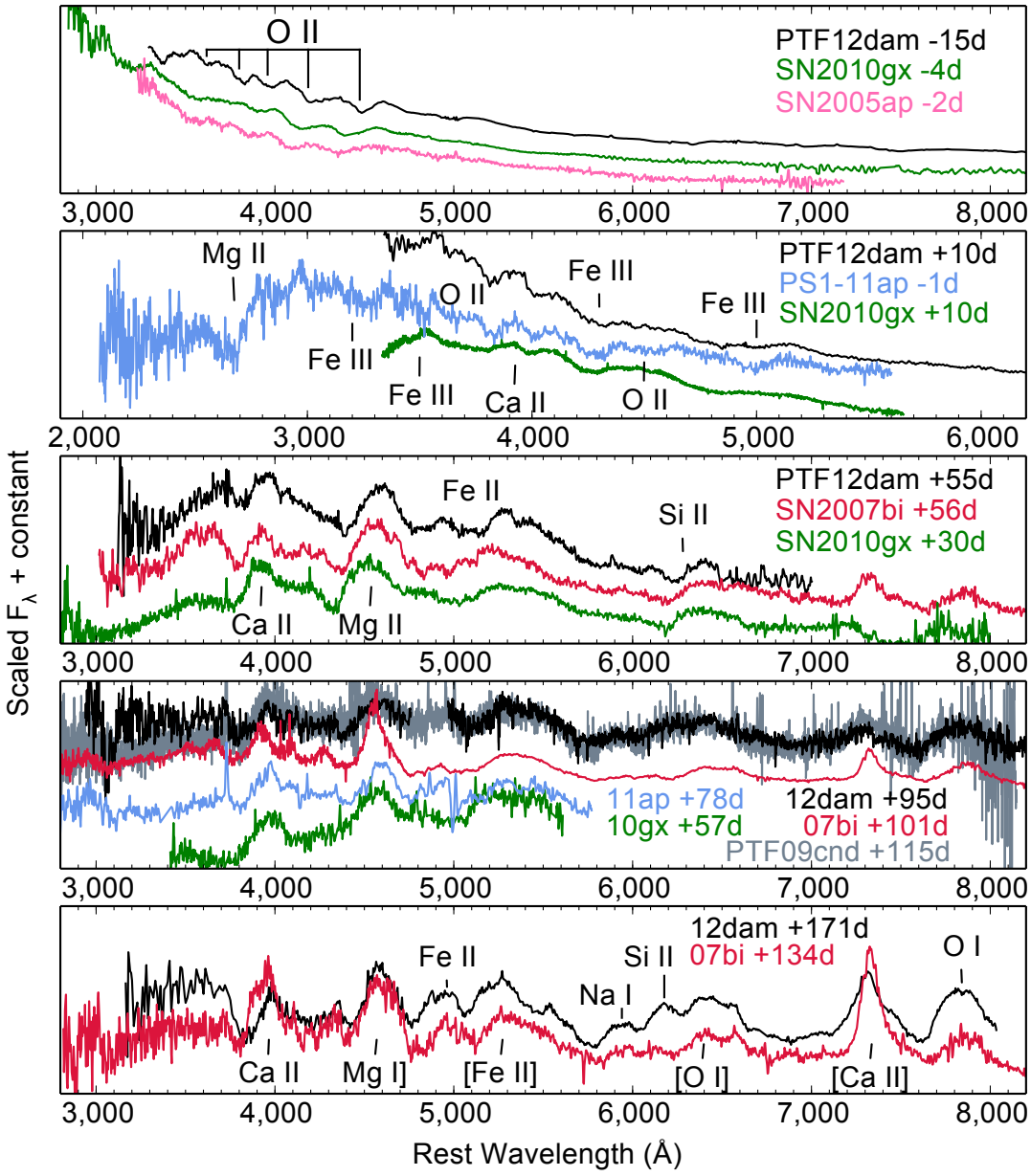

Figure 4.5: Spectra of PTF12dam, PS1-11ap, SN 2007bi, and the well-studied SLSNe Ic, SN 2010gx (Pastorello et al. 2010), SN 2005ap (Quimby et al. 2007), and PTF09cnd (Quimby et al. 2011). Our spectra have been corrected for extinction and shifted to respective rest-frames, and scaled to facilitate comparison. Phases are given in rest-frame days relative to maximum light. No hydrogen or helium are detected at any stage. Before and around peak, PTF12dam and PS1-11ap show blue continua and O II absorptions, common to SLSNe Ic (Quimby et al. 2011; Gal-Yam 2012; Inserra et al. 2013). However, by 55 d after peak, PTF12dam is virtually identical to SN 2007bi. Note that PTF12dam still resembles SN 2010gx at this phase, but seems to be evolving on a longer timescale (consistent with the slower light curve evolution).

4.4.2 Spectral evolution

The full spectral evolution of PTF12dam is shown in Figure 4.4. In Figure 4.5, we compare PTF12dam and PS1-11ap to SN 2007bi and other SLSNe, and label most of the dominant lines. The spectra of PTF12dam and PS1-11ap also show them to be similar supernovae, and almost identical to SN 2007bi after 50 days from peak. At the epochs after peak luminosity, while PTF12dam and PS1-11ap are still in the photospheric phase, the spectral lines are assumed to be those identified for SN 2007bi by Gal-Yam et al. (2009), as the spectra are closely matched. However the early spectra of PTF12dam and PS1-11ap, before and around maximum light, probe new epochs for these slowly-declining objects. We determine the main features of our spectra before maximum light using SYNOW (Branch et al. 2002). Single-ion spectra were generated for common ions in ejecta with temperatures and velocities appropriate to our spectra ($T \sim 15000$ K and $v \sim 11000\,\mathrm{km\,s^{-1}}$). We find that all of the main features can be accounted for with O II, Ca II, Fe III, Mg II and Si II.

The blue continua and O II absorptions in the early spectra of PTF12dam bear a striking similarity to normal (fast-declining) SLSNe Ic, such as those shown in Chapter 3. The lines in the slowly-evolving objects are at lower velocities than those in SLSNe 2010gx and 2005ap. Shortly after maximum light, Fe III features emerge, along with the Mg II and Ca II lines that dominate typical SLSNe Ic at this phase. Even by 55 days after peak, when PTF12dam is virtually identical to SN 2007bi, there is still a close resemblance to SN 2010gx. The spectra of PTF12dam and SN 2007bi at +55 d look remarkably like SN 2010gx at +30 d, suggesting that the slow-declining SLSNe are in fact closely linked to the fast-declining events. The slower spectroscopic evolution is consistent with the broader light curve. At $\sim$ 100 days after peak, PTF12dam also matches PTF09cnd (Quimby et al. 2011), which faded slowly for an SLSN Ic after a 50 d rise. In the final panel of the figure, the spectra are quasi-nebular, dominated by emission lines of Ca II H&K, Mg I] λ 4571, Mg I λ 5183 + [Fe II] 5200 Å blend, [O I] $\lambda\lambda$ 6300,6364, [Ca II] $\lambda\lambda$ 7291,7323, and O I λ 7774, but some continuum flux is still visible.

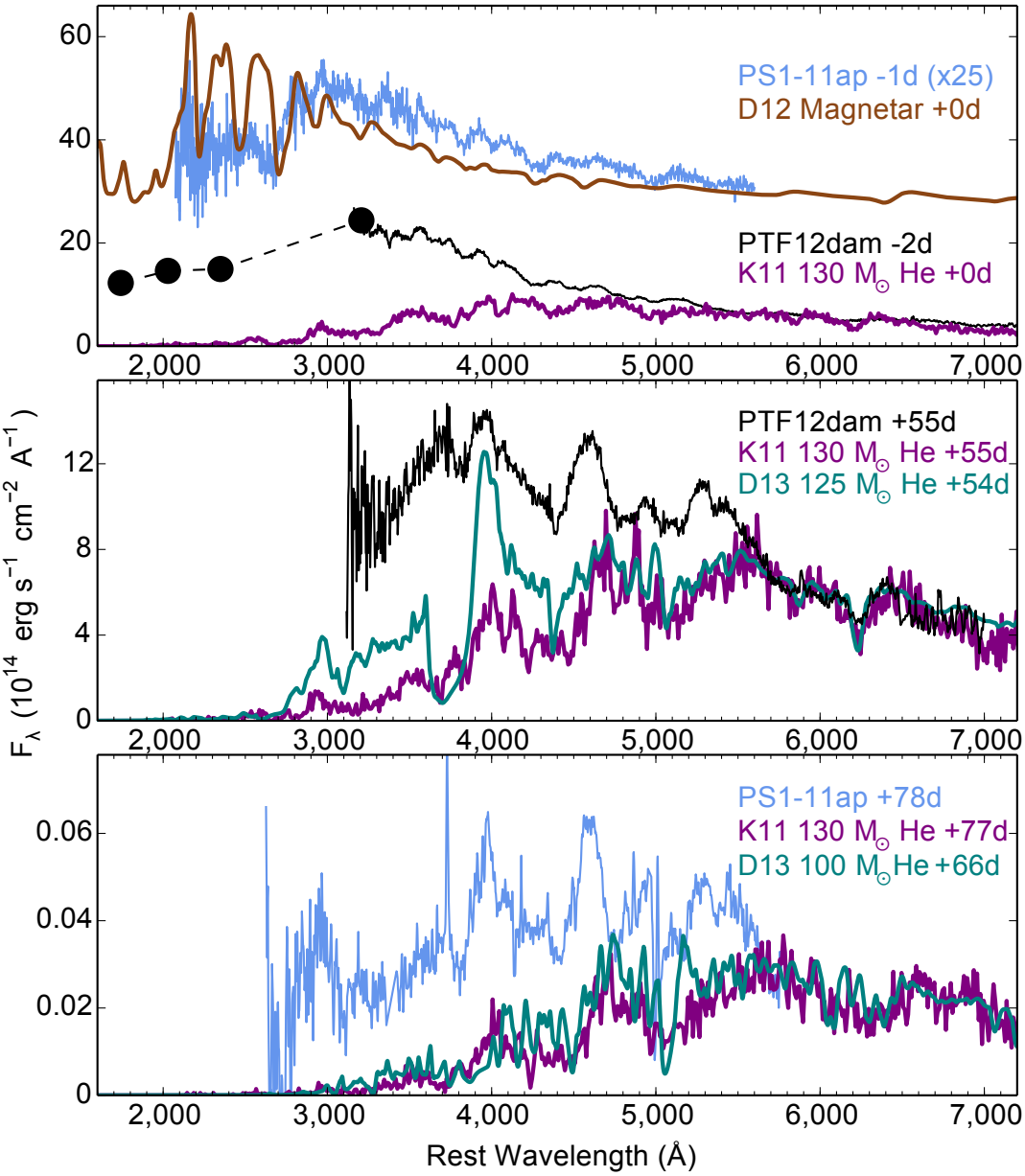

Figure 4.6: Comparison of spectra with published PISN and magnetar models (Kasen et al. 2011; Dessart et al. 2012b, 2013). Model spectra are matched to the observed flux in the region 5500-7000 Å. Our spectra are significantly bluer than PISN models, which are red due to iron-group line blanketing below 5000 Å. The magnetar-driven model (Dessart et al. 2012b) gives a good match to the spectra at maximum light (model spectra at later epochs do not currently exist in the literature), and reproduces the observed colours.

4.4.3 Comparison with model spectra

We compare our UV and optical data, from peak to ~ 70 d, to the predictions of He core PISN models (Kasen et al. 2011; Dessart et al. 2013) and Wolf-Rayet progenitor magnetar models (Dessart et al. 2012b). The observed blue colours are in stark contrast to the predictions of the PISN models, which show cool continua below 5000 Å and marked drop-offs in the UV. Particularly around and after maximum light, PISN colours are expected to evolve to the red due to increasing line blanketing from the large mass of iron-group elements and intermediate-mass elements abundant in their ejecta. In our rest-frame UV photometry of PTF12dam, and the UV spectra of PS1-11ap, we see no evidence of line blanketing even down to 2000 Å. This points to lower iron-group abundances and a higher degree of ionization in these SLSNe compared to PISN models.

Such conditions are fulfilled in models of ejecta reheated by magnetars (Kasen & Bildsten 2010; Woosley 2010; Dessart et al. 2012b). In the model shown, the energy input is equivalent to several solar masses of ^{56}Ni, but in only 6.94 $M_\odot$ ejecta. The high ratio of internal energy to ejected mass keeps the ejecta hot and relatively highly ionized, resulting in a bluer continuum. Moreover, this energy source does not demand the high mass of metals intrinsic to the PISN scenario (Kasen et al. 2011; Dessart et al. 2012b). Redwards of the Mg II line at 2800 Å, this model shows many of the same Fe III and O II lines identified in the early spectrum of PS1-11ap, though the strengths of the predicted Si III and C III lines in the NUV are discrepant with the data. The pressure of the magnetar wind on the inner ejecta is expected to lead to a dense shell at near-constant photospheric velocity (Kasen & Bildsten 2010; Woosley 2010). For PTF12dam, the velocities of spectral lines are indeed found to be quite constant in time (Section 4.5.3).

One of the main arguments put forward by Gal-Yam et al. (2009) in favour of a PISN interpretation for SN 2007bi was a model for the nebular spectrum. They showed that the main optical lines at $\sim$ 400-500 days after peak could be reproduced by ejecta with moderately high oxygen and magnesium masses (10-15 $M_\odot$ and $\sim 0.1\,M_\odot$, respectively) and 4-7 $M_\odot$ of ^{56}Ni. However, Dessart et al. (2013) calculated the spectral evolution of realistic PISN models, and pointed out a number of discrepancies with the nebular spectrum of SN 2007bi. Their PISN simulation showed much lower nebular line velocities ($< 4000\,\mathrm{km\,s^{-1}}$), extreme line blanketing of flux redwards of $\sim$ 5500 Å, and a very prominent [Fe II] λ 7155 line that was not observed in SN 2007bi. In the study of Nicholl et al. (2013), A. Jerkstrand carried out nebular line flux calculations, and showed that the observed line strengths in SN 2007bi can be reproduced by oxygen-dominated ejecta of $\sim 20\,M_\odot$, with modest amounts of magnesium and iron. A large

^{56}Ni mass is not required, but some power source is needed to maintain a temperature of ~ 5000 K. This scenario is consistent with our magnetar model.

4.5 Light curve models

4.5.1 Bolometric light curve

To compare with the bolometric properties of the PISN models, and to fit with our own light curve models, we constructed a bolometric light curve for PTF12dam, from the *Swift* UV bands to the NIR. Zero flux was assumed outside of the observed wavelength range (1700-23000 Å). Between epochs -11 d and $+21$ d, we have full rest-frame flux coverage across this range. Outside of this time period, we make simple extrapolations to account for missing UV and NIR data. To correct the early epochs (i.e. more than 11 days before peak) for missing UV and NIR data, we extrapolated the flux contribution by assuming a linear gradient in colour evolution in each filter with respect to *r*-band. This is reasonable, since the colour evolution is very close to linear over the epochs where we have full coverage. To correct the late epochs for missing UV data, we simply extrapolated the UV light curves linearly. This is because the rapid fall off in the near-UV after maximum light means that it contributes little to the total luminosity beyond $\sim$ 40d post-peak, so the lack of coverage does not have a significant effect.

4.5.2 The rise time of PISN models

The bolometric light curve of PTF12dam is shown in Figure 4.7. The long rise times of existing PISN models (also shown in the figure) from Kasen et al. (2011); Dessart et al. (2013) seem to rule out the PISN scenario. The rise time argument is central to our assertion that these slowly-evolving SLSNe are not PISNe, so one may ask whether more sophisticated models (taking into account rotation, magnetic fields, mixing and higher dimensions) could have substantially shorter rise times?

Multi-dimensional simulations of PISNe by Joggerst & Whalen (2011) have suggested that mixing in the ejecta is negligible in these explosions. However, consequences of mixing have been studied for ^{56}Ni-powered SNe Ia (Piro & Nakar 2014) and Ibc (Dessart et al. 2012a; Bersten et al. 2012). In fact, mixing serves to flatten the early parts of model light curves, since photons begin diffusing out earlier, but the time taken to reach maximum light is not significantly affected as the bulk of the nickel still resides in the inner ejecta. Very extreme outward mixing of ^{56}Ni would be required to substantially shorten the rise time, in contrast to the predictions of Joggerst & Whalen (2011). Mixed models also display redder spectra (Dessart et al. 2012a). This suggests

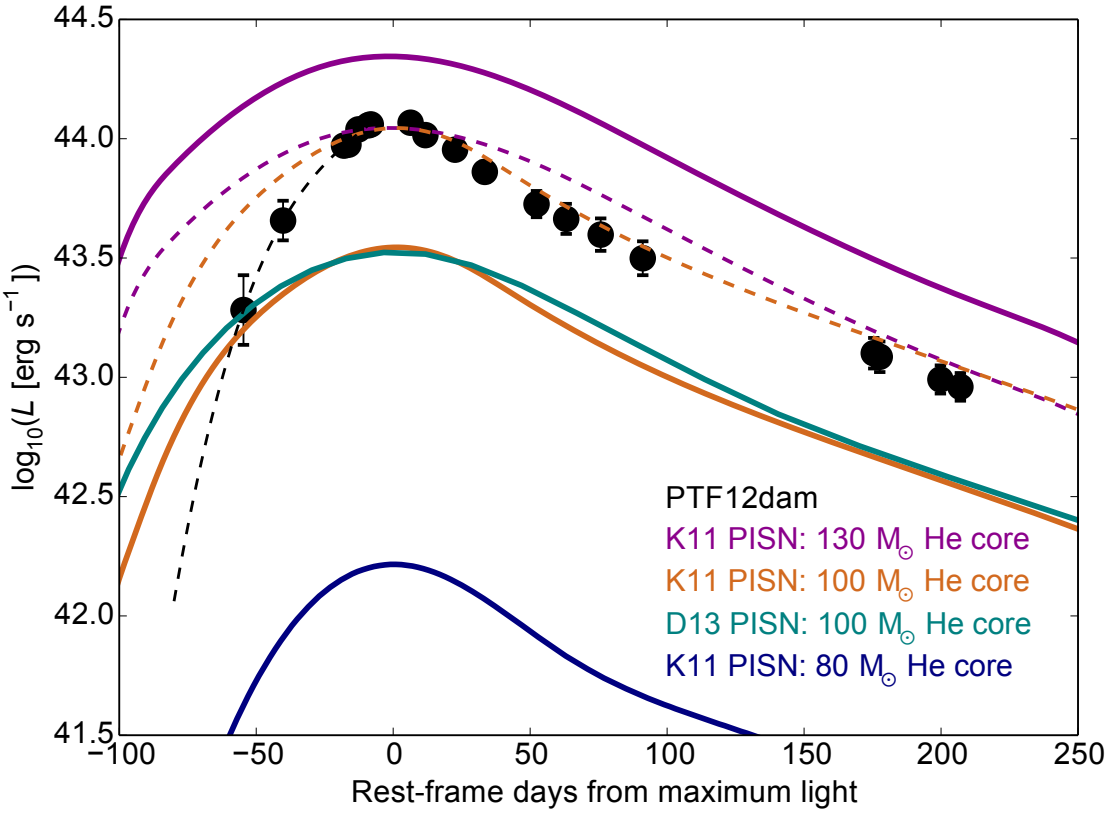

Figure 4.7: PTF12dam bolometric light curve, comprising Swift observations in the near-UV and ground-based *grizJHK* data. A cubic fit to the rise is shown to guide the eye (black dashed line). The solid lines are the PISN models of (Kasen et al. 2011; Dessart et al. 2013). The coloured dashed lines are the 130 and 100 $M_\odot$ PISN models shifted to match the peak luminosity of PTF12dam for ease of comparison. Again we see that the rise of PTF12dam is about twice as fast as the predictions of PISN models.

that the discrepancy between PISN models and the observed light curve and colours of PTF12dam should be even greater in higher dimensions.

Rotation and magnetic fields are also unable to resolve the discrepancy, as simple arguments show that these parameters have at most a small effect on the rise time. For a fixed power input (e.g. ^{56}Ni-decay), the rise time of a supernova is set primarily by the diffusion timescale (Arnett 1982, see also Section 2.4), given by

$$\tau_m = 450\mathrm{d}\left(\frac{\kappa}{0.2\,\mathrm{cm^2\,g^{-1}}}\right)^{1/2}\left(\frac{M_{\mathrm{ej}}}{100\,\mathrm{M_\odot}}\right)^{3/4}\left(\frac{E_k}{10^{51}\,\mathrm{erg}}\right)^{-1/4}, \tag{4.1}$$

where E_k is the kinetic energy of the explosion, M_ej the ejected mass and κ the opacity. In the rising phase, the gas will be highly ionized, so κ must be close to $0.2\,\mathrm{cm^2\,g^{-1}}$. For a $100\,\mathrm{M_\odot}$ sphere, this gives diffusion times of 246 d or 140 d for an explosion with $E_\mathrm{k} = 10^{52}$ erg or 10^{53} erg, respectively. If the ejected mass of ^{56}Ni is $5\,\mathrm{M_\odot}$, a self-consistent set of parameters is $E_\mathrm{k} \sim 4\times10^{52}$ erg and $M_\mathrm{ej} \sim 100\,\mathrm{M_\odot}$. The diffusion time

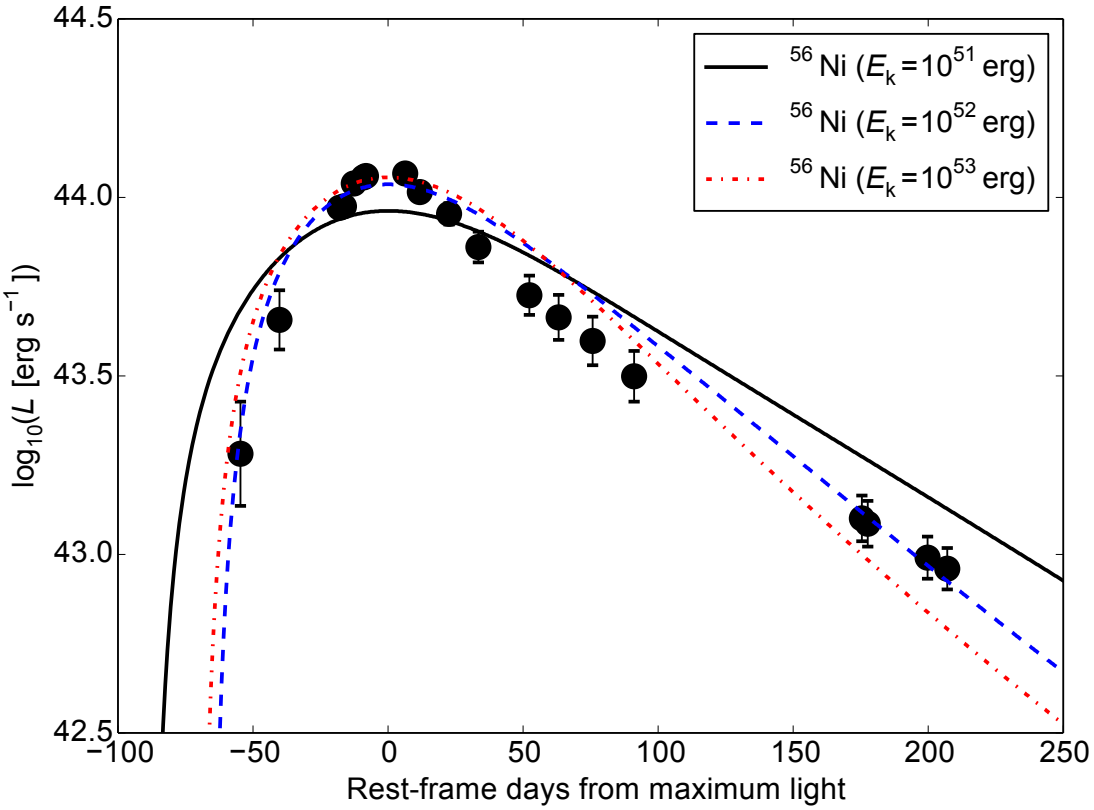

Figure 4.8: ^{56}Ni-powered fits to the light curve of PTF12dam. Fit parameters are given in Table 4.5. None of the combinations of ejecta mass, nickel mass and kinetic energy are compatible with realistic physical models (see Section 4.5.2).

Table 4.5: Fit parameters for ^{56}Ni-powered diffusion model

Energy (erg)	$M_{\rm ej}$ ($M_\odot$)	$M_{\rm Ni}$ ($M_\odot$)	Rise time (days)	χ^2/d.o.f.
10^{51}	14.7	14.1	88.9	8.7
10^{52}	21.5	14.1	64.4	1.8
10^{53}	52.2	16.1	64.4	3.0

is then 175 d – much greater than the observed rise time in PTF12dam.

We test this calculation by performing light curve fits with our ^{56}Ni-powered model. Three fits are shown in Figure 4.8, along with the fitting parameters. We find that the rise times in the model are indeed very close to the corresponding diffusion times, with $t_{\rm rise} \sim 1.1\,\tau_m$. The timescales calculated in this way are independent of more complicated effects like rotation or magnetic fields; the only physics is radiative diffusion (in the particularly simple regime where electron scattering dominates the opacity). Even if we conservatively assumed that the rise time was half of the diffusion time, a superluminous pair-instability event like that proposed for SN 2007bi should still have a rise

time $\gtrsim$ 100d.

Our best-fitting ^{56}Ni-powered model, for a canonical kinetic energy $E_k = 10^{51}$ erg, has ejecta mass $M_{ej} \sim 15\,M_\odot$, with a quite unphysical ^{56}Ni mass of greater than $14\,M_\odot$. Formally, better fits can be obtained with higher explosion energies of 10^{52} and 10^{53} erg, but again very high ^{56}Ni masses of $14\,M_\odot$ and $17\,M_\odot$ are required. While this results in M_{Ni}/M_{ej} ratios that are unphysically high for an iron core-collapse supernova, the most energetic models exhibit ratios that could be produced in thermonuclear events. However, the associated total ejecta mass is not compatible with any proposed progenitor of such an explosion. $M_{ej} \sim 50\,M_\odot$ is much too high for a SN Ia-like model. As for pair-instability models: producing more than $10\,M_\odot$ of ^{56}Ni seems to require helium cores of more than $110\,M_\odot$ (Kasen et al. 2011), so we would expect much more massive ejecta compared to the $50\,M_\odot$ in our fit. Thus, we are in a region of parameter space that does not correspond to any quantitative physical model. Reasonable ^{56}Ni-powered models therefore seem to be unable to reproduce our data.

4.5.3 Magnetar model

We have seen that the combination of relatively fast rise times and blue spectra observed for PTF12dam and PS1-11ap (and likely SN 2007bi) rule out an interpretation as pair-instability explosions. Here we suggest a model that can consistently explain the data.

In Section 4.4.2, we found that the spectroscopic evolution of slowly-declining SLSNe (2007bi-like) is consistent with the evolution of normal SLSNe Ic (2005ap-like), but occurring over a longer timescale. One of the best candidates to explain the 2005ap-like objects is the magnetar spin-down model, as shown in Chapter 3. This mechanism has also been proposed for SN 2007bi, by Kasen & Bildsten (2010) and independently by Woosley (2010). We fit our magnetar-powered diffusion model to the bolometric light curve of PTF12dam (Figure 4.9 and Table 4.6), and find a good fit to both the rise and decline for a magnetic field $B = 1.1 \times 10^{14}$ G and spin period $P = 2.6$ ms. A large ejecta mass of 10-16 $M_\odot$ is required (for opacity in the range 0.1-0.2 cm^2 g^{-1}) – significantly higher than typically found for SNe Ibc (Drout et al. 2011), but similar to the highest estimates for SN 2011bm (Valenti et al. 2012) and SN 2003lw (Mazzali et al. 2006b). This is of course well below the $> 80\,M_\odot$ expected in PISNe. At peak, the r-band luminosities of PTF12dam and PS1-11ap are ~ 1.5 times that of SN 2007bi. Rescaling the PTF12dam light curve to match the peak of SN 2007bi, our model implies similar ejected mass for SN 2007bi, with a longer magnetar spin period ($P \sim 3.3$ ms), comparable to previous models (Kasen & Bildsten 2010). The magnetar

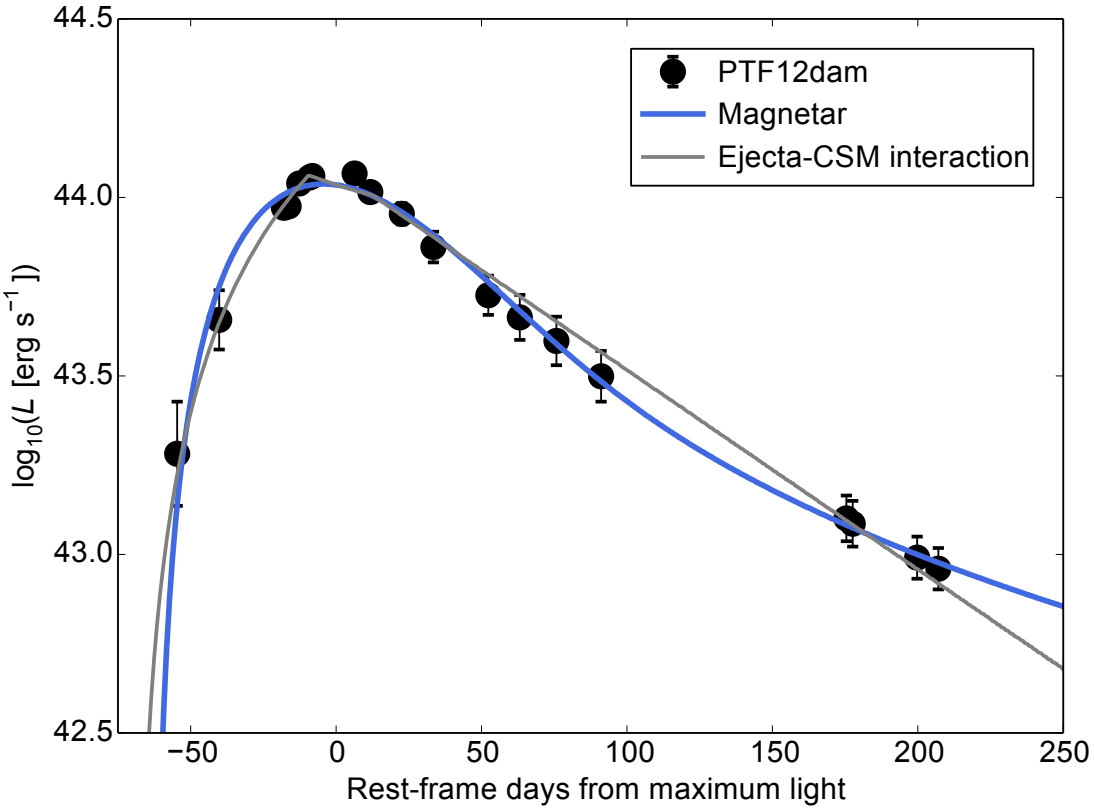

Figure 4.9: Magnetar- and interaction-powered model fits to PTF12dam. The fit parameters are given in Table 4.6. Both models can satisfactorily reproduce the light curve, in contrast to PISN and other (physically realistic) ^{56}Ni-powered models.

model can also produce high temperatures before and around maximum light, with a decline rate matching the data (Figure 4.10). This is in contrast to PISN models, which are seen to be much too cool.

As in Chapter 3 (and following Inserra et al. 2013), we have assumed that the magnetar input is fully trapped, which gives a good fit over the duration of the light curve. Kotera et al. (2013) investigated the deposition of pulsar emission in SNe, and found that hard radiation leakage should become significant at ~ 100 d if $M_{\rm ej} \approx 5\,{\rm M}_{\odot}$, so our assumption of full trapping over the observed light curve is reasonable for PTF12dam, which seems to have a larger ejected mass by a factor of a few. Allowing for the effect of incomplete trapping by setting the γ-ray opacity to $\kappa_{\gamma} = 0.01\,{\rm cm}^2\,{\rm g}^{-1}$, Chen et al. (2015) found a best-fit magnetar model for PTF12dam with an ejected mass of $10\,{\rm M}_{\odot}$ (for optical opacity $\kappa = 0.1\,{\rm cm}^2\,{\rm g}^{-1}$). While this is slightly lower than our estimate ($16\,{\rm M}_{\odot}$ for the same opacity), it shows that the inclusion of leakage is not crucial to our analysis here. The most sensitive parameter to variations in trapping is the B-field, as this mainly determines the late-time decline rate. Chen et al. (2015) found $B = 0.7 \times 10^{14}$ G for PTF12dam.

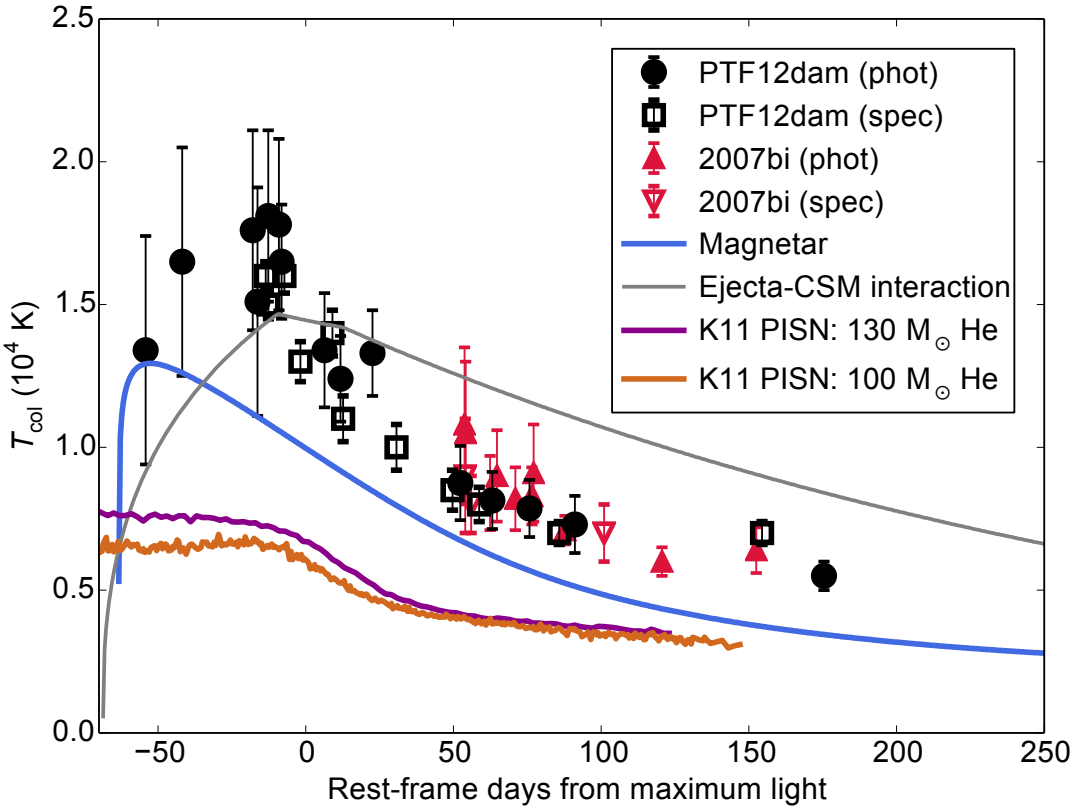

Figure 4.10: PTF12dam temperature evolution. Colour temperatures were estimated by fitting blackbody curves to multi-colour photometry and spectra. PISN temperatures were measured using the same method on synthetic photometry from the models. PISN models exhibit temperatures well below our data, whereas magnetar and interaction models are much closer to the high observed temperatures. Note that our light curve fits give the *effective* temperature (from the total luminosity) rather than the colour temperature (from the slope of the SED in the optical).

The velocity evolution is plotted in Figure 4.11. There is very little decline shown in over 200 days after maximum light, consistent with the predictions of a magnetar wind bubble (Kasen & Bildsten 2010, see Section 4.4.3). PTF12dam exhibits slightly lower velocities (as measured from spectral line widths of Fe II and Mg I]) than fast declining SLSNe Ic (Figures 4.11, 4.4, 3.13-3.15). This is naturally explained by larger ejected mass and weaker magnetar wind from the slower spin-down. Figure 4.11 shows that the magnetar model fit under-predicts the velocities observed in PTF12dam by about a factor of 2, whereas in Chapter 3, we found agreement to within about $\sim 30\%$ between the models and data for LSQ12dlf and SN 2013dg (for SSS120810, the model significantly *over*-predicted the velocity – the fit was not well constrained, as no rise time was measured). Equation 2.5 shows that for a fixed diffusion time in our fit, doubling the velocity means doubling the ejected mass. Thus, the mass inferred from our magnetar light curve fit may be an underestimate by up to a factor of 2 (the reverse is true for SSS120810, which should have much lower mass than the $\sim 12\,M_\odot$ estimated in Sec-

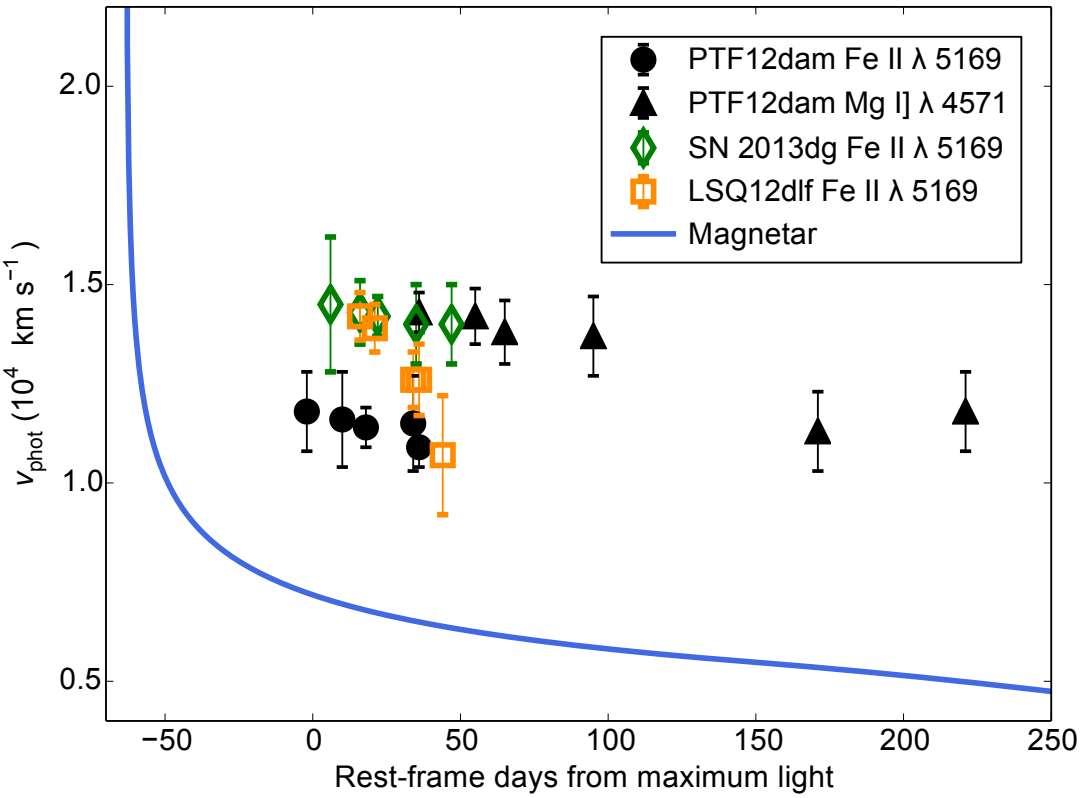

Figure 4.11: PTF12dam velocity evolution, compared to our magnetar model and some fast-declining SLSNe Ic. Velocities were measured from the P Cygni minimum of the Fe II λ 5169 line at early times, and from the FWHM of the Mg I] λ 4571 emission line at late times.

tion 3.5). Our best estimate for the ejected mass in the magnetar model of PTF12dam should therefore be revised upwards to $M_{\rm ej} \approx 20\,{\rm M}_{\odot}$. A larger velocity and ejected mass compared to the parameters used in our fit would also indicate a higher explosion energy than the fiducial 10^{51} erg.

Fits to other SLSNe in Chapters 2 and 3, and fits presented by Inserra et al. (2013) using the same model, found lower ejected masses and higher magnetic fields compared to PTF12dam. Thus in the context of the magnetar theory, the diversity in SLSNe Ic can be easily explained in terms of the fit parameters, which can produce a wide variety of light curves. Large ejecta mass results in a slow light curve rise and broad peak compared to other SLSNe Ic (and would explain the slower spectroscopic evolution, including why the spectrum is not fully nebular at 200 d). The weaker B-field in slowly-declining objects means that the magnetar radiates away its rotational energy less rapidly, so that more of the heating takes place at later times; this gives the slow decline that mimics ^{56}Co decay. These concepts are illustrated in Figure 4.12. This suggests that all SLSNe Ic could be members of a single class, powered by magnetar

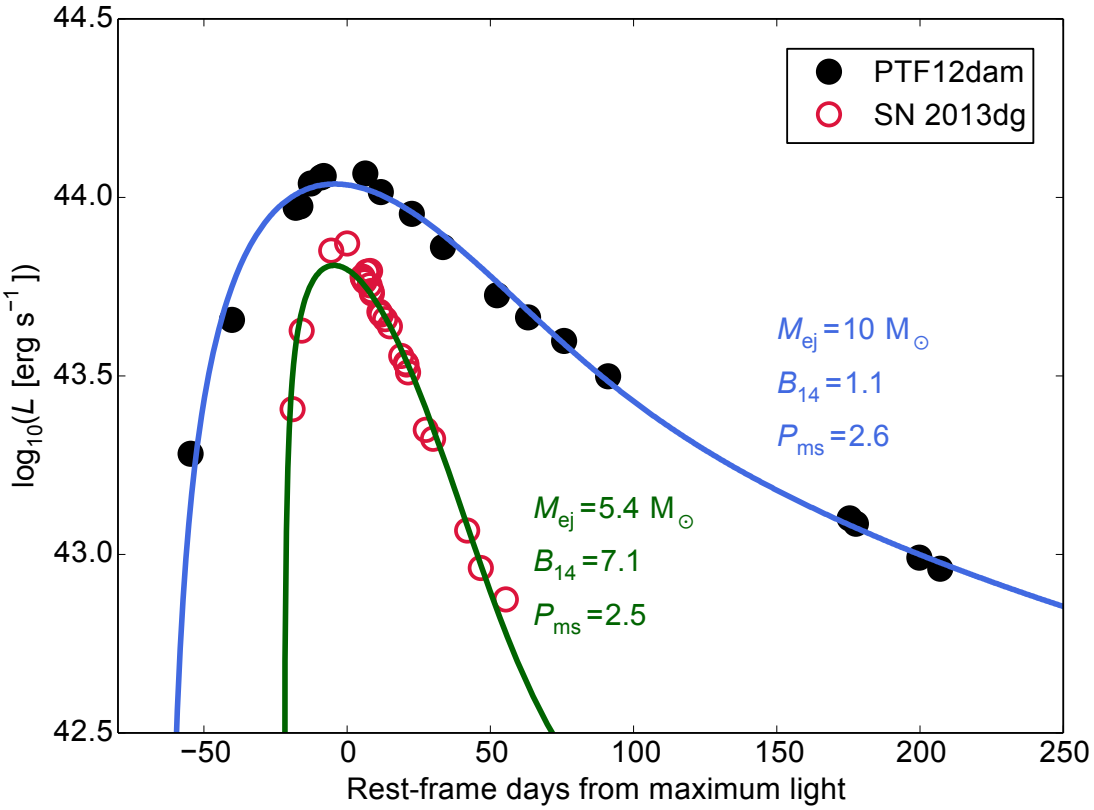

Figure 4.12: The magnetar fit for PTF12dam compared to that for SN 2013dg (Chapter 3). To first order, larger ejecta mass and weaker B-field result in a longer rise and slower decline (respectively) for PTF12dam. B_{14} is the magnetic field in units of 10^{14} Gauss, and $P_{\rm ms}$ is the spin period in milliseconds.

spin-down or a similar central engine, with the width of the light curve determined in each case by the interplay between the diffusion timescale and the rate of heating from the central engine. This is in contrast to previous claims that slowly declining SLSNe form a separate group of objects (Gal-Yam 2012). The spectroscopic similarity (Figure 4.5) also indicates a single class.

4.5.4 Interaction model

In Figure 4.9 we also show an interaction-powered model for PTF12dam. This fit requires $M_{\rm ej} \gtrsim 20\,{\rm M}_\odot$, similar to our inferred mass in the magnetar model, as well as half as much mass again in the CSM (the fit parameters are listed in Table 4.6). The CSM model does a good job of fitting the light curve. However, $13\,{\rm M}_\odot$ of CSM seems too high to be produced by stellar winds or an LBV outburst. One mechanism which can provide such massive CSM shells has already been proposed to explain SLSNe: the pulsational pair-instability (Woosley et al. 2007, see also Sections 1.6.3 and 3.5.4).

Table 4.6: Light curve fit parameters for PTF12dam (Figure 4.9), assuming $\kappa = 0.2(0.1)\,\mathrm{cm^2\,g^{-1}}$.

Magnetar					
$M_{\rm ej}/\mathrm{M_\odot}$	$B/10^{14}\mathrm{G}$	P/ms	$\chi^2/\mathrm{d.o.f.}$		
10.0 (16.0)	1.1	2.6	0.64		
CSM interaction					
$M_{\rm ej}/\mathrm{M_\odot}$	$M_{\rm CSM}/\mathrm{M_\odot}$	$E_{\rm k}/10^{51}\mathrm{erg}$	$\log(\rho_{\rm CSM}/\mathrm{g\,cm^{-3}})$	$\chi^2/\mathrm{d.o.f.}$	$R_{\rm ph}/10^{15}\mathrm{cm}^*$
26.3	13.0	1.9	−12.06	0.45	2.6

*Determined by other fit parameters

However, models presented so far have involved large amounts of hydrogen and/or helium (Woosley et al. 2007; Chatzopoulos & Wheeler 2012a) at relatively low velocities ($\sim 10^3\,\mathrm{km\,s^{-1}}$) and are therefore expected to display narrow H/He lines. Chatzopoulos & Wheeler (2012b) predicted O-rich shells if the progenitor was rapidly rotating, but the shell mass was found to decrease with rotation. Their maximum shell mass was only $\sim 7\,\mathrm{M_\odot}$, well below that required for our light curve fit. Furthermore, to reach the luminosities of SLSNe ($L \sim 10^{44}\,\mathrm{erg\,s^{-1}}$), the first shell must have reached a significant radius before the second shell collides with it (in order to avoid adiabatic losses), and at typical radii of 10^{15}-$10^{16}\,\mathrm{cm}$, the models produced by Woosley et al. (2007) were faint in the U and B bands, unlike PTF12dam. In our semi-analytic model (Figure 4.10), we do see a high effective temperature around maximum light, but the prediction of the model at very early times is far below the data.

In our interaction-powered fit, the forward shock breaks out of the CSM at approximately the time of maximum light (the light curve rise is powered by photons diffusing out ahead of the shock). Yet our spectra of PTF12dam obtained two weeks before maximum light show broad lines that can only have arisen from material with $v \gtrsim 10000\,\mathrm{km\,s^{-1}}$ (i.e. SN ejecta). It is difficult to imagine how the ejecta could be visible behind a $13\,\mathrm{M_\odot}$ shell, which should be highly ionized as the shock passes through it. Perhaps a non-spherical geometry (e.g. a disk or ring) for the CSM shell could allow us direct sight of the ejecta. Due to the large parameter space available to interaction-powered models, it is difficult to rule them out completely, but the spectral data seem to disfavour this scenario for PTF12dam. This is a stronger constraint than we found in Chapter 3, where for each of our interaction model fits to SLSNe, the forward shock had already swept up the CSM before the start of our spectral coverage.

4.6 Do PISNe exist in the local Universe?

4.6.1 The PISN rate

The analysis of PTF12dam shows that it is almost certainly not a PISN. McCrum et al. (2014) have shown the same for PS1-11ap, using similar arguments. Because of the close similarity between these objects and the previous PISN candidate, SN 2007bi, we are left with no unambiguous PISNe within redshift $z < 2$. Using the properties of the PS1 Medium Deep Survey (MDS), we can constrain the local rate of stripped-envelope PISNe. We simulate MDS observations of PISNe using the light curve templates from Kasen & Bildsten (2010) and our own Monte-Carlo code (Young et al. 2008). This code was originally written by D. R. Young as part of his thesis, and he re-coded it in PYTHON for our use here.

The code generates a random array of redshifts within the range $0 < z < 1$, and explosion epochs within the survey year for 50000 PISNe, and converts the model rest-frame light curves to observer-frame light curves, including K-corrections, time dilation and average extinction. The rate of occurrence as a function of redshift is computed from the change in volume and cosmic star-formation history. We assume that a fixed fraction of the star formation leads to core-collapse (0.007 with a Salpeter IMF), and that the PISN rate is itself a fixed fraction of the core-collapse rate (this is the number we hope to constrain). The models are then subjected to a simulated survey with the depth and cadence of MDS in order to calculate the number we should expect to see. The survey observes to a typical nightly depth of ~ 23.5 mag (e.g. Inserra et al. 2013), in *gri*-like filters (see Section 2.1.1). In order to qualify as a 'detected PISN candidate', a light curve must peak at an apparent magnitude < 21 in at least one bandpass, and have a continuous 100 d (observer-frame) window of MDS monitoring.

We use the 80, 100 and 130 $M_\odot$ He-core PISN models (Kasen et al. 2011), and initially assume a rate of $R_{\mathrm{PISN,X}} = 10^{-5} R_{\mathrm{CCSN}}$ for each model with mass X, where R_{CCSN} is the core-collapse SN rate (Dahlen et al. 2004). With this prescription, the simulated survey typically finds 5 of the intermediate (100 $M_\odot$) PISN candidates per year, at $z < 0.6$. The 130 $M_\odot$ explosions have peak NUV magnitudes of $M_U \approx -22$, resulting in apparent r_{P1} and i_{P1} magnitudes < 20 mag. PS1 should detect $> 90\%$ of these within $z < 0.6$, corresponding to $\gtrsim 10\,\mathrm{yr}^{-1}$. Clearly, if the most massive PISN explosions occur at any significant rate at low-to-moderate redshift, we would expect to have detected them by now.

We now examine the more conservative result for the intermediate-mass model in more detailed. In Nicholl et al. (2013) we claimed that PS1 had not discovered any transient matching the properties of this model in the 3 years of MDS. This result

is supported by the thesis of M. McCrum, which has now formally concluded. McCrum et al. (2015) searched for all MDS transients that were hostless or in faint hosts, and no candidate event was found that clearly matched models of PISNe. The lack of detections in PS1 is inconsistent with our assumed rate of $10^{-5} R_{\rm CCSN}$ at a level of 3.9σ (assuming Poisson statistics). This implies a 3σ upper limit on their rate of $R_{\rm PISN, M>100M_\odot} < 6 \times 10^{-6} R_{\rm CCSN}$, within $z < 0.6$. Even allowing for another factor ~ 2 to conservatively cover detection issues such as bad pixels or bright nearby stars, the rate of super-luminous, Type Ic PISNe must be at least a factor 10 lower than the overall SLSN Ic rate (Gal-Yam 2012; Quimby et al. 2013; McCrum et al. 2014).

However, our calculation suggests that virtually all of the low-mass PISNe ($80\,M_\odot$), which are not super-luminous (see Figure 4.7), would escape detection. These explosions are faint because they produce much less ^{56}Ni than their more massive counterparts ($M_{\rm Ni} = 0.2\,M_\odot$, compared to 5 and $40\,M_\odot$ for the 100 and $130\,M_\odot$ models; Kasen et al. 2011). Future searches for PISNe should target these fainter explosions at lower redshift (and larger volumes), or the more luminous candidates at $z > 1$.

As a sanity check, we also carry out a rough manual calculation of the approximate rate limit we would expect to recover. The MDS fields cover 70 deg^2 (Tonry et al. 2012a), which corresponds to a volume within redshift $z < 0.6$ of $V = 0.07\,{\rm Gpc}^3$. The brightest models have absolute peak magnitudes in the NUV of $M_U \sim -22$ (AB magnitude; Gal-Yam et al. 2009; Berger et al. 2012), giving apparent peak magnitudes $r_{\rm P1}$, $i_{\rm P1} \lesssim$ 20-21. With the typical PS1 nightly detection limit of 23.5 mag, these objects should be detectable 2-3 magnitudes before and after maximum light, corresponding to 130-200d in the observer frame. The observing window for each MDS field during a single year is 150 days, long enough to observe the slow and distinctive rise or decline of PISNe. However, for about half of the events, the light curve peak will fall outside of the survey season (such events would have incomplete light curves). Assuming that a detection of the peak is a requirement to classify a transient as a PISN candidate, the detection efficiency is approximately $E = 0.5$. The volumetric rate is given by $R_{\rm PISN} = N_{\rm PISN}/(VE\Delta t)$, where $N_{\rm PISN}$ is the number of PISNe detected in a time Δt. In 3 years of MDS ($\Delta t = 3$), we have detected no supernova-like transients (within $z < 0.6$) peaking at these magnitudes and exhibiting a PISN-like rise time, and only PS1-11ap has shown a slow decline. We therefore derive an upper limit on the super-luminous PISN rate $R_{\rm PISN} < 10\,{\rm Gpc}^{-3}\,{\rm yr}^{-1}$. Taking the core-collapse SN rate at $0.5 < z < 0.9$ from Dahlen et al. (2004), $R_{\rm CCSN} = 4 \times 10^{-4}\,{\rm SNe\,Mpc}^{-3}\,{\rm yr}^{-1}$, the PISN rate corresponds to $\lesssim 10^{-5}$ of the core-collapse rate, in agreement with the results of our simulation. These bright PISN candidates thus appear to be a factor of a few (perhaps up to 10) less common than the general population of SLSNe Ic (Gal-Yam 2012; Quimby et al. 2013; McCrum et al. 2014).

4.6.2 PISN candidates at higher redshift

Two SLSNe, at redshifts 2.05 and 3.90, were recently presented by Cooke et al. (2012), and suggested to be PISNe. These objects exhibited rise times of around 50 days, similar to PTF12dam (though not so well constrained), and were shown to match the PISN model light curves from Kasen et al. (2011) quite well (the same models that PTF12dam clearly does not match; see Figures 4.3 and 4.7). This apparent contradiction results from their high redshifts. The observed optical photometry actually probes rest-frame UV light. The PISN models quickly fade in the UV relative to the optical, due to line blocking (Kasen et al. 2011; Dessart et al. 2013). Integrating the SEDs of the PISN models between 1500 and 2500 Å, the approximate wavelength range sampled by the high-z observations, we find that the resultant light curves do indeed reach peak in ~ 50 days, before fading in a further ~ 150 days. Thus, we cannot exclude the possibility that these high-redshift SLSNe are the first observed examples of PISNe. Unfortunately, the lack of spectra and rest-frame optical data preclude a firm classification.

PISNe were originally expected only at high redshift, as the required massive cores are difficult to form except at low metallicities. While we still expect very massive stars and PISNe to be more common in the early Universe, it should be noted that recent simulations by Yusof et al. (2013) show that stars of initial mass 100-290 $M_{\odot}$ may end their lives in hydrogen-free PISNe at SMC metallicity.

4.7 Discussion and conclusions

We have presented the data from an extensive follow-up campaign for PTF12dam. This SLSN exhibited an unusually slow light curve decline, previously witnessed only in the case of SN 2007bi, which was thought to be a radioactively-powered 'Type R' SLSN and a candidate for a pair-instability explosion (Gal-Yam et al. 2009; Gal-Yam 2012). Early detections and multi-wavelength data show that this is not the case for PTF12dam. The relatively 'fast' rise time of $\sim$ 50-60 days, given the slow decline, is incompatible not only with our semi-analytic ^{56}Ni-powered model, but also radiation hydrodynamic simulations of PISNe (Kasen et al. 2011; Dessart et al. 2013). Moreover, the slope of the SED, constrained into the UV by *Swift* photometry, is much bluer than the PISN models at all times. The spectrum of PTF12dam beyond 50 days after maximum light looks virtually identical to SN 2007bi, suggesting that the two are likely the same type of explosion and that SN 2007bi was therefore not a PISN (no earlier spectra of SN 2007bi exist).

The spectroscopic evolution of PTF12dam at early times in fact closely resembles the more common, fast-declining SLSNe Ic. The PTF12dam light curve can be well

fit by both central-engine and circumstellar interaction models, which are the two main theories explaining the light curves of the fast-declining objects. The slow photometric and spectroscopic evolution seen in PTF12dam could be caused by larger ejected mass, along with slower energy input from the central engine or a more massive CSM shell. In either case, PTF12dam, SN 2007bi, and other slow-declining SLSNe such as PS1-11ap, are fully consistent with being a subset of the general SLSN Ic population. Their grouping into a separate SLSN 'Type R' class is no longer observationally supported. We favour the central-engine model to explain these objects, as the spectrum shows a clear resemblance to numerical calculations of magnetar-heated ejecta (Dessart et al. 2012b) and the flat velocity evolution matches the predictions of Kasen & Bildsten (2010). The properties of PTF12dam appear to be fully consistent with a magnetar-powered explosion ejecting $\sim 20\,M_{\odot}$.

Using a simulated survey based on the depth and cadence of the PS1 Medium Deep Survey and the PISN light curve models of Kasen et al. (2011), we find that the rate of PISNe within $z < 0.6$ is less than 1 in 10^5 of massive star explosions. PISNe are predicted to produce distinctive chemical abundance patterns (Heger & Woosley 2002), but the chemical enrichment signatures in metal poor stars and damped Lyman-alpha systems do not show evidence of PISN nucleosynthesis (Kobayashi et al. 2011). The low upper limit on their rate of occurrence reduces their potential impact on cosmic chemical evolution within $z < 1$, helping to relieve this possible tension.

Chapter 5

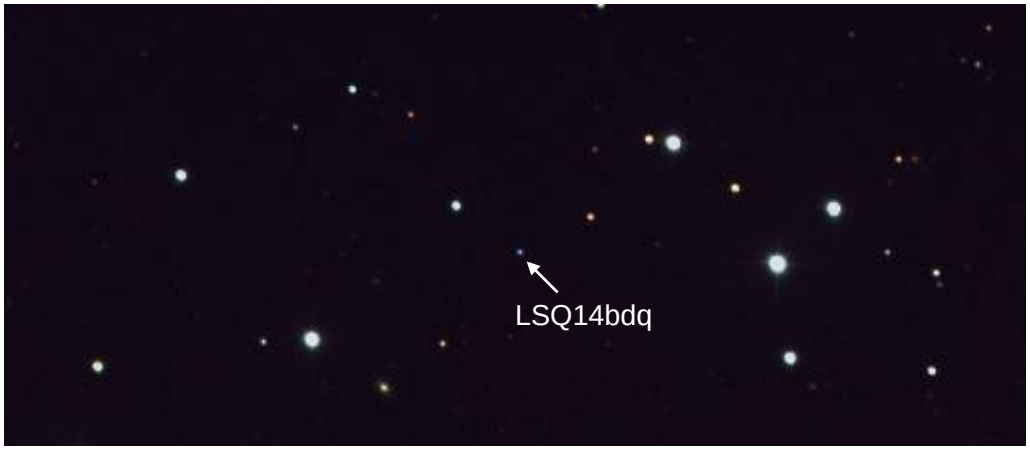

LSQ14bdq: a SLSN Ic with a double-peaked light curve

Murray: "Intergalactic real estate... Only $50 a star, including a certificate!"

Later...

Murray: "It's not good news: 'Planet Jemaine' supernova-ed. There's nothing left apparently – just a huge, gaseous cloud and the beginnings of a black hole"

Jemaine: "When did this happen?"

Murray: "About 4 million years ago"

Jemaine: "Well, that was a waste of 50 bucks"

- Flight of the Conchords ('Sally Returns')

5.1 Introduction

A major goal of modern transient surveys, as described in Chapter 2, is to detect SNe as soon as possible after explosion. Early observations are important for a variety of reasons. Detection of UV/X-ray radiation from the shock-breakout phase can be used to constrain the density profile in the stellar envelope, pre-explosion mass-loss rates, and the physics of the shock itself. Although this phase is notoriously difficult to detect (lasting only seconds to hours depending on the progenitor radius; Chevalier & Fransson 2008; Ensman & Burrows 1992; Klein & Chevalier 1978), shock-breakout radiation has been observed serendipitously by the *Swift* and GALEX satellites for a number of core-collapse SNe (Soderberg et al. 2008; Modjaz et al. 2009; Gezari et al. 2008, 2015; Schawinski et al. 2008).

Following shock breakout, the SN luminosity is controlled by cooling of the shocked stellar envelope (e.g. Nakar & Sari 2010), on timescales of hours to days. More compact progenitors cool faster due to adiabatic losses. Post-shock cooling emission declines bolometrically, but can show an apparent optical rise as the peak of the cooling SED moves from the UV through the optical filters (Piro & Nakar 2013). This phase is followed by the normal radioactive or recombination-powered phases that dominate most SN observations. The luminosity during the cooling phase scales approximately as $L \propto (E_{\rm k}/M_{\rm ej})\, R_\star$ (Rabinak & Waxman 2011), where $E_{\rm k}$ and $M_{\rm ej}$ have their usual definitions and $R_\star$ is the radius of the progenitor star. Data during the cooling phase is thus a useful constraint on the radius, and is more accessible to observation than the shock breakout phase. For very extended progenitors (red supergiants), the shock cooling can be comparable in brightness to the hydrogen recombination plateau, and last for $\gtrsim$10 days; this phase is thus responsible for the optical rise times of Type II SNe (Gall et al. 2015). Conversely, the cooling phase for Type Ia SNe, with progenitor radii $< 0.01\,{\rm R}_\odot$, is expected to be faint (Piro et al. 2010), and has not yet been observed.

Early data for SLSNe has an additional advantage, in that we can use the early light curve shape to discriminate between the competing models for the progenitor and power source. This was vividly demonstrated in the previous chapter, where the well-constrained rise time of PTF12dam was used to rule out pair-instability models. In this chapter, we will focus on a recent SLSN, LSQ14bdq, which has even earlier photometric detections revealing a clear double-peaked structure. We present the discovery of this object and classification as a SLSN in Section 5.2. In Section 5.3, we describe the photometric data reduction and analyse the main light curve peak. The precursor peak is modelled in Section 5.4. We summarise our findings and conclude in Section 5.5.

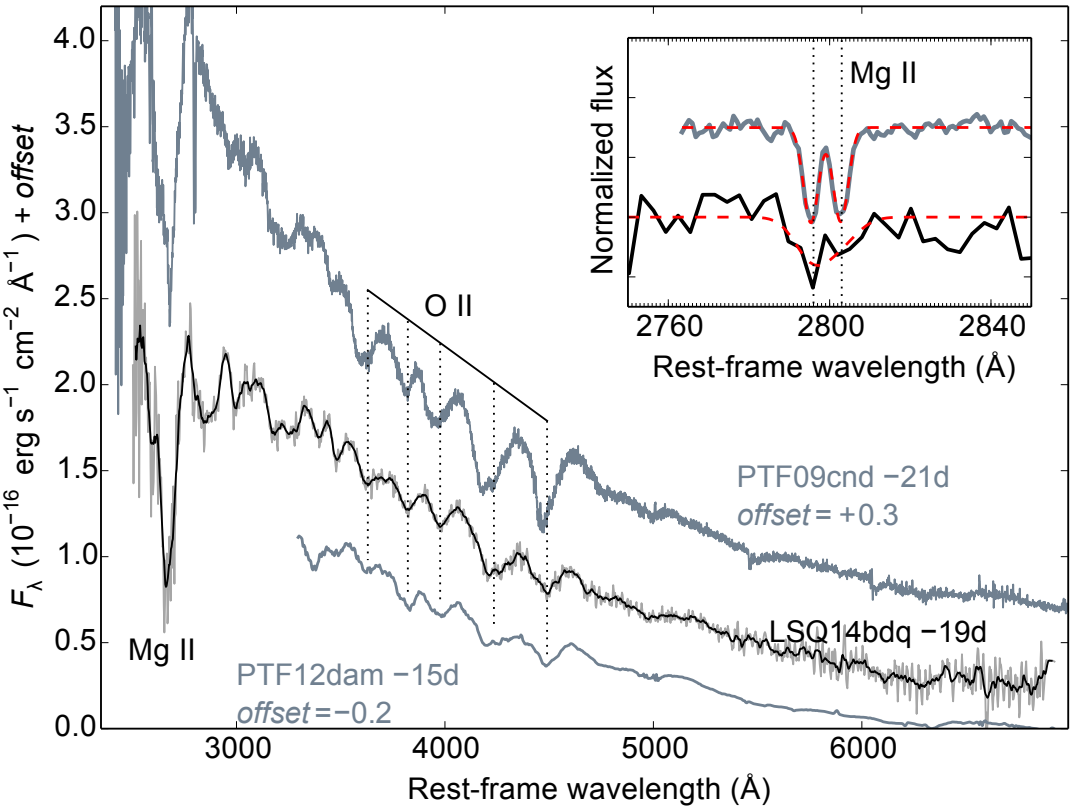

Figure 5.1: The pre-maximum spectrum of LSQ14bdq (smoothed using 10-pixel moving average), compared to PTF12dam and PTF09cnd (Quimby et al. 2011). The spectra are at similar phases from peak, and have been corrected for Galactic reddening using $E(B-V) = 0.056$ for LSQ14bdq and $E(B-V) = 0.02$ for PTF09cnd (Schlafly & Finkbeiner 2011). See Chapter 4 for PTF12dam extinction correction. The redshift is determined by fitting double-gaussian profiles (at instrumental resolution) to narrow Mg II absorption (inset, including PTF09cnd); the components are blended for the LSQ14bdq spectrum. The fluxes of PTF12dam and PTF09cnd have been scaled to the same luminosity distance as LSQ14bdq, with offsets added for presentation.

5.2 Discovery and spectroscopic classification

LSQ14bdq was discovered by LSQ, at coordinates RA = 10:01:41.60, Dec = −12:22:13.4, in images taken on 2014 April 5.1 UT (though earlier detections exist; Section 5.3). It was classified by Benitez et al. (2014), as part of PESSTO, as a SLSN Ic. The classification spectrum (1500 s exposure) was taken on 2014 May 4.9 UT with the NTT and EFOSC2, using Grism#13, and was followed by a longer exposure (2×1800 s) on the next night. A third spectrum was taken using Grism#11 (blue grism; 2400 s), on 2014 May 7.0 UT. These were reduced using the PESSTO pipeline, applying bias-subtraction, flat-fielding, wavelength and flux calibration

and telluric correction (Smartt et al. 2015). The absolute fluxes were matched to contemporaneous photometry. The PESSTO data are available from the ESO archive or WISeREP (Yaron & Gal-Yam 2012).

Figure 5.1 shows the spectrum summed over these three nights. The Grism#11 spectrum, with a resolution of 13.8 Å, shows interstellar Mg II $\lambda\lambda$ 2795.5,2802.7 absorption, giving a redshift of $z = 0.345$ from Gaussian fits (see inset on Figure 5.1). We estimate that the mean rest-frame phase of the combined spectrum is 19 d before maximum brightness (Section 5.3). We compare the spectrum to other SLSNe Ic with spectra at a few weeks before maximum: PTF12dam, discussed in detail in Chapter 4, and PTF09cnd, from Quimby et al. (2011). The spectra are clearly well matched, confirming the classification as a young SLSN Ic. The broad absorption features between ~ 3500-4500 Å are ubiquitous in these objects before maximum light. They have been attributed to O II, and appear to be a defining feature of the class (Quimby et al. 2011). The deep Mg II absorption matches that in PTF09cnd and other objects with near-ultraviolet spectroscopy (e.g. Chomiuk et al. 2011; Leloudas et al. 2012; Lunnan et al. 2013; Vreeswijk et al. 2014). Unfortunately, we have no spectra of LSQ14bdq during the declining phase, as the SN went into solar conjunction soon after being classified and was too faint for NTT spectroscopy when we picked it up again the following season.

5.3 Photometry

5.3.1 Data reduction

The observed light curve of LSQ14bdq is shown in Figure 5.2, with photometric data listed in Table 5.1. The rise from 2014 March 22.1 UT was measured with the automated LSQ pipeline (Baltay et al. 2013), employing PSF-fitting forced photometry, and the data are calibrated to SDSS r (AB system). However, subsequent inspection of pre-discovery LSQ data showed clear variable flux at the SN position *before* the first pipeline detection. We applied manual PSF photometry to the LSQ images using SNOoPY (Section 2.3.2), and discovered an early peak prior to the main rise. Non-detections (Table 5.1) suggest that the explosion occurred on MJD = 56721 ± 1, assuming a smooth rise to the first peak. A stack of all LSQ images from 2012 and 2013 shows no host galaxy to a limiting magnitude of $r = 24.1$, hence image subtraction is unimportant for our observations.

After classifying the SN, we triggered multicolour follow-up imaging using EFOSC2, the Liverpool Telescope and the LCOGT network. PSF magnitudes were

Table 5.1: Observed photometry of LSQ14bdq

Date	MJD	Phase*	g	r	i	z	Inst.
02-03-2014	56718.0	-66.2		>22.85			LSQ
04-03-2014	56720.0	-64.7		>22.40			LSQ
06-03-2014	56722.0	-63.2		21.78 (0.32)			LSQ
08-03-2014	56724.0	-61.7		21.24 (0.20)			LSQ
10-03-2014	56726.0	-60.2		21.08 (0.32)			LSQ
12-03-2014	56728.0	-58.7		21.16 (0.25)			LSQ
14-03-2014	56730.0	-57.3		20.99 (0.23)			LSQ
18-03-2014	56734.0	-54.3		22.04 (0.08)			LSQ
20-03-2014	56736.1	-52.7		22.05 (0.28)			LSQ
22-03-2014	56738.1	-51.2		22.21 (0.21)			LSQ
24-03-2014	56740.1	-49.7		22.21 (0.03)			LSQ
26-03-2014	56742.1	-48.3		22.06 (0.08)			LSQ
28-03-2014	56744.1	-46.8		21.55 (0.16)			LSQ
30-03-2014	56746.1	-45.3		21.44 (0.10)			LSQ
03-04-2014	56750.1	-42.3		21.05 (0.02)			LSQ
05-04-2014	56752.1	-40.9		20.84 (0.15)			LSQ
07-04-2014	56754.0	-39.4		20.67 (0.08)			LSQ
09-04-2014	56756.1	-37.9		20.47 (0.03)			LSQ
13-04-2014	56760.1	-34.9		20.18 (0.06)			LSQ
15-04-2014	56762.1	-33.4		20.12 (0.03)			LSQ
17-04-2014	56764.0	-31.9		19.93 (0.05)			LSQ
19-04-2014	56766.0	-30.5		19.88 (0.02)			LSQ
21-04-2014	56768.0	-28.9		19.89 (0.07)			LSQ
23-04-2014	56770.0	-27.5		19.74 (0.01)			LSQ
25-04-2014	56772.1	-25.9		19.71 (0.05)			LSQ
28-04-2014	56775.5	-23.4		19.64 (0.19)			PS1
06-05-2014	56783.1	-17.8	19.55 (0.09)	19.35 (0.12)	19.45 (0.05)		NTT
07-05-2014	56784.7	-16.6	19.29 (0.11)	19.31 (0.20)			LCOGT
12-05-2014	56789.9	-12.7	19.27 (0.04)	19.26 (0.12)	19.18 (0.06)	19.48 (0.12)	LT
20-05-2014	56797.9	-6.8	19.27 (0.04)	19.16 (0.02)	19.16 (0.06)	19.40 (0.04)	LT
23-11-2014	56984.2	131.8		21.15 (0.23)			LSQ
23-11-2014	56984.3	131.8		20.99 (0.10)	20.89 (0.06)		NTT
27-11-2014	56988.2	134.7		21.05 (0.24)			LSQ
28-11-2014	56989.2	135.5		21.36 (0.30)			LSQ
18-12-2014	57009.2	150.3		21.27 (0.33)			LSQ
20-12-2014	57011.5	152.0		21.51 (0.24)			PS1
23-11-2014	57024.2	161.5		21.78 (0.38)			LSQ
02-01-2015	57033.2	168.2		21.65 (0.23)			LSQ
20-01-2015	57042.0	174.3		22.16 (0.20)			PS1
12-02-2015	57065.3	192.0	23.29 (0.11)	22.41 (0.04)	22.30 (0.08)	22.00 (0.17)	GROND
26-02-2015	57079.2	202.4	23.74 (0.14)	22.89 (0.13)	22.82 (0.31)	22.79 (0.41)	NTT
13-03-2015	57094.1	213.5	24.35 (0.13)	23.43 (0.16)	22.87 (0.24)	22.45 (0.32)	NTT
Host (2012-2013 stack)				>24.08			LSQ

K-corrections†	$K_{g\to u}$	$K_{r\to g}$	$K_{i\to r}$	$K_{z\to i}$
Phase <0 (LSQ14bdq spectrum, −19d)	−0.30	−0.32	−0.49	−0.38
Phase >0 (PTF12dam spectrum, +171d)	−0.22	−0.16	−0.18	−0.20

Near-infrared (Vega system)			J	H	K	
12-02-2015	57065.3	192.0	20.70 (0.17)	>20.03	>18.39	GROND

*Rest-frame days relative to the estimated date of r-band maximum, MJD=56807.
†Defined by $m = M + \mu + K$

calibrated using a sequence of local field stars, themselves calibrated against standard fields on photometric nights. LSQ14bdq set for the season in late-May 2014. A polynomial fit, shown in Figure 5.2, suggests that our last data point during the rise is $\lesssim$1 week before the SN reached maximum brightness. We continued our follow-up campaign when the object returned in late 2014, by this stage well into the declining phase of the light curve. Our late-time data are from a variety of sources. As well as EFOSC2 and LSQ images, we also have detections from PS1 (Magnier et al. 2013). The PS1 data

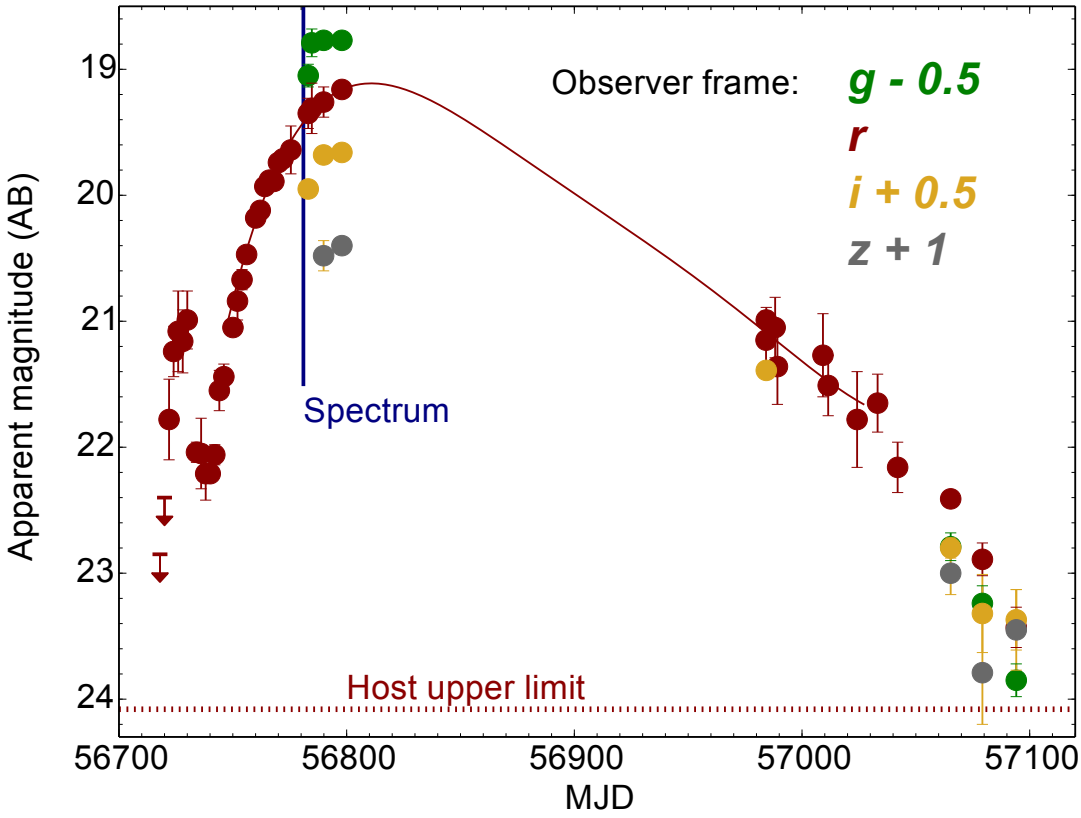

Figure 5.2: Observed photometry of LSQ14bdq in *griz* filters. Polynomial fitting suggests a peak on MJD = 56807, at $r = 19.15$, just before the SN entered solar conjunction.

were taken in the $w_{\rm P1}$-band (effectively a *gri* composite, see Figure 2.2; Tonry et al. 2012b) from the Pan-STARRS NEO Science Consortium survey (Huber et al. 2015). We calibrated photometry obtained on the $w_{\rm P1}$ images to the more standard *r*-band.

The Gamma-Ray Optical/Near-infrared Detector (GROND; Greiner et al. 2007, 2008), mounted on the MPG/ESO 2.2 m telescope at La Silla, imaged the field simultaneously in four optical (*griz*) and three NIR (JHK_s) bands on 2015 February 12, under photometric conditions. The observations each comprised 6 dithered exposures of 360 s. The data were reduced in a standard fashion (bias subtraction, flat-fielding, co-adding) with a customized pipeline (For details see Yoldaş et al. 2008, Krühler et al. (2008)). The NIR photometry was tied to 2MASS standards (Skrutskie et al. 2006). However, the SN was detected clearly only in *J*-band.

5.3.2 Light curve comparison

We converted observed *r*-band magnitudes to rest-frame *g*-band for comparison with other SLSNe (at this redshift, observed g, r, i, z are similar to rest-frame u, g, r, i). The

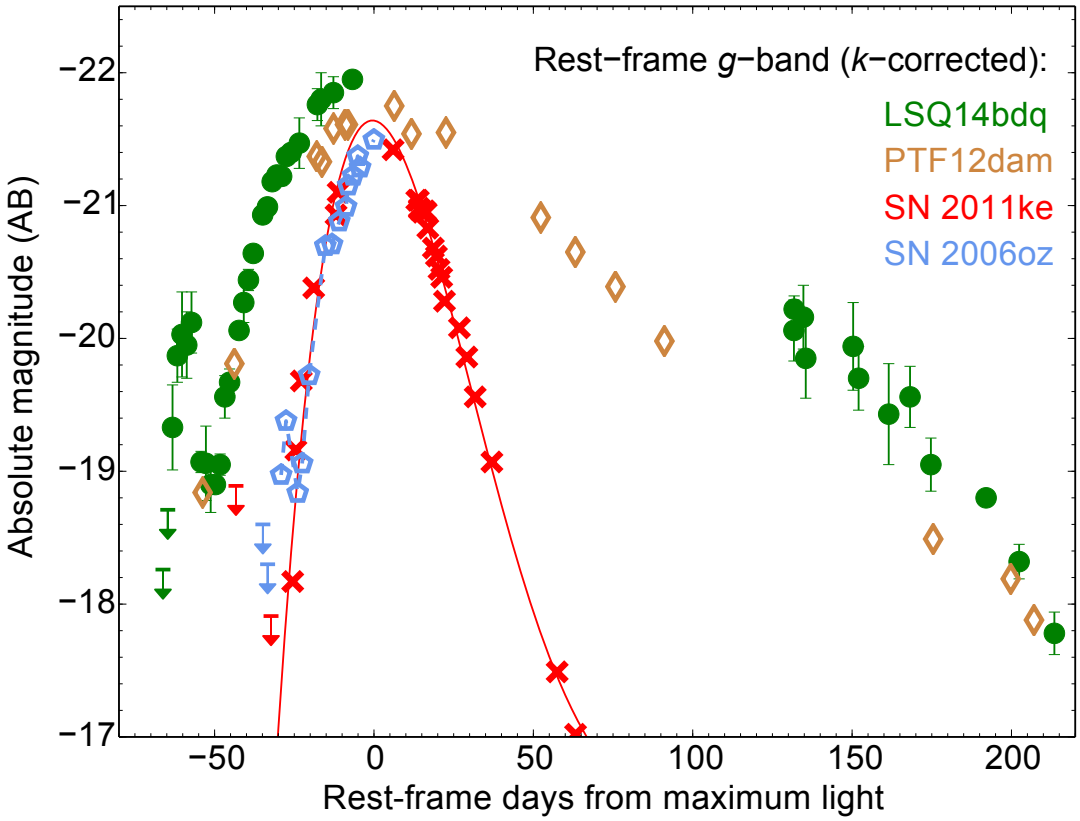

Figure 5.3: Absolute light curve in rest-frame g-band, after K-correction and de-reddening. LSQ14bdq is a slowly evolving SLSN, resembling PTF12dam. SLSN 2006oz (Leloudas et al. 2012), the other object with a detection of a double-peak, is a faster event like SN 2011ke (Inserra et al. 2013).

K-correction before peak is calculated from synthetic photometry on the LSQ14bdq spectrum ($K_{r\to g} \simeq -0.3$). As we only have essentially one spectrum, our post-peak data use a K-correction calculated in a similar manner, but from the spectrum of PTF12dam at +171 d. LSQ14bdq has a broad light curve like PTF12dam, as shown in Figure 5.3. A polynomial fit suggests $M_g = -21.96$ at maximum light. The initial peak, with a rise of 5 days and a total width of $\sim$ 15 days, is much narrower than the second peak. However, at $M_g = -20.01$ it is a remarkably luminous event in itself.

Leloudas et al. (2012) presented pre-rise data for SN 2006oz, the only other SLSN Ic with multiple observed peaks. Of the other SLSNe with strict explosion constraints, SN 2011ke (Inserra et al. 2013) shows a similar rise to SN 2006oz (and much faster than LSQ14bdq), but non-detections shortly before discovery limit any early peak to be fainter than those observed for LSQ14bdq and SN 2006oz. The two early peaks are qualitatively similar (see also Figure 5.5). The precursor phase for SN 2006oz appears to be shorter than in LSQ14bdq, in keeping with the rest of the light curve evolution.

The early peak is not as pronounced as for LSQ14bdq, although the time-sampling

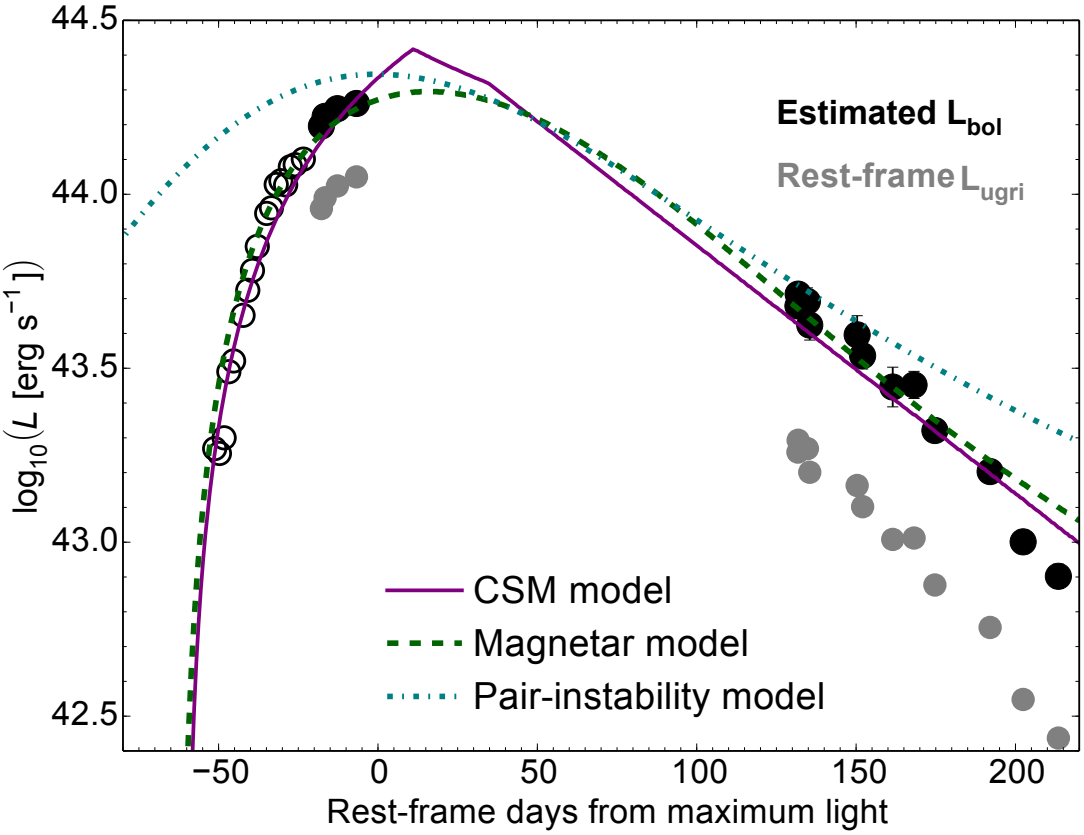

Figure 5.4: The main peak of the bolometric light curve can be fit by magnetar and interaction models (see Section 5.3.3). The rise of the PISN model is too slow to match the observations. Empty circles indicate points that are estimated from single-filter photometry.

from SDSS was sparser than the LSQ data we present here. However, SN 2006oz had the advantage of detections in the *u*, *g*, *r* and *i* filters. Although noisy, the data suggest that the bolometric luminosity is declining, similar to the shock cooling radiation discussed in Section 5.1. Leloudas et al. (2012) did not quantitatively model the early phase, but qualitatively discussed the helium star explosion models of Dessart et al. (2011). In such a scenario, the high initial luminosity of SN 2006oz would indicate a large radius, so Leloudas et al. (2012) suggested that the early emission could be powered by recombination in extended CSM, rather than a stellar envelope. The measured temperature, ~ 10000 K, is too high for hydrogen recombination, but could be consistent with O III recombining to O II.

5.3.3 Bolometric light curve and fits to main peak

We constructed the bolometric light curve of LSQ14bdq in two steps. First we integrated the flux in the rest-frame *u*- to *i*-bands, following the procedure described in

Table 5.2: Light curve fit parameters for LSQ14bdq (Figure 5.4), assuming $\kappa = 0.2\,\mathrm{cm^2\,g^{-1}}$.

Magnetar					
τ_m/days	$(M_{\rm ej}/\mathrm{M_\odot})^\dagger$	$B/10^{14}$G	P/ms	χ^2/d.o.f.	
90.0	(11.7)	0.6	1.7	12.5	
CSM interaction					
$M_{\rm ej}/\mathrm{M_\odot}$	$M_{\rm CSM}/\mathrm{M_\odot}$	$E_{\rm k}/10^{51}$erg	$\log(\rho_{\rm CSM}/\mathrm{g\,cm^{-3}})$	χ^2/d.o.f.	$R_{\rm ph}/10^{15}$cm*
30.0	16.0	5.0	-12.52	0.45	2.6

*Determined by other fit parameters
†Assuming $E_{\rm k} = 10^{51}$ erg; this restriction will later be removed

Inserra et al. (2013). Before −20 d, we caution that points were derived using the earliest available colour information. To estimate the full bolometric light curve, we took the fractional flux outside of this range to be the same as for PTF12dam (Chapter 4; see also Chen et al. 2015). This seems reasonable, at least in the late-time NIR, as the J-band luminosity at 192 days is similar to that in PTF12dam (Table 5.1). Both the observed *ugri*-pseudobolometric and the estimated full bolometric light curve are shown in Figure 5.2, to illustrate the uncertainty due to the missing filters.

We can reproduce the main peak with models powered by a central engine (we again take the magnetar model as representative) or by ejecta-CSM interaction. Details of the models were given in Section 2.4 (see also Inserra et al. 2013; Chatzopoulos et al. 2012). The fits are shown in Figure 5.4. The CSM model has ejected mass $M_{\rm ej} = 30.0\,\mathrm{M_\odot}$, CSM mass $M_{\rm CSM} = 16.0\,\mathrm{M_\odot}$ (assuming $\kappa = 0.2\,\mathrm{cm^2\,g^{-1}}$), and explosion energy $E_{\rm k} = 5.0 \times 10^{51}$ erg. The estimated masses in this model are very similar to those for PTF12dam (Chapter 4).

We have fixed the time of explosion in the magnetar model to coincide with the first detection, on the precursor peak. This fit has magnetic field $B = 0.6 \times 10^{14}\,\mathrm{G}$, spin period $P = 1.7\,\mathrm{ms}$ and diffusion time $\tau_m = 90\,\mathrm{d}$. In this case we focus on the diffusion time rather than the associated mass, in contrast to previous chapters, for reasons that will become clear in Section 5.4.2. The full set of fit parameters are listed in Table 5.2. The luminosity drops more quickly at late times than in PTF12dam (Figure 5.3), and to get a reasonable fit to the light curve we must include an estimate of the γ-ray leakage, following the procedure of Chen et al. (2015) with an opacity $\kappa_\gamma = 0.01\,\mathrm{cm^2\,g^{-1}}$. Including this leakage results in a lower estimate of the B-field compared to our PTF12dam magnetar fit in Chapter 4.

We also compare LSQ14bdq to the brightest PISN model of Kasen et al. (2011)

(the 130 $M_\odot$ bare helium core model, which we compared to PTF12dam in Chapter 4). The model reproduces the peak luminosity, but the rise-time is highly discrepant: the well-constrained main rise of LSQ14bdq lasts for 50 days, whereas the PISN model rises for over 100 days, and declines more slowly than LSQ14bdq. We therefore rule out this model for LSQ14bdq, just as we did previously for PTF12dam.

5.4 Models for the early emission

5.4.1 A ^{56}Ni-powered precursor?

The first scenario we investigate for the early peak is an initially normal SN, powered by the radioactive decay of ^{56}Ni, before the mechanism powering the super-luminous second peak kicks in. We compare our early light curve to ^{56}Ni-powered SNe (core-collapse and thermonuclear) in Figure 5.5, choosing filters with similar effective wavelengths. As the late-time spectra of Type Ic SLSNe closely resemble ordinary SNe Ic, we first compare to SN 1994I, a well-observed example of this class. The narrow light curve exhibited by SN 1994I suggested that it ejected a mass $M_{\rm ej} \lesssim 1\,M_\odot$ (Richmond et al. 1996). The first light curve peak in LSQ14bdq is slightly narrower, with a steeper rise, but is roughly comparable. However, it is 2.3 magnitudes brighter. We fit the light curves with our ^{56}Ni-powered model, assuming a blackbody SED and applying synthetic photometry to the model using PYSYNPHOT in order to convert the bolometric luminosity to a g/B-band magnitude. LSQ14bdq requires an almost pure ^{56}Ni ejecta of $\simeq 1\,M_\odot$, which is difficult to produce with core-collapse SNe. For comparison, our fit to SN 1994I has $M_{\rm Ni} = 0.15\,M_\odot$. Type Ia SNe produce $\approx$ 0.5-1 $M_\odot$ of ^{56}Ni, but comparing with SN 2005cf (Pastorello et al. 2007) shows that SNe Ia have light curves that are too broad. The fast rise of LSQ14bdq would necessitate a very large explosion energy, even for the lowest possible ejecta mass, $M_{\rm ej} = M_{\rm Ni}$. A fit shows that we require $E_{\rm k} = 2.5 \times 10^{52}$ erg. Because complete burning of 1 $M_\odot$ of carbon/oxygen to ^{56}Ni liberates only $\sim 10^{51}$ erg, we can also rule out a thermonuclear explosion. Thus, if the early peak is 'a supernova in itself', it cannot be a normal ^{56}Ni-powered event.

5.4.2 Shock cooling with a central engine

In Figure 5.6, we show an alternative scenario, comparing the early emission from LSQ14bdq to other SNe with two observed peaks. The basic light curve morphology of SNe 1987A, 1993J and 2008D has been interpreted as an initial cooling phase, releasing heat deposited by the shock wave, before a second peak is driven by delayed heating from ^{56}Ni (Shigeyama & Nomoto 1990; Woosley et al. 1994; Modjaz et al.

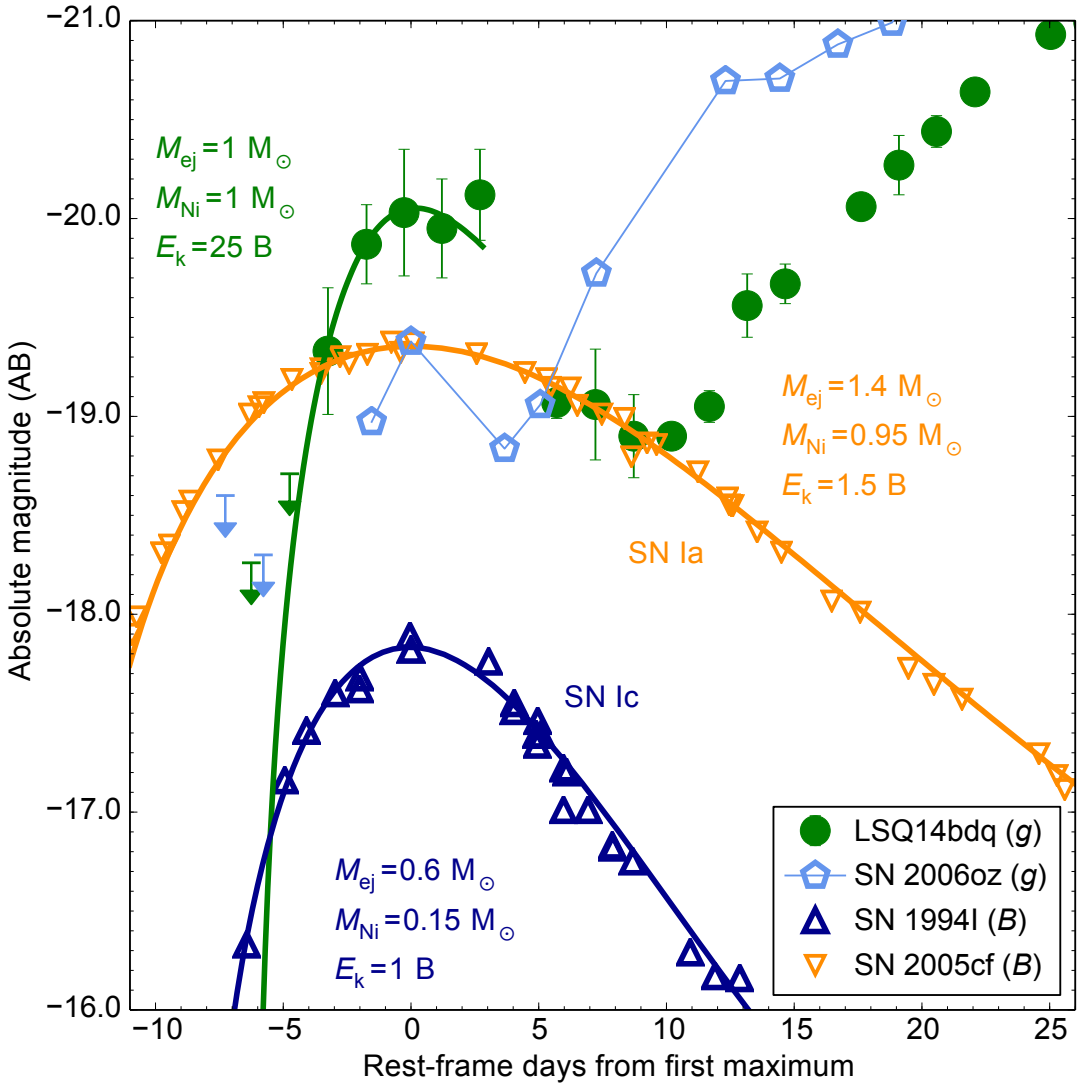

Figure 5.5: ^{56}Ni-powered model for the precursor peak. The early light curve of LSQ14bdq is similar to SN 1994I (Type Ic) but is much brighter, whereas it is much narrower than the Type Ia SN 2005cf. The combination of high luminosity and very short rise-time rules out a physically-plausible ^{56}Ni-powered SN for this peak. Energy is given in units of Bethe, where 1 B = 10^{51} erg.

2009). The light curve of LSQ14bdq is qualitatively similar to these objects, suggesting that the light curve could be explained by a shock cooling phase, followed by internal reheating (e.g. by a central engine). While bolometric luminosity in the cooling phase should decline monotonically, single-filter light curves show maxima as the peak of the SED moves into and out of the optical wavelength range. Unfortunately, we only have observations in rest-frame *g*-band, and so do not know how the bolometric light curve evolves during this phase.

We fit the early rise using analytic approximations from Rabinak & Waxman (2011), giving the parameters in Figure 5.6. We use their blue supergiant (radiative envelope),

red supergiant (convective envelope) and Wolf-Rayet models for SNe 1987A, 1993J and 2008D, respectively. The progenitor radius, $R_\star$, determines the slope and duration of the rise, while the luminosity scale is set by both $R_\star$ and by the explosion energy per unit mass, $E_\mathrm{k}/M_\mathrm{ej}$. The values of $R_\star$ and $E_\mathrm{k}/M_\mathrm{ej}$ used to fit the literature objects are in line with previous estimates. As noted by Rabinak & Waxman (2011), the model assumptions begin to break down after a few days. Formally, the equations do not hold once the photosphere has receded to a mass coordinate where the geometry can no longer be approximated as planar (Rabinak & Waxman 2011). Further uncertainty is introduced by the effects of recombination, as the authors use only an approximate treatment for the resultant changes in opacity. This becomes important when the envelope cools to $\sim 10000\,\mathrm{K}$, which occurs typically 2-5 days after explosion. We end the simulations at the cut-off time prescribed by equation 17 of Rabinak & Waxman (2011), taking their lower value for all envelope types. The model for SN 1993J is still rising slowly as it goes through the peak. The discrepancy with observations may be due to the very simple density profile assumed in the model. Detailed models of SN 1993J have had $\lesssim 0.1\mathrm{M}_\odot$ in the extended envelope, with most of the mass concentrated in the core.

To model LSQ14bdq, we set $E_\mathrm{k}/M_\mathrm{ej} = C$, where C is arbitrary and in units of $(10^{51}\,\mathrm{erg})/\mathrm{M}_\odot$. To try to break the degeneracy between E_k and M_ej, we assume that the diffusion time during the early peak is the same as in our central-engine fit to the main peak. We neglect late-time kinetic energy input from the magnetar, $\approx 10^{51}\,\mathrm{erg}$ for our model, because this is small compared to the initial energy found for the shock cooling, as will be seen below. We then have

$$\tau_m = \frac{1.05}{(13.7c)^{1/2}}\kappa^{1/2}\left(\frac{M_\mathrm{ej}^3}{E_\mathrm{k}}\right)^{1/4} = 90\,\mathrm{days}. \tag{5.1}$$

For $\kappa = 0.2\,\mathrm{cm^2\,g^{-1}}$, this leads to:

$$M_\mathrm{ej} = 40.1\,C^{1/2}\,\mathrm{M}_\odot; \tag{5.2}$$

$$E_\mathrm{k} = 40.1\,C^{3/2} \times 10^{51}\,\mathrm{erg}. \tag{5.3}$$

The uncertainty in τ_m in the magnetar fit (taking the range where $\chi^2 < 2\chi^2_\mathrm{min}$) is $\sim 30\%$, meaning M_ej and E_k are constrained to within a factor of 2.

Figure 5.6 shows models for 3 progenitors: a Wolf-Rayet star with $R_\star = 10\,\mathrm{R}_\odot$, and extended stars with $R_\star = 100$ and $500\,\mathrm{R}_\odot$ (extended models are insensitive to the choice of radiative/convective envelope). For the compact model, we derive $M_\mathrm{ej} \approx 270\,\mathrm{M}_\odot$; de-

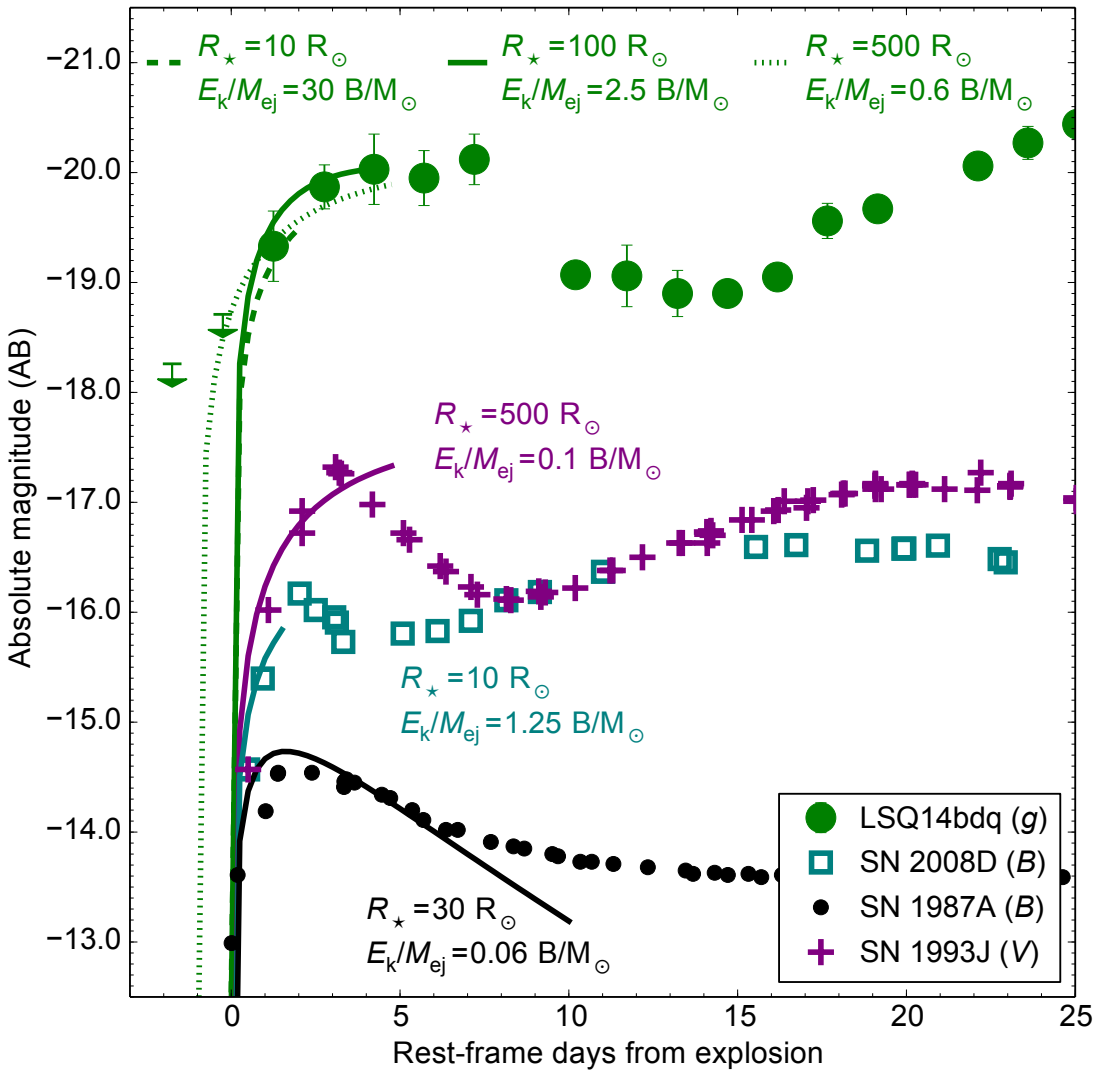

Figure 5.6: Post-shock cooling models for LSQ14bdq and other double-peaked SNe. We show both compact and extended models. Mass and energy can be inferred from the fits using equations 5.2 and 5.3. Energy is given in units of Bethe, where 1 B = 10^{51} erg. More extended progenitors can reproduce the peak brightness with lower M_{ej} and E_k.

pending on the precise mass, the implied progenitor should either explode as a PISN or collapse totally (hence invisibly) to a black hole (Heger & Woosley 2002), neither being consistent with the light curve. The inferred energy, $E_k > 10^{54}$ erg, is also unrealistic.

An extended envelope (or a wind acting as such; Ofek et al. 2010) is therefore a requirement to generate a shock cooling precursor with reasonable mass and energy. The 100 R$_\odot$ model requires $M_{ej} \approx 60\,M_\odot$ and $E_k \approx 1.5 \times 10^{53}$ erg. This energy is greater than the canonical neutron star gravitational binding energy of 10^{53} erg, of which only $\sim 1\%$ is normally accessible to power the explosion. The energy released in forming a black hole is higher than for neutron stars and could meet the requirement, if this energy could couple to the ejecta. A possible mechanism is via an accretion disk, such

as in the collapsar model of long GRBs (Woosley 1993). In this case the engine would be black hole accretion (Dexter & Kasen 2013) rather than a magnetar. This accretion engine has a characteristic power law, $L \propto t^{-n}$, similar to the magnetar, with $n_{\rm mag} = 2$ and $n_{\rm acc} = 5/3$. Therefore we would expect a similar τ_m, and that equations 5.2 and 5.3 would still hold.

The final model shown is for $R_\star = 500\,{\rm R}_\odot$. The inferred mass is $M_{\rm ej} \approx 30\,{\rm M}_\odot$, with $E_{\rm k} \approx 2 \times 10^{52}$ erg, which may also favour a black hole engine over a neutron star, and is similar to the kinetic energy in GRB-SNe. However, magnetars have also been proposed as GRB engines, and recent theory predicts that the final fate (neutron star or black hole) of massive stars is non-monotonic in mass (O'Connor & Ott 2011; Dessart et al. 2012c; Clausen et al. 2015). Therefore we do not exclude the magnetar model for the central engine. For this model, the velocity, $v \sim \sqrt{10E_{\rm k}/(3M_{\rm ej})} = 10000\,{\rm km\,s^{-1}}$, is in good agreement with the observed spectrum.

The radius used in our final model is very large for a hydrogen-free star, but similar to SN 1993J, which had only a very diffuse hydrogen envelope, and by maximum light had evolved to resemble a SN Ib. This could allow the extended envelope of LSQ14bdq to contain some hydrogen, provided the tenuous envelope is transparent by the time of our spectrum. However, modelling this non-trivial density profile is beyond the scope of the Rabinak & Waxman (2011) framework. Recently, Piro (2015) modelled our early light curve of LSQ14bdq with low-mass extended material, finding similar radius to our fit here (or even greater radius), but with only $\sim 0.5\,{\rm M}_\odot$ in the extended envelope.

5.4.3 CSM interaction

An alternative scenario to consider is that the main peak arises from CSM interaction on scales of $\sim 10^4\,{\rm R}_\odot$, as has been suggested for other SLSNe (e.g. Chatzopoulos et al. 2013, and see previous chapters here). CSM fits for the main peak (Figure 5.2) require $E_{\rm k}/M_{\rm ej} \sim 0.2$, lower than any of the shock cooling models shown in Figure 4. This is fairly inflexible for the CSM model, as $E_{\rm k}$ and $M_{\rm ej}$ are the two strongest drivers of the peak luminosity (see Section 2.4.3) – e.g. models with $E_{\rm k}/M_{\rm ej} \sim 0.4$ are too bright by about 0.5 dex (and rise too quickly). To reproduce the early emission with shock cooling and $E_{\rm k}/M_{\rm ej} \sim 0.2$, the Rabinak & Waxman (2011) models would need initial radius $R_\star \sim 2000\,{\rm R}_\odot$. This is uncomfortably large for any reasonable progenitor. However models have been proposed in which the cooling phase arises from shock breakout in an inner region of dense CSM rather than the progenitor envelope (Ofek et al. 2010); this may be a viable explanation for LSQ14bdq. However, if shock breakout occurs in the CSM, we would require a novel CSM structure to get two distinct peaks purely from interaction (i.e. without falling back on an engine to power the second peak).

A model for SN 2006oz was put forward by Moriya & Maeda (2012), in which a single CSM interaction produces a double-peaked light curve due to a sudden increase in CSM ionisation (and hence opacity) in the collision. However, this model does not specify the source of the early emission before the collision, which for LSQ14bdq we have shown rises too steeply to be explained as a conventional SN. Multi-peaked light curves from interaction could also arise within the pulsational pair-instability model (Woosley et al. 2007). Here, multiple shells are ejected with $v \sim 3000\text{-}5000\,\mathrm{km\,s^{-1}}$, and could produce distinct interaction events with a range of luminosities and timescales. Suppose SN ejecta collide with an inner shell at the beginning of our observations, and the resulting merged ejecta/shell then hit an outer shell fifteen days later, generating the second peak. For a shell separation $R_{\mathrm{CSM}} \sim 10^{15}\,\mathrm{cm}$ (from our CSM fit and the Woosley et al. 2007 models), this would require a velocity for the ejecta and swept-up inner shell of $v_{\mathrm{ej+inner}} \sim 10^{4}\,\mathrm{km\,s^{-1}}$, which is similar to the observed line widths. This may provide a reasonable alternative to the shock cooling scenario, although the massive outer shell must also be accelerated to avoid showing narrow spectral lines (the epoch where we obtained our spectrum, which was during the second peak, would be after the second collision with the outermost shell). We also note that the Woosley et al. (2007) models are much redder than our observations. However, the parameter space of pulsation PISN models is likely very large, and has not yet been explored systematically. Hence further detailed modelling is needed to assess the viability of this scenario for LSQ14bdq.

5.5 Discussion and conclusions

The detection of a double-peaked light curve provides a new opportunity to constrain the physics powering SLSNe Ic. We find that the early peak is not likely to be a normal ^{56}Ni-powered SN. We also disfavour the CSM interaction model, since a consistent physical scenario seems to require a helium star with an extremely large radius $R_{\star} > 2000\,\mathrm{R_{\odot}}$, within a more extended (and hydrogen poor) CSM of $R_{\mathrm{CSM}} \gtrsim 10^{4}\,\mathrm{R_{\odot}}$. Pulsational pair-instability models remain a possibility, but do not yet quantitatively reproduce the observed data.

We propose that the initial peak could arise from post-shock cooling, and provide a simple physical interpretation consistent with the main light curve. The first peak is itself remarkably bright ($M_g = -20.0$), suggesting a large stellar radius or high explosion energy, or both. The broad width of the second peak implies a large ejected mass, and can be powered by a central engine. We find good fits for an explosion with $E_{\mathrm{k}} \sim 10^{52}\,\mathrm{erg}$, in a star with $R_{\star} \sim 500\,\mathrm{R_{\odot}}$, that ejected a mass of $\sim 30\,\mathrm{M_{\odot}}$. This en-

ergy and mass scale may favour a black hole accretion engine (Dexter & Kasen 2013), though the magnetar remains a viable alternative. The energy is similar to kinetic energies measured in long GRBs.

The extended radius is surprising, and argues against a compact progenitor ($R \ll 100\,R_{\odot}$) at the time of explosion, since it would imply unrealistic ejecta mass and explosion energy. Although such extended helium stars are not known in the local Universe, the fact that SLSNe may be confined to very low metallicity galaxies and are intrinsically rare ($\sim$ 1 in 10,000 massive star deaths) may explain the lack of known counterparts. It has recently been shown that energy leakage from the core could generate waves that heat the envelope and cause expansion (Shiode & Quataert 2014; Mcley & Soker 2014). This could occur shortly before explosion, during the later stages of nuclear burning in the core, or be powered by some other source of energy such as a binary merger (N. Soker, private communication). The merger scenario could help to provide the large angular momentum required by the central engine models. Theoretical stellar evolution models with binarity and rotation should be explored in detail for a viable progenitor.

Further, early observations of SLSNe will determine whether or not double-peaked light curves are common. Figure 5.7 shows several SLSNe from the literature with well-observed rise times and hints of an early luminosity excess (compared to simple polynomial fits). The objects are PTF09cnd (Quimby et al. 2011), PS1-10ahf, PS1-10pm (McCrum et al. 2015), iPTF13ajg (Vreeswijk et al. 2014) and SNLS 06D4eu (Howell et al. 2013), in addition to SN 2006oz (Leloudas et al. 2012) and LSQ14bdq. If we scale the light curve of LSQ14bdq to match the light curves of the other objects, the intrinsic shape looks very similar, and the early data are consistent with a double-peaked structure. The scaling is done via a simple stretch and shift in both time and magnitude. PS1-10pm shows particularly strong evidence for a double-peak. The success of matching both peaks of the fast-evolving objects with the LSQ14bdq light curve and a single stretch in time suggests that the widths of the two distinct peaks may obey a proportionality relationship. However, with only two well-sampled comparisons (SN 2006oz and PS1-10pm), it is too early to say for sure. An important future step will be to constrain the rates of double-peaked SLSNe by compiling objects with possible precursors, and making an estimate of the detection efficiency in current surveys. If it turns out that most or all SLSNe exhibit similar precursor peaks, this should place important constraints on the progenitors and explosion mechanisms.

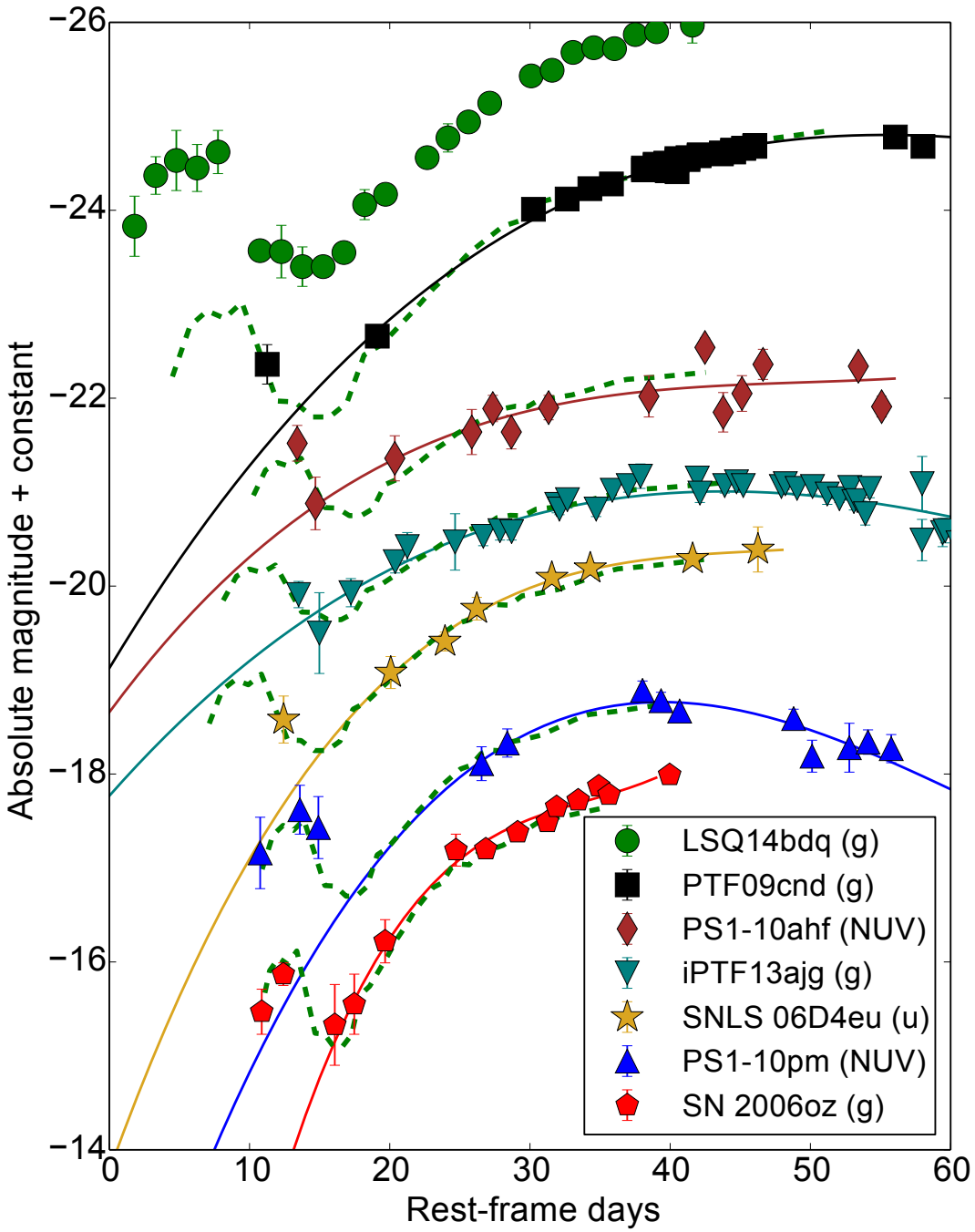

Figure 5.7: Other SLSNe with indications of a precursor. In the literature, only SN 2006oz has been claimed to exhibit a double-peaked light curve. However, the rising light curves of several other published SLSNe show an initial excess compared to third-order polynomial fits (solid lines). Scaling the light curve of LSQ14bdq to match the rise times of the other objects (dashed green lines) indicates that such excesses could be under-sampled detections of an early peak similar to that observed in LSQ14bdq.

Chapter 6

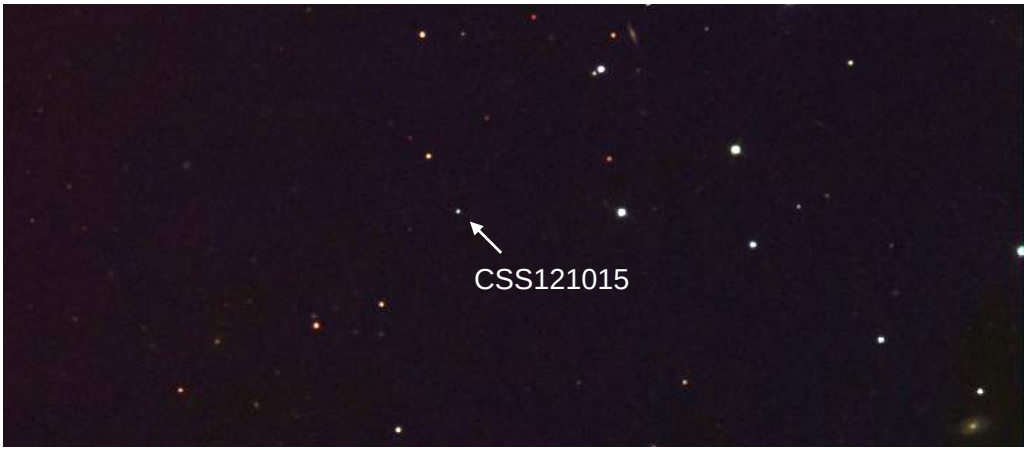

Studying SLSNe as a class

"They were watching, out there past men's knowing,
where stars are drowning
and whales ferry their vast souls
through the black and seamless sea"
- Cormac McCarthy (Blood Meridian)

6.1 Introduction

As SLSNe are extremely rare, and were largely unknown before the discoveries of SN 2005ap (Quimby et al. 2007) and SCP06F6 (Barbary et al. 2009), the paucity of observed events has so far restricted the analysis of their properties as a group. This situation is now beginning to change, as transient surveys are becoming better at picking out these objects and dedicating resources to follow them up. The first studies of SLSN samples were recently conducted by Inserra et al. (2013) and Inserra & Smartt (2014), who showed that their properties could be explained by magnetar-powered models, and their potential utility as standardisable candles for cosmology, respectively.

Many outstanding questions can only be answered by investigating their properties as a class (e.g. Gal-Yam 2012). The overall diversity, and hence the parameter space, of SLSNe is constrained only weakly by existing studies. Do SLSNe Ic all follow a similar evolution, or are there fundamental differences between the events with the broadest and narrowest light curves (see Chapter 4)? Is there a continuum of events between fast and slow decliners? What about the minority group of SLSNe II that do not show narrow lines from CSM, and their possible resemblance to SLSNe Ic (Benetti et al. 2014)? As all of the theoretical scenarios so-far invoked to power SLSNe likely require stars more massive than typical SN progenitors, SLSNe should have systematically higher ejected mass than normal-luminosity stripped-envelope SNe, but is this borne out by observations? Examining many objects simultaneously and looking for correlations in the data may help to break the degeneracies encountered when modelling the light curves of SLSNe.

In this chapter, we construct the largest sample of SLSNe to date: a total of 24 objects, composed of 7 from PESSTO (Benetti et al. 2014; Nicholl et al. 2014, 2015, Inserra et al. in prep., Chen et al. in prep.), and 17 from the literature. In Section 6.2, we describe the SLSNe in our sample, including the new PESSTO objects. The construction of our bolometric light curves is outlined in Section 6.3. We investigate the light curve timescales in Section 6.4, leading to an analysis of generalised light curve shapes in Section 6.5, and a search for evidence of a bimodal SLSN Ic population (i.e. with rapid and slow decline rates after maximum luminosity) in Section 6.6. The typical spectral evolution is investigated in Section 6.7. Velocity measurements from spectra are described in Section 6.8, and these are used to estimate SLSN masses in Section 6.9. Throughout, we compare to a sample of well-observed normal-luminosity SNe from stripped progenitors (Types Ib and Ic, collectively known as SNe Ibc). We summarise our main results in Section 6.10.

Table 6.1: SLSNe in the sample

Name	Type	z	M_{griz}*	Reference
'Gold' sample: rest-frame *gri*(*z*) coverage				
SN2007bi	Ic†	0.127	-20.20	Gal-Yam et al. (2009)
SN2008es	II	0.205	-21.43	Gezari et al. (2009); Miller et al. (2009)
SN2010gx	Ic	0.230	-20.64	Pastorello et al. (2010); Quimby et al. (2011)
SN2011ke	Ic	0.143	-20.69	Inserra et al. (2013)
SN2011kf	Ic	0.245	-20.80	Inserra et al. (2013)
SN2012il	Ic	0.175	-20.73	Inserra et al. (2013)
SN2013dg	Ic	0.265	-20.30	Nicholl et al. (2014)
SN2013hx	II	0.130	-20.84	Inserra et al. (in prep)
LSQ12dlf	Ic	0.255	-20.68	Nicholl et al. (2014)
LSQ14mo	Ic	0.253	-19.95	Chen et al. (in prep)
LSQ14bdq	Ic†	0.347	-21.68	Nicholl et al. (2015)
PTF10hgi	Ic	0.100	-19.61	Inserra et al. (2013)
PTF11rks	Ic	0.190	-20.01	Inserra et al. (2013)
PTF12dam	Ic†	0.107	-20.56	Nicholl et al. (2013)
CSS121015	II	0.287	-22.00	Benetti et al. (2014)
SSS120810	Ic	0.156	-20.45	Nicholl et al. (2014)
PS1-11ap	Ic†	0.524	-21.22	McCrum et al. (2014)
'Silver' sample: rest-frame *g*-band with bolometric correction				
SN2005ap	Ic	0.283	-21.56	Quimby et al. (2007)
SCP06F6	Ic	1.189	-21.34	Barbary et al. (2009)
PTF09cnd	Ic	0.258	-21.15	Quimby et al. (2011)
PTF09cwl	Ic	0.349	-21.24	Quimby et al. (2011)
PS1-10ky	Ic	0.956	-20.54	Chomiuk et al. (2011)
PS1-10bzj	Ic	0.650	-20.32	Lunnan et al. (2013)
iPTF13ajg	Ic	0.740	-21.50	Vreeswijk et al. (2014)

*Pseudobolometric magnitude at maximum light
†Described in the literature as a slowly-declining event

6.2 The sample

In this work we focus on the Type Ic SLSNe, but we also include three Type II events. While SLSNe Type IIn, such as SN 2006gy (Ofek et al. 2007; Smith et al. 2007), show prominent multicomponent Balmer lines indicating circumstellar interaction, the three objects used in our sample showed only weak and/or broad hydrogen lines. As the power source for these objects is ambiguous, they may be related to SLSNe Ic. A full summary of the sample is given in Table 6.1. A comparison sample of normal-luminosity stripped-envelope SNe, of types Ib, Ic and broad-lined Ic (SN Ic-BL) is listed in Table 6.2. Although the spectra of SNe Ib display helium lines that are not seen in SLSNe Ic, we include some such objects here because their light curve properties and physics are similar to SNe Ic, and there is likely a continuum of helium envelope

mass between the two classes. The sample contains a compilation of SNe Ibc from the literature that have good photometric data in *griz*, as well as the homogeneous SDSS II sample of Taddia et al. (2015).

6.2.1 Published PESSTO objects

The first batch of SLSNe Ic classified by PESSTO were presented and analysed in Chapter 3. These were LSQ12dlf, SSS120810 and SN 2013dg. Each object exhibited spectral evolution typical of the class, despite their light curves being quite diverse. We also include LSQ14bdq. This exhibited a broad light curve, as well as a bright precursor peak, which was studied in detail in Chapter 5. As none of the other objects in the sample show a clear precursor, we do not discuss this early phase any further in the current chapter. The data for all of these objects have been published by Nicholl et al. (2014, 2015).

Another PESSTO SLSN, CSS121015, was studied by Benetti et al. (2014). This object was an extremely luminous SLSN II, but bore resemblance to SLSNe Ic in both the spectrum and overall light curve shape. Fitting with magnetar- and CSM-powered models (see Section 2.4.4) showed that for a given power source, the CSS121015 models occupied a similar region of parameter space to the SLSNe Ic (see Chapter 2). Including CSS121015 in our sample may help to clarify the existence of a link between normal SLSNe Ic, and some SLSNe II.

6.2.2 LSQ14mo

LSQ14mo was discovered rising steadily in LSQ observations taken from 2014 Jan 12.2 UT. The transient is located at RA=10:22:41.53, Dec=-16:55:14.4 (J2000.0). A spectrum taken by PESSTO on 2014 Jan 31.2 UT was dominated by a blue continuum and O II absorption at around 4000 Å, revealing it to be a SLSN Ic at a phase of $\sim$ 1 week before peak luminosity. The spectrum was an excellent match to PTF09cnd (Quimby et al. 2011) at a redshift $z \sim 0.25$. A precise redshift of $z = 0.253$ was subsequently determined from narrow Mg II $\lambda\lambda$ 2795,2802 absorption (Leloudas et al. 2014). PESSTO has collected extensive data on this target, which will be presented in full in a future publication (Chen et al., 2015, in prep.).

6.2.3 SN 2013hx

A hostless transient was first detected by SkyMapper on 2013 Dec 27 UT at coordinates RA=01:35:32.83, Dec=-57:57:50.6. It was given the survey designation

Table 6.2: Comparison sample

Name	Type	M_{griz}	Reference
Well-observed SNe in the literature			
SN1994I	Ic	−16.79	Filippenko et al. (1995); Richmond et al. (1996)
SN1998bw	IcBL‡	−16.84	Patat et al. (2001)
SN1999ex	Ic	−16.84	Stritzinger et al. (2002)
SN2002ap	IcBL	−16.49	Mazzali et al. (2002); Gal-Yam et al. (2002)
SN2003jd	IcBL	−18.19	Valenti et al. (2008a)
SN2004aw	Ic	−17.24	Taubenberger et al. (2006)
SN2007gr	Ic	−16.36	Valenti et al. (2008b)
SN2008D	Ib	−16.24	Soderberg et al. (2008); Modjaz et al. (2009)
SN2009jf	Ic	−17.34	Valenti et al. (2011)
SN2010bh	IcBL‡	−16.97	Cano et al. (2011)
SN2011bm	Ic	−17.63	Valenti et al. (2012)
SN2012bz	IcBL‡	−18.82	Schulze et al. (2014)
SDSS II sample from Taddia et al. (2015)			
SN2005hl	Ib	−17.55	
SN2005hm	Ib	−15.85	
SN2006fe	Ic	−17.04	
SN2006fo	Ib	−17.26	
14475	IcBL	−19.46	
SN2006jo	Ib	−18.25	
SN2006lc	Ib	−17.31	
SN2006nx	IcBL	−19.71	
SN2007ms	Ic	−16.95	
SN2007nc	Ic	−16.82	

‡ Associated with observed GRB

SKYJ1353283-5757506. PESSTO observed the object on 2014 Feb 20 UT after it had risen in luminosity for ≳30 days. The spectrum showed Hα emission at $z = 0.13$, at which redshift the absolute magnitude was ~ -22, as well as broad features in the blue. It showed similarity to both SN 2010gx (a prototypical SLSN Ic; Pastorello et al. 2010) and CSS121015 (SLSN II; Benetti et al. 2014). The SN has been followed up by PESSTO and given the IAU name, SN 2013hx. A separate follow-up paper will present the full dataset (Inserra et al., in prep.)

6.2.4 SLSNe from the literature

The amount of data available for objects in the literature is highly variable. In some cases, they have only been observed in one or two filters; in others, they are at high

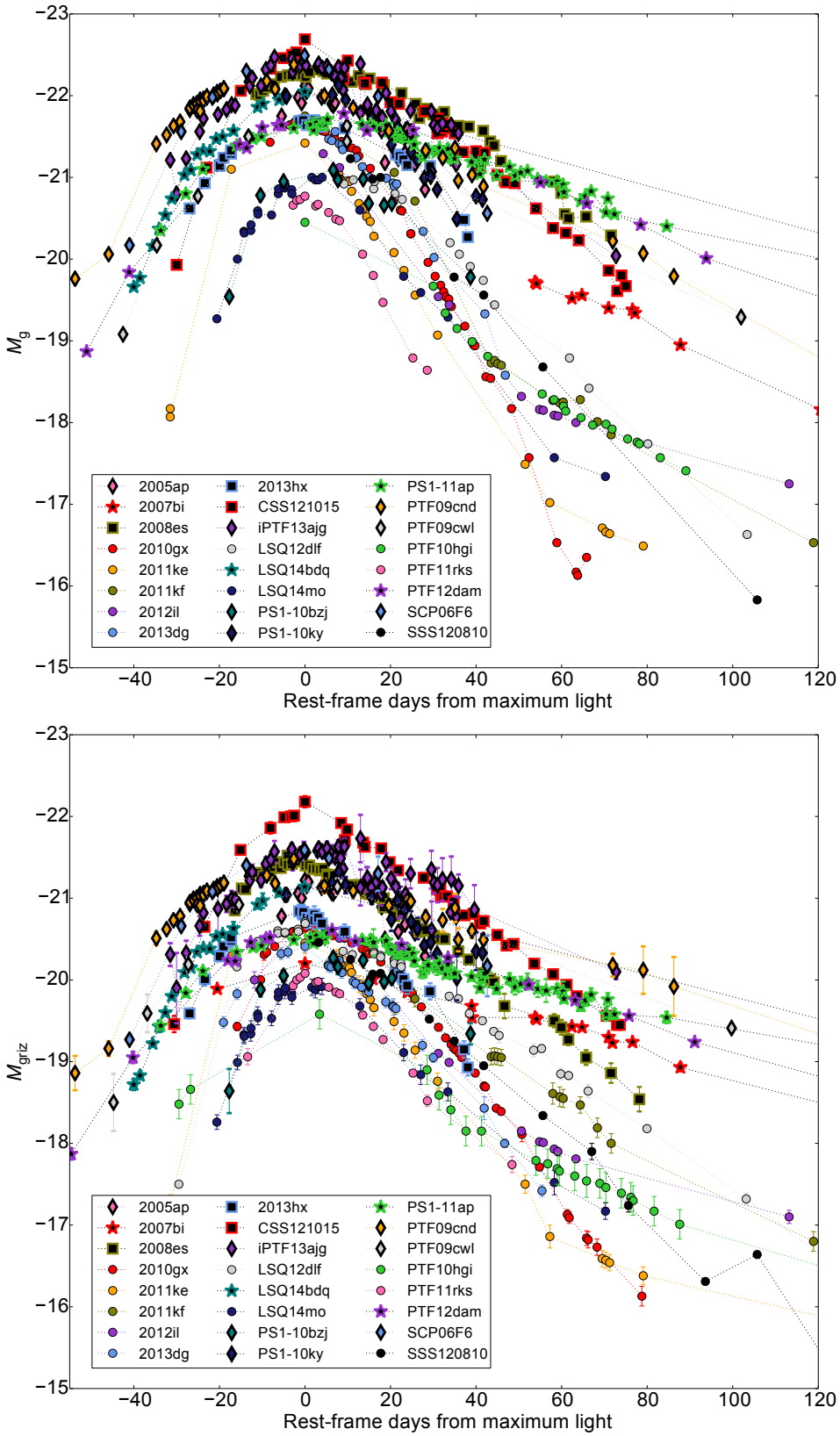

Figure 6.1: Complete set of rest-frame *g*-band (*top*) and *griz* pseudobolometric (*bottom*) light curves, after extinction and *K*-corrections.

redshift and the observed optical light corresponds to ultraviolet (UV) emission in the SN rest-frame. High-redshift SNe also tend to have sparse spectral data, as they are fainter for observers.

The objects in our sample have therefore been divided into two bins ('Gold' and 'Silver' samples), depending on whether they have good coverage at rest-frame optical wavelengths. This can be seen in Table 6.1. The mean redshift for Gold objects is $\langle z \rangle = 0.22$. All but two of the SLSNe at $z < 0.3$ have extensive photometry in observer-frame g, r, i and in most cases z filters, which at this redshift covers the rest-frame optical regime. This includes all of the PESSTO objects, the 5 low-z SLSNe Ic from Inserra et al. (2013), the prototypical SN 2010gx (Pastorello et al. 2010), 3 slowly declining SLSNe Ic (classified as SN2007bi-like; Gal-Yam et al. 2009; Nicholl et al. 2013; McCrum et al. 2014) and one further Type II event (SN2008es Gezari et al. 2009). PS1-11ap, at $z = 0.524$, falls in this group because of photometry in the NIR Pan-STARRS1 y filter, which corresponds to rest-frame i-band at this redshift (McCrum et al. 2014).

In the Silver sample (with a mean of $\langle z \rangle = 0.63$), we have two more objects from the Pan-STARRS1 Medium Deep Survey – PS1-10ky at $z \sim 0.9$ (Chomiuk et al. 2011) and PS1-10bzj at $z \sim 0.6$ (Lunnan et al. 2013) – while most of the others featured in the original Quimby et al. (2011) sample that defined the SLSN Ic class. Although several of these objects are at redshifts $0.25 < z < 0.3$, the reddest available photometry is in the R-band, which corresponds to rest-frame B/g. SCP06F6 ($z = 1.189$) has *HST* i and z photometry (Barbary et al. 2009), which corresponds to rest-frame emission between the u- and g-bands. The final Silver object is iPTF13ajg (Vreeswijk et al. 2014), which has excellent photometric and spectroscopic coverage, but at $z = 0.74$ this mostly probes rest-frame UV. This means that for these objects we must rely on an estimated correction to obtain bolometric light curves.

6.3 Bolometric light curves

To analyse the light curves of our SLSNe in the most homogeneous way possible, we constructed two sets of light curves: rest-frame g-band magnitudes, M_g, and pseudobolometric light curves covering rest-frame SDSS $griz$ filters. The first step was to apply K-corrections to the observed magnitudes, to transform them to the rest-frames of our objects. The K-correction procedure was described in Section 2.3.3. These corrections were then linearly interpolated to the epochs with photometry. For most cases we simply corrected $g_{\rm obs} \rightarrow g_{\rm RF}$ etc., except for the following: LSQ14bdq ($r_{\rm obs} \rightarrow g_{\rm RF}$); SN 2005ap, PTF09cnd, PTF09cwl ($R_{\rm obs} \rightarrow g_{\rm RF}$); PS1-11ap ($i_{\rm obs} \rightarrow g_{\rm RF}$; K-corrections taken from McCrum et al. 2014); PS1-10bzj, iPTF13ajg ($i_{\rm obs} \rightarrow g_{\rm RF}$); PS1-10ky ($z_{\rm obs} \rightarrow g_{\rm RF}$); SCP06F6 ($i_{\rm obs}, z_{\rm obs} \rightarrow g_{\rm RF}$). For the objects of Quimby et al.

(2011), sometimes only one spectrum was available. In this case we also used the spectra of SN 2010gx from Pastorello et al. (2010) (a spectroscopically typical event, with good temporal coverage), after artificially placing them at the desired redshift. Magnitudes were also corrected for Milky Way extinction according to the dust maps of Schlafly & Finkbeiner (2011), though host reddening was assumed to be negligible.

For the Gold sample, the bolometric light curve was then calculated using the rest-frame photometry from the g to z filters. For LSQ14mo, the z-band was estimated using the colours of SN 2013dg, to which it has a very similar light curve in the *gri*-bands, while the z-band magnitudes for PS1-11ap and LSQ14bdq were taken from PTF12dam, as in McCrum et al. (2014). Most objects have good coverage before peak in one filter only. In these cases, the colours were assumed to be constant, with values from the first epoch that had multi-colour photometry available. This is a reasonable assumption, as the colours show little evolution until 1-2 weeks after maximum light (Inserra et al. 2013). The SED was constructed by converting magnitudes into fluxes at the effective wavelength of each filter. For all objects, the flux was set to zero bluewards of the g-band and redwards of z. The luminosity, L_{griz}, was then calculated by integrating this SED over wavelength. We express this in terms of pseudobolometric magnitude, using:

$$M_{griz} \equiv -2.5 \log_{10}\left(\frac{L_{griz}}{3.055 \times 10^{35}\,\mathrm{erg\,s^{-1}}}\right), \tag{6.1}$$

based on the standard definition of bolometric luminosity. Our complete set of g-band and pseudobolometric light curves are shown in Figure 6.1.

However, a different process was needed to derive the M_{griz} light curves of the Silver objects. We found the average bolometric correction, $M_{griz}-M_g$, as a function of time (we define $t = 0$ as the epoch of maximum luminosity) for the Gold sample, and applied this correction to the Silver sample. This correction is shown in Figure 6.2. Unfortunately, there is significant scatter, but it is clear that the bolometric correction becomes more negative as a function of time. This is expected; as the SNe cool, bluer wavelengths fade faster at late times. We fit only points where $t > 0$, assuming a constant correction before this. Our best fit is $M_{griz}-M_g = 0.90 - 0.012t$ for $t > 0$ and $M_{griz}-M_g = 0.90$ for $t < 0$. The uncertainty in this correction is ~ 0.5 magnitudes by 50 days after peak, hence at late phases the M_{griz} light curves of Silver objects may become unreliable. However, note that only two Silver objects have data at this phase: PTF09cnd and PTF09cwl. Both of these objects closely resemble PTF12dam in rest-frame g (but were not classified as being 2007bi-like), and this resemblance is preserved in the pseudobolometric light curves. Hence we feel justified including these objects in our sample.

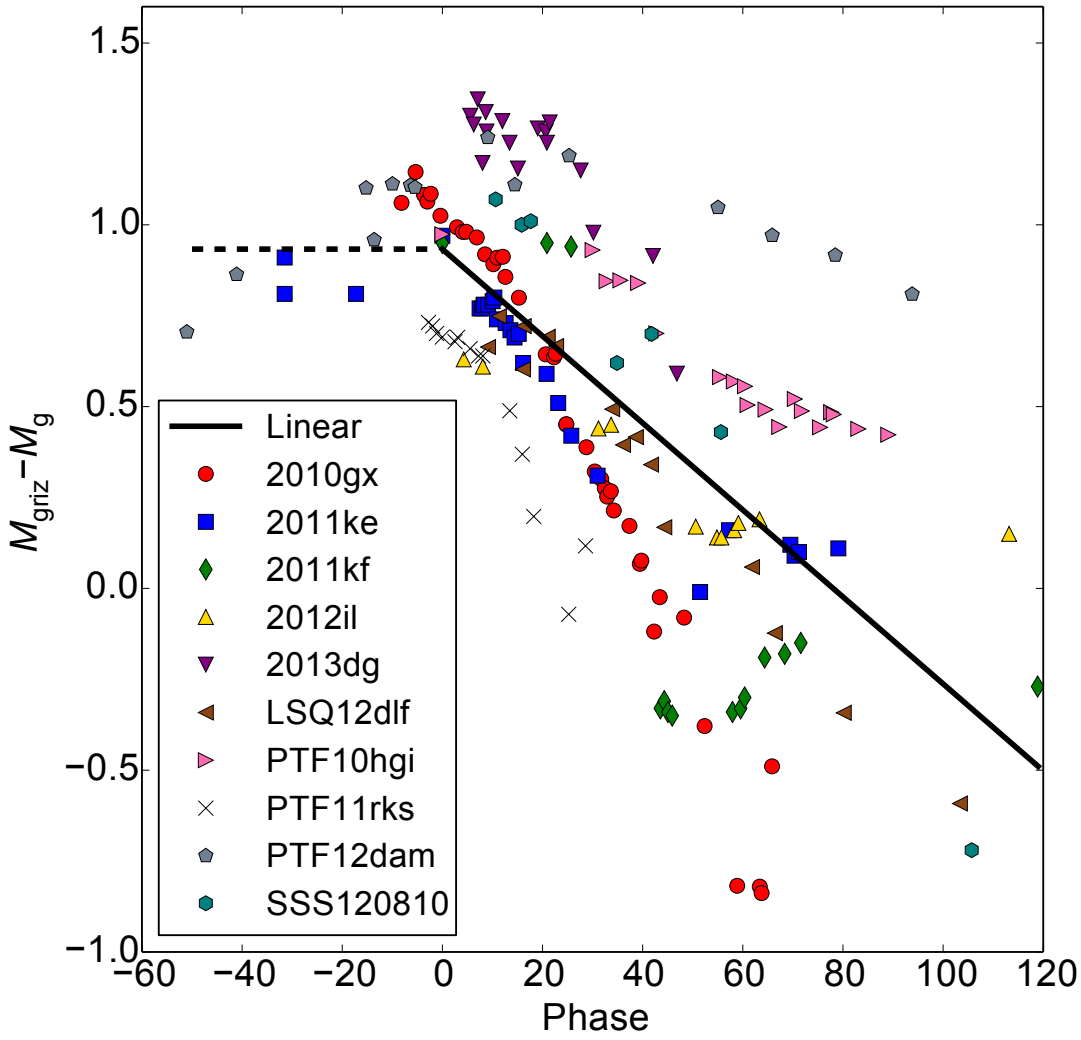

Figure 6.2: Estimating the time-dependent bolometric correction for a typical SLSN. Our best fit is $M_{griz}-M_g = 0.90 - 0.012t$ for $t > 0$, though the gradient can vary from this by a factor ~ 2 for individual objects. Uncertainty in the y-intercept term has no effect on our analysis of the light curve timescales.

6.4 Light curve timescales

6.4.1 Measurements

Having constructed our pseudobolometric light curves, we proceeded to measure the rates at which these SNe brightened to their maximum luminosity, and subsequently declined. We define:

- $\tau_{\rm rise}$ (the rise timescale): the time ($t < 0$) relative to maximum light ($L_{\rm max}$) at which $L_{griz} = L_{\rm max}/e$

- $\tau_{\rm dec}$ (the decline timescale): the time ($t > 0$) relative to maximum light ($L_{\rm max}$) at which $L_{griz} = L_{\rm max}/e$.

We made our measurements by fitting the light curves with low-order polynomials. Order four polynomials were found to give a good fit to all of our light curves for epochs $t \lesssim 50$ d. The fits were used to make a new estimate of the date when the pseudobolometric luminosity peaks. This tends to be later than the peak in g-band, as one would expect since the ejecta cool over time. We defined the new peak, and then measured the quantities described above by interpolating the light curves with the polynomial fits. The method is demonstrated in Figure 6.3. In some cases, the rise time had to be estimated by extrapolation using our polynomials. We consider this to be reliable for most objects, where we extrapolate only by a few days, but the rise time is poorly constrained for SNe 2007bi, 2005ap, and PS1-10ky. For slowly declining objects, the fourth-order fit to the peak was not always reliable at late epochs. For these objects, we made one fit to $t \lesssim 50$ d to estimate the peak and the rise time, as for the rest of our sample, and then measured the decline time by fitting another polynomial to only the post-maximum data points (fourth-order and linear fits gave similar results). Our measurements are given in Table 6.3. The rise time of SSS120810 could not be constrained from the available data.

6.4.2 Correlation

We plot the rise times vs decline times for our sample in Figure 6.4. The best-fit lines were calculated separately for our Gold and complete samples as follows: we represented each data point by a two-dimensional Gaussian, with a mean given by our measured values of $\tau_{\rm rise}$ and $\tau_{\rm dec}$, and standard deviations by the error bars. A Monte-Carlo method was then employed. A point was drawn at random from each probability distribution defined by these Gaussians, and we used standard PYTHON routines to calculate a straight-line fit, as well as Spearman and Pearson correlation coefficients, for the resulting rise-decline relation. This was repeated 10000 times. As can be seen in Figure 6.5, the data are clearly correlated with high significance: Spearman's rank correlation coefficient is 0.77 ± 0.10 for the entire SLSN sample (0.75 ± 0.11 for the Gold sample only). Pearson's test gives 0.81 ± 0.15 (0.84 ± 0.14). The best-fit straight line to the data is $\tau_{\rm dec} = (1.65 \pm 0.33)\,\tau_{\rm rise} + (7.38 \pm 7.79)$ for the full sample, and $\tau_{\rm dec} = (1.96 \pm 0.46)\,\tau_{\rm rise} + (-0.10 \pm 10.19)$ for the Gold objects. Although the formal best fit is different for the full sample compared to the Gold SLSNe only, the entire population is clearly consistent with a straight line, and the two fits agree within the

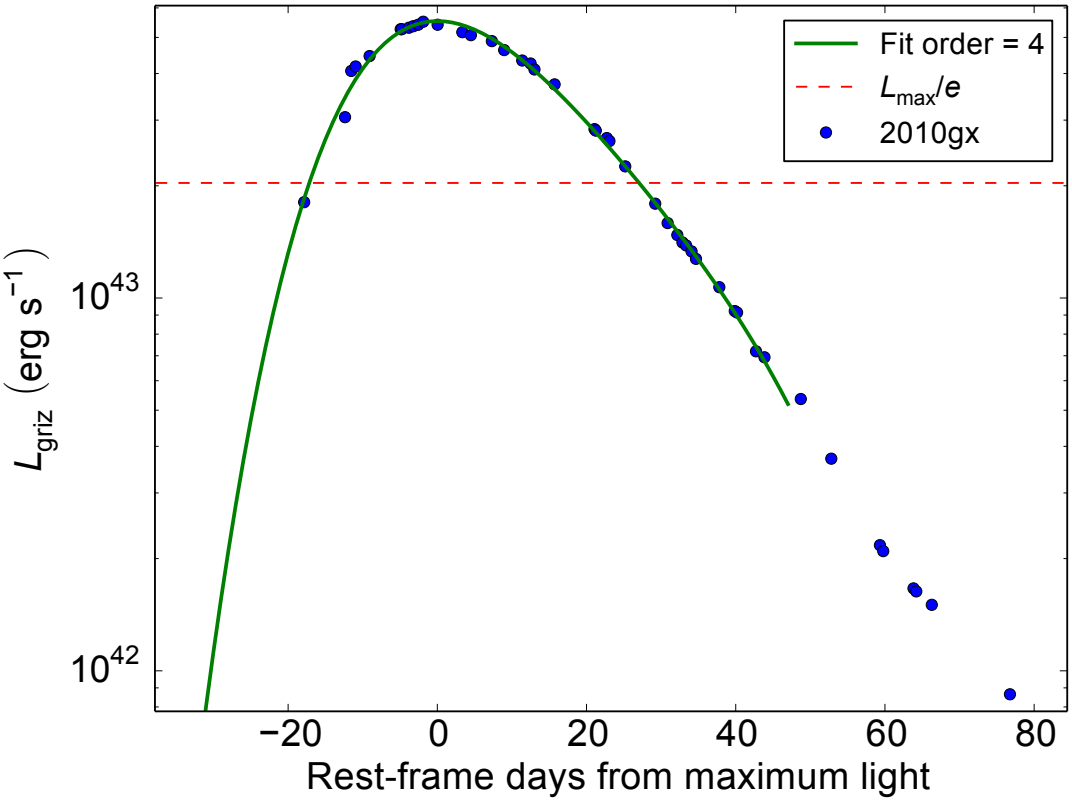

Figure 6.3: Interpolating the light curve of SN 2010gx. The times at which the dashed line intersects the polynomial fit give the exponential rise and decline times.

errors. It is no surprise that the gradient is greater than unity, as the light curves of other SN types (both Type Ia and core-collapse) rise to maximum more quickly than they decline. We also measured rise and decline timescales for the SNe Ibc in Table 6.2. They obey a similar correlation as for SLSNe, but with shorter timescales compared to their more luminous cousins.

6.4.3 Models: overview

To interpret our correlation, we compare it to the predictions of our synthetic light curve code. The models were fully described in Section 2.4, but we recap some of the essential points here. For a fixed form of the power input (e.g. an exponentially-declining heat injection from radioactive decay, or a central engine with a power-law decline), our model takes three parameters: a diffusion timescale, a power input timescale (which we call $\tau_{\rm in}$), and an overall energy scale (which affects the luminosity of the light curve, but not the shape; see Equation 2.4). The diffusion time scales as $\tau_m \propto (\kappa M_{\rm ej}/v)^{1/2}$, where κ is the opacity, $M_{\rm ej}$ is the ejected mass, and v is a scaling velocity for homologous expansion (Arnett 1980, 1982). For a given opacity and velocity, the diffusion

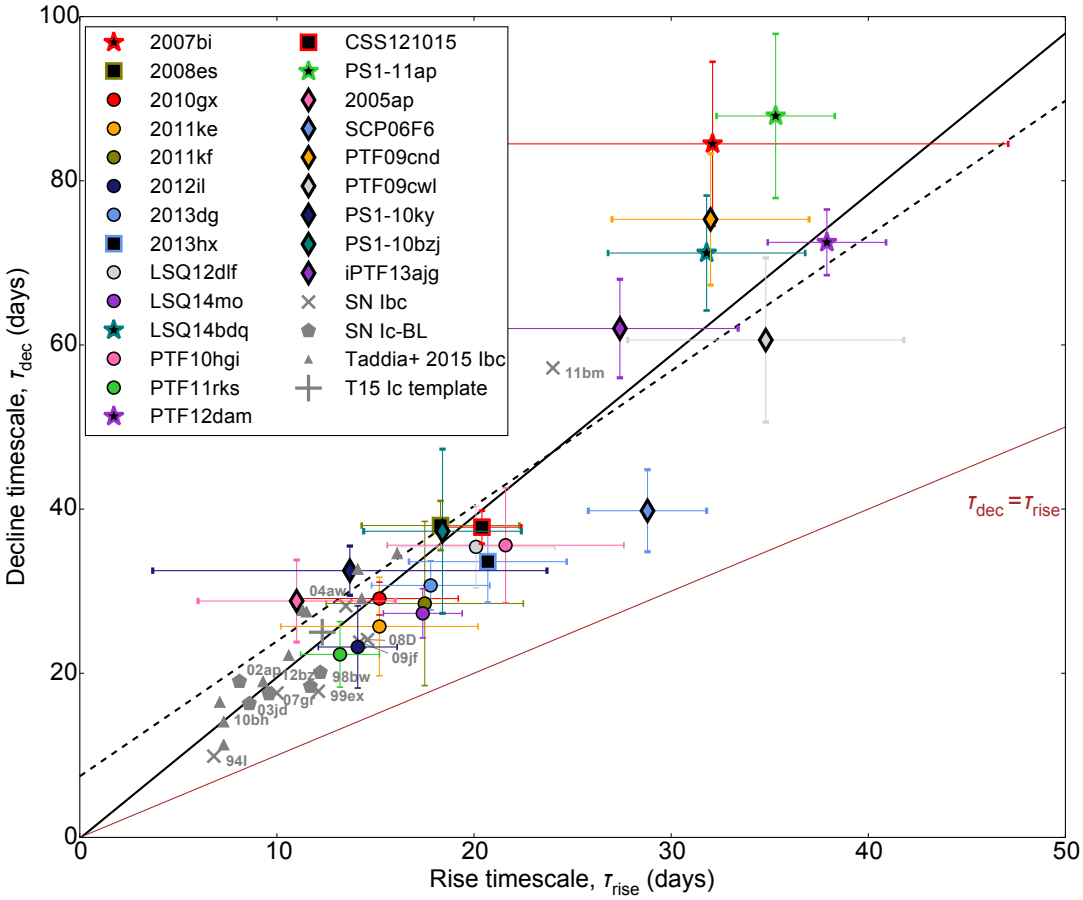

Figure 6.4: Rise vs decline timescales for SLSNe and normal stripped-envelope SNe. The rise and decline times are clearly correlated, and in a similar way for both samples. The dashed black line gives the best linear fit to the entire SLSN sample ($y = 1.65x + 7.38$), and the solid black line to the Gold sample only ($y = 1.96x - 0.10$). The T15 SN Ic light curve was constructed by integrating the *griz* templates for SDSS SNe Ibc from Taddia et al. (2015).

timescale thus allows us to derive the mass. Other authors have taken the observed rise times of SNe as an estimate of τ_m (most recently Wheeler et al. 2015). This is a reasonable approximation for ^{56}Ni-powered light curves, where the decay time is well known, and is closely matched to the typical diffusion times (a coincidence that results in the high peak luminosities in Type Ia SNe). It is not surprising that the normal-luminosity hydrogen-poor sample shown in Figure 6.4 obeys a tight rise-decline correlation. The power input timescale is the same for all these ^{56}Ni-powered SNe, and hence the diversity in both rise and decline times is driven by only one parameter: the diffusion time. The fact that the SLSNe obey such a similar correlation suggests that the diffusion time may also drive the correlation in these objects.

However, for SLSNe the power input time, $\tau_{\rm in}$, is unknown, and may span a wide range of values. If $\tau_{\rm in}$ is very different from τ_m, it can have a large influence on the observed rise time, which is no longer a reliable proxy to τ_m. A better method here is

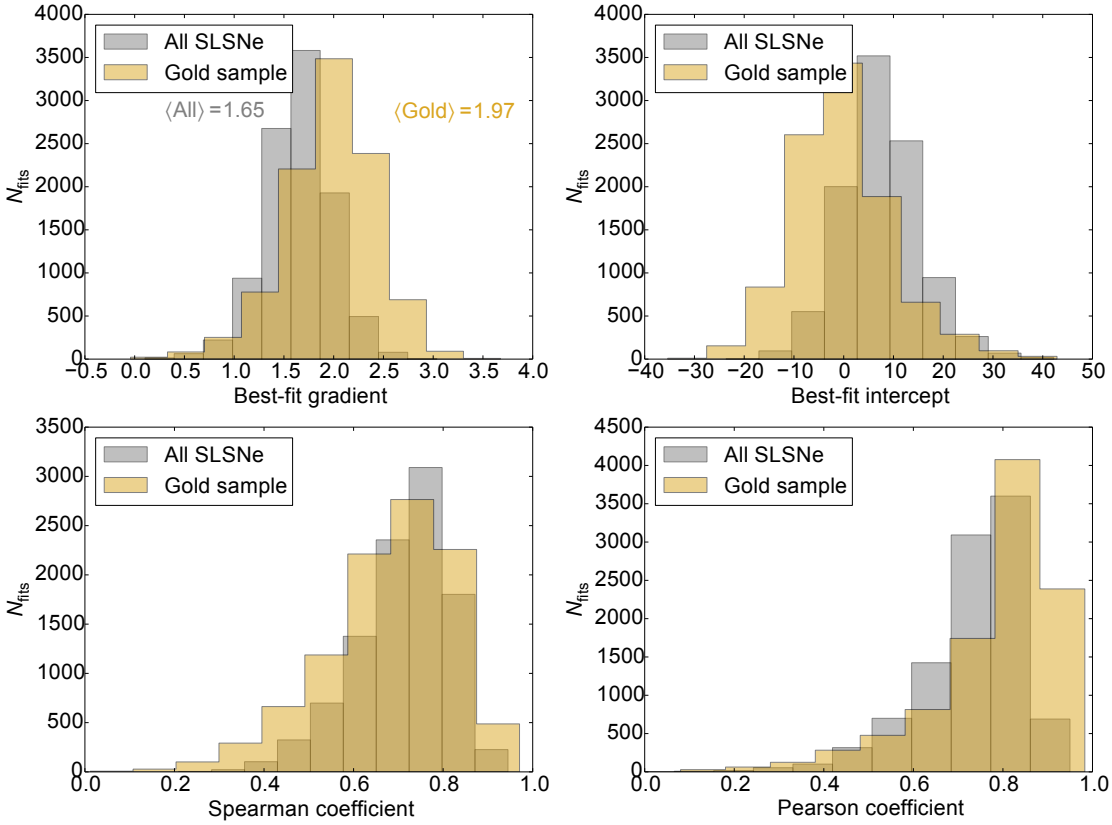

Figure 6.5: Fit parameters for the rise-decline timescale correlation.

to use the light curve width: we estimate that the diffusion time through the ejecta is $\tau_m \sim (\tau_{\rm rise} + \tau_{\rm dec})/2$. This is explored in detail for the following models, and will be important when we later attempt to estimate masses, in Section 6.9.

6.4.4 Models: ^{56}Ni and generalised exponential models

As a first step towards investigating the SLSN parameter space, we generated an array of models with a hypothetical exponentially decaying power source (i.e., with the same functional form as ^{56}Ni decay, but for a variable lifetime). While this power source is not motivated by any proposed physical model, it aids in understanding the relevant timescales, by virtue of being the simplest possible scenario. This model takes only two parameters: the diffusion time (τ_m) and the input time ($\tau_{\rm in}$), with $L_{\rm in} = L_0 \exp(-t/\tau_{\rm in})$ (L_0 is arbitrary). We varied the diffusion time between 10 and 120 days, in steps of 10 days. Figure 6.6 shows a subset of these models. We see that, if SLSNe are powered by some universal, exponentially declining process, such a process must have a lifetime of $\sim$ 10-20 days (the smaller points shown are spaced by 1 d in $\tau_{\rm in}$). However, if the timescale for power input is variable, SLSNe in the top right can have longer timescales (shown by the red curve and larger points, with $\tau_{\rm in} = 50$ d). Most importantly, this figure

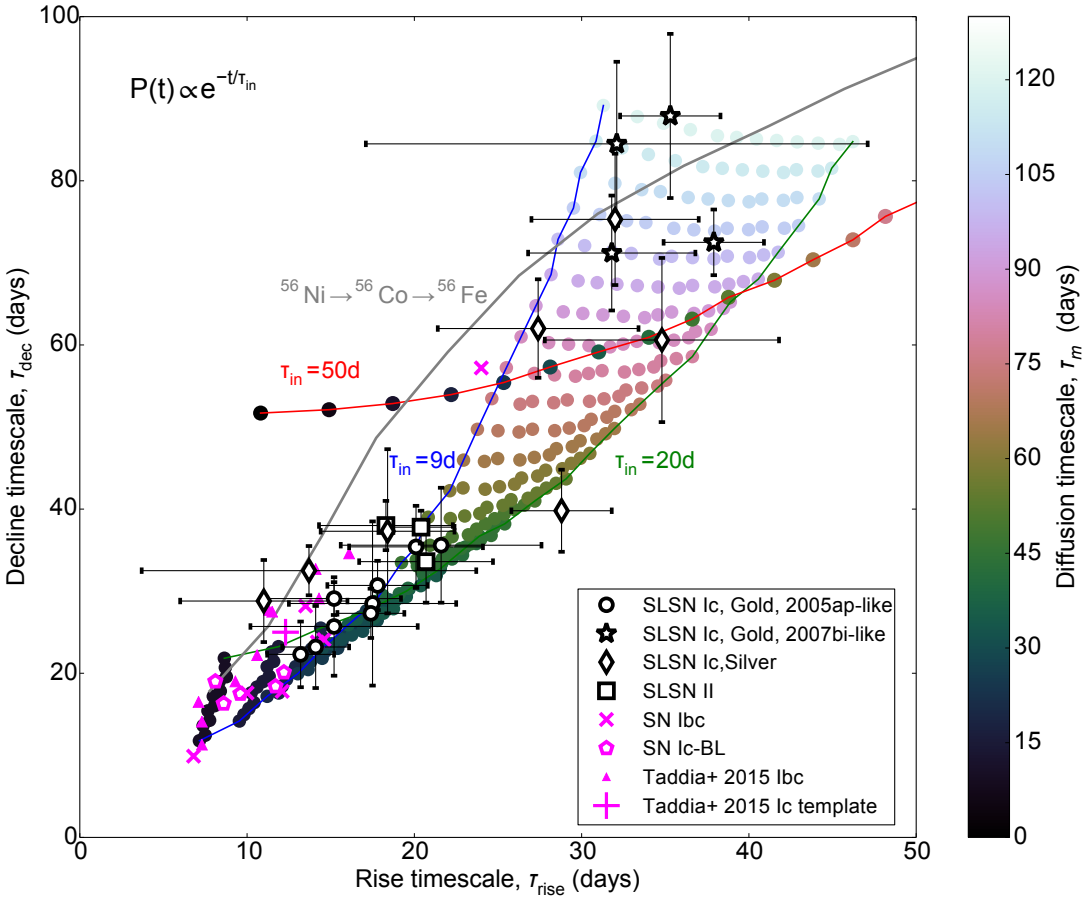

Figure 6.6: The observed rise and decline timescales of our sample overlaid on a grid of diffusion models (Arnett 1982), with a central heating term that decays exponentially with time. Input times of 10-20 d are needed to reproduce the SLSN correlation, which is then driven by variation in the diffusion timescale, as shown by the colour-bar. ^{56}Ni/^{56}Co models are also shown (grey curve). This roughly matches the normal-luminosity SNe Ibc, although there is a slight offset, which depends on the efficiency of gamma-ray trapping (the model here uses the trapping formalism of Arnett (1982), with a velocity of 10000 km s^{-1}).

shows that for this simple model, the correlation in rise and decline timescales is driven by τ_m, as seen in the colour scale.

Figure 6.7 shows the relationship between diffusion time and measured rise/decline times for a full grid of models, with τ_m,$\tau_{\rm in}$ = 10-120 d, in steps of 10 days. Clearly, there is no straightforward way to deduce the diffusion time directly from either the rise or the decline. However, we find a strong correlation when the quantities are combined: $\tau_{\rm rise} + \tau_{\rm dec} \approx \tau_m + \tau_{\rm in}$. This holds over the full range in τ_m and $\tau_{\rm in}$. Hence if we know the timescale of our exponential power source, we can accurately recover the diffusion time by measuring the rise and decline timescales. Measurement of the ejected mass through light curve fitting has been applied for many years to SNe Ibc. Since the input timescale is known for ^{56}Ni-powered SNe, the light curve width is typically a measure-

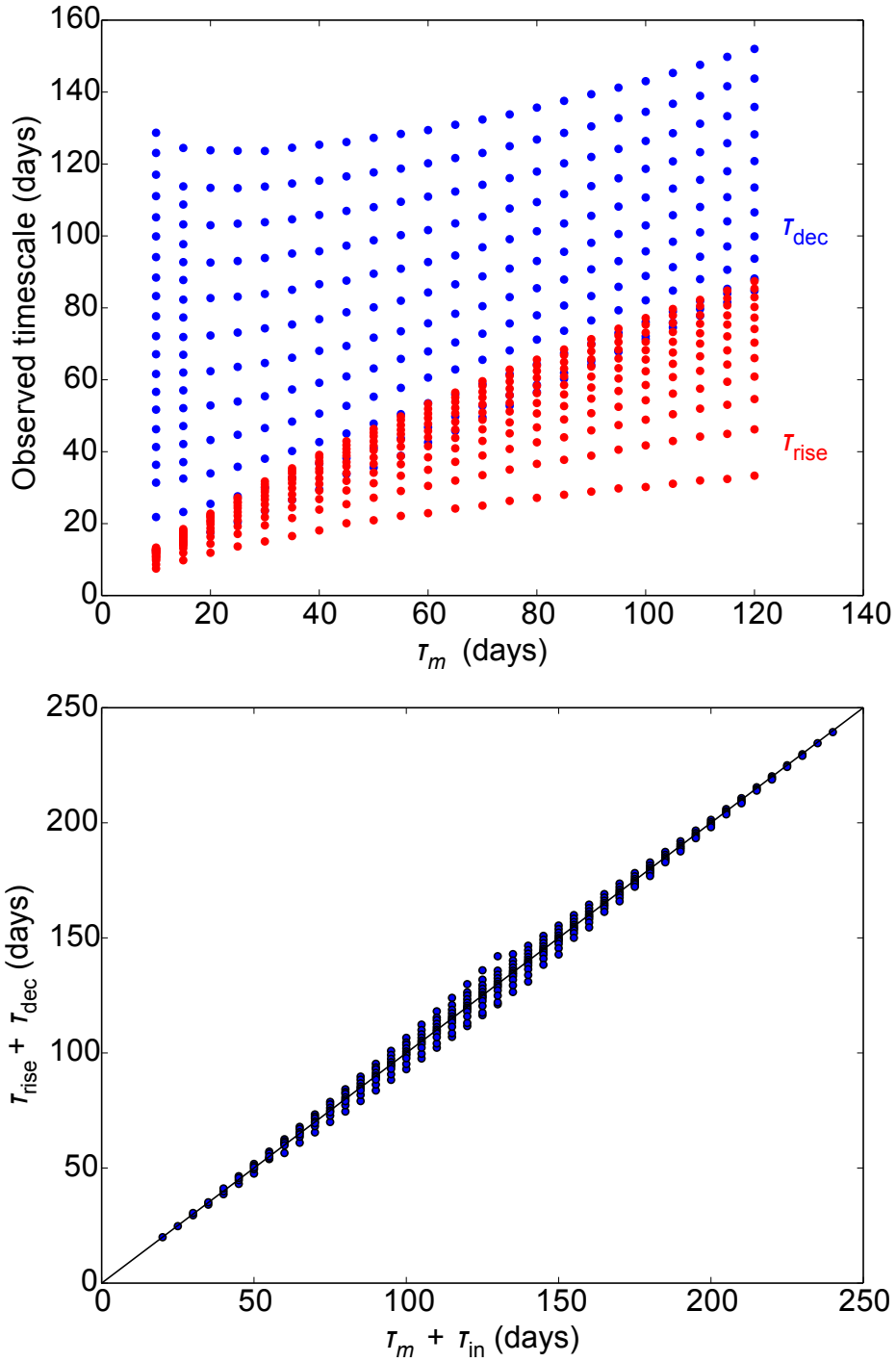

Figure 6.7: The relationships between various timescales in the simple exponential model. While neither the rise nor decline timescale is a good tracer of the diffusion time (*top*), the light curve width is determined by the sum of the power input and diffusion times, such that τ_m can be deduced from observed $\tau_{\rm rise}$ and $\tau_{\rm dec}$ for a given $\tau_{\rm in}$ (*bottom*).

ment of the diffusion time (e.g. Arnett 1982; Drout et al. 2011; Valenti et al. 2008a). For SLSNe, most of the best-fitting exponential models have $\tau_{\rm in} \sim \tau_m$. Therefore, from our relationship between the 4 important timescales, an estimate of the diffusion time is given by $\tau_m \approx (\tau_{\rm rise} + \tau_{\rm dec})/2$.

Figure 6.6 also shows the expected rise-decline curve for models powered by ^{56}Ni-decay. In this case, the only important variable is the diffusion time (^{56}Ni mass sets the overall luminosity, but not the light curve width). We see that this model does predict the correlation exhibited by SNe Ibc, which must be controlled by the diffusion time as mentioned in the previous subsection. Although some of fast rising and fast decaying SLSNe Ic lie close to this ^{56}Ni decay curve, that power source has already been ruled out for these. As discussed in Chomiuk et al. (2011), Quimby et al. (2011) and Pastorello et al. (2010), the peak luminosity means that the ^{56}Ni mass would have to be greater than or similar to the total ejecta mass. Such expanding balls of ^{56}Ni are unphysical and ruled out by the observed spectra.

6.4.5 Models: magnetar

In one of the most popular models, SLSNe are powered by a central engine which re-shocks the ejecta after it has expanded to a large radius, thus overcoming adiabatic losses. In the magnetar spin-down model, the energy source is the rotational energy of a millisecond pulsar, which is tapped via a strong magnetic field. This model has been discussed extensively in previous chapters, and has a functional form for the power input given by Equation 2.7 (which is proportional to t^{-2} at late times). The energy input timescale in days is given by $\tau_p = 4.75\,(B/10^{14}\,{\rm G})^{-2}\,(P/{\rm ms})^2$, where B is the magnetic field and P is the initial spin period. The shortest possible rotation period (corresponding to the largest energy reservoir) is $P \sim 1$ ms; any shorter and centrifugal forces would lead to breakup. Galactic magnetars have $B < 10^{15}$ G (e.g. Davies et al. 2009, Table 3). This combination makes it difficult to achieve spin-down timescales $\tau_p \ll 0.1$ d.

We ran a grid of magnetar models, uniformly varying τ_m (in steps of 5 days), B and P (in unit steps of 10^{14} G and milliseconds, respectively), which we compare to the data in Figure 6.8. However, it is not obvious that we can vary B and P independently. The high magnetic field is likely generated by a dynamo mechanism during core-collapse (Duncan & Thompson 1992), as a primordial B-field in the progenitor core would couple the core angular momentum to the envelope, braking the core and likely precluding formation of a millisecond pulsar at collapse. The simplest assumption for the dynamo

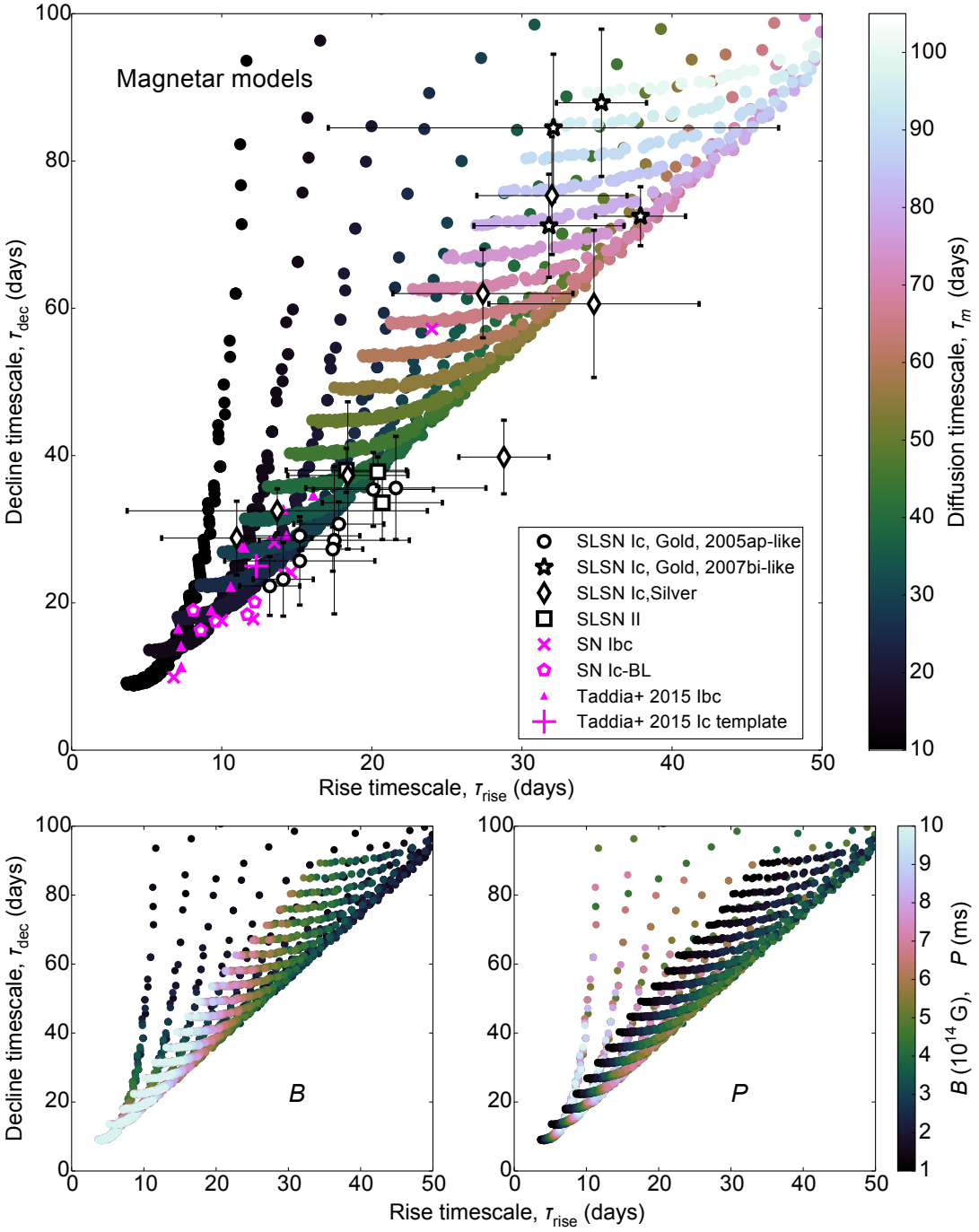

Figure 6.8: We overlay a grid of magnetar-powered diffusion models with different spin period (P), magnetic field (B) and diffusion time (τ_m). All are varied in uniform steps. Only models with $L_{\rm peak} > 3\times10^{43}\,{\rm erg\,s^{-1}}$ are plotted. The top panel shows how increasing the diffusion timescale, τ_m, traces out the correlation we see in our data, and that τ_m is the parameter most strongly driving the diversity in our light curves. The lower panels show the effect of varying P and B. The bottom left region (where normal SNe Ibc reside) is difficult to reach with magnetar models, as very high B is required. SLSNe lie along the lower right edge of the magnetar distribution, where P and B are least extreme (for given τ_m).

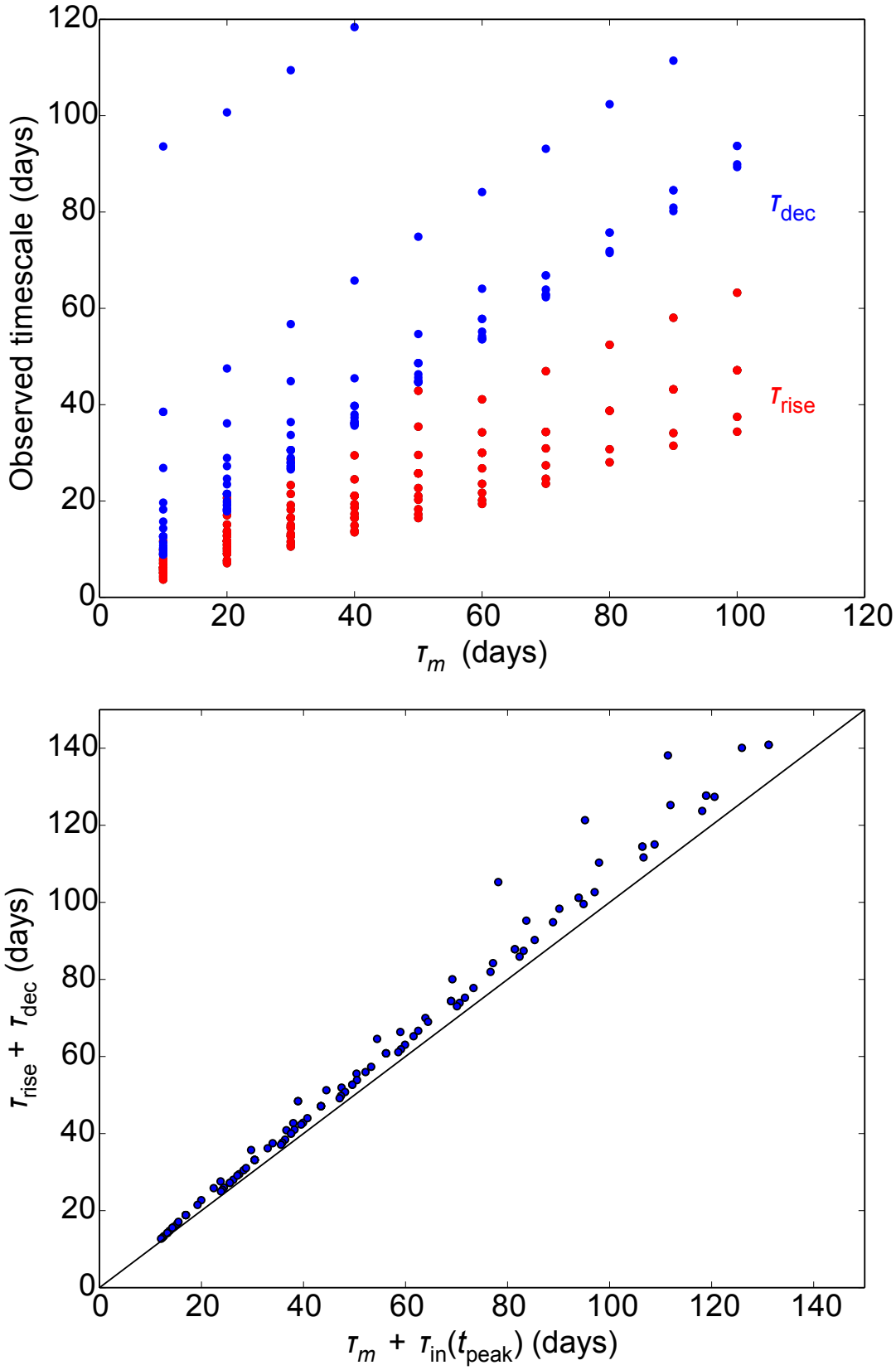

Figure 6.9: Same as Figure 6.7, but for our magnetar model grid. The models shown have diffusion times of 10-100 d (steps of 10 d), $B = \{1,3,5,7,9\} \times 10^{14}$ G, and $P = \{1,3,5,7,9\}$ ms. Only models with peak luminosity greater than 3×10^{43} erg s^{-1} are plotted.

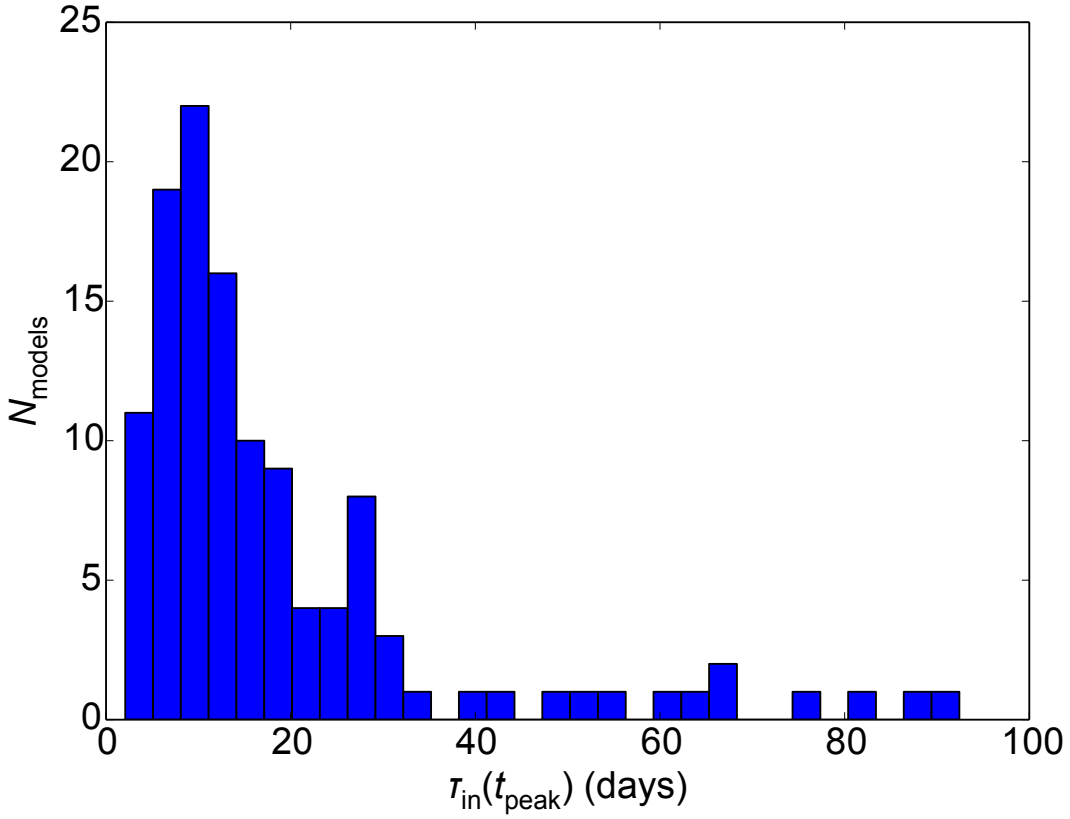

Figure 6.10: The distribution of the power input timescales at maximum light, for the magnetar models in Figure 6.9. We caution that this is for a uniform distribution in B and P, whereas we do not know what initial spins and magnetic fields magnetars are likely to form with. In particular, models with $\tau_{\rm in} < 10$ d require high magnetic field and fast spin.

mechanism is that a constant fraction of the rotation energy, $E_{\rm rot} \propto P^{-2}$, is converted to magnetic energy, $E_{\rm mag} \propto B^2$. In this case, we would have $B \propto 1/P$. Using this approach (with uniformly distributed P), rather than uniformly distributed B and P, results in no significant effect on the distribution of rise and decline timescales in Figure 6.8. Bearing in mind that we do not know the initial distribution of spin periods (and hence B-fields), we will continue our analysis assuming that B and P are independent parameters for simplicity.

Only models that are brighter than the faintest SLSN in our sample (PTF10hgi) are plotted. We produced many more models of course, but the only ones that are relevant are those producing luminosities of the same order as the SLSNe. The models shown display a correlation in rise and decline timescales similar to that observed in SLSNe, although a small number of models have very slow declines relative to the rise time. The colour map shows that increasing τ_m drives the models to longer rise and decline times, tracing out the observed correlation. We also investigate the effect of B and P. The B-field influences the rise time, but has little effect on the decline shortly after

peak (though it does affect the late-time decline rate, not probed by our measurement here; see Chapter 4). $B \sim 10^{15}$ G is needed to reach $\tau_{\rm rise} \lesssim 10$ d. This could explain why no SLSNe are seen with such short rise times. The corollary also holds: if we were to observe SLSNe with rise times less than about 10 days, the magnetar model would struggle to explain them. Models with long P tend to rise quickly, but this is not a necessary condition, unlike the constraint on B.

Most of our SLSNe lie below the magnetar grid, but are consistent (within the errors) with lying along the locus of points on the sharp lower-right edge of the model distribution. This locus corresponds to weaker B, and $P \sim$ 2-5 ms. If SLSNe are powered by millisecond magnetars, the less-extreme magnetic field may account for why the data preferentially lie at the lower edge of the model distribution. Overall, magnetar models satisfactorily reproduce the basic trend we see in the data. For a sensible range of parameters, it is the diffusion time that dominates the diversity in the observed timescales, just as we saw previously for the simplest models with a central (exponential) power source.

Although most of the energy injection in this model takes place within a time τ_p, the power input timescale is not a constant, unlike in exponential models. Using the definition $\tau_{\rm in} = |L_{\rm in}(t)/(dL/dt)|$, we find that for magnetars, $\tau_{\rm in}(t) = \frac{1}{2}(\tau_p + t)$, whereas for radioactive sources, $\tau_{\rm in}$ is simply the lifetime of the nucleus. In setting the peak width, the important timescale (in addition to τ_m) is $\tau_{\rm in}(t_{\rm peak}) = \frac{1}{2}(\tau_p + t_{\rm peak})$. Using this definition, we recover almost exactly the same correlation between the 4 timescales: $\tau_{\rm rise} + \tau_{\rm dec} \approx \tau_m + \tau_{\rm in}(t_{\rm peak})$. This is shown in Figure 6.9. Does this mean that we can assume $\tau_m \approx (\tau_{\rm rise} + \tau_{\rm dec})/2$ in this case also? Figure 6.10 shows the distribution of $\tau_{\rm in}(t_{\rm peak})$ for our magnetar grid. The mean is 19 days (standard deviation: 18 d). Of all the models, 76% have $\tau_{\rm in}$ between 5 and 30 days at peak; however those with $\tau_{\rm in}(t_{\rm peak}) <$ 10 d need both fast rotation and strong magnetic field. This corresponds to the bottom left region in Figure 6.8, where we do not have any observed SLSNe. Therefore the relevant models have timescales mostly in the range 10-30 d, with a tail extending to many tens of days. This is good news, as the assumption that $\tau_{\rm in} \sim \tau_m$ is thus also reasonable for magnetar models. Hence we conclude that indeed $\tau_m \approx (\tau_{\rm rise} + \tau_{\rm dec})/2$, for a range of sensible models with central power sources.

6.4.6 Models: CSM interaction

Alternatively, we can attempt to fit the observed correlations with our parameterised model in which the ejecta collide with a dense CSM. This has been another popular model invoked to explain SLSNe (Ginzburg & Balberg 2012; Chevalier & Irwin 2011; Moriya & Maeda 2012). As discussed in Section 2.4.3, this model has many free pa-

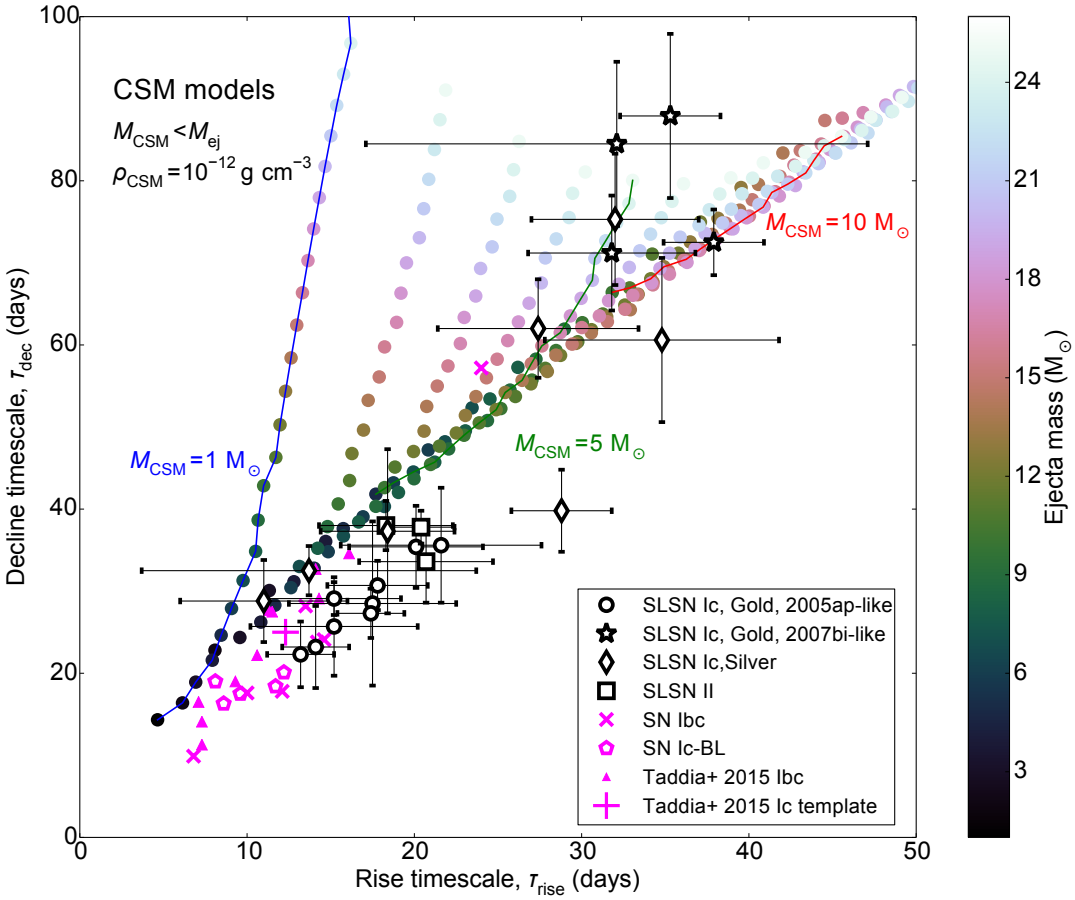

Figure 6.11: Same as Figure 6.8, but for interaction-based models. In this case, we vary the ejected mass and CSM mass, and CSM density. We find that the shape of the rise-decline distribution is highly sensitive to the CSM density – the observed correlation is approximately recovered for $\rho_{CSM} = 10^{-12}\,g\,cm^{-3}$. All of the light curve fits in this thesis (and many by Chatzopoulos et al. 2013) found $\rho_{CSM} \sim 10^{-12}\,g\,cm^{-3}$. Increasing the ejecta mass moves light curves along our correlation, while increasing the CSM mass primarily affects the rise time. It can be seen that the correlation is best reproduced by the subset of models with $M_{CSM} \sim M_{ej}/2$ – another general property common to our individual light curve fits. Models with lower CSM mass rise too quickly for a given decline rate. If ejecta-CSM interaction does power all SLSNe, our rise-decline correlation puts tight constraints on the progenitor systems.

rameters: ejected mass; CSM mass, radius and density (and density profile); explosion energy; ^{56}Ni mass. We ran a grid of models with fixed explosion energy (10^{51} erg; this mostly just affects the peak luminosity) and inner CSM radius (10^{13} cm; the light curve is quite insensitive to this parameter), and assume no ^{56}Ni. The CSM is taken to be a spherically symmetric shell of constant density – its mass and density therefore determine its radial extent. We varied the ejected mass, M_{ej}, in unit steps from 1-25 $M_\odot$, and the CSM mass, M_{CSM}, in similar steps from 1-15 $M_\odot$, with the additional restriction $M_{CSM} < M_{ej}$. The CSM density was initially set to $\rho_{CSM} = 10^{-12}\,g\,cm^{-3}$.

The results are shown in Figure 6.11. At a given $M_{\rm CSM}$, increasing $M_{\rm ej}$ increases both $\tau_{\rm rise}$ and $\tau_{\rm dec}$, in the same way as the diffusion time, τ_m, did for our magnetar models. Illustrative lines of fixed $M_{\rm CSM}$ have been marked, and the observed rise-decline correlation is best reproduced by models with $M_{\rm CSM} \gtrsim M_{\rm ej}/2$. This was a common feature of model fits to individual SLSNe in Chapters 2-5, and in fact is probably a requirement for SLSNe powered by interaction, as the CSM mass must be an appreciable fraction of the ejecta mass to thermalise the bulk of the expansion kinetic energy.

More restrictive, but perhaps more interesting, is the effect of CSM density on our light curves. The rise-decline relationship is similar to our data for $\rho_{\rm CSM} = 10^{-12}\,{\rm g\,cm^{-3}}$. In Figure 6.12, we show the effect of varying $\rho_{\rm CSM}$ for a few representative models. Marked on the figure is the approximate slope of the observed correlation for SLSNe. Changing $\rho_{\rm CSM}$ to $10^{-11}\,{\rm g\,cm^{-3}}$ or $10^{-13}\,{\rm g\,cm^{-3}}$ moves our models to regions of the rise-decline plot far from where our data reside.

Why does this density have such a strong effect on the ratio of rise and decline times in our models? The dominant energy source is the forward shock from the interaction, which deposits heat as it propagates through the CSM. At some point, the shock breaks out of the CSM shell, and can no longer contribute energy (a similar effect occurs with the reverse shock in the ejecta, but the forward shock turns out to be dominant in most cases); at this point our light curve usually peaks. The time taken for the forward shock to propagate through the CSM decreases with increasing density (Chatzopoulos et al. 2012, Equation 15 of). The model subsequently declines, as the stored energy diffuses out of the CSM, on the characteristic CSM diffusion timescale. This timescale *increases* with the CSM density, so that models with earlier peaks fade more slowly. Thus, for all other parameters fixed, there is an inverse relationship between rise and decline timescales as we vary $\rho_{\rm CSM}$, as seen in Figure 6.12.

Clearly, if SLSNe are powered by interaction with a dense CSM, our observed rise-decline relationship can place narrow constraints on the range of CSM densities present. All of the interaction model fits in previous chapters of this thesis (to CSS121015, LSQ12dlf, SSS120810, SN 2013dg, PTF12dam, LSQ14bdq) had densities in the range $-12.54 < \log_{10}\rho_{\rm CSM} < -11.74$. It seems contrived that virtually all H-poor SLSNe would have such similar circumstellar densities, particularly when modelling indicates that a range of densities can generate the observed peak magnitudes (e.g. Chatzopoulos et al. 2013, who also fit H-rich events).

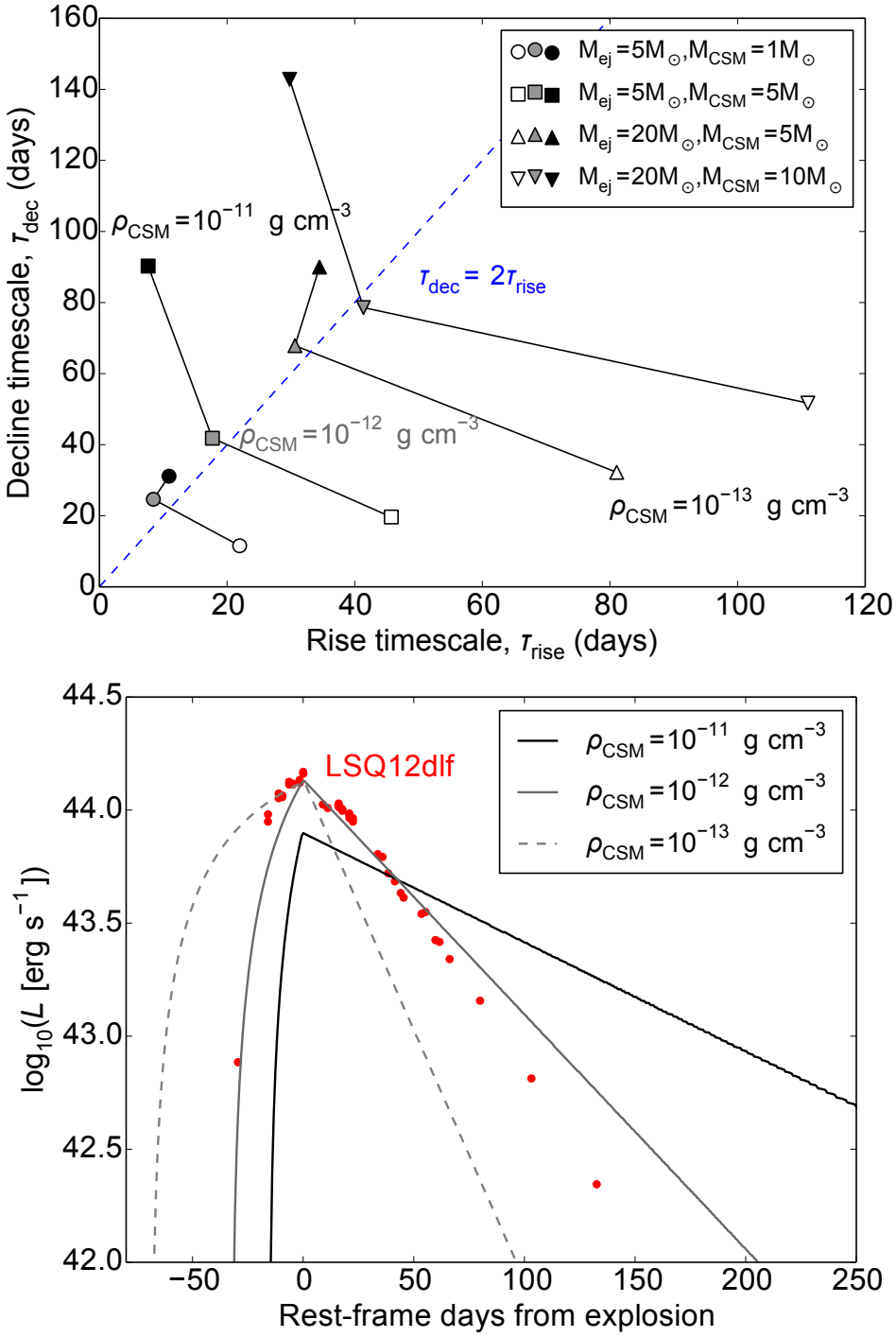

Figure 6.12: Rise vs decline timescales for synthetic light curves powered by ejecta-CSM interaction. The relationship is strongly dependent on the density of the CSM. Models with $\rho_{CSM} \sim 10^{-12}\,\mathrm{g\,cm^{-3}}$ (shown in Figure 6.11) correspond best to our data. This can also be seen here in the lower panel, where we compare the SLSN LSQ12dlf to 3 models with $M_{ej} = M_{CSM} = 5\,M_\odot$, and varying CSM density. The light curves peak when the forward shock from the ejecta-CSM collision breaks out of the CSM, and the subsequent decline is controlled mainly by the diffusion time in the CSM. Denser CSM results in faster shock propagation (shorter rise) and slower diffusion (longer decline), giving the inverse relationship between rise and decline times apparent in the top panel.

Three possibilities exist. The first and most obvious is that ejecta-CSM interaction is not the power source in SLSNe Ic. Alternatively, our simple model may not be a good description of interacting SLSNe (for example, the shape of the CSM density profile may be important, and not a uniform shell). One very important weakness in this analysis is that this interaction model treats the shocks following Chevalier & Fransson (1994), whose derivation was for $M_{\rm CSM} \ll M_{\rm ej}$, and it is unclear how the picture changes for massive CSM. Finally, some process in the evolution of SLSN progenitors might somehow be capable of consistently producing circumstellar environments within this density range. The homogeneity in the spectral properties of SLSNe would then result from the similar physical conditions in the CSM. The last of these possibilities is intriguing, and determining this process could prove an important clue to understanding what kinds of stars produce SLSNe. However, observations of SNe known to be powered by CSM interaction (SNe IIn) show huge diversity and variation in their observed characteristics and inferred physical configurations. In any case, CSM models will have to be able explain our observed correlation, if we are to continue to accept them as a valid explanation for SLSNe.

6.5 Generalised light curves and peak luminosity

The correlation in rise and decline timescales, presented in the previous section, was found to be the same for SLSNe Ic and for normal-luminosity, hydrogen-poor core-collapse SNe. This suggested that the two populations have the same basic light curve shape (and we inferred that the slower evolution of SLSNe was due to longer diffusion timescales). To further investigate the relationship between SLSN and normal SN Ibc light curves, we construct a generalised light curve for each type of SN. We do this simply by taking the area in magnitude-time parameter space that contains all of the light curves in each sample (SLSNe of Type II are excluded from this analysis). This is shown in Figure 6.13, where we also include the SN Ibc light curve template from Taddia et al. (2015), and a number of SNe Ibc with unusually high luminosity.

As expected, the SLSN light curves are much brighter and broader than typical SNe Ibc. In the unscaled SN Ibc light curve, the decline rate starts to change at around 30 days after peak. This is because the ejecta are becoming optically thin, and the luminosity begins to track the decay of ^{56}Co. We do not typically see this behaviour in SLSNe, for two reasons. For most SLSNe, the decline after peak is too fast to be compatible with realistic ^{56}Ni-driven models with such a high peak luminosity, as discussed in Section 6.4.4. If they do contain some small amounts of ^{56}Co (comparable to that in SNe Ibc), this is masked by the bright luminosity source that powers the peak. The more slowly declining SLSNe (SN 2007bi-like), on the other hand, do match the

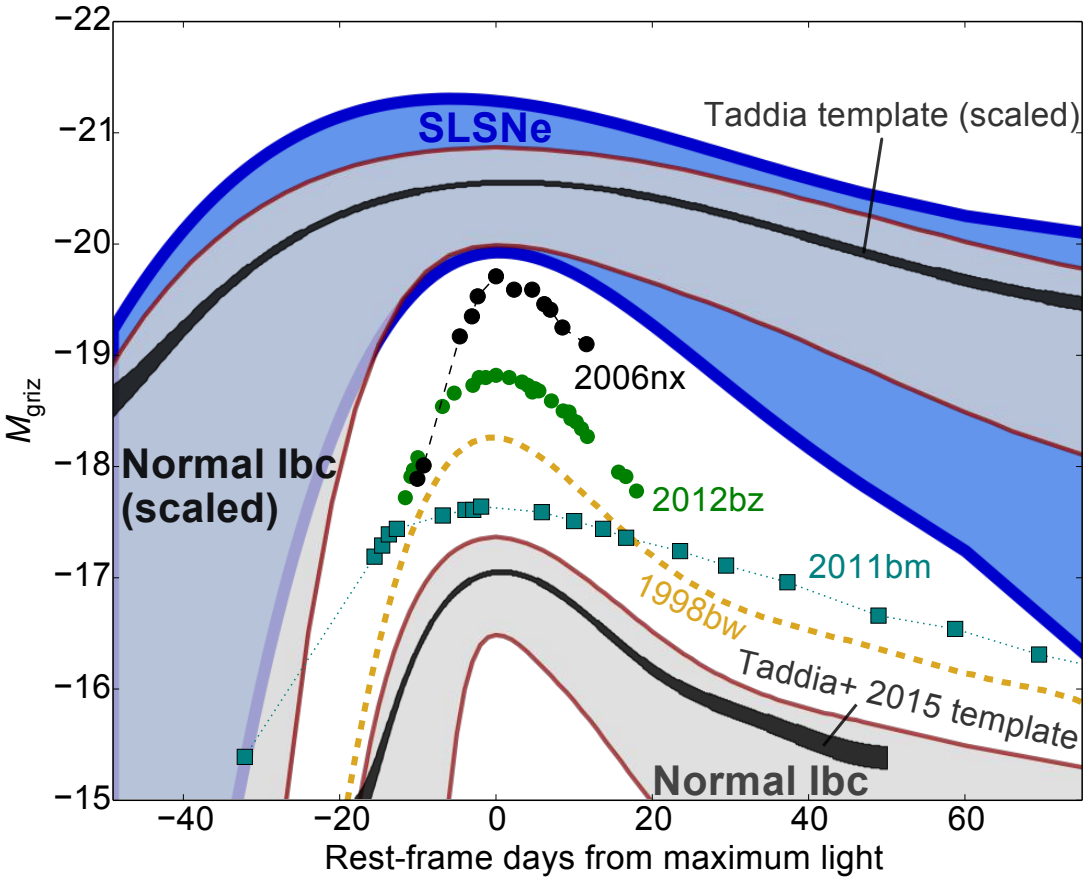

Figure 6.13: Generalised light curves for SLSNe compared with lower luminosity SNe Ibc (normal and broad-lined). The blue area represents SLSNe, while the grey area represents normal SNe Ibc in our well-observed literature sample. and those of Taddia et al. (2015). SN Ibc light curves can be mapped onto the SLSNe by a 3.5 magnitude increase in brightness and a stretch along the time axis by a factor of 3. Some SNe Ic-BL lie in the magnitude gap, but tend to have narrower light curves than SLSNe. SN 2011bm (Valenti et al. 2012) exhibited a normal Ic spectral evolution, but has a light curve width comparable to SLSNe.

^{56}Co decay rate. If they were radioactively powered, the long rise times and broad peaks would allow them to join smoothly onto the ^{56}Co decay tail after maximum.

We find that a very simple transformation maps the SN Ibc light curves onto those of the SLSNe: an increase along the *y*-axis by 3.5 magnitudes (a multiplicative factor of ≈ 25 in luminosity), and a broadening in time by a factor 3. The most obvious interpretation of this correspondence is that the two sets of light curves are determined by the same underlying physics: the rapid expansion of shocked gas with a small initial radius, heated by some internal power supply. The broader light curves of the SLSNe are indicative of a longer diffusion timescale (higher mass and/or lower velocity) compared to the SNe Ibc. The higher peak luminosity tells us that some additional energy source is heating the ejecta, compared to $\sim$ 0.1-1 $M_\odot$ of ^{56}Ni in SNe Ibc (this could be,

for example, a millisecond magnetar). Indeed, this is the established theory explaining the diversity within the SN Ic class, where higher ejecta mass and ^{56}Ni mass result in broader and brighter light curves, respectively.

If SLSNe Ic were powered by interaction of SN Ic ejecta with dense (and hydrogen-poor) CSM, the light curve physics would be quite different: a combination of forward and reverse shocks in the ejecta and CSM, with a strong dependence on the various density profiles. In fact, for the massive, optically thick CSM needed to generate super-luminous peak magnitudes, we should not actually see direct emission from the SN ejecta until well after maximum light (Benetti et al. 2014). It would therefore be surprising to recover such a trivial transformation between normal and super-luminous Ic light curves. Circumstellar interaction can generate a range of light curve shapes (as shown in Figure 6.12). For instance, the most conclusive example of a Type Ic SN interacting with H-deficient CSM is SN 2010mb (Ben-Ami et al. 2014), which had an extremely unusual light curve shape with a plateau lasting for hundreds of days.

One interesting question is whether there is a continuum of peak luminosities between normal and super-luminous Type Ic SNe. Since the discovery and characterisation of SLSNe, an apparent gap has been recognised. Richardson et al. (2014) have compiled large samples of SNe Ibc to determine absolute magnitude distributions in the standard Johnson B-band. Their study attempted to correct for bias and derive volume limited absolute magnitude distributions, however the targets do not all have enough data to determine bolometric luminosities (M_{griz} at maximum). There are some typing inaccuracies in the Richardson et al. sample (e.g. SN 2006oz as a Ib, and SN 2005ap as a Type II), however the normal and broad-lined Ibc population does appear to have an upper limit to their peak brightness of around -18 to -19, with the SLSNe sitting 3 magnitudes brighter.

We compare the brightness distributions of our SLSNe and other SNe in Figure 6.14. The SLSNe Ic peak at $M_{griz} = -20.72 \pm 0.59$ magnitudes, while the normal SNe Ibc tend to peak at $M_{griz} = -17.03 \pm 0.58$. We note here that Inserra & Smartt (2014) derived peak absolute magnitudes for a sample of 16 SLSNe (with a large overlap with our sample) in a synthetic bandpass centred on 400 nm. They found $\langle M_{400} \rangle = -21.86 \pm 0.35$. This seems to be more uniform than M_{griz}, though it is worth bearing in mind that in some cases our derived M_{griz} has been estimated using assumed colours, introducing additional uncertainty, whereas Inserra & Smartt (2014) had observations fully covering their synthetic bandpass for all of their objects at maximum light.

Selection effects and bias in our sample mean we cannot definitively say whether there is an excess of hydrogen-poor SNe with peak absolute magnitudes brighter than $M_{griz} \sim -20$ (i.e. SLSNe), or whether such events are the bright tail of a continuous

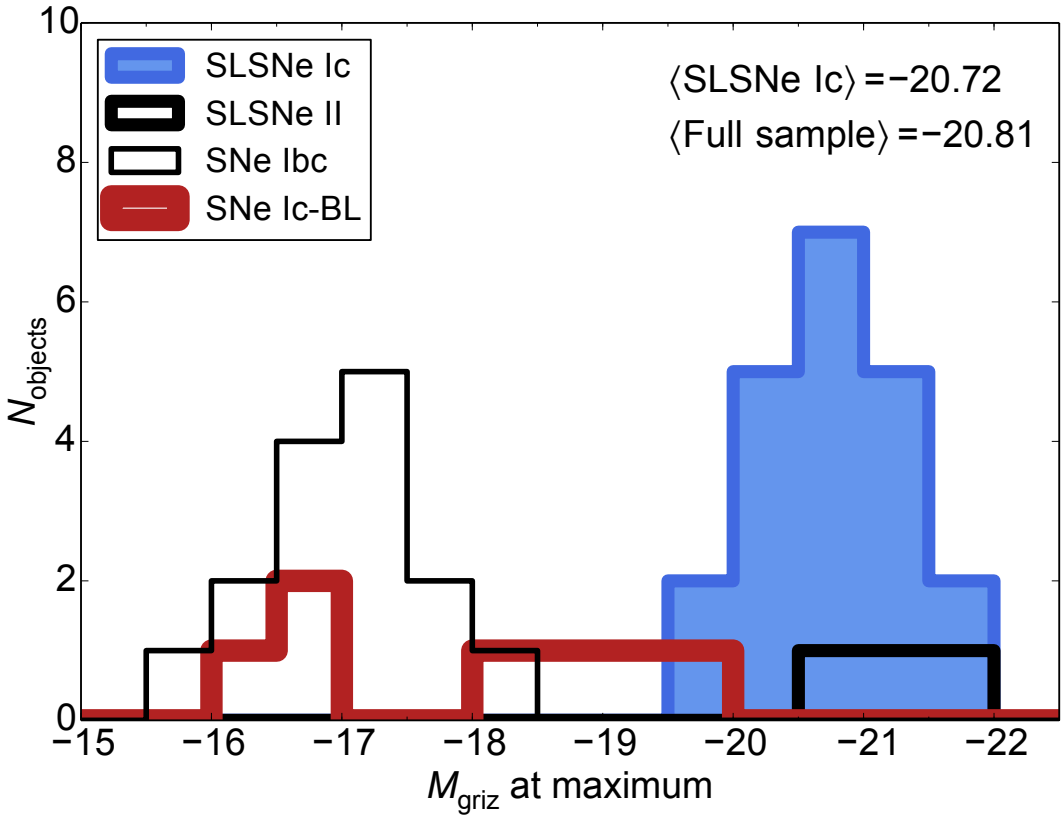

Figure 6.14: The distribution of magnitudes at maximum light. The scatter is quite low, with a standard deviation of only 0.50 magnitudes (0.58 if we include the two SLSNe II). The mean peak magnitude for normal SNe Ibc is −17.03. A few SNe Ic-BL have luminosity comparable to the fainter SLSNe. The data are binned in 0.5 mag intervals.

magnitude distribution. The plot in Figure 6.14 is not meant be be a representative luminosity function. For this, one would require accurate relative numbers in either a magnitude- or volume-limited survey. We know definitively that SLNSe are rare and that their relative rate with respect to normal SNe Ibc is of order 1 SLSNe per 3000-10000 SNe Ibc (Quimby et al. 2013; McCrum et al. 2015). The SLSNe are obviously over-represented in our sample, relative to their rates of occurrence in nature, as we have compiled similar numbers of SLSNe and comparison SNe Ibc. To prove statistically that SLSNe comprise a separate population of events from the brightest 'normal' SNe Ibc would require careful consideration of the selection factors in surveys such as PTF, PS1 and LSQ+PESSTO, in order to determine unbiased relative numbers and construct meaningful luminosity functions (e.g. as done for normal SNe in Li et al. 2011)

Nevertheless we can make some comments on the luminosity differences observed if we assume that the SNe Ibc we have compiled are fairly representative of the general population of such stripped envelope SNe. None of our spectroscopically normal SNe Ibc are observed to peak at $M_{griz} \approx -19$. However, some SNe Ic-BL do have peak

magnitudes spanning the gap between normal and super-luminous SNe. SNe Ic-BL are often high ^{56}Niproducers, and some have been shown to be associated with observed GRBs (Woosley & Bloom 2006). The large ^{56}Ni mass makes them brighter than typical SNe Ic. Figure 6.13 shows two GRB-SNe, SN 1998bw (Patat et al. 2001) and SN 2012bz (Schulze et al. 2014). The brightest Ic-BL in the sample of Taddia et al. (2015) is also shown. The object, SN 2006nx, was discovered at redshift $z = 0.137$, but if there was an associated GRB, it was not seen. SN 2006nx actually has a similar peak magnitude to SLSNe, suggesting that it may in fact be a member of that class. However, its light curve is quite narrow not only compared to SLSNe, but also for such a luminous ^{56}Ni-powered SN. Its unknown spectral evolution precludes a robust answer to the question of whether it is physically related to the SLSN population.

It is interesting that some SNe Ic-BL/GRB-SNe do lie in the gap between SNe Ibc and SLSNe, as some authors have suggested that SLSNe and GRBs are in fact related. Lunnan et al. (2014) argued that the two types of explosion occur in similar low-metallicity environments. Leloudas et al. (2015) also claimed that their host galaxies are similar, but that SLSN hosts are more intensely star-forming than those of GRBs, perhaps implying more massive progenitors for SLSNe. Magnetar/engine-powered models have been invoked to explain both the high luminosities in SLSNe and the relativistic jets in GRB-SNe (Thompson et al. 2004; Metzger et al. 2011). However, the required magnetar parameters in GRB models are more extreme than for SLSNe, with spin periods ~ 1 ms and magnetic fields 10-100 times stronger, in order to drive a jet that punches through the stellar envelope (Bucciantini et al. 2009). Gal-Yam (2012) notes that some SNe Ic-BL, such as SN 2007D (Drout et al. 2011) and SN 2010ay (Sanders et al. 2012), reached peak magnitudes close to those of SLSNe, and likely required an additional energy source on top of the inferred $\sim 1\,M_\odot$ of ^{56}Ni. Perhaps bright SNe Ic-BL represent events where the central engine enhances the luminosity as well as the kinetic energy of the explosion, but not to the same degree as in SLSNe, where the additional power source overwhelms the input from ^{56}Ni decay. In this framework, there could thus be a continuum in luminosity between the various subclasses of SNe Ic, depending on the properties of the engine.

If, however, there is a significant gap in peak brightness, with very few objects intermediate between normal and super-luminous SNe Ic, it may be difficult to explain for circumstellar interaction models. For example, Type II SNe show a broad but continuous distribution in peak magnitudes: from SNe II-P through SNe II-L, to bright SNe IIn and finally SLSNe IIn. Some authors have argued that this hierarchy is driven by varying degrees of circumstellar interaction (Chevalier & Fransson 1994; Richardson et al. 2002; Gal-Yam 2012). A gap between normal and super-luminous SNe Ic could

Table 6.3: Measured properties and derived masses

SN	$\tau_{\rm rise}$(d)[a]	$\tau_{\rm dec}$(d)[b]	v_{5169} (km s^{-1})[c]	$M_{\rm ej}/{\rm M}_\odot$
Super-luminous SNe				
SN2007bi	32.1	84.5	11900	$31.1^{+34.3}_{-21.7}$
SN2008es[*]	18.3	38.0	–	$3.7^{+3.0}_{-2.1}$
SN2010gx	15.2	29.1	10900	$4.4^{+3.2}_{-2.3}$
SN2011ke	15.2	25.7	10200	$3.3^{+1.9}_{-1.5}$
SN2011kf	17.5	28.5	9000	$3.7^{+2.0}_{-1.5}$
SN2012il	14.1	23.2	9100	$2.4^{+1.3}_{-1.0}$
SN2013dg	17.8	30.7	14000	$6.3^{+3.8}_{-2.9}$
SN2013hx	20.7	33.6	6000	$3.4^{+1.8}_{-1.4}$
LSQ12dlf	20.1	35.4	13700	$8.1^{+5.1}_{-3.9}$
LSQ14mo	17.4	27.3	10200	$3.9^{+1.9}_{-1.5}$
LSQ14bdq[†]	31.8	71.2	–	$20.4^{+18.6}_{-12.6}$
PTF10hgi	21.6	35.6	4800	$3.0^{+1.7}_{-1.3}$
PTF11rks	13.2	22.3	18100	$4.4^{+2.5}_{-2.0}$
PTF12dam	37.9	72.5	10500	$27.0^{+19.6}_{-14.3}$
CSS121015	20.4	37.8	10000[‡]	$6.5^{+4.5}_{-3.3}$
SSS120810	–	30.2[††]	11200	$5.7^{+3.6}_{-2.1}$
PS1-11ap[†]	35.3	87.9	–	$29.2^{+30.3}_{-19.6}$
SN2005ap[†]	>11	28.8	–	$3.0^{+3.3}_{-2.1}$
SCP06F6[†]	28.8	39.8	–	$9.1^{+3.1}_{-2.7}$
PTF09cnd[†]	32.0	75.3	–	$22.2^{+21.5}_{-14.3}$
PTF09cwl[†]	34.8	60.6	–	$17.5^{+10.8}_{-8.2}$
PS1-10ky[†]	13.7	32.5	–	$4.1^{+4.0}_{-2.7}$
PS1-10bzj	18.4	37.3	13000	$7.8^{+6.2}_{-4.4}$
iPTF13ajg	27.4	62.0	9100	$14.0^{+12.9}_{-8.7}$
Other H-poor SNe				
SN1994I	6.8	9.9	10100	$0.5^{+0.2}_{-0.2}$
SN1998bw	12.2	20.1	26600	$5.3^{+2.9}_{-2.3}$
SN1999ex	12.1	17.8	9300	$1.6^{+0.7}_{-0.6}$
SN2002ap	8.1	19.0	20400	$2.9^{+2.8}_{-1.9}$
SN2003jd	9.6	17.5	16400	$2.3^{+1.5}_{-1.2}$
SN2004aw	13.5	28.2	12100	$4.1^{+3.4}_{-2.4}$
SN2007gr	10.0	17.6	8400	$1.2^{+0.8}_{-0.6}$
SN2008D	14.6	24.1	8700	$2.5^{+1.4}_{-1.1}$
SN2009jf	14.2	23.8	10100	$2.8^{+1.6}_{-1.2}$
SN2010bh	8.6	16.3	35000	$4.2^{+3.0}_{-2.2}$
SN2011bm[†]	24.0	57.2	–	$12.7^{+12.5}_{-8.3}$
SN2012bz	11.7	18.4	23000	$4.0^{+2.0}_{-1.6}$
SN2005hl	14.3	29.1	5450[‡]	$2.0^{+1.6}_{-1.1}$
SN2005hm	11.5	27.5	9470[‡]	$2.8^{+2.7}_{-1.8}$
SN2006fe	11.3	27.7	5000[‡]	$1.5^{+1.5}_{-1.0}$
SN2006fo	14.1	32.7	10500[‡]	$4.4^{+4.2}_{-2.8}$
14475	7.3	14.1	18700[‡]	$1.6^{+1.2}_{-0.9}$
SN2006jo	7.3	11.3	14400[‡]	$1.0^{+0.5}_{-0.4}$
SN2006lc	9.3	19.0	9100[‡]	$1.4^{+1.1}_{-0.8}$
SN2006nx	7.1	16.5	15400[‡]	$1.7^{+1.6}_{-1.1}$
SN2007ms	16.1	34.6	11400[‡]	$5.6^{+4.9}_{-3.4}$
SN2007nc	10.6	22.2	12700[‡]	$2.6^{+2.2}_{-1.5}$

Mass from eq. 6.2 with $\kappa = 0.1\,{\rm cm^2\,g^{-1}}$ and $\tau_m = (\tau_{\rm rise} + \tau_{\rm dec})/2$. [a]Rise-time, defined $\tau_{\rm rise} \equiv t(L_{\rm peak}/e)$ for $t < t_{\rm peak}$; [b]time to fade, $\tau_{\rm dec} \equiv t(L_{\rm peak}/e)$ for $t > t_{\rm peak}$; [c]Velocity from Fe II λ5169; [*]Assumes $v \sim 6000\,{\rm km\,s^{-1}}$, from SN 2013hx; [‡]From literature, not necessarily Fe II; [†]Assumes $v = 10000\,{\rm km\,s^{-1}}$; [††]Assumes $\tau_{\rm rise} = \tau_{\rm dec}/1.6$ (Figure 6.4).

be more indicative of a threshold process – for example, only progenitors above some critical mass can form magnetars, or undergo a particular instability (e.g. pulsational pair instability; Woosley et al. 2007). In the magnetar model, there may also exist an observational 'desert' between cases where the spin-down power is sufficient to drive a stable jet (GRB), and cases where the spin-down is weaker and slower, forming a wind nebula and enhancing the late-time luminosity instead (SLSN). If the magnetar spins down very quickly but the jet does not break the stellar envelope, there may be neither a GRB nor an enhancement in optical brightness (B. Metzger, private communication.) In summary, peak magnitude distributions of SNe from large, homogeneous samples are needed, and will provide an important constraint on the possible relationships between SLSNe and other SNe Ibc.

6.6 Two types of SLSN Ic?

For most SLSNe, the data unambiguously exclude ^{56}Ni and ^{56}Co decay as the main power source around light curve maximum: the ^{56}Ni mass needed to power the peak is of the order of the total ejected mass inferred from light curve fitting, and moreover exceeds the limiting ^{56}Ni mass constrained by the late-time luminosity (e.g. Inserra et al. 2013). However, Gal-Yam (2012) proposed that the events with broader light curves, such as SN 2007bi, are radioactively powered, and likely exploded as pair-instability SNe. These would be fundamentally different from the other SLSNe, having a different explosion mechanism and power source, and would be characterised observationally by longer light curve timescales. Our analysis in Chapters 4 and 5 showed that the slowly evolving SLSNe seem to have more in common with the usual fast-declining events than with PISN models. We now look to see if we can distinguish two distinct classes in our larger sample. In fact, Figure 6.4 shows a relative lack of SLSNe with $\tau_{\rm rise} \sim$ 25-30 d and with $\tau_{\rm dec} \sim$ 40-60 d. To make this clearer, we plot histograms of $\tau_{\rm rise}$, $\tau_{\rm dec}$, and the g-band decline in magnitude 30 days after maximum light. This is a proxy for the decline timescale that is much simper to measure observationally, and particularly useful for parameterising the decline in high-redshift SLSNe, which may not have good rest-frame coverage in the redder bands. The data are shown in Figure 6.15.

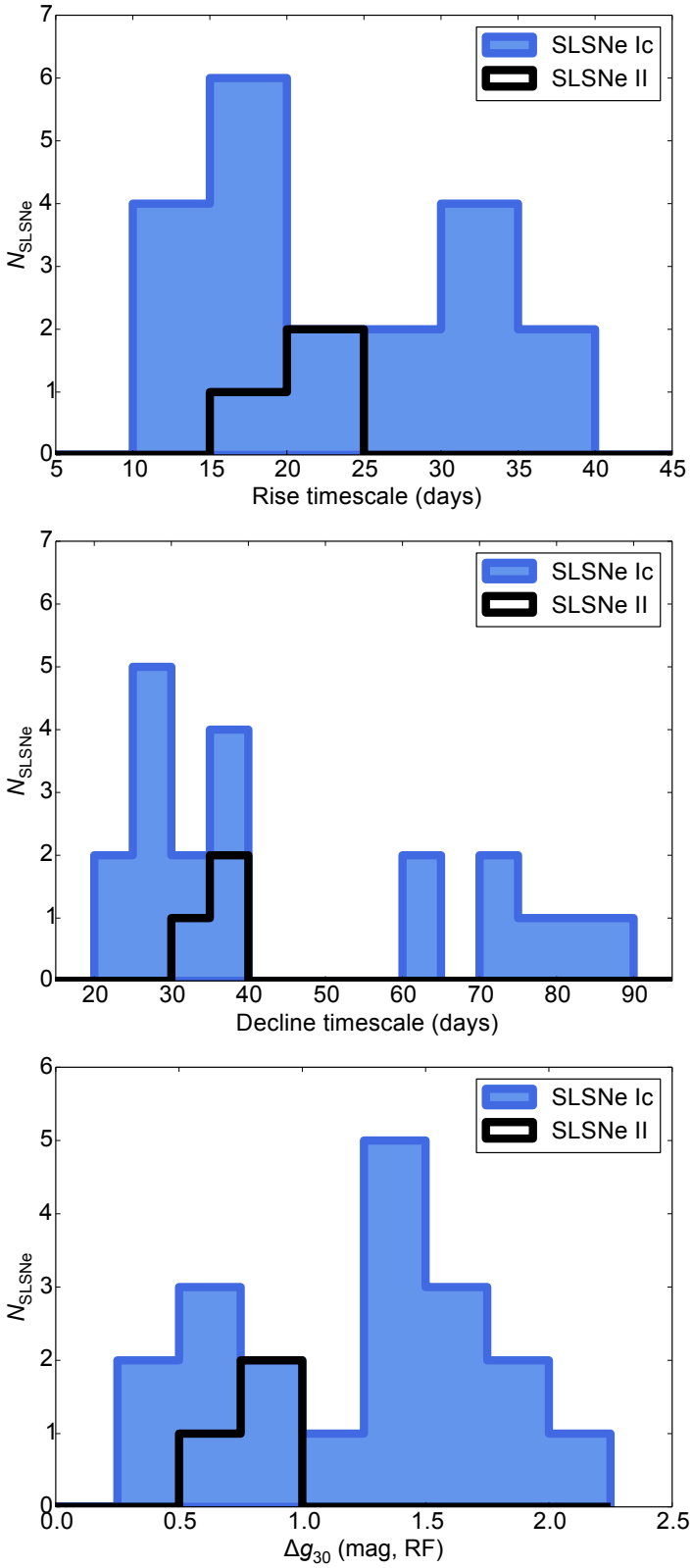

Figure 6.15: Histograms showing the rise (*top*) and decline (*middle*) timescales (binned in 5 day intervals), and the g-band decline (binned in 0.25 mag intervals) in 30 days after maximum (*bottom*). While the distributions show some indication of bimodality by eye, applying Hartigan's Dip Test (Hartigan & Hartigan 1985) shows that this is not statistically significant.

Table 6.4: Significance testing for bimodality

Property	Sample	Dip Statistic, D	p-value
Rise time	Full sample	0.060	0.801
	SLSNe Ic	0.069	0.666
Decline time	Full sample	0.067	0.605
	SLSNe Ic	0.077	0.439
Δg_{30}	Full sample	0.069	0.722
	SLSNe Ic	0.078	0.357
Estimated mass	Full sample	0.044	0.992
	SLSNe Ic	0.050	0.974

'Full sample' includes the 3 events with hydrogen lines in their spectra.

We apply the Dip Test of Hartigan & Hartigan (1985) to each parameter. The dip statistic, D, measures the maximum difference between the empirical distribution and a unimodal distribution chosen so as to minimise D. A larger value of D indicates that the data are not well described by a unimodal probability distribution function (PDF). We test for multi-modality using a bootstrapping method. We construct 5000 random sets of length n, where n is the size of our SLSN sample (n = 19 for our full sample), drawn from a uniform PDF, and calculate D for each set. The probability p-value for the null hypothesis to be correct (i.e. that the data are unimodal) is then given by $p = N(D_{\rm SLSNe} < D_{\rm boot})/5000$ (this is the fraction of random sets, drawn from a uniform PDF, which appear to be less unimodal than our data).

The results of the test (D and p) are shown in Table 6.4. In no case do we find statistically significant evidence for bimodality. Therefore we have no confidence in rejecting the null hypothesis, and cannot confirm the existence of two sub-classes (fast/slow) of SLSNe. The similarity in overall light curves (up to some stretch factor) presented in Sections 6.4-6.5 may actually be evidence in favour of a single class, and if so, likely a single distribution in timescales. We note, however, that we do see lower p-values when we remove the hydrogen-rich events from the sample – but not low enough to exclude a unimodal distribution of light curve timescales. Many more objects will need to be observed before a stronger statement can be made. If the SLSN population does turn out to be significantly bimodal when a larger sample is constructed, it could indicate either two separate explosion mechanisms, or two progenitor channels for the same explosion mechanism.

6.7 Spectral evolution

Quimby et al. (2011) first presented pre-maximum spectra of a sample of SLSNe from

PTF; the high degree of similarity enabled the authors to determine that these objects together formed a new class of SN. Since Pastorello et al. (2010) showed the spectroscopic evolution of SLSN 2010gx into a more typical SN Ic, all H-poor SLSNe have been seen to follow this path, including slowly-declining objects (Chapter 4). Here we compile high signal-to-noise spectra of 11 objects from our sample, to construct the complete spectral evolution, shown in Figure 6.16. The data for these are from the references in Table 6.1, and are available from WISeREP (Yaron & Gal-Yam 2012) or via the PESSTO data release through the ESO archive (Smartt et al. 2015).

The spectra before maximum are extremely blue, peaking at around 2500 Å, and are dominated by high-ionisation lines – particularly O II at around 4000 Å, which is seen here mainly in absorption. Blackbody fits at this phase give a colour temperature $T_{\rm col} \sim$ 15000 K. There is a major change at around maximum light: as the ejecta cool, the O II lines disappear (oxygen, with an ionisation potential of 13.6 eV, is mostly neutral O I at $T < 15000$ K), leaving the optical spectrum largely featureless. Within 10-20 days after the luminosity peaks, broad P Cygni lines of singly-ionised metals (with lower first ionisation potentials, $\sim$ 6-8 eV) emerge: mainly Ca II H&K, Mg II, Fe II blends (particularly between 5000-5500 Å) and Si II. By 30 days, these lines are strong, and the spectra closely resemble a conventional SN Ic at around maximum light (though even at this phase, SLSNe are often bluer than SNe Ic at peak). This similarity, and the slightly bluer colours, were highlighted in Figure 3.6.

The next lines to appear are O I λ7774 and the Ca II near-infrared triplet, along with the semi-forbidden Mg I] λ4571 emission. This line becomes dominant over the Mg II/Fe II P Cygni line somewhere around 30-50 days after maximum, and can be difficult to disentangle from the allowed transitions in the region. Strong forbidden emission lines do not appear in the spectra until over 100 days after maximum light (slowly declining objects such as PTF12dam are still not fully nebular at 200 days). In a normal SN Ic, [O I] $\lambda\lambda$6300,6363 and [Ca II] $\lambda\lambda$7291,7323 are already prominent at 60-100 days after peak. These do eventually become the strongest lines in our very late spectra (PTF12dam at 500 d; Chen et al. 2015). The late appearance of nebular lines in SLSNe may indicate densities higher than those in normal SNe Ic. However, the nebular transition point depends most strongly on the opacity of the ejecta, which is in turn determined by the ionisation of the dominant elements (opacity drops by several orders of magnitude when these recombine). Therefore the higher temperatures in SLSN ejecta could account for the slower evolution towards the nebular phase.

In Figure 6.17, we plot the colour temperatures measured from blackbody fits to our spectra (using the whole observed range in wavelength), as well as fits to the photom-

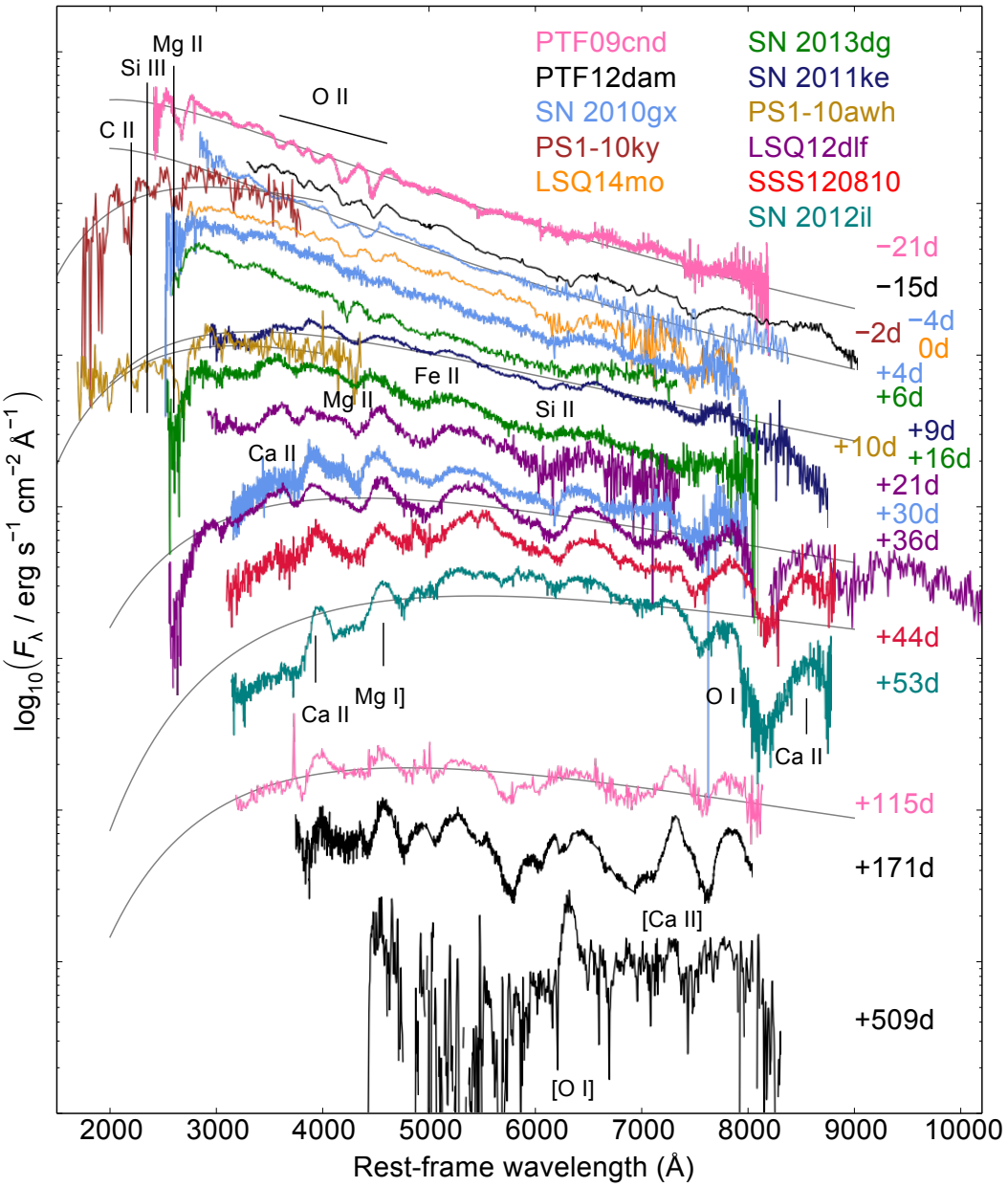

Figure 6.16: Typical spectroscopic evolution of SLSNe Ic. The grey curves are representative blackbody fits to determine the colour temperature (shown in Figure 6.17). The main line-forming ions are also marked.

etry of some well-observed low-z SLSNe Ic. The temperature evolution is markedly different from other Type Ic SNe, including the energetic SN 1998bw. SLSNe display (and maintain) much higher temperatures before and around peak light, and cool much more slowly afterwards. This requires significant heating over an extended period of time (several tens of days); therefore the abnormally high UV emission in SLSNe is a consequence of sustained energy input rather than a shock breakout phenomenon. This could plausibly be explained either by central engine models, or by CSM-interaction models, provided the CSM is sufficiently extended that the forward shock continues to

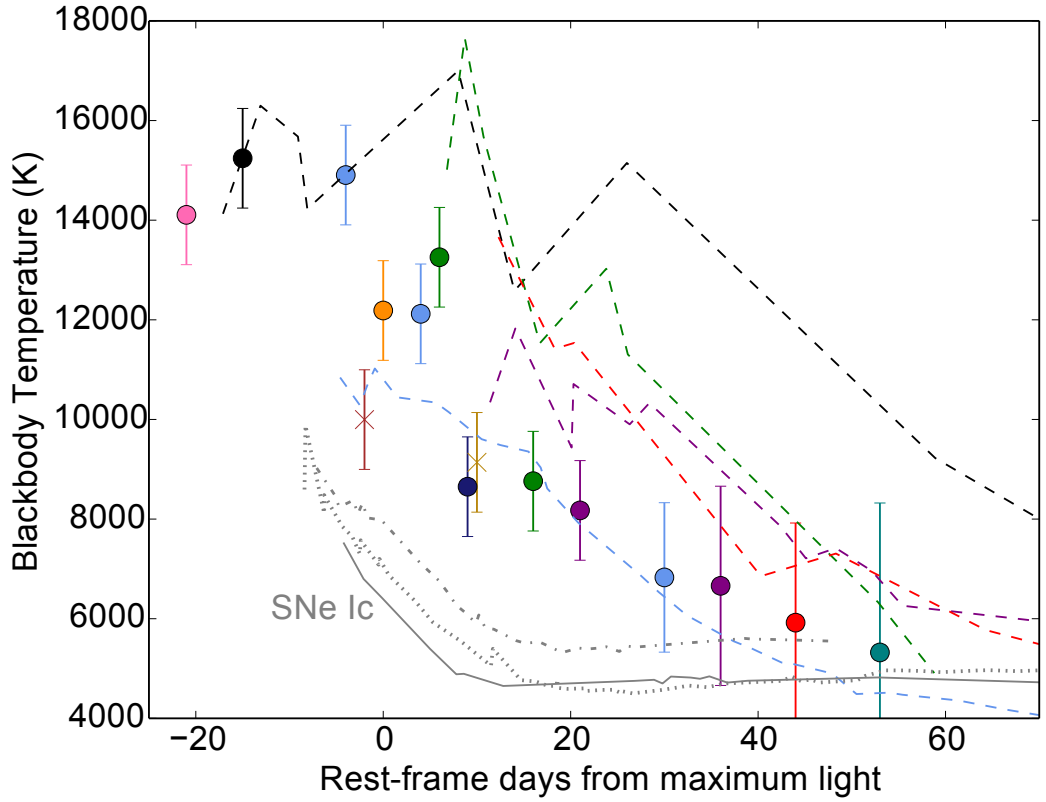

Figure 6.17: The evolution of the colour temperature for SLSNe Ic and normal SNe Ic. Colours are the same as in Figure 6.16. Temperatures are derived from blackbody fits to spectra (points) and photometry (lines). Photometric measurements tend to be hotter, as there is a lack of U-band data to constrain the fit at ~ 3000 Å, which is not a problem for the spectral fits. Crosses indicate UV spectra ($\lambda < 2000$ Å). The SNe Ic are 1994I (solid), 2007gr (dotted) and 1998bw (dot-dashed). SLSNe appear to have a slow evolution in colour temperature before maximum light, with typical $T_{\rm col} \sim 15000$ K. Around maximum light, the colour temperature drops rapidly, reaching ~ 10000 K approximately 10 days later. This is partly due to decreasing gas temperature, but the evolution is accelerated at this phase due to the emergence Mg II, Ca II and Fe II lines, which absorb flux in the blue. The SLSNe then cool at a constant rate for 50-60 days. Normal SNe Ic do most of their cooling soon after explosion, and reach a constant temperature (~ 5000 K) 10-20 days after maximum light.

propagate and deposit heat for tens of days after the SN becomes visible. The temperature behind a strong shock is approximately $T_s = 3/16 m v_s^2 k_B^{-1}$, where v_s is the shock speed, m is the average particle mass and k_B is the Boltzmann constant (McKee & Draine 1991). For singly-ionised, oxygen-rich material, the shock speed needed to reach $T \sim 15000$ K is $v_s \sim 12000\,{\rm km\,s^{-1}}$. In 10 days, such a shock travels $\sim 10^{15}$ cm, which is approximately the blackbody radius of the photosphere in SLSNe – thus the temperature evolution does seem to be consistent with interaction models.

However, there are several features of SLSN spectral evolution which may be difficult to reconcile with interaction-powered models. In particular

- We do not see narrow lines from slow-moving material in any SLSN Ic (though we do in CSS12105).
- Moreover, the dense, massive CSM required to match the luminosity should be extremely optically thick, so the spectral lines seen at early times should be from the outermost material. These lines are puzzlingly broad ($> 10000\,\mathrm{km\,s^{-1}}$) if they are not SN ejecta.
- The spectral evolution is very homogeneous among SLSNe. SNe which are known definitively to be interacting with their CSM (i.e. SNe IIn) exhibit quite diverse spectra, generally showing gas with a range of velocities.

These problems have been pointed out previously in Chapters 3-5. Thus, the spectral evolution is more easily explained without circumstellar interaction. The most natural interpretation is that the ejecta from SLSNe have a similar composition to that of SNe Ic, but have much higher temperatures due to heating from a power source equivalent to several solar masses of nickel. For this reason, we do not see normal SN Ic spectral lines until later in the evolution, instead seeing a very blue continuum and high ionisation lines around peak. The slow spectral evolution may be exacerbated by higher densities in SLSNe.

6.8 Velocity measurements

The analysis in Section 6.4 demonstrated that diffusion time in the ejecta is the most important factor in generating the observed diversity in SLSN light curves. As shown by Equation 2.5, this timescale is a function of ejected mass, velocity and opacity. Since all of our SLSNe Ic have very similar spectral evolution, we expect that they have similar compositions and ionisation states, and hence similar opacity. This leaves us with a degeneracy in M_{ej} and the expansion velocity, v. Velocities can be estimated using the spectra, allowing us to break this degeneracy, and to determine whether it is variations in M_{ej} or v that are most important between the SNe (super-luminous and normal) in our sample. We measure velocities using the absorption minimum of the Fe II λ5169 P Cygni profile. In Figure 6.18, we show spectra of all our SLSNe at phases of 20-30 d after maximum, in the wavelength region around this line.

For a few objects, we have sufficient temporal coverage and signal-to-noise to measure the velocity over a period of more than 30 days, and follow how it evolves. This is shown in Figure 6.19. The velocities are remarkably constant in time, declining by at most $2000\,\mathrm{km\,s^{-1}}$in the first 30 days after maximum light (and in many cases showing no clear decline at all). This is quite discrepant with the velocity evolution

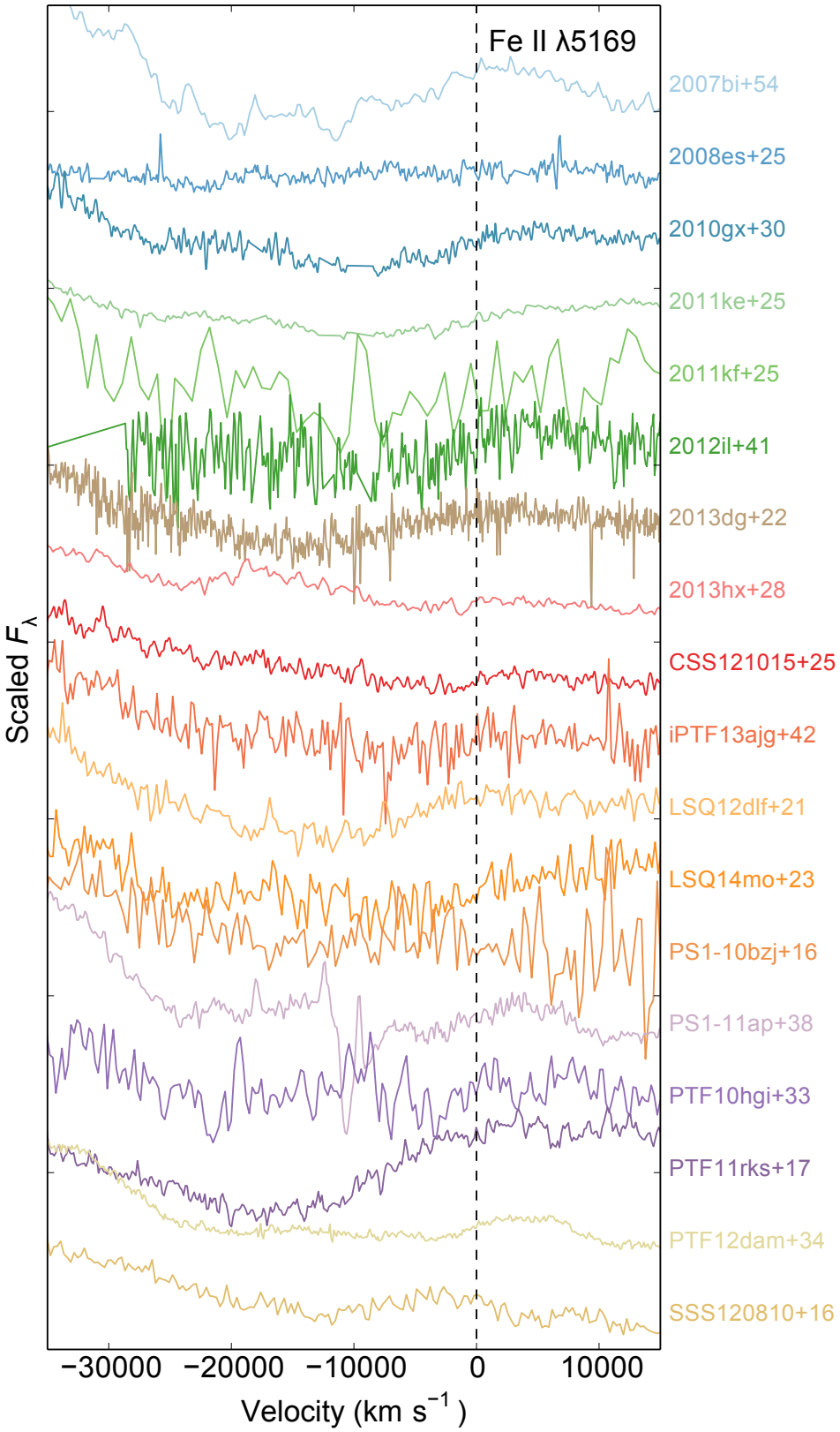

Figure 6.18: The Fe II λ 5169 line profile in SLSNe at $\sim$ 20-30 days after maximum light. The minimum of the absorption trough gives an indication of the photospheric velocity. The line is clearly weaker (or absent entirely) in our SLSNe II (2008es, 2013hx and CSS121015) – it does not become prominent in these objects until $\gtrsim$ 40 d after maximum light (Benetti et al. 2014).

of other SNe Ic, such as the sample from Valenti et al. (2012) also shown in the figure. In normal SNe Ic, the ejecta expand in a roughly homologous fashion (a natural consequence of a spherical shock; Arnett 1980). Thus, as the ejecta expand and the photosphere recedes to deeper layers, we see more of the relatively slow-moving inner material, and hence measure lower velocities. Constant velocities, on the other hand, are predicted by the magnetar models of Kasen & Bildsten (2010), who showed that for magnetars with rotational energy greater than the kinetic energy of the SN ejecta (i.e. $\gtrsim 10^{51}$ erg), essentially all of the ejecta is swept up into a dense shell of uniform velocity. This is an unavoidable consequence of the central overpressure, and thus far the clearest observational test for engine-powered SNe. The fairly flat velocity curves of our SLSNe are therefore consistent with the Kasen & Bildsten (2010) models. This was also pointed out by Chomiuk et al. (2011), in their study of SLSNe PS1-10ky and PS1-10awh. Moreover, because of this slow evolution, we can use velocity measurements at 20-30 days after maximum light as a reasonable proxy to the velocity at day 0, which is useful as for most objects we do not have good detections of Fe II until the later phases.

The velocity measurements from the Fe II line are given in Table 6.3, as well as velocities for the SDSS SN Ibc sample from Taddia et al. (2015), and the distributions for SLSNe and SNe Ibc are shown in Figure 6.20. The velocity distributions of SLSNe and normal SNe Ibc are almost indistinguishable within the errors: the median velocity for SLSNe is 10500 km s^{-1}, with a standard deviation of 3100 km s^{-1}, while the median for normal SNe Ibc is 9800 km s^{-1}, with a standard deviation of 2500 km s^{-1}. The SNe Ic-BL, on the other hand, all have velocities greater than 15000 km s^{-1}. The similarity between typical photospheric velocities at peak light for super-luminous and normal SNe Ic indicates that the broader light curves and slower spectral evolution in SLSNe are not caused by slower expansion. However, there is a possible caveat to this: since SLSNe have higher temperatures, and therefore higher ionisation, the photosphere may be formed further out in mass coordinate compared to normal SNe Ic, and therefore amidst faster moving ejecta. This would give a high velocity at the photosphere even if the bulk expansion was slower. Inserra et al. (2013) looked at the widths of [Ca II] and Mg I] emission lines in late spectra of SLSNe, which give an independent trace of the expansion velocity, finding typical values of 10000 km s^{-1}, fully consistent with our estimates from the Fe II P Cygni lines. We did the same for PTF12dam in Chapter 4, finding a similar result. This gives us confidence that SLSNe expand at least as fast as other SNe Ic.

Two of our objects, LSQ12dlf and SSS120810, do show significant velocity evolu-

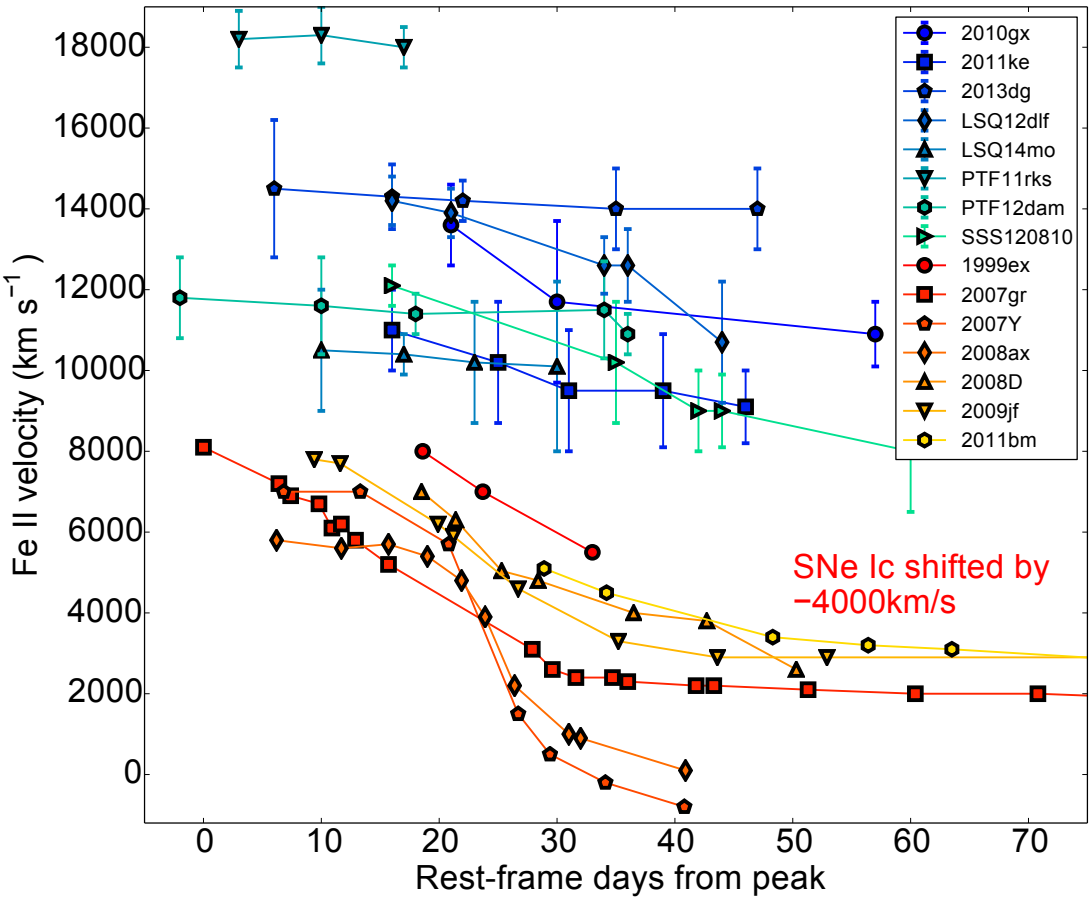

Figure 6.19: Velocity evolution of well-observed SLSNe Ic. All velocities have been measured from Fe II λ5169 absorption minima. The SN Ic velocities are taken from Valenti et al. (2012), who used the same method; these have been shifted downwards by 4000 km s^{-1} for clarity of presentation. The velocity curves for SLSNe are seen to be much flatter than those of SNe Ic, where we see a rapid decline after maximum light.

tion. We also note that Inserra et al. (2013) found evidence of decreasing photospheric velocity in some SLSNe Ic, compatible with the predictions of simple spherical models, rather than dense shells. They presented Fe II velocities close to maximum light for a number of objects, whereas here we had difficulty in reliably determining the Fe II profiles at such early epochs, when the line is very weak. The apparent velocity decline shown in their study also relied on measurements of different lines at different epochs, including emission line widths at late times. In fact, their Fe II velocities after 15-20 days from peak are flatter than at early times, and in reasonable agreement with our measurements here. However, if these objects do show an initial velocity gradient, it may indicate that the process causing the flat velocity evolution (for example, a second shock) has not yet terminated, or may suggest a tail in the ejecta distribution extending to high velocity. Another possibility is that the overpressure from a central engine is anisotropic (stronger along the polar axes; Bucciantini et al. 2007). An observer might

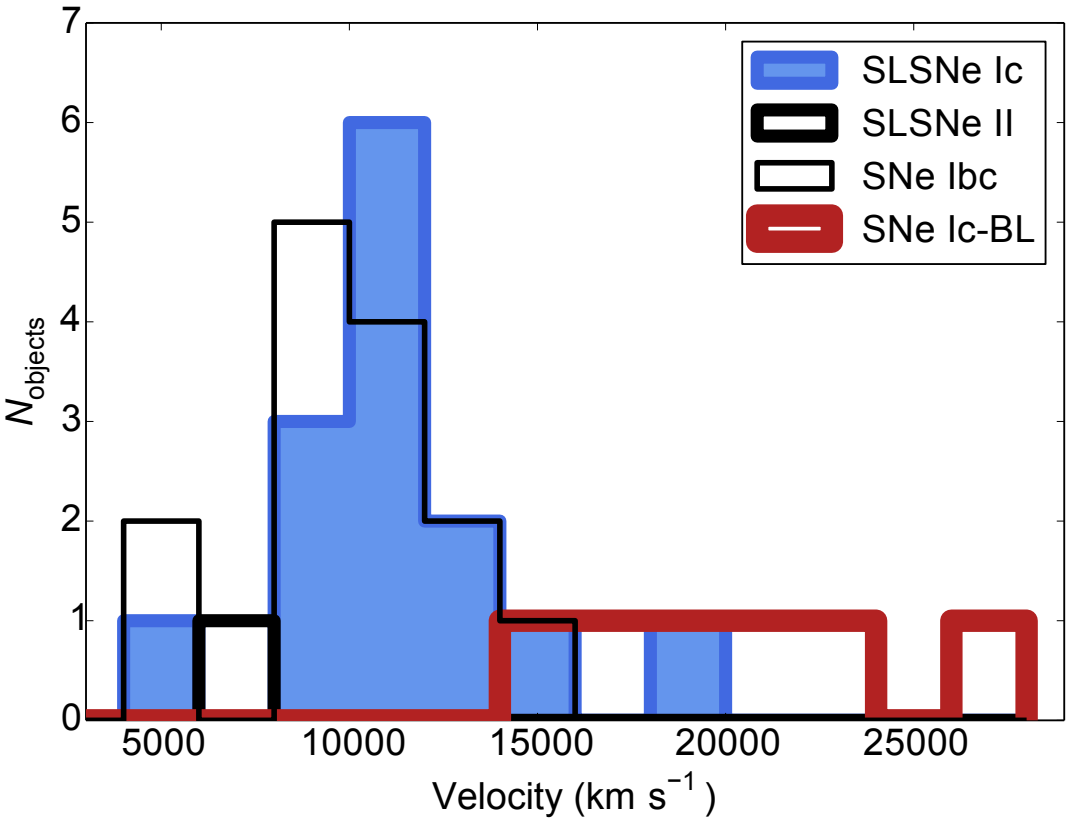

Figure 6.20: Photospheric velocities measured from the lines shown in Figure 6.18, compared with the velocities of SNe Ic at maximum light (the same objects in Figure 6.4). Bin size is 2000 km s^{-1}. Most SLSNe have velocities close to the mean value, $\approx$ 10800 km s^{-1}, with a standard deviation of $\approx$ 3000 km s^{-1}. The outliers are PTF11rks (fast) and PTF10hgi (slow). The other slow object is CSS121015, though the Fe II line is very weak at this epoch (and not robustly detected in SN 2008es or SN 2013hx, the other SLSNe II). The median velocities are 10500 km s^{-1}, 9800 km s^{-1} and 20400 km s^{-1} for SLSNe, normal SNe Ibc and SNe Ic-BL, respectively.

initially see high velocities from the faster polar region, with lower τ_m, before later seeing the contribution from the slower, higher-τ_m equatorial material. In any case, if peak velocities estimated from our measurements at 20-30 days are really lower limits, higher velocities at peak in SLSNe compared to normal SNe Ibc would only serve to strengthen our conclusion: the broad light curves of SLSNe cannot be explained by low velocities.

6.9 Mass estimates

Having shown that velocity is not the parameter driving the diversity in SLSN timescales, and if the opacity is similar for all of our objects, we are left with the

ejected mass as the most important factor. Equation 2.5 can be rearranged to give

$$M_{\rm ej} = 7.7 \times 10^{-7} \left(\frac{\kappa}{0.1\,{\rm cm^2\,g^{-1}}} \right)^{-1} \frac{v}{\rm km\,s^{-1}} \left(\frac{\tau_m}{\rm days} \right)^2 {\rm M_\odot}, \tag{6.2}$$

where all variables have their usual meanings, and our velocity measurements are taken from Section 6.8. There is an important caveat to these velocities: we have measured the velocity of the photosphere ($v_{\rm ph}$), whereas the v in Equation 6.2 is the ejecta 'scale velocity' (Arnett 1980, 1982). There is no simple way to measure this scaling velocity, and it is unclear whether the photospheric velocity is a good representation of it. However, we will proceed with the assumption that $v \sim v_{\rm phot}$.

In previous chapters, we have assumed in most cases an opacity $\kappa = 0.2\,{\rm cm^2\,g^{-1}}$ for SLSNe (i.e. the gas is close to fully ionised). However, as discussed in section 2.4, this is subject to significant uncertainty. Inserra et al. (2013) used a value $\kappa = 0.1\,{\rm cm^2\,g^{-1}}$. They showed that this is a reasonable approximation for opacity dominated by electron scattering, if the temperature behind the photosphere is $\sim 10^5$ K. In that case, abundant species such as oxygen, carbon and iron will then be roughly half ionised. Shortly after explosion, we expect full ionisation, but this drops as the expanding SN cools. Assuming that oxygen is the most abundant element in SLSN ejecta, the prevalence of O II lines in the spectra before maximum light, and their prompt disappearance afterwards, suggests that the ionisation is close to full for the duration of the light curve rise, but that after peak the ionisation fraction drops to about a half. The opacity will therefore vary over the duration of the light curve, from $\kappa \approx 0.2\,{\rm cm^2\,g^{-1}}$ before maximum to $\kappa \approx 0.1\,{\rm cm^2\,g^{-1}}$ afterwards.

However, variable opacity is not taken into account in the Arnett (1982) formalism. For modelling normal SNe Ic in this scheme, most authors use constant (essentially, time-averaged) opacities of $\kappa = 0.07 - 0.1\,{\rm cm^2\,g^{-1}}$. The additional energy source may maintain higher ionisation and opacity for longer in SLSNe, but this is unlikely to be by more than a small factor (at least during the declining phase when the spectra are similar), simply because progressively more energy is required to remove successive electrons from an ion. From Equation 6.2, increasing the opacity decreases the derived mass by the same factor. In order to make a clean comparison between SLSNe and normal SNe Ibc, we will first use a fiducial opacity $\kappa = 0.1\,{\rm cm^2\,g^{-1}}$ for all objects, and then investigate the effect of doubling the opacity in SLSNe.

The final parameter to estimate is the diffusion timescale, τ_m. This was discussed in detail, both in general and for specific models, in Section 6.4, but we recap here for convenience. It is common practice to use the rise time as an estimate of τ_m (for a recent example, see Wheeler et al. 2015). This is approximately true in the origi-

nal formulation of Arnett (1982), but that derivation was only for ^{56}Ni-powered SNe (^{56}Ni having an exponential lifetime of 8.8 days, comparable to the diffusion time in SNe Ia). As the decay time of ^{56}Ni is fixed, the power input is the same for all normal Type I SNe, and any variation in light curve timescales depends only on the diffusion time. However, SLSNe may have a range of power input times, for example magnetars can have different spin-down times, which may be much longer or shorter than the diffusion time. While it remains true that the diffusion time should generally be represented in the shape of the light curve around peak, we lack a straightforward mapping between τ_m and either $\tau_{\rm rise}$ or $\tau_{\rm dec}$. As a best estimate, we take $\tau_m \approx (\tau_{\rm rise} + \tau_{\rm dec})/2$, which is true for many scenarios (see Sections 6.4.3-6.4.5), and use the rise and decline timescales as upper and lower limits on τ_m. The uncertainty in mass owing to the choice of timescale is a factor of $\lesssim 2$.

More precise determinations can only be done through detailed modelling. Our goal here is not to derive the most exact masses, but to provide estimates for our sample in the most general and homegeneous way possible, thus exposing any underlying trends. One caveat we should add is that we have referred to the *ejected* mass, but this assumes that the entire diffusion mass associated with the light curve is SN material; if SLSNe Ic are powered by CSM-interaction, the diffusion mass we are probing is a combination of ejecta *and* CSM. However, most of our analysis in this paper indicates that SLSNe are governed by generally similar physics to SNe Ibc, i.e. rapidly expanding material being heated from the inside. We therefore propose that our derived masses are likely representative of the ejecta. In the final chapter, we will compare these simple mass estimates with the results of direct model-fitting.

The masses derived using our method are given in Table 6.3 (with lower and upper error bars calculated using $\tau_m = \tau_{\rm rise}$ and $\tau_m = \tau_{\rm dec}$, respectively). The mean ejecta mass in the SLSN sample is 10.1 $M_\odot$ (standard deviation: 9.0 $M_\odot$), compared to 3.1 $M_\odot$ (2.9 $M_\odot$) and 3.1 $M_\odot$ (1.3 $M_\odot$) for the normal and broad-lined SNe Ibc, respectively. The median masses are 6.0 $M_\odot$, 2.5 $M_\odot$, and 2.9 $M_\odot$ for the three samples. While we are sensitive to small-number statistics here, the peak of the SN Ic-BL mass distribution appears to be at higher mass than the distribution for normal SNe Ibc, especially if the extreme outlier SN 2011bm is neglected (giving a mean/median SN Ibc mass of 2.4/2.3 $M_\odot$). Taking only the SNe with an observed GRB counterpart (SNe 1998bw, 2010bh and 2012bz), the mean of 4.5 $M_\odot$ is intermediate between SNe Ibc and SLSNe. Figure 6.21 shows the ejecta mass distributions for SLSNe, SNe Ibc and SNe Ic-BL, with the ejected mass higher for SLSNe by a factor of 2-3. Although the SNe Ic-BL appear to be skewed towards higher mass than normal SNe Ibc, overall they seem to eject significantly less mass than the SLSNe. This supports the view of Leloudas et al. (2015), who suggested that SLSNe have more massive progenitors than

long GRBs, but may be in tension with the results of Lunnan et al. (2015), who found that SLSNe do not trace host galaxy UV light (star formation) as closely as do long GRBs, implying older/lower-mass progenitors.

There are clearly several very massive ($M_{\rm ej} \sim$ 20-30 $\rm M_{\odot}$) SLSNe compared to the normal/broad-lined Ibc sample, for which only SN 2011bm hints at a high-mass tail. Five SLSNe eject over 20 $\rm M_{\odot}$, yet there are only two objects in the 10-20 $\rm M_{\odot}$ regime. To check whether this high-mass tail could be fully explained as a consequence of greater ionisation in SLSNe (e.g. due to the hard radiation field from a magnetar; Metzger et al. 2014), we rescale the masses to $\kappa = 0.2\,\rm cm^2\,g^{-1}$ in the bottom panel of the figure. In this case, the bulk of the SLSN sample have masses consistent with the normal SN Ibc population. However, there is still a clear excess of events with $M_{\rm ej} \gtrsim 10\,\rm M_{\odot}$. Therefore even if many of the SLSN light curves can be explained as a consequence of high ionisation, there remains a substantial number of events that must eject significantly more mass than normal stripped SNe.

As a quick check of whether these high masses are consistent with more detailed modelling, we look at the magnetar fit to PTF12dam in Chapter 4. The derived mass for PTF12dam was $\sim 20\,\rm M_{\odot}$ (after correcting for the velocity offset between the data and the model; see Table 4.6 and Figure 4.11), using an opacity $\kappa = 0.2\,\rm cm^2\,g^{-1}$. We also note that Kasen & Bildsten (2010) reproduced the light curve of SN 2007bi with a magnetar model and 20 $\rm M_{\odot}$ ejecta, for the same opacity. In our estimates here, we have used $\kappa = 0.1\,\rm cm^2\,g^{-1}$. For a fixed explosion energy and diffusion time, halving the opacity means increasing the ejecta mass by a factor ~ 1.6 (Section 2.4). Our simple estimates of 27.0 and 31.1 $\rm M_{\odot}$, for PTF12dam and SN 2007bi respectively, are thus quite consistent with detailed light curve models. This gives us confidence in our simple mass derivations.

The interesting question, then, is whether we have detected a separate population of high-mass SLSNe, arising from a different progenitor, explosion mechanism, or power source. Effectively, this is the physical interpretation of the simple observational result illustrated in Figure 6.4 (and discussed in Section 6.6) that the rise-decline correlation visually picks out two groups of objects. We apply Hartigan's Dip Test, as described in Section 6.6, to our distribution of SLSN masses. We find that $D = 0.050$ and $p = 0.974$, showing that the most massive SLSNe are fully consistent with being the tail of a continuous distribution. However, many more objects will be required in order to test this more robustly. There may also be an observational bias here: broad light curves are easier to detect than fast ones, which could lead to the more massive objects being over-represented.

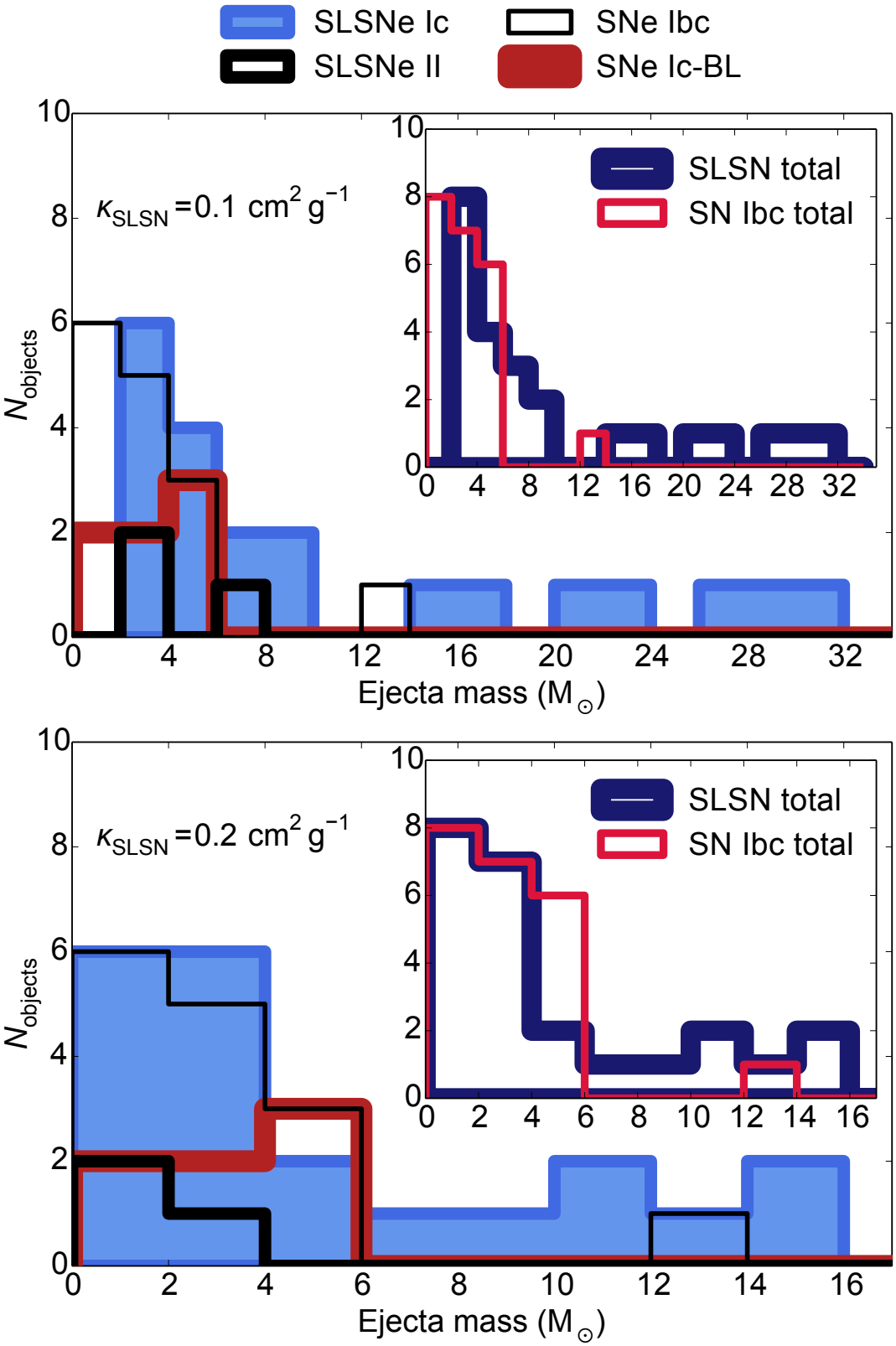

Figure 6.21: The ejecta mass distribution for SLSNe and other H-poor SNe. SLSNe seem to arise from explosions ejecting $\gtrsim 2$ times the mass, on average, ejected by normal and broad-lined SNe Ibc. However, the mass distributions appear more similar if the opacity in SLSNe is a factor 2 higher than in other SNe Ibc. A magnetar wind is a good candidate to increase the ionisation (hence opacity) in the ejecta (Metzger et al. 2014).

The masses also place constraints on explosion models. A core-collapse explosion ejecting $20\,M_\odot$ might be expected to produce a black hole rather than a neutron star (Heger et al. 2003). However, recent theoretical results have shown that the final fate of a massive stellar core (neutron star or black hole) is unlikely to be monotonic in mass (e.g. O'Connor & Ott 2011; Clausen et al. 2015). In particular, Dessart et al. (2012c) have shown that in rapidly-rotating stars (potential GRB and SLSN progenitors), magnetars are produced more naturally. Nevertheless, if a black hole is formed in the core collapse, the central engine mechanism could still apply, in this case in the form of fall-back accretion (Dexter & Kasen 2013) rather than magnetorotational powering. It should be noted that the fall-back models considered by Dexter & Kasen (2013) only produced super-luminous light curves if the progenitors retained their hydrogen envelopes, in order to delay fall-back to later times. The progenitors of SLSNe are expected to be stripped of their hydrogen, though in Chapter 5 we saw evidence that they may exhibit an inflated He envelope at the time of explosion (see also Piro 2015).

Taking our upper limits on ejecta mass (from the decline timescales), the most massive objects may eject as much as 40-60 $M_\odot$, suggesting that pair-instability explosions should be considered as viable models. However quantitative comparisons do not lead to comfortable agreement between the observed timescales and detailed models. Firstly, as shown by Gal-Yam et al. (2009), Kasen et al. (2011), Dessart et al. (2012b) and our analysis in Chapter 4, H-poor PISN models with $M_{\rm ej} \gtrsim 100\,M_\odot$ are needed in order to match the observed peak luminosities of SLSNe. This is a factor 2 higher than our most optimistic mass estimates. There is also a larger problem, which is independent of our mass estimates. The $120\,M_\odot$ model of Kasen et al. (2011) has $\tau_{\rm rise} = 72$ d and $\tau_{\rm dec} = 99$ d, defined in the same way as for our objects (in these PISN models, the decline timescale is mainly set by ^{56}Co decay, which has a timescale of 111 d). A few of our objects have $\tau_{\rm dec} \gtrsim 80$ d, but all have $\tau_{\rm rise}$ shorter than the PISN model by at least a factor of 2. This is the same problem we found when investigating PISN models for PTF12dam. Our measurements here reinforce the conclusion: that even the 2007bi-like SLSNe do not quantitatively match the pair-instability explosion models.

6.10 Summary of results

Many results have been presented in this chapter, so for convenience we summarise our main findings here:

- SLSNe Ic typically have *griz* pseudobolometric magnitudes in the range $-20 \gtrsim M_{griz} \gtrsim -21.5$, with a mean of -20.72 and a standard deviation of 0.55.

- Their light curves obey a fairly tight relationship between rise and decline rates around maximum light, with $\tau_{\rm dec} \approx 2\,\tau_{\rm rise}$. This is naturally produced by simple diffusion models, but the lack of scatter may be difficult to explain with models requiring circumstellar interaction. For CSM interaction models to be the sole explanation, they must have CSM mass comparable to the ejected mass (at a large radius). In addition they require the CSM to have a surprisingly narrow range of densities across all the objects.

- The shape of the light curve around peak is intrinsically very similar to that of normal SNe Ibc, except SLSNe are broader and brighter. SNe Ic-BL, including GRB-SNe, may span the magnitude gap between spectroscopically normal SNe Ic and SLSNe.

- SLSNe Ic span a wide range of light curve timescales, but there is not yet statistically significant evidence for separate populations of fast- and slowly-evolving objects. It may be one continuous distribution.

- The spectroscopic evolution requires sustained heating around peak, to maintain a temperature $T_{\rm col} \sim 15000\,{\rm K}$ despite weeks of expansion. At around one month after maximum light, SLSNe have cooled to temperatures comparable to normal SNe Ic at maximum, at which point the spectra show very similar photospheric-phase lines. This implies similar ejecta composition.

- The temperature evolution is consistent with both central-engine and circumstellar-interaction light curve models.

- The broad lines at all phases, lack of narrow lines in any object, similarity to SNe Ic, and the overall homogeneity of SLSN spectra all argue against significant modification of the spectra by CSM.

- SLSNe and normal SNe Ibc have similar photospheric velocities around maximum light. After 0-10 days from peak, this velocity stays remarkably constant in time for many SLSNe. This could be explained by a re-shock from their central power source, sweeping the ejecta up into a uniform shell (Kasen & Bildsten 2010).

- For a given opacity, the ejected mass, derived from measured Fe II λ 5169 velocities and simple estimates of the diffusion timescale, are on average $\gtrsim 2$ times higher than the masses in normal and energetic SNe Ibc (although there is overlap). However, an alternative explanation is that the opacity in SLSNe is twice as high as in other SNe Ibc. Such an effect could possibly arise from a magne-

tar ionisation wind (Metzger et al. 2014). There is no statistical evidence for a bimodal mass distribution in SLSNe.

- SLSNe may eject as much as several tens of solar masses of material. Our estimates are consistent with masses derived from magnetar-powered light curve fits. The masses seem to be too low (and the light curve evolution too fast) to be consistent with pair-instability models.

To conclude, we have investigated the physical properties of the largest sample of super-luminous SNe constructed to date, and have found that they appear to be closely linked with normal SNe Ic. All of the properties of the class can be explained by taking a normal SN Ic, increasing the ejected mass, and re-shocking the ejecta using a powerful central energy input, such as the emission from magnetar spin-down. The key observables are a peak luminosity boosted by ~ 3 magnitudes, a broader light curve from the large diffusion mass, and a flat velocity evolution caused by the hydrodynamical impact of the additional energy source. At late times, the light curve shape deviates from that of a normal SN Ic, which follows the radioactive decay of ^{56}Co after a few diffusion times from peak. In super-luminous objects, the ^{56}Co decay is masked by some other dominant heat source, for example magnetar radiation.

Chapter 7

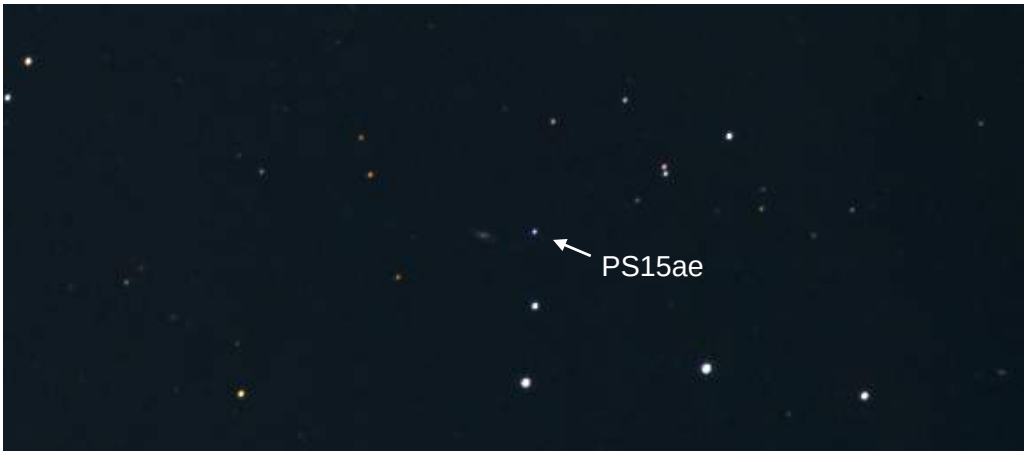

Discussion and conclusions

"Logical validity is not
a guarantee of truth"
- David Foster Wallace ('Infinite Jest')

7.1 What do we know about super-luminous supernovae?

In the course of this thesis, we have presented detailed studies of a number of low-redshift SLSNe Ic, with some of the best light curve and spectral coverage of such objects to date, and have supplemented our data with other SLSNe from the literature to construct a large sample of these objects for a homogeneous analysis. We comment on some of the main observational results and their significance.

SLSNe Ic are hydrogen- and helium-poor explosions characterised by broad, luminous light curves, peaking 30-60 days after explosion at absolute magnitudes $-21 \gtrsim g_{\rm AB} \gtrsim -22.5$. The width of the light curve relative to the more common population of SNe Ic suggests that SLSNe Ic eject more mass or have a higher opacity in the ejecta (or some combination of the two). The large scatter in widths within the SLSN class implies a large range of ejected masses, from a few solar masses up to possibly several tens.

We have discovered non-monotonic light curves for two of our objects. Such a phenomenon has only been seen previously in SN 2006oz (Leloudas et al. 2012). Similar to that event, LSQ14bdq exhibited a bright, fast optical peak a few days after explosion and before the main rise to maximum light. The luminosity of the early peak ($M_g \approx -20$) suggests a surprisingly large radius ($> 100\,{\rm R}_\odot$) at shock breakout. Constraining the rate of these precursor peaks within the SLSN population will offer an important insight into their progenitors. On the other hand, SSS120810 showed a secondary peak during the declining phase of the light curve. This behaviour has not been seen before in any SLSN, and its origin is highly uncertain. The presence of such bumps shows the need for dense photometric sampling across the light curve.

The spectra before and around light curve maximum are very blue, with colour temperatures of $T_{\rm col} \approx 15000\,{\rm K}$. At this time, the main atomic lines visible in the optical are attributed to singly-ionised oxygen. After 10-30 days from peak, the temperature has cooled to a regime comparable to normal-luminosity SNe Ic at peak ($\lesssim 10000\,{\rm K}$), and the spectra then exhibit singly-ionised lines from other metals with lower ionisation potential, commonly seen in SNe Ic: iron, magnesium, calcium and silicon. Line widths suggest typical velocities of $v_{\rm ph} \approx 10000\,{\rm km\,s^{-1}}$, with many objects showing little sign of deceleration over many weeks. This likely indicates the presence of a dense shell of ejecta with uniform velocity.

7.2 Discussion of models

Semi-analytic models, building on the work of Inserra et al. (2013) and Chatzopoulos et al. (2012) have been developed and applied in a bid to constrain the power source behind these remarkable objects. We will discuss the successes and failures of each class of model below.

7.2.1 ^{56}Ni-powered models

In nearly all cases, radioactive ^{56}Ni-decay models require unrealistically high ratios of nickel mass to ejecta mass ($M_{\rm Ni}/M_{\rm ej} \sim 1$) and are thus excluded as the origin of SLSNe. The objects with the slowest declines after maximum light, such as SN 2007bi, were previously thought to be ^{56}Ni-powered 'SLSNe R'. The most promising physical explosion for producing the necessary $M_{\rm Ni}$ (at least 4-7 $\rm M_{\odot}$; Gal-Yam et al. 2009) is a pair-instability explosion of an extremely massive star. However, our data for PTF12dam and LSQ14bdq (Chapters 4 and 5) show that the rise times of these objects are faster by about a factor of two compared to hydrodynamical PISN calculations by Kasen et al. (2011) and Dessart et al. (2013). The implied ejecta masses are much lower (10-30 $\rm M_{\odot}$) than the core masses needed to produce a PISN ($M_{\rm core} > 65\,\rm M_{\odot}$), and particularly a luminous PISN ($M_{\rm core} \gtrsim 90\,\rm M_{\odot}$). The PISN interpretation of these SLSNe is therefore not observationally or physically motivated. We found that in fact the slowly evolving SLSNe Ic are virtually identical to the faster objects apart from a stretch in time. We thus propose that no super-luminous PISNe have yet been observed, and that such objects are rarer than other SLSNe by about a factor of 10.

7.2.2 Central engine models

Two main models have been found to consistently reproduce SLSN light curves with physically plausible input parameters. The first of these is the central engine scenario, best exemplified by the well-studied magnetar spin-down model. Fitting our objects with the magnetar model yields the following typical parameters:

- $M_{\rm ej}$~ 4-20 $(\kappa_{0.2\rm cm^2 g^{-1}})^{-1}\,\rm M_{\odot}$
- $B \sim$ a few $\times 10^{14}$ G
- $P \sim 2$ ms

Decreasing the opacity (incomplete ionisation) increases the derived mass. This uncertainty in the opacity is probably the biggest limitation in deriving parameters from our

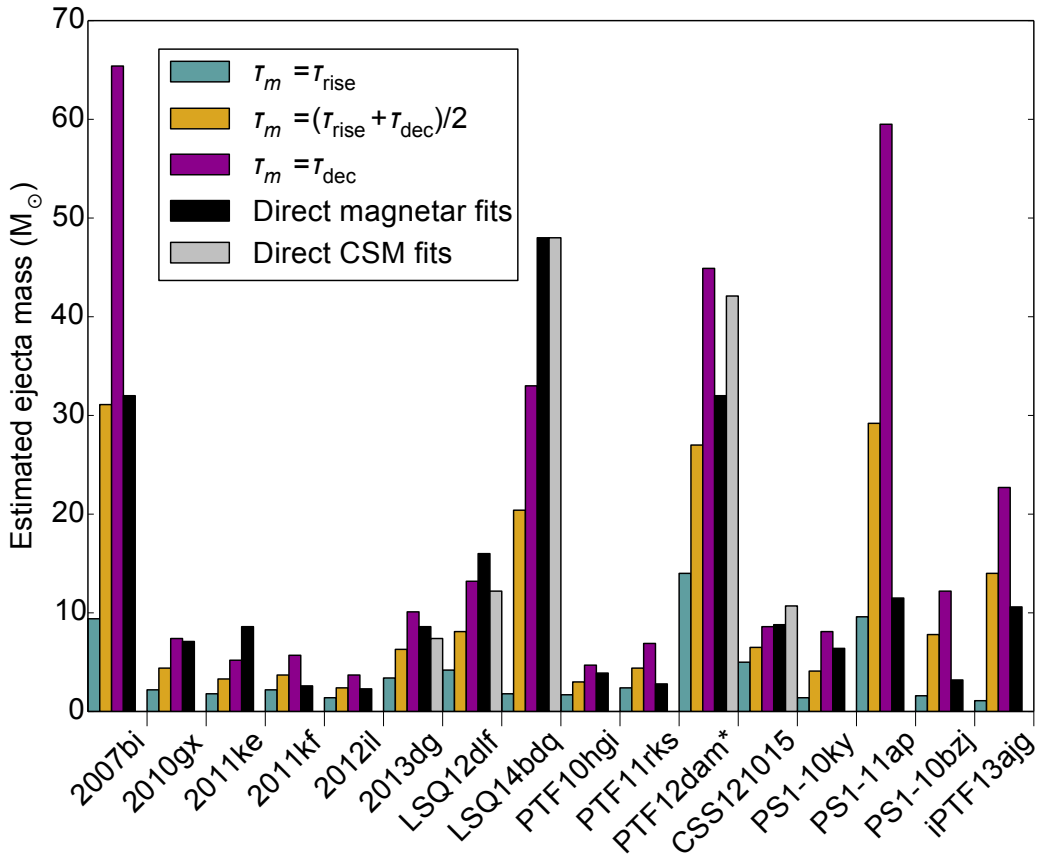

Figure 7.1: Mass estimates from light curve timescales (Chapter 6) compared to detailed models from earlier chapters and the literature (see references in Table 6.1). The yellow bars correspond to our best estimates, while the teal and magenta bars give the upper and lower limits (Table 6.3). This simple method for estimating masses gives good agreement with direct magnetar and interaction model fitting. All model masses have been scaled to $\kappa = 0.1$ cm^2 g^{-1}. The magnetar model for PTF12dam has also been corrected for a velocity discrepancy (see Section 4.5.3).

simplified models. The best-fit masses in this model are found to be quite consistent with estimates that are independent of the power source, where we use the light curve width to measure the diffusion time (Chapter 6). Figure 7.1 compares the masses from magnetar fitting (here and in the literature) with our simple estimates from Chapter 6. In most cases, we find reasonable agreement between the masses from the two methods if we take $\tau_m \approx (\tau_{\rm rise} + \tau_{\rm dec})/2$, supporting our assertion in Sections 6.4.5 and 6.9 that the average of the rise and decline timescale gives the best estimate of the diffusion time.

Other central engine models have been proposed, for example fallback accretion onto a newly-formed black hole (Dexter & Kasen 2013). The fallback scenario may allow for larger initial kinetic energies (Chapter 5). However, if the progenitors are compact, the rate of fallback is expected to peak too early to power a super-luminous

light curve (Dexter & Kasen 2013, B. Metzger private communication). This would of course be problematic for SLSNe Ic, if their progenitors resemble typical Wolf-Rayet stars. In any case, it is magnetar models that have been explored most in the literature. The magnetar model has several appealing features. Dessart et al. (2012b) presented calculations of model SLSN spectra based on magnetar radiation in SN ejecta from Wolf-Rayet progenitor stars. One of these models is shown in Figure 4.6 and compared to PTF12dam and PS1-11ap. Howell et al. (2013) presented parameterised models, putting a bright (but arbitrary) central energy source inside carbon- and oxygen-rich ejecta, such as might be expected from a stripped-envelope SN. In both cases, good matches were found to observational data. Moreover, the central over-pressure from the magnetar wind is predicted to sweep up the ejecta into a shell of constant velocity (Kasen & Bildsten 2010; Woosley 2010), which would naturally explain the flat velocity curves of several SLSNe shown in Figure 6.19. Kasen et al. (2015) have also shown that the magnetar-driven shock can lead to a bright breakout transient resembling the precursor peak observed in LSQ14bdq.

The fundamental lower limit on a neutron star spin period is $P \sim 1\,\mathrm{ms}$, and Galactic magnetars have magnetic fields $B < 10^{15}\,\mathrm{G}$. None of the SLSNe yet discovered – neither the slowly declining objects, such as PTF12dam, nor the brightest SLSNe, like CSS121015 (Benetti et al. 2014) – have emitted an integrated luminosity higher than that expected for magnetars with spin periods in the range 1-10 ms. Integrating the bolometric light curves of PTF12dam and CSS121015 gives total energies of 1.2×10^{51} and 3.7×10^{51} erg, respectively, which are comfortably below the rotational energy available from a maximally rotating neutron star: $E_{\mathrm{rot}} \approx 2\times10^{52}$ erg (Kasen & Bildsten 2010). It would be a problem for the magnetar model of SLSNe if an object was discovered that could only be fit with a sub-ms spin period or magnetic field $B \gg 10^{15}\,\mathrm{G}$, but otherwise looked like a typical SLSN Ic. This could be one way to discriminate between competing models with different central engines. Very recently, Dong et al. (2015) presented ASASSN-15lh, an object that seems to resemble SLSNe Ic but with even higher luminosity ($M_u = -23.5$) and temperature ($T > 20000\,\mathrm{K}$). The integrated radiation is close to the theoretical limit for magnetar-powered SNe, and late-time observations will be needed to fully test whether this object is compatible with the magnetar model (or indeed whether it belongs in the same class as the other SLSNe Ic).

7.2.3 Interaction-powered models

Good fits to SLSN Ic light curves were also obtained with models powered by interaction of the ejecta with a massive CSM. The typical properties of our interaction fits are:

- $M_{\rm ej} \approx$ 5-30 $M_\odot$
- $M_{\rm ej}/M_{\rm CSM} \sim$ 1-2
- $E \sim$ a few $\times 10^{51}$ erg
- $R_{\rm ph} \sim 10^{15}$ cm
- $\log(\rho/{\rm g\,cm^{-2}}) \sim -12$.

One advantage of these models is that we know mass loss to be a ubiquitous phenomenon in the lives of massive stars. We also know that many SLSNe (of Type IIn; see Section 1.5.3) are very likely powered by collision with CSM. Benetti et al. (2014) showed that CSS121015, a SLSN II with similarity to SLSNe Ic in the blue part of the spectrum, exhibited time-variable narrow Balmer lines, proving that there was low-velocity material close to the SN.

However, it remains to be seen whether interaction models can reproduce the observed spectra of SLSNe Ic. These lack narrow/multicomponent lines, the traditional signature of interaction, and exhibit broad SN lines in the early spectra, which would seem to be inconsistent with the presence of an obscuring CSM shell. Perhaps a geometric effect (non-spherical CSM) could allow us to see the fast ejecta at early times, but the lack of any narrower lines from material moving at velocities significantly less than 10000 km s^{-1} could be very challenging to explain in the context of CSM interaction. By definition, SLSNe Ic do not display hydrogen or helium lines in their spectra. Does this require that the CSM is deficient in these elements? Only detailed spectral modelling of interacting SLSNe will be able to resolve these issues. Chevalier & Irwin (2011) suggested that if shock breakout occurs close to the surface of a dense wind, narrow lines could be avoided. Moriya & Tominaga (2012) extended this idea to the case of non-steady mass loss, and showed that the slope of the density profile may determine the presence/absence of narrow lines in the spectrum.

Another issue is that the interaction model has so many tuneable parameters that a wide range of models will need to be produced to compare with observations. However, light curve fitting shows that spectral modellers should focus on the SNe with several solar masses of ejecta and CSM, with $\rho_{\rm CSM} \sim 10^{-12}\,{\rm g\,cm^{-3}}$. The allowed density range seems to be quite narrow, as we saw in Section 6.4.6, because this density determines the relative slopes of the light curve rise and decline. The peak luminosity also constrains the required CSM density: a few solar masses of material (needed to efficiently thermalise the ejecta kinetic energy) distributed uniformly over 10^{15} cm (the typical blackbody radius inferred for SLSNe) gives a density of approximately

$\rho \sim 10^{33}/(10^{15})^3 = 10^{-12}\,\mathrm{g\,cm^{-3}}$. The fact that the light curve widths and their luminosity scale independently point to this density is encouraging, but the mechanism by which the CSM shells could form (with consistently similar densities) warrants further investigation. Note, however, that the flat density profile assumed for these shells may be an over-simplification. As we saw in Section 3.5.4, it is difficult to achieve dense, massive CSM at this radius through conventional stellar winds. Possible alternative scenarios include giant eruptions, perhaps powered by the pair-instability (Woosley et al. 2007), or mass loss due to binary interaction (Justham et al. 2014).

7.2.4 Concluding remarks on modelling

Direct light curve fitting has struggled to differentiate between central engines and circumstellar interaction as the primary power source in SLSNe. These models can both reproduce the observed light curves of SLSNe, and in most cases give similar (and plausible) ejecta masses and explosion energies. On the other hand, we lack a full understanding of the required progenitors to form either millisecond magnetars or such massive CSM shells.

However, taking an overview of the full spectroscopic and photometric evolution of observed SLSNe, the central engine model seems to explain their properties more consistently. In particular, the similarity of SLSNe to normal SNe Ic in their overall light curve shape (Figures 6.4 and 6.13) and late-time spectra (Figure 3.6) indicates that the two classes are likely governed by similar physics. The light curve morphology shows that a simple stretch in time (physically: a higher mass or opacity) and a boost in luminosity (increase in internal heating, compared to the 0.1 $M_\odot$ of ^{56}Ni present in SNe Ic) can map a SN Ic light curve to that of a SLSN. There is no obvious reason to expect this kind of correspondence if the luminosity increase were due to external shocks in CSM. Interacting Type IIn supernovae show a variety of light curve shapes that do not conform to a simple template (Kiewe et al. 2012; Taddia et al. 2013), and in general do not resemble the light curves of SNe Ic.

Moreover, a rapidly expanding, hydrogen-poor ejecta with a powerful internal heat source has been shown to produce a spectrum that matches the early spectra of SLSNe (Dessart et al. 2012b; Howell et al. 2013). Observations show that 20-30 days after peak, when the SLSN ejecta have cooled to a temperature regime more typical of SNe Ic, their spectra show the same lines as SNe Ic, suggesting similar ejecta composition between normal and super-luminous objects. The delayed appearance of the usual spectroscopic features (Fe II, Mg II, Ca II, Si II) in SLSNe can be explained by increased ionisation due to the higher temperature in the SLSN ejecta, in turn due to the additional heat source. This ionisation would lead to higher opacity than in other SNe Ic,

which could contribute to the broader light curves. Thus the spectra of SLSNe suggest an explosion similar to SNe Ic, differentiated only by the additional heat. If the extra energy were provided by interaction, a consistent model would need to explain why we see so little modification to the spectrum by the massive CSM, which may have a composition very different from the ejecta. In fact, in the interaction model the photosphere is expected to reside in the CSM rather than in the ejecta (e.g. Dessart et al. 2015), whereas for a central power source the photosphere and spectral formation region will necessarily be in the ejecta, as in a ^{56}Ni-powered SN Ic.

As noted above in sections 7.2.2 and 7.2.3, line velocities can be a powerful discriminant between models. The CSM model may struggle to produce a spectrum dominated by broad P Cygni lines, with $v \gtrsim 10000\,\mathrm{km\,s^{-1}}$, as most interacting SNe show narrow-line-dominated spectra. In contrast, central engine SNe should have velocities at least as high as normal SNe Ic, which is what we saw in Figure 6.20. The flat velocity curves in many SLSNe are also more consistent with an internal energy source: while the central engine tends to sweep up the ejecta into a dense shell, collision with external material should decelerate the ejecta as the kinetic energy is thermalised and lost as radiation. The caveat here is that if all of the deceleration occurs before shock breakout (such as might be the case for a very optically thick CSM), we may not observe this deceleration (Smith et al. 2008).

The final point that may disfavour the interaction model is the homogeneity of SLSN spectra. This is best seen in Figure 3.4, which shows the identical evolution of our three initial PESSTO objects and SN 2010gx, and Figure 4.5, which shows the spectroscopic similarity between the objects with fast and slow light curve evolution. Other interacting supernovae (Type IIn) show quite diverse spectra, possibly due to variations in progenitor mass-loss rates (Kiewe et al. 2012; Taddia et al. 2013).

Overall, we feel that while interaction-powered models can satisfactorily fit the light curves of SLSNe Ic, an uncomfortable degree of fine-tuning seems to be required to accommodate their other properties. If both are powered by interaction, why do SLSNe IIn show narrow lines while SLSNe Ic do not? If hydrogen-free shells are required, at large radius and with moderate velocity, this could indicate pulsational pair-instability eruptions (Woosley et al. 2007). However, this model predicts a range of velocities, collision radii and even the numbers of CSM shells. Could SLSNe Ic exhibit such homogeneous spectroscopic evolution under such a wide range of physical conditions? And why do light curve models seem to indicate such a narrow range of CSM densities (which should depend on the mass lost, its velocity, and the time since ejection)?

Based on our analysis, we propose that explosions of massive, stripped stellar cores forming magnetars (or more generally, central engines) are the most natural explana-

tion for SLSNe Ic. This model accommodates all of their observed photometric and spectroscopic properties, including peak luminosities, light curve shapes and diverse widths, blue colours, hydrogen-free spectra, and resemblance to normal SNe Ic.

7.3 Outlook and future work

Much work remains to be done to constrain the properties of SLSNe. Surveys should focus on finding more low redshift SLSNe in order to improve on the statistics, which are currently limited by the low number of objects. This should reveal more clearly whether, for example, all SLSNe Ic are drawn from a continuous population, or if there is an excess of very massive events. Additionally, we should aim to detect very young SLSNe with good photometric sampling, in order to find out the rate of LSQ14bdq-like precursor peaks. This will require repeatedly observing the same fields every night to a limiting magnitude of at least 22, though this should be a trivial task for planned future surveys, such as the Zwicky Transient Facility (Bellm 2014) and the Large Synoptic Survey Telescope (Ivezic et al. 2008). These will discover orders-of-magnitude more SNe than current surveys, among which should lurk many SLSNe. Multicolour observations at the earliest times will be essential to constrain the SEDs during the cooling phase.

Observations of SLSNe have mainly been focused on the UV, optical and NIR. Levan et al. (2013) presented the results of a search for X-rays from these events, finding mostly upper limits. However, they detected very bright X-rays from SCP06F6, at $z = 1.189$, at a surprisingly late phase from explosion. The high redshift implies a very high luminosity of $L_X \sim 10^{45}\,\mathrm{erg\,s^{-1}}$. More high-energy observations of low-redshift SLSNe are required in order to construct X-ray light curves, which may be an important clue to their power source. Magnetar models predict a late-time breakout of X-rays/γ-rays when the ionisation front, driven by the magnetar wind, reaches the ejecta surface (Metzger et al. 2014; Kotera et al. 2013). Hence regular X-ray observations are required (even if no flux is detected at early epochs) to look for an X-ray brightening weeks to months after explosion. It would be interesting to see if such events coincided with bumps in the optical light curve, such as that seen in SSS120810 (Chapter 3). Interaction models may struggle to match the observed luminosity in SCP06F6, particularly if emitted X-rays are re-absorbed in the dense CSM.

Understanding the properties of these remarkable events is essential, particularly in preparation for the future era of the James Webb Space Telescope (*JWST*) and 30m-class ground-based facilities, which will allow us to find SLSNe at redshifts up to $z \sim 10$. By understanding their physics and observational properties at low redshift, we may be able to use these explosions to probe cosmological expansion in the very

young Universe. Inserra & Smartt (2014) showed that SLSN peak magnitudes may be standardisable based on the light curve decline rate and colours. A large statistical sample is essential to better constrain the slope and scatter in this relation. Only SLSNe are luminous enough to observe in the optical and NIR at such distances, being > 10 times brighter than SNe Ia.

Additionally, SLSNe can illuminate high-redshift dwarf galaxies (Berger et al. 2012), and probe the first generation of star-formation in the Universe. So far, GRBs have been used to trace star-formation up to $z = 8.2$ (Tanvir et al. 2012; Hjorth et al. 2012). SLSNe should be used as complementary tracers. Their progenitors may be as massive as those of GRBs, or even more so (Lunnan et al. 2014; Leloudas et al. 2015), and therefore should give a more complete picture of how massive stellar populations change with redshift.

High-redshift observations may also finally discover definitive evidence for PISNe. Whalen et al. (2013) showed that PISNe may be detectable in the NIR by *JWST* as far out as $z \sim 30$. Thus the limiting factor in finding these events will not be their luminosity. The real challenge to overcome would appear to be their scarcity. Hummel et al. (2012) found an upper limit to the observable rate of 0.01 PISN per *JWST* field-of-view per year. An additional problem arises in actually identifying high-redshift PISNe as transients. The combination of their broad light curves with extreme time dilation at $z > 10$ means that many would show very little variation in magnitude over several years. Survey strategies should be carefully planned, and aim for moderate depth over a very wide area. Cadence can be sacrificed in favour of search area: 2 images per year of a PISN at $z = 10$ would correspond to a photometric measurement every ≈ 16 days in the SN rest-frame, providing reasonable temporal sampling considering that the light curve timescales are ~ 100 days.

On the theoretical side, future work should focus on calculating the spectra predicted by various models. This would be particularly useful in determining the viability of CSM interaction models for SLSNe Ic. Until such time as these synthetic spectra exist, the central engine model remains the most promising explanation for SLSNe Ic.

Bibliography

Ahn, C. P., Alexandroff, R., Prieto, C. A., et al. 2012, The Astrophysical Journal Supplement Series, 203, 21

Alard, C. & Lupton, R. H. 1998, The Astrophysical Journal, 503, 325

Aldering, G., Antilogus, P., Bailey, S., et al. 2006, The Astrophysical Journal, 650, 510

Anderson, J. P., González-Gaitán, S., Hamuy, M., et al. 2014, The Astrophysical Journal, 786, 67

Arnett, W. D. 1980, The Astrophysical Journal, 237, 541

Arnett, W. D. 1982, The Astrophysical Journal, 253, 785

Baade, W. & Zwicky, F. 1934, Proceedings of the National Academy of Sciences of the United States of America, 20, 254

Baltay, C., Rabinowitz, D., Hadjiyska, E., et al. 2012, The Messenger, 150, 34

Baltay, C., Rabinowitz, D., Hadjiyska, E., et al. 2013, Publications of the Astronomical Society of the Pacific, 125, 683

Barbary, K., Dawson, K. S., Tokita, K., et al. 2009, The Astrophysical Journal, 690, 1358

Barkat, Z., Rakavy, G., & Sack, N. 1967, Physical Review Letters, 18, 379

Bellm, E. C. 2014, arXiv preprint arXiv:1410.8185

Ben-Ami, S., Gal-Yam, A., Mazzali, P. A., et al. 2014, The Astrophysical Journal, 785, 37

Benetti, S., Nicholl, M., Cappellaro, E., et al. 2014, Monthly Notices of the Royal Astronomical Society, 441, 289

Benitez, S., Polshaw, J., Inserra, C., et al. 2014, The Astronomer's Telegram, 6118, 1

Berger, E., Chornock, R., Lunnan, R., et al. 2012, The Astrophysical Journal Letters, 755, L29

Bersten, M. C., Benvenuto, O. G., Nomoto, K., et al. 2012, The Astrophysical Journal, 757, 31

Bode, M. F. & Evans, A. 1985, Cambridge Astrophysics Series

Branch, D., Benetti, S., Kasen, D., et al. 2002, The Astrophysical Journal, 566, 1005

Brown, T., Baliber, N., Bianco, F., et al. 2013, Publications of the Astronomical Society of the Pacific, 125, 1031

Bucciantini, N., Quataert, E., Arons, J., Metzger, B., & Thompson, T. A. 2007, Monthly Notices of the Royal Astronomical Society, 380, 1541

Bucciantini, N., Quataert, E., Metzger, B., et al. 2009, Monthly Notices of the Royal Astronomical Society, 396, 2038

Buras, R., Rampp, M., Janka, H.-T., & Kifonidis, K. 2003, Physical Review Letters, 90, 241101

Buzzoni, B., Delabre, B., Dekker, H., et al. 1984, The Messenger, 38, 9

Campana, S., Mangano, V., Blustin, A., et al. 2006, Nature, 442, 1008

Cano, Z., Bersier, D., Guidorzi, C., et al. 2011, The Astrophysical Journal, 740, 41

Chatzopoulos, E. & Wheeler, J. C. 2012a, The Astrophysical Journal, 748, 42

Chatzopoulos, E. & Wheeler, J. C. 2012b, The Astrophysical Journal, 760, 154

Chatzopoulos, E., Wheeler, J. C., & Vinko, J. 2012, The Astrophysical Journal, 746, 121

Chatzopoulos, E., Wheeler, J. C., Vinko, J., Horvath, Z., & Nagy, A. 2013, The Astrophysical Journal, 773, 76

Chatzopoulos, E., Wheeler, J. C., Vinko, J., et al. 2011, The Astrophysical Journal, 729, 143

Chen, T.-W., Smartt, S. J., Bresolin, F., et al. 2013, The Astrophysical Journal, 763, L28

Chen, T.-W., Smartt, S. J., Jerkstrand, A., et al. 2015, Monthly Notices of the Royal Astronomical Society, 452, 1567

Chevalier, R. A. 1982, The Astrophysical Journal, 258, 790

Chevalier, R. A. & Fransson, C. 1994, The Astrophysical Journal, 420, 268

Chevalier, R. A. & Fransson, C. 2008, The Astrophysical Journal Letters, 683, L135

Chevalier, R. A. & Irwin, C. M. 2011, The Astrophysical Journal Letters, 729, L6

Chilingarian, I. V., Melchior, A.-L., & Zolotukhin, I. Y. 2010, Monthly Notices of the Royal Astronomical Society, 405, 1409

Chilingarian, I. V. & Zolotukhin, I. Y. 2012, Monthly Notices of the Royal Astronomical Society, 419, 1727

Chomiuk, L., Chornock, R., Soderberg, A., et al. 2011, The Astrophysical Journal, 743, 114

Clausen, D., Piro, A. L., & Ott, C. D. 2015, The Astrophysical Journal, 799, 190

Colgate, S. A., Petschek, A. G., & Kriese, J. T. 1980, The Astrophysical Journal, 237, L81

Cooke, J., Sullivan, M., Gal-Yam, A., et al. 2012, Nature, 491, 228

Couch, S. M. & Ott, C. D. 2015, The Astrophysical Journal, 799, 5

Crowther, P. A. 2007, Annual Review of Astronomy & Astrophysics, 45, 177

Dahlen, T., Strolger, L.-G., Riess, A., et al. 2004, The Astrophysical Journal, 613, 189

Davies, B., Figer, D. F., Kudritzki, R.-P., et al. 2009, The Astrophysical Journal, 707, 844

Dessart, L., Audit, E., & Hillier, D. J. 2015, arXiv preprint arXiv:1503.05463

Dessart, L., Hillier, D. J., Li, C., & Woosley, S. 2012a, Monthly Notices of the Royal Astronomical Society, 424, 2139

Dessart, L., Hillier, D. J., Livne, E., et al. 2011, Monthly Notices of the Royal Astronomical Society, 414, 2985

Dessart, L., Hillier, D. J., Waldman, R., Livne, E., & Blondin, S. 2012b, Monthly Notices of the Royal Astronomical Society: Letters, 426, L76

Dessart, L., O'Connor, E., & Ott, C. D. 2012c, The Astrophysical Journal, 754, 76

Dessart, L., Waldman, R., Livne, E., Hillier, D. J., & Blondin, S. 2013, Monthly Notices of the Royal Astronomical Society, 428, 3227

Dexter, J. & Kasen, D. 2013, The Astrophysical Journal, 772, 30

Dong, S., Shappee, B. J., Prieto, J. L., et al. 2015, ArXiv e-prints

Drake, A., Djorgovski, S., Mahabal, A., et al. 2009, The Astrophysical Journal, 696, 870

Drake, A., Djorgovski, S., Prieto, J., et al. 2010, The Astrophysical Journal Letters, 718, L127

Drout, M. R., Soderberg, A. M., Gal-Yam, A., et al. 2011, The Astrophysical Journal, 741, 97

Duncan, R. C. & Thompson, C. 1992, The Astrophysical Journal, 392, L9

Dwarkadas, V. V. 2007, The Astrophysical Journal, 667, 226

Ensman, L. & Burrows, A. 1992, The Astrophysical Journal, 393, 742

Faran, T., Poznanski, D., Filippenko, A., et al. 2014, Monthly Notices of the Royal Astronomical Society, 445, 554

Filippenko, A. 1997, Annu. Rev. Astro. Astrophys., 35, 309

Filippenko, A. V., Barth, A. J., Matheson, T., et al. 1995, The Astrophysical Journal Letters, 450, L11

Gaensler, B., McClure-Griffiths, N., Oey, M., et al. 2005, The Astrophysical Journal Letters, 620, L95

Gal-Yam, A. 2012, Science, 337, 927

Gal-Yam, A., Mazzali, P., Ofek, E., et al. 2009, Nature, 462, 624

Gal-Yam, A., Ofek, E. O., & Shemmer, O. 2002, Monthly Notices of the Royal Astronomical Society, 332, L73

Galama, T., Vreeswijk, P., Van Paradijs, J., et al. 1998, Nature, 395, 670

Gall, E., Polshaw, J., Kotak, R., et al. 2015, arXiv preprint arXiv:1502.06034

Gezari, S., Chornock, R., Rest, A., et al. 2012, Nature, 485, 217

Gezari, S., Dessart, L., Basa, S., et al. 2008, The Astrophysical Journal Letters, 683, L131

Gezari, S., Halpern, J., Grupe, D., et al. 2009, The Astrophysical Journal, 690, 1313

Gezari, S., Jones, D., Sanders, N., et al. 2015, The Astrophysical Journal, 804, 28

Ginzburg, S. & Balberg, S. 2012, The Astrophysical Journal, 757, 178

Gräfener, G. & Hamann, W.-R. 2008, Astronomy & Astrophysics, 482, 945

Greiner, J., Bornemann, W., Clemens, C., et al. 2008, Publications of the Astronomical Society of the Pacific, 120, 405

Greiner, J., Bornemann, W., Clemens, C., et al. 2007, The Messenger, 130, 12

Guetta, D. & Della Valle, M. 2007, The Astrophysical Journal Letters, 657, L73

Hartigan, J. A. & Hartigan, P. 1985, The Annals of Statistics, 70

Heger, A., Fryer, C., Woosley, S., Langer, N., & Hartmann, D. 2003, The Astrophysical Journal, 591, 288

Heger, A. & Woosley, S. 2002, The Astrophysical Journal, 567, ,

Hillier, D. J. & Miller, D. 1999, The Astrophysical Journal, 519, 354

Hjorth, J., Malesani, D., Jakobsson, P., et al. 2012, The Astrophysical Journal, 756, 187

Hjorth, J., Sollerman, J., Møller, P., et al. 2003, Nature, 423, 847

Hogg, D. W., Baldry, I. K., Blanton, M. R., & Eisenstein, D. J. 2002, arXiv preprint astro-ph/0210394

Hook, I., Jørgensen, I., Allington-Smith, J., et al. 2004, Publications of the Astronomical Society of the Pacific, 116, 425

Howell, D., Kasen, D., Lidman, C., et al. 2013, The Astrophysical Journal, 779, 98

Huber, M., Chambers, K., Flewelling, H., et al. 2015, The Astronomer's Telegram, 7153, 1

Hummel, J. A., Pawlik, A. H., Milosavljević, M., & Bromm, V. 2012, The Astrophysical Journal, 755, 72

Inserra, C., Smartt, S., Jerkstrand, A., et al. 2013, The Astrophysical Journal, 770, 128

Inserra, C. & Smartt, S. J. 2014, The Astrophysical Journal, 796, 87

Inserra, C., Smartt, S. J., Fraser, M., et al. 2012, The Astronomer's Telegram, 4329, 1

Ivezic, Z., Tyson, J., Abel, B., et al. 2008, arXiv preprint arXiv:0805.2366

Janka, H.-T., Langanke, K., Marek, A., Martínez-Pinedo, G., & Müller, B. 2007, Physics Reports, 442, 38

Janka, H.-T. & Müller, E. 1996, Astronomy and Astrophysics, 306, 167

Joggerst, C. & Whalen, D. J. 2011, The Astrophysical Journal, 728, 129

Jordi, K., Grebel, E. K., & Ammon, K. 2006, Astronomy & Astrophysics, 460, 339

Justham, S., Podsiadlowski, P., & Vink, J. S. 2014, The Astrophysical Journal, 796, 121

Kaiser, N., Burgett, W., Chambers, K., et al. 2010, in SPIE Astronomical Telescopes+ Instrumentation, International Society for Optics and Photonics, 77330E–77330E

Kasen, D. & Bildsten, L. 2010, The Astrophysical Journal, 717, 245

Kasen, D., Metzger, B., & Bildsten, L. 2015, ArXiv e-prints

Kasen, D., Woosley, S., & Heger, A. 2011, The Astrophysical Journal, 734, 102

Keller, S. C., Schmidt, B. P., Bessell, M. S., et al. 2007, Publications of the Astronomical Society of Australia, 24, 1

Kiewe, M., Gal-Yam, A., Arcavi, I., et al. 2012, The Astrophysical Journal, 744, 10

Klein, R. & Chevalier, R. 1978, The Astrophysical Journal, 223, L109

Kobayashi, C., Tominaga, N., & Nomoto, K. 2011, The Astrophysical Journal Letters, 730, L14

Kotera, K., Phinney, E. S., & Olinto, A. V. 2013, Monthly Notices of the Royal Astronomical Society, 432, 3228

Krühler, T., Küpcü Yoldaş, A., Greiner, J., et al. 2008, The Astrophysical Journal, 685, 376

Kulkarni, S. & Kasliwal, M. 2009, in Proc. RIKEN Symp.), ed. N. Kawai, T. Mihara, M. Kohama, & M. Suzuki (Saitama: RIKEN), Vol. 312

Leitherer, C., Schaerer, D., Goldader, J. D., et al. 1999, The Astrophysical Journal Supplement Series, 123, 3

Leloudas, G., Chatzopoulos, E., Dilday, B., et al. 2012, Astronomy & Astrophysics, 541, A129

Leloudas, G., Ergon, M., Taddia, F., et al. 2014, The Astronomer's Telegram, 5839, 1

Leloudas, G., Schulze, S., Krühler, T., et al. 2015, Monthly Notices of the Royal Astronomical Society,, 449, 917

Levan, A. J., Read, A., Metzger, B., Wheatley, P., & Tanvir, N. 2013, The Astrophysical Journal, 771, 136

Li, W., Leaman, J., Chornock, R., et al. 2011, Monthly Notices of the Royal Astronomical Society, 412, 1441

Lucy, L. 1987, Astronomy & Astrophysics, 182, L31

Lunnan, R., Chornock, R., Berger, E., et al. 2014, The Astrophysical Journal, 787, 138

Lunnan, R., Chornock, R., Berger, E., et al. 2013, The Astrophysical Journal, 771, 97

Lunnan, R., Chornock, R., Berger, E., et al. 2015, The Astrophysical Journal, 804, 90

MacFadyen, A. & Woosley, S. 1999, The Astrophysical Journal, 524, 262

Magnier, E., Kaiser, N., & Chambers, K. C. 2006, in The Advanced Maui Optical and Space Surveillance Technologies Conference, Vol. 1, 50

Magnier, E., Liu, M., Monet, D., & Chambers, K. 2008, in IAU Symposium, Vol. 248, 553–559

Magnier, E., Schlafly, E., Finkbeiner, D., et al. 2013, The Astrophysical Journal Supplement Series, 205, 20

Matheson, T., Garnavich, P., Stanek, K., et al. 2003, The Astrophysical Journal, 599, 394

Mazzali, P., Deng, J., Maeda, K., et al. 2002, The Astrophysical Journal Letters, 572, L61

Mazzali, P. A., Deng, J., Nomoto, K., et al. 2006a, Nature, 442, 1018

Mazzali, P. A., Deng, J., Pian, E., et al. 2006b, The Astrophysical Journal, 645, 1323

McCrum, M., Smartt, S., Kotak, R., et al. 2014, Monthly Notices of the Royal Astronomical Society, 437, 656

McCrum, M., Smartt, S. J., Rest, A., et al. 2015, Monthly Notices of the Royal Astronomical Society, 448, 1206

McKee, C. F. & Draine, B. T. 1991, Science, 252, 397

Mcley, L. & Soker, N. 2014, Monthly Notices of the Royal Astronomical Society, 445, 2492

Metzger, B. D., Giannios, D., Thompson, T. A., Bucciantini, N., & Quataert, E. 2011, Monthly Notices of the Royal Astronomical Society, 413, 2031

Metzger, B. D., Vurm, I., Hascoët, R., & Beloborodov, A. M. 2014, Monthly Notices of the Royal Astronomical Society, 437, 703

Miller, A., Chornock, R., Perley, D., et al. 2009, The Astrophysical Journal, 690, 1303

Modjaz, M., Kewley, L., Kirshner, R., et al. 2008, The Astronomical Journal, 135, 1136

Modjaz, M., Li, W., Butler, N., et al. 2009, The Astrophysical Journal, 702, 226

Modjaz, M., Stanek, K., Garnavich, P., et al. 2006, The Astrophysical Journal Letters, 645, L21

Moorwood, A., Cuby, J.-G., & Lidman, C. 1998, The Messenger, 91, 9

Moriya, T., Tominaga, N., Tanaka, M., Maeda, K., & Nomoto, K. 2010, The Astrophysical Journal, 717, L83

Moriya, T. J. & Maeda, K. 2012, The Astrophysical Journal Letters, 756, L22

Moriya, T. J. & Tominaga, N. 2012, The Astrophysical Journal, 747, 118

Nagataki, S., Mizuta, A., & Sato, K. 2006, The Astrophysical Journal, 647, 1255

Nakar, E. & Sari, R. 2010, The Astrophysical Journal, 725

Neill, J. D., Sullivan, M., Gal-Yam, A., et al. 2011, The Astrophysical Journal, 727, 15

Nicholl, M., Smartt, S., Jerkstrand, A., et al. 2013, Nature, 502, 346

Nicholl, M., Smartt, S., Jerkstrand, A., et al. 2015, The Astrophysical Journal Letters, 807, L18

Nicholl, M., Smartt, S. J., Jerkstrand, A., et al. 2014, Monthly Notices of the Royal Astronomical Society, 444, 2096

Nordhaus, J., Burrows, A., Almgren, A., & Bell, J. 2010, The Astrophysical Journal, 720, 694

Ochsenbein, F. 1994, Bulletin d'Information du Centre de Donnees Stellaires, 44, 19

O'Connor, E. & Ott, C. D. 2011, The Astrophysical Journal, 730, 70

Ofek, E., Cameron, P., Kasliwal, M., et al. 2007, The Astrophysical Journal Letters, 659, L13

Ofek, E., Rabinak, I., Neill, J., et al. 2010, The Astrophysical Journal, 724, 1396

Ofek, E. O., Fox, D., Cenko, S. B., et al. 2013, The Astrophysical Journal, 763, 42

Oke, J. & Sandage, A. 1968, The Astrophysical Journal, 154, 21

Osterbrock, D. E. 1989, Astrophysics of gaseous nebulae and active galactic nuclei

Ostriker, J. P. & Gunn, J. E. 1971, The Astrophysical Journal, 164, L95

Ott, C. D., Abdikamalov, E., Mösta, P., et al. 2013, The Astrophysical Journal, 768, 115

Pastorello, A., Smartt, S., Botticella, M., et al. 2010, The Astrophysical Journal Letters, 724, L16

Pastorello, A., Taubenberger, S., Elias-Rosa, N., et al. 2007, Monthly Notices of the Royal Astronomical Society, 376, 1301

Patat, F., Barbon, R., Cappellaro, E., & Turatto, M. 1994, Astronomy & Astrophysics, 282, 731

Patat, F., Cappellaro, E., Danziger, J., et al. 2001, The Astrophysical Journal, 555, 900

Pei, Y. C. 1992, The Astrophysical Journal, 395, 130

Perlmutter, S., Aldering, G., Goldhaber, G., et al. 1999, The Astrophysical Journal, 517, 565

Phillips, M. M. 1993, The Astrophysical Journal, 413, L105

Piro, A. L. 2015, arXiv preprint arXiv:1505.07103

Piro, A. L., Chang, P., & Weinberg, N. N. 2010, The Astrophysical Journal, 708, 598

Piro, A. L. & Nakar, E. 2013, The Astrophysical Journal, 769, 67

Piro, A. L. & Nakar, E. 2014, The Astrophysical Journal, 784, 85

Podsiadlowski, P., Mazzali, P., Nomoto, K., Lazzati, D., & Cappellaro, E. 2004, The Astrophysical Journal Letters, 607, L17

Poole, T., Breeveld, A., Page, M., et al. 2008, Monthly Notices of the Royal Astronomical Society, 383, 627

Poznanski, D., Prochaska, J. X., & Bloom, J. S. 2012, Monthly Notices of the Royal Astronomical Society, 426, 1465

Prieto, J. L., Garnavich, P. M., Phillips, M. M., et al. 2007, ArXiv e-prints

Quimby, R., Arcavi, I., Sternberg, A., et al. 2012, The Astronomer's Telegram, 4121, 1

Quimby, R. M., Aldering, G., Wheeler, J. C., et al. 2007, The Astrophysical Journal Letters, 668, L99

Quimby, R. M., Kulkarni, S., Kasliwal, M. M., et al. 2011, Nature, 474, 487

Quimby, R. M., Yuan, F., Akerlof, C., & Wheeler, J. C. 2013, Monthly Notices of the Royal Astronomical Society, 431, 912

Rabinak, I. & Waxman, E. 2011, The Astrophysical Journal, 728, 63

Rabinowitz, D., Schwamb, M. E., Hadjiyska, E., & Tourtellotte, S. 2012, The Astronomical Journal, 144, 140

Rakavy, G. & Shaviv, G. 1967, The Astrophysical Journal, 148, 803

Rau, A., Kulkarni, S. R., Law, N. M., et al. 2009, Publications of the Astronomical Society of the Pacific, 121, 1334

Rest, A., Foley, R., Gezari, S., et al. 2011, The Astrophysical Journal, 729, 88

Richardson, D., Branch, D., Casebeer, D., et al. 2002, The Astronomical Journal, 123, 745

Richardson, D., Jenkins, III, R. L., Wright, J., & Maddox, L. 2014, The Astrophysical Journal, 147, 118

Richmond, M. W., Van Dyk, S., Ho, W., et al. 1996, The Astronomical Journal, 111, 327

Riess, A. G., Filippenko, A. V., Challis, P., et al. 1998, The Astronomical Journal, 116, 1009

Sanders, N. E., Soderberg, A., Valenti, S., et al. 2012, The Astrophysical Journal, 756, 184

Schawinski, K., Justham, S., Wolf, C., et al. 2008, Science, 321, 223

Schlafly, E. F. & Finkbeiner, D. P. 2011, The Astrophysical Journal, 737, 103

Schlegel, E. M. 1990, Monthly Notices of the Royal Astronomical Society, 244, 269

Schulze, S., Malesani, D., Cucchiara, A., et al. 2014, Astronomy & Astrophysics, 566, A102

Shigeyama, T. & Nomoto, K. 1990, The Astrophysical Journal, 360, 242

Shiode, J. H. & Quataert, E. 2014, The Astrophysical Journal, 780, 96

Skrutskie, M. F., Cutri, R. M., Stiening, R., et al. 2006, The Astronomical Journal, 131, 1163

Smartt, S. J. 2009, Annu. Rev. Astro. Astrophys., 47, 63

Smartt, S. J., Nicholl, M., Inserra, C., et al. 2013, The Astronomer's Telegram, 5128, 1

Smartt, S. J., Smith, K. W., Wright, D., et al. 2014, The Astronomer's Telegram, 5850, 1

Smartt, S. J., Valenti, S., Fraser, M., et al. 2015, Astronomy & Astrophysics, 579, A40

Smith, N., Chornock, R., Li, W., et al. 2008, The Astrophysical Journal, 686, 467

Smith, N., Li, W., Foley, R. J., et al. 2007, The Astrophysical Journal, 666, 1116

Smith, N. & McCray, R. 2007, The Astrophysical Journal Letters, 671, L17

Soderberg, A., Berger, E., Page, K., et al. 2008, Nature, 453, 469

Sollerman, J., Jaunsen, A., Fynbo, J., et al. 2006, Astronomy & Astrophysics, 454, 503

Stanek, K. Z., Matheson, T., Garnavich, P., et al. 2003, The Astrophysical Journal Letters, 591, L17

Steele, I. A., Smith, R. J., Rees, P. C., et al. 2004, Astronomical Telescopes and Instrumentation, 679

Stephenson, F. R. & Green, D. A. 2002, Historical supernovae and their remnants

Stritzinger, M., Hamuy, M., Suntzeff, N. B., et al. 2002, The Astronomical Journal, 124, 2100

Taddia, F., Sollerman, J., Leloudas, G., et al. 2015, Astronomy & Astrophysics, 574, A60

Taddia, F., Stritzinger, M., Sollerman, J., et al. 2013, Astronomy & Astrophysics, 555, A10

Tanvir, N., Levan, A., Fruchter, A., et al. 2012, The Astrophysical Journal, 754, 46

Taubenberger, S., Pastorello, A., Mazzali, P., et al. 2006, Monthly Notices of the Royal Astronomical Society, 371, 1459

Thomas, R., Nugent, P., & Meza, J. 2011, Publications of the Astronomical Society of the Pacific, 123, 237

Thompson, T. A., Chang, P., & Quataert, E. 2004, The Astrophysical Journal, 611, 380

Tonry, J., Stubbs, C., Kilic, M., et al. 2012a, The Astrophysical Journal, 745, 42

Tonry, J., Stubbs, C., Lykke, K., et al. 2012b, The Astrophysical Journal, 750, 99

Umeda, H. & Nomoto, K. 2008, The Astrophysical Journal, 673, 1014

Valenti, S., Benetti, S., Cappellaro, E., et al. 2008a, Monthly Notices of the Royal Astronomical Society, 383, 1485

Valenti, S., Elias-Rosa, N., Taubenberger, S., et al. 2008b, The Astrophysical Journal Letters, 673, L155

Valenti, S., Fraser, M., Benetti, S., et al. 2011, Monthly Notices of the Royal Astronomical Society, 416, 3138

Valenti, S., Taubenberger, S., Pastorello, A., et al. 2012, The Astrophysical Journal Letters, 749, L28

Van Dokkum, P. G. 2001, Publications of the Astronomical Society of the Pacific, 113, 1420

Vernet, J., Hjorth, J., Guinouard, I., et al. 2011, Astronomy & Astrophysics, 536, 105

Vreeswijk, P. M., Savaglio, S., Gal-Yam, A., et al. 2014, The Astrophysical Journal, 797, 24

Wang, S., Wang, L., Dai, Z., & Wu, X. 2015, The Astrophysical Journal, 799, 107

Whalen, D. J., Even, W., Frey, L. H., et al. 2013, The Astrophysical Journal, 777, 110

Wheeler, J. C., Johnson, V., & Clocchiatti, A. 2015, Monthly Notices of the Royal Astronomical Society, 450, 1295

Woosley, S. 1993, The Astrophysical Journal, 405, 273

Woosley, S. 2010, The Astrophysical Journal Letters, 719, L204

Woosley, S., Blinnikov, S., & Heger, A. 2007, Nature, 450, 390

Woosley, S. & Bloom, J. 2006, Annu. Rev. Astron. Astrophys., 44, 507

Woosley, S., Eastman, R. G., Weaver, T. A., & Pinto, P. A. 1994, The Astrophysical Journal, 429, 300

Wright, D., Smartt, S., Smith, K., et al. 2015, arXiv preprint arXiv:1501.05470

Wright, E. L. 2006, Publications of the Astronomical Society of the Pacific, 118, 1711

Wyrzykowski, L., Kostrzewa-Rutkowska, Z., Kozlowski, S., et al. 2014, Acta Astronomica, 64, 197

Yaron, O. & Gal-Yam, A. 2012, Publications of the Astronomical Society of the Pacific, 124, 668

Yoldaş, A. K., Krühler, T., Greiner, J., et al. 2008, in American Institute of Physics Conference Series, Vol. 1000, American Institute of Physics Conference Series, ed. M. Galassi, D. Palmer, & E. Fenimore, 227

Young, D., Smartt, S., Mattila, S., et al. 2008, Astronomy & Astrophysics, 489, 359

Young, D., Smartt, S., Valenti, S., et al. 2010, Astronomy & Astrophysics, 512, A70

Yusof, N., Hirschi, R., Meynet, G., et al. 2013, Monthly Notices of the Royal Astronomical Society, 433, 1114

Zwicky, F. 1939, Physical Review, 55, 726